THÈSE

En vue de l'obtention du

DOCTORAT DE L'UNIVERSITÉ DE TOULOUSE

Délivré par : *l'Université Toulouse 3 Paul Sabatier (UT3 Paul Sabatier)*

Présentée et soutenue le *24/02/2022* **par :**

Duy Thai TO

Variabilité interannuelle et intrasaisonnière de l'Upwelling du Sud Vietnam: le rôle du forçage atmosphérique haute fréquence, de la dynamique océanique hauturière et côtière et de la variabilité intrinsèque océanique

---

JURY

Rosemary MORROW	LEGOS	Président du Jury/Examinatrice
Alexei SENTCHEV	ULCO	Rapporteur
François COLAS	IRD, LOCEAN	Rapporteur
Luong Hong Phuoc VO	HCMUS	Rapporteur
Hong Long BUI	IO, VAST	Invité
Marine HERRMANN	IRD, LEGOS	Co-directrice de thèse
Claude ESTOURNEL	CNRS, LEGOS	Directrice de thèse

École doctorale et spécialité :
SDU2E : Océan, Atmosphère, Climat

Unité de Recherche :
Laboratoire d'Études en Géophysique et Océanographie Spatiales (UMR 5566)

Directeur(s) de Thèse :
Claude ESTOURNEL et *Marine HERRMANN*

Rapporteurs :
Alexei SENTCHEV, *François COLAS* et *Luong Hong Phuoc VO*

THESIS

In order to obtain the
DOCTORATE FROM THE UNIVERSITY OF TOULOUSE
Awarded by the University of Toulouse 3 - Paul Sabatier

Presented and supported by

Duy Thai TO

February 24, 2022

Interannual to intraseasonal variability of the South Vietnam Upwelling. The role of high frequency atmospheric forcing, mesoscale dynamics, coastal circulation and intrinsic variability

Doctoral school: **SDU2E - Geosciences, Astrophysics, Space and Environmental Sciences**

Specialty: **Ocean, Atmosphere, Climate**

Research Unit :

LEGOS - Laboratory of Space Geophysical and Oceanographic Studies

Thesis directed by

Claude ESTOURNEL and Marine HERRMANN

Jury

Mr. Alexei SENTCHEV, Rapporteur
Mr. François COLAS, Rapporteur
Ms. Luong Hong Phuoc VO, Rapporteur
Ms. Rosemary MORROW, Examiner
Ms. Claude ESTOURNEL, Thesis director
Ms. Marine HERRMANN, Thesis director
Mr. Hong Long BUI, guest member

Acknowledgements

Now, when I look back on the journey that I have been able to complete this thesis, I found that I really have gone a long way and have too many people to remember and can hardly describe in words.

This thesis was started in March 2018 under the guidance of Dr. Marine Herrmann (IRD/LEGOS research director), one of my thesis supervisors, was also my master's internship instructor in 2016, when she was Header of WEO department, USTH-VAST. Since then I've been sticking to this field so far. I would like to deeply thank Dr. Marine for offering me this ambitious and very interesting thesis topic, who always wanted me to go further in the study with a bit of pressure on the job, yet very friendly.

I also would like to express my sincerest thanks to my thesis director, Dr. Claude Estournel (CNRS/LEGOS research director). I am grateful to her for her time, her encouragement, her support and her sympathy throughout this project. Thank you for always listening and thank you for teaching me a lot, in particular during my first year PhD in France.

This thesis would never have seen the light of day without the support of the people of the SIROCCO and ECOLA groups in LEGOS. I warmly thank Patrick Marsaleix, Thomas Duhaut, Cyril Nguyen, Nadia Ayoub, and Caroline Ulses for their involvement, not only in the technical aspect but also in the scientific orientation of the project. I really appreciated the warm welcome they gave me and the very friendly working environment within the group. In particular Thomas, who supported me a lot during the time I started to come to France, not only that, he also supported me with all the difficulties that I encountered throughout the thesis, even after I graduated and return to Vietnam.

I address my sincere thanks to the IT team of the LAERO and LEGOS: Didier Gazen, Laurent Cabanas, Jeremy Leclercq, Caroline David-Martin, and to Kien (the engineer in charge of the Hilo cluster), for their great support, competence and their availability each time I encountered difficulties.

To complete the thesis well, it is impossible not to mention the logistics of LAERO and LEGOS. I would like to express my sincere thanks to Madam Marisa Vialet and "my mother" Brigitte Cournou for always accompanying and helping me in all difficulties.

I also do not forget to thank my friends who have helped me a lot during my thesis work: Margaux Hilt, Azusa Takeishi at LAERO, Violaine, Simon, Roberto Ray-Herrera, Quentin and the community Vietnam at LEGOS: Ngoc, Tung, Viet, Hanh, Thai em, Hue, and also Da (who gave me a lot of advice and talked to me a lot during the COVID-19 period and inspired me to keep going the running. So, I can run the first 21km).

During my time in France, I also received very enthusiastic help from the Vietnamese association in Toulouse, I would like to thank my very close friends: Uncle Liem and his wife, Huong, Tam, Tien , Mr. Phuong, Ms. Thuy, Kien-Hoa family; My group "Chu du Toulouse": Minh Anh, Nguyen, Nga Ngoet, Quyen, Tien, Nhien, Giap, Truong; and the tennis team when I'm stressed: Mr. Phong, Bojan, Damien; distant friends: Mai Chan, Trang, and Hanh.

I would also like to thank the Institut de Recherche pour le Développement (IRD) and the French Embassy in Hanoi for the financial support I received during my doctorate.

I would also like to thank my colleagues in the Department of Marine Physics, Institute of Oceanography, especially Professor Bui Hong Long, who guided and imparted to me a lot about his research experiences. To be able to attend a Phd course at LEGOS-Université Toulouse III Paul Sabatier, I can not do without the help of my colleagues in Vietnam, so I would like to thank them also.

Finally, during the time away from home to focus on the thesis, a solid rear is the foundation for me to study with peace of mind, I would like to express my deepest gratitude to my wife, who has always takes care of our family and our young children (Tona and Tony) well. Besides, I would like to thank my Daddy and Mom, who have always supported me the most on my research path. This thesis is dedicated to them.

Toulouse, December 09, 2021.

Tô Duy Thái.

Table of Contents

List of Figures

LIST OF FIGURES

List of Tables

Résumé

L'Upwelling du Sud Vietnam (SVU) se développe en été au large de la côte vietnamienne (mer de Chine du Sud, SCS) sous l'influence des vents de mousson du sud-ouest. Une configuration haute résolution (1 km à la côte) du modèle SYMPHONIE a été développée pour étudier le fonctionnement, la variabilité et l'influence du SVU. Une simulation a d'abord été réalisée sur la période 2009-2018. Le réalisme de cette simulation en termes de représentation de la dynamique océanique et des masses d'eau, des échelles journalière à interannuelle, et côtière à régionale, a été évalué en détail par comparaison avec les données satellitaires disponibles et quatre jeux d'observations in-situ. Cette simulation a ensuite été utilisée pour examiner la variabilité interannuelle du SVU sur ses principales zones de développement: les zones côtières sud (BoxSC) et nord (BoxNC), et la zone offshore (BoxOF). Pour BoxSC et BoxOF, nos résultats confirment que l'intensité moyenne estivale du vent dans la région et de la circulation induite pilotent au premier ordre cette variabilité Ils révèlent de plus qu'elle est modulée par l'organisation spatiale et temporelle des structures océaniques de méso-échelle et du forçage atmosphérique de haute fréquence. Pour BoxNC, la variabilité interannuelle de l'upwelling est principalement déterminée par la circulation côtière et les structures de méso-échelle: des conditions de vent estivales similaires peuvent être associées à des intensités d'upwelling très contrastées, et vice versa, en fonction de la circulation dans la zone. Nous avons ensuite réalisé un ensemble de 10 simulations jumelles avec des conditions initiales perturbées pour examiner les mécanismes impliqués dans la variabilité journalière à intrasaisonnière de l'upwelling. Cet ensemble révèle le rôle de la chronologie quotidienne à intrasaisonnière du vent, mais aussi la forte influence de la variabilité intrinsèque de l'océan (OIV), liée à l'influence de la circulation côtière et de mésoéchelle.

Abstract

The South Vietnam Upwelling (SVU) develops off the Vietnamese coast (South China Sea, SCS) under the influence of southwest summer monsoon winds. A high resolution configuration (1 km at the coast) of the SYMPHONIE model was developed to study the functioning, variability and influence of the SVU. A simulation was first performed over the period 2009-2018. The realism of the simulation in terms of representation of ocean dynamics and water masses, from daily to interannual, and coastal to regional scales, was assessed in detail by comparison with available satellite data and four sets of in-situ observations. The interannual variability of the SVU is examined over its main areas of development: the southern (BoxSC) and northern (BoxNC) coasts, and the offshore area (BoxOF). For BoxSC and BoxOF, our results confirm the driving role of the summer regional mean wind and induced circulation. They moreover reveal that the spatial and temporal organization of mesoscale ocean structures and high frequency atmospheric forcing modulate this interannual variability. For BoxNC, the upwelling interannual variability is mainly determined by coastal circulation and mesoscale structures: similar summer wind conditions can be associated with very contrasting upwelling intensities, and vice versa, depending on the circulation in the BoxNC area. We then perform an ensemble of 10 twin simulations with perturbed initial conditions to examine the mechanisms involved in the daily to intraseasonal variability of upwelling. This ensemble reveals the role of the daily to intraseasonal chronology of wind forcing, but also the strong influence of Ocean Intrinsic Variability (OIV), related to the influence of coastal and mesoscale circulation.

Introduction Générale

L'upwelling est un processus dynamique important dans l'océan (LaFond, 1963). Il se produit lorsque des eaux profondes denses et froides remontent à la surface, remplaçant les eaux de surface plus chaudes qui ont été éloignées de la côte par le transport d'Ekman induit par le vent parallèle à la côte (Fig. 0.1). Cette eau remontée, généralement riche en nutriments, provoque la prolifération du phytoplancton à la surface. Par conséquent, l'upwelling joue un rôle très important dans la circulation thermohaline car il constitue une branche de retour de l'océan profond vers la surface, et influence les écosystèmes marins. Les 5 principales zones d'upwelling permanent sont: Canaries (Afrique du Nord-Ouest), Benguela (Afrique du Sud), Californie, le système de Humboldt (Pérou et Chili) et Somalie (Somalie et Oman). Ces zones fournissent d'abondantes ressources halieutiques (environ 25% de la production mondiale de poisson est capturée dans ces 5 régions, bien qu'elles ne représentent que 5% de la surface de la mer, Jennings, 2001). L'upwelling se développe également de manière plus intermittente ou saisonnière dans d'autres zones, comme nous le verrons dans cette thèse. L'upwelling peut être détecté à partir de données satellites car il induit une faible température de surface de la mer (SST) et une forte concentration de chlorophylle-a en surface (Anderson et al., 1993, Sarhan et al., 2000). Par exemple, la Fig. 0.2 montre la moyenne des SST d'été calculée à partir des données AVHRR en Mer de Chine méridionale (SCS), révélant clairement une zone de faible SST dans le centre de la SCS, au large de la côte vietnamienne, qui correspond à l'Upwelling du Sud Vietnam (SVU).

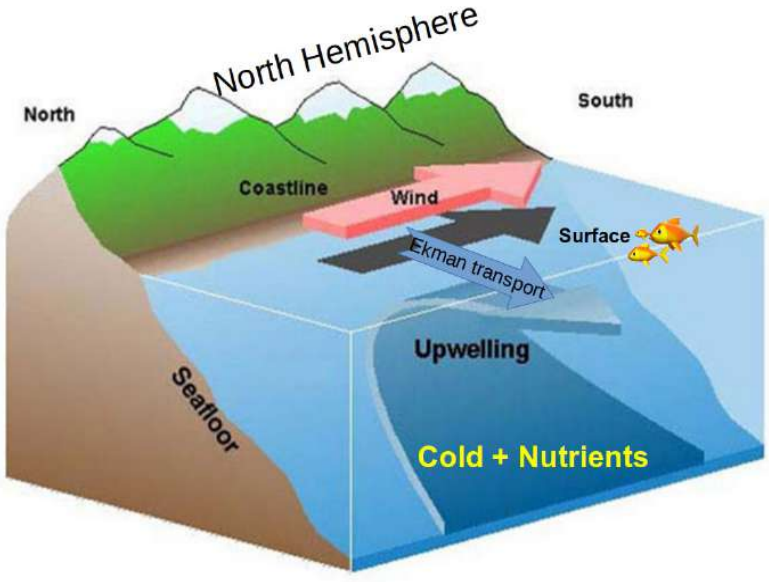

Figure 0. 1 explication schématique de l'upwelling

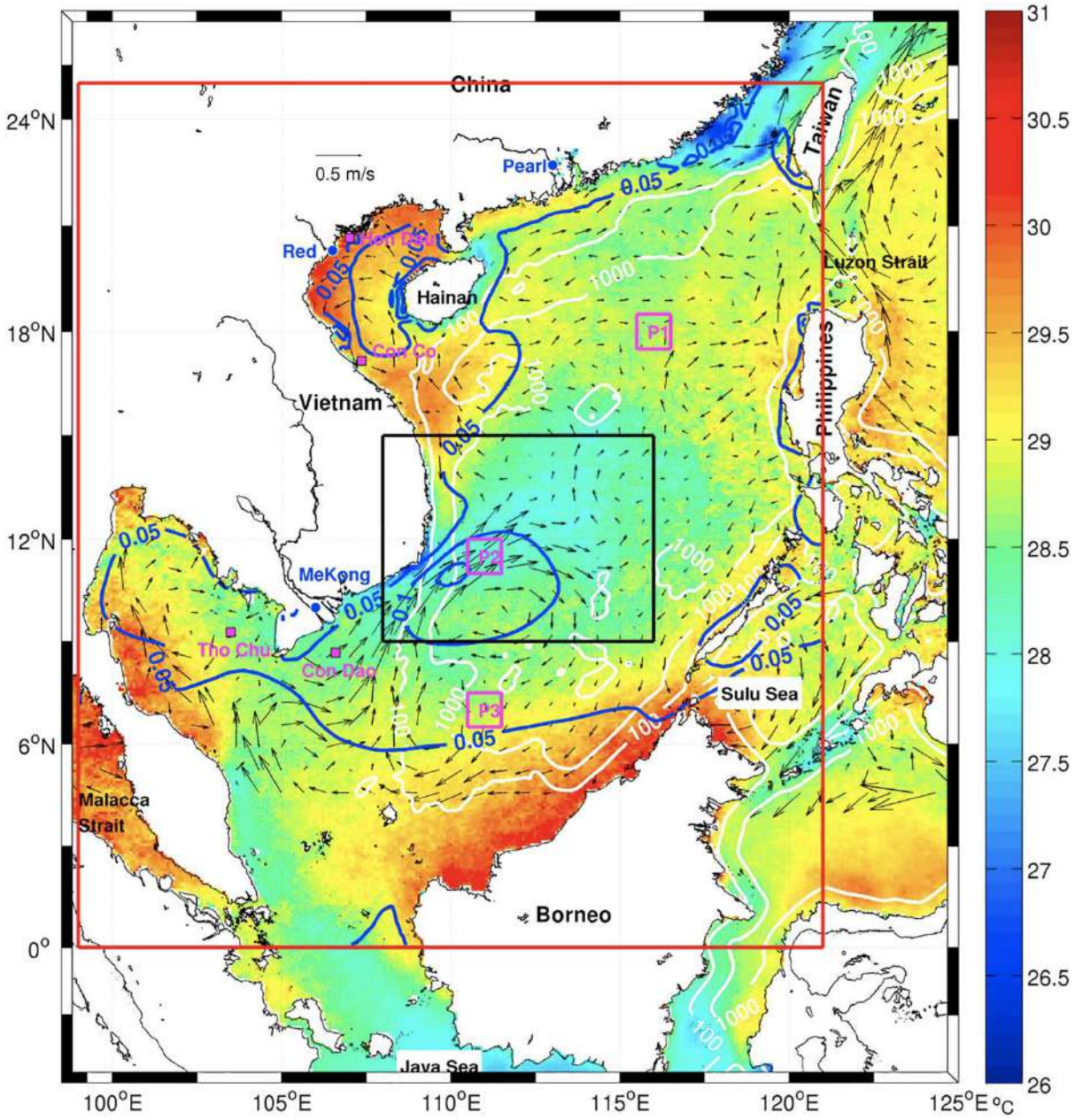

Figure 0. 2 La région de SCS et du SVU, extrait de Da et al., (2019). Contours de bathymétrie de 100 et 1 000 m (lignes blanches continues). Sont également représentés la SST moyenne climatologique du mois d'août (°C, couleurs, à partir des données satellitaire de SST Advanced Very High Resolution Radiometer, Casey et al., 2010), la circulation géostrophique de surface (m/s, vecteurs noirs, à partir des données altimétriques CMEMS, http://marine.copernicus.eu/), et les contours de stress de vent moyen (N/m2, lignes continues bleues, à partir de la réanalyse CFSR du National Center for Atmospheric Research, Saha et al., 2010).

L'upwelling du sud du Vietnam (SVU) se produit au large des côtes vietnamiennes, en SCS, pendant la mousson d'été du sud-ouest (Fig. 0.2). Il affecte fortement les écosystèmes marins, et cette région est une zone clé pour la biodiversité et les ressources halieutiques. Selon le Bureau général des statistiques du Vietnam (Statistical Yearbook of Vietnam, https://www.gso.gov.vn/en/data-and-statistics/), la production halieutique dans le centre-sud du Vietnam a atteint 734 000 tonnes/an (soit 11 % de la production nationale) au cours de la

période 2010-2019. La circulation estivale à grande échelle sur le SCS est généralement caractérisée par une circulation anticyclonique globale résultant des vents de mousson d'été du sud-ouest (Wang et al., 2004). Elle est composée plus précisément d'un courant de bord ouest et d'une structure dipolaire qui se développe le long de la côte vietnamienne, avec un gyre anticyclonique (AC) au sud et un gyre cyclonique (C) au nord (Fig. 0.2). Cette structure dipolaire induit des courants côtiers longeant la côte vers le nord/sud qui sont les composantes occidentales des gyres AC/C, et un jet offshore marqué vers l'est qui se développe au niveau de la zone de convergence des deux courants côtiers et entre les deux gyres, autour de ~12°N (Xu et al., 1982, Fang et al., 2002, Xie et al., 2003,2007, Chen et Wang 2014, Li et al., 2014, 2017).

Les premières études observationnelles de l'upwelling au large des côtes du Vietnam ont été réalisées par Chevey (1934) et Krenpf & Chevey (1934), qui ont observé une augmentation de la production halieutique en été le long de la côte du Vietnam. Le projet NAGA axé sur le SVU a ensuite été réalisé par Wyrtki (1961), Robinson (1961) et LaFond (1961). Le Vietnam a réalisé d'autres études sur le SVU avec le programme 48B (1981 - 1990) et le programme KT.03 (1991-1995) dirigé par l'Institut Océanographique (IO, Nha Trang, Vietnam). Des études in-situ du SVU ont ensuite été réalisées dans le cadre du projet de coopération entre le Vietnam (IO) et l'Allemagne (The Leibniz Institute for Baltic Sea Research Warnemünde, and Institute of Biogeochemistry and Marine Chemistry) en 2003-2006. Ces campagnes ont permis d'identifier l'extension régionale (de 10,5°N à 11,5°N) et la période (de mai à septembre, plus forte en juillet-août) du SVU (Dippner et al., 2007, Hein, 2008). De plus, ces campagnes ainsi que les études d'observation et de modélisation réalisées au cours des deux dernières décennies ont grandement contribué à améliorer notre compréhension du fonctionnement et de la variabilité du SVU.

Le forçage des vents d'été et la circulation à grande échelle qui en résulte induisent le SVU. Le SVU est induit au premier ordre par le forçage atmosphérique, à savoir le transport d'Ekman induit par le vent de mousson du sud-ouest (Xie et al., 2003). Il est en outre renforcé par le jet dirigé vers l'est qui augmente l'advection vers le large des eaux côtières (Dippner et al., 2007) et par la combinaison du pompage d'Ekman induit par le vent et de la vorticité positive de surface associée aux tourbillons cycloniques dans la zone du large (Da et al., 2019, Ngo and Hsin, 2021). Des campagnes de terrain (Dippner et al., 2007, Bombar et al., 2010, Loick-Wilde et al., 2017), des observations satellitaires (Xie et al., 2003, Kuo et al., 2004, Ngo et Hsin, 2021) et des études de modélisation (Li et al., 2014, Da et al., 2019), ont montré que le SVU peut fortement varier d'une année à l'autre. Cette variabilité interannuelle dépend notamment de l'intensité du vent de mousson d'été de sud-ouest et d'ENSO, mais aussi des vents trans-équatoriaux (Wu et al., 2019) et de la variabilité climatique décennale

(Wang et al., 2020). Deux études récentes basées sur de longues simulations ou des ensembles de données ont établi des relations statistiques entre la variabilité interannuelle de l'intensité du SVU, le forçage atmosphérique et la circulation générale. Elles ont quantifié le lien entre la variabilité interannuelle de l'upwelling et l'intensité de la circulation océanique estivale (jet vers l'est, dipôle AC/C et courants de bord associés) induite par le vent de mousson d'été. Ces études ont en outre montré que l'upwelling se développe parfois le long de la partie nord de la côte, de 11°N à 15°N. Da et al., (2019) ont également révélé et quantifié la contribution importante de la variabilité intrinsèque océanique (OIV) dans la variabilité interannuelle de la SVU dans la zone offshore, principalement liée au rôle de la vorticité associée à des structures de mésoéchelle de nature fortement chaotique.

La plupart des études précédentes étaient basées sur des ensembles de données numériques ou observationnelles associés à plusieurs contraintes méthodologiques: périodes d'étude courtes et couverture spatiale limitée des jeux de données in-situ, résolution des modèles supérieure pas plus fine que ~10 km, couverture nuageuse et proximité de la côte nuisant à la qualité des données satellitaires, courants grillés construits à partir de données altimétriques « alongtrack » qui ne peuvent pas capturer les dynamiques à petite échelle et non-géostrophiques, approche synoptique basée sur des indicateurs intégrés spatialement et saisonnièrement, pas de représentation ou représentation simplifiée des marées et des panaches fluviaux.... Ceci a limité la capacité de ces travaux à capturer ou représenter la gamme complète d'échelles impliquées dans la variabilité de l'upwelling, qui va de la circulation régionale à la dynamique sub-mésoéchelle et côtière et de la variabilité journalière à interannuelle. Des investigations supplémentaires sont donc nécessaires pour mieux comprendre le rôle de ces processus à différentes échelles et leurs interactions, afin d'améliorer notre connaissance de la dynamique océanique et de son influence en SCS et dans la région du SVU. Ceci est l'objectif principal de cette thèse.

L'objectif du travail présenté ici est donc à la fois méthodologique et scientifique. Dans le but de mieux modéliser et comprendre le fonctionnement, la variabilité et l'influence du SVU, nous avons développé une configuration à très haute résolution d'un modèle numérique océanique, capable de représenter la dynamique océanique et les masses d'eau à toutes les échelles depuis la côte vietnamienne jusqu'à la zone au large. Notre objectif spécifique était de nous concentrer sur de petites échelles temporelles et spatiales, peu étudiées jusqu'à présent, afin de comprendre leur rôle dans la variabilité saisonnière à interannuelle de l'upwelling: haute fréquence du forçage atmosphérique, structures océaniques mésoéchelles, circulation côtière, variabilité intrinsèque de l'océan.

La structure de ce manuscrit de thèse est la suivante. Le chapitre 1 fournit une description de la région du SCS et du SVU (caractéristiques géographiques, forçages

physiques et circulation et processus hydrodynamiques), détaille les connaissances existantes sur le SVU et les limitations associées, et enfin identifie les principales questions ouvertes sur le SVU. Le chapitre 2 décrit notre méthodologie, c'est-à-dire la configuration haute résolution développée pour l'étude du SVU et les jeux de données de forçage utilisés pour les conditions limites et l'évaluation du modèle. Le chapitre 3 présente l'évaluation de notre outil numérique basée sur des comparaisons avec les observations satellitaires et les mesures in-situ, en examinant sa capacité à simuler la circulation océanique et les masses d'eau à différentes échelles sur le domaine de calcul. Le chapitre 4 analyse les résultats d'une simulation réalisée sur la période 2009-2018 pour évaluer et expliquer physiquement la variabilité interannuelle du SVU sur ses principales zones d'occurrence. Ensuite, grâce à un ensemble de 10 simulations avec des conditions initiales perturbées, nous étudions dans le chapitre 5 les mécanismes impliqués dans la variabilité quotidienne à intrasaisonnière du SVU pour l'étude de cas de l'été 2018. Enfin, le chapitre 6 résume les principaux résultats de la thèse, et discute de certaines des questions restantes qui seront explorées dans des travaux futurs.

General Introduction

Upwelling is a prominent dynamic process in the ocean (LaFond, 1963). It occurs when dense and cold deep water is moved upward the surface, replacing warmer surface water that has been brought away from the coast by the Ekman transport induced by alongshore wind (Fig. 0.1). This usually nutrient-rich upwelled water induces phytoplankton blooms at the surface. Therefore, upwelling plays a very important role in the overturning circulation as it is the return path from the interior ocean to the surface, and strongly impacts marine ecosystems. The 5 main areas of permanent upwelling are: Canary (Northwest Africa), Benguela (South Africa), California, the Humboldt system (Peru and Chile) and Somali (Somalia and Oman). These areas provide abundant fishery resources (about 25% of global fish production is caught from these 5 regions, although they account for only 5% of the sea surface, Jennings, 2001). Upwelling also develops more intermittently or seasonally in other areas, as will be seen in this PhD thesis. Upwelling can be detected from satellite data since it induces low sea surface temperature (SST) and high chlorophyll-a surface concentrations (Anderson et al., 1993, Sarhan et al., 2000). For example, Fig. 0.2 shows the average summer SST retrieved from AVHRR data in the South China Sea (SCS), clearly revealing an area of low SST in the central SCS, off the Vietnamese coast, that corresponds to the South Vietnam Upwelling (SVU).

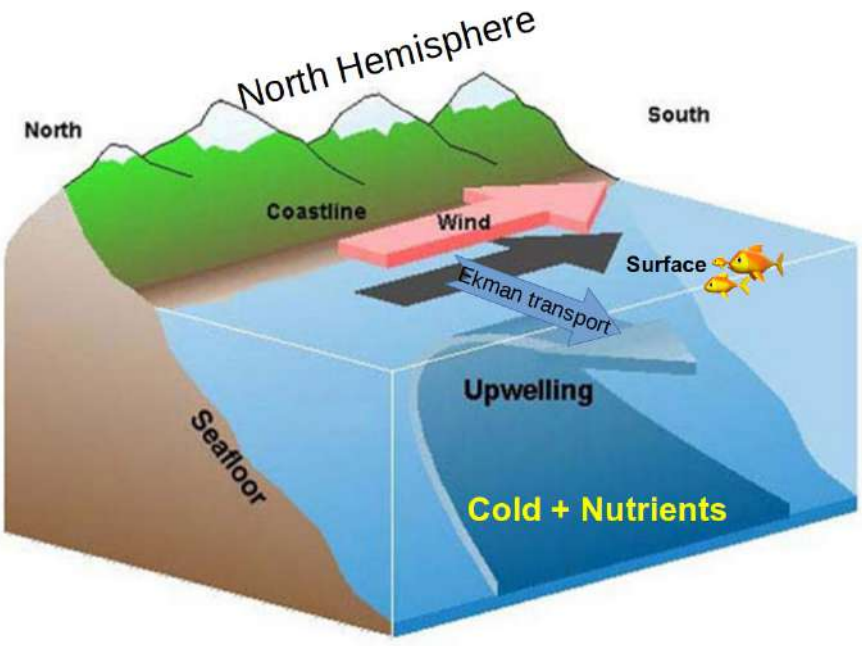

Fig. 0. 1 Schematic explanation of coastal Ekman-transport induced upwelling

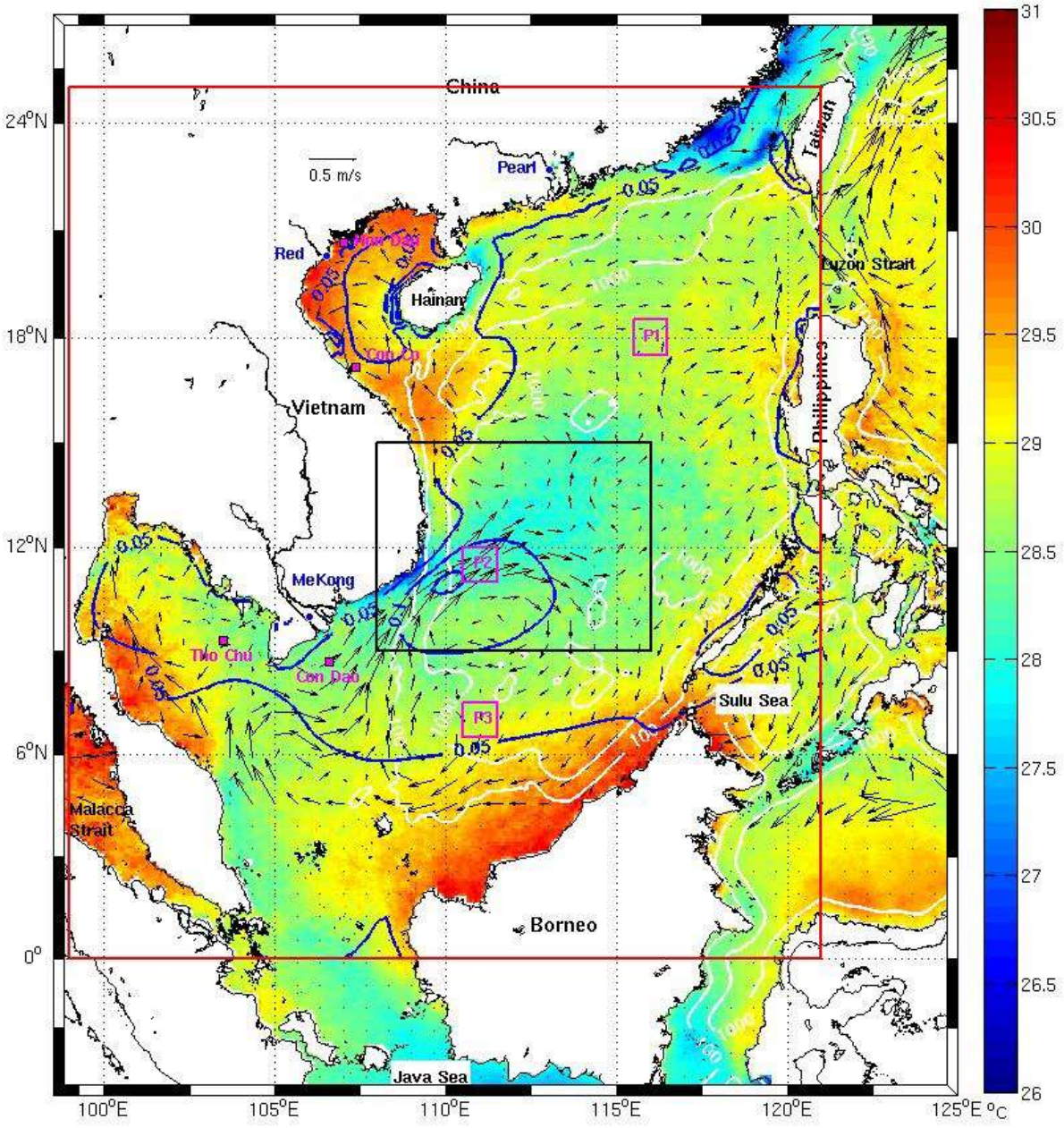

Fig. 0. 2 The SCS and SVU region, extracted from Da et al., (2019). Bathymetry contours of 100 and 1,000 m (white solid lines), August mean sea SST (°C, color shade, from Advanced Very High Resolution Radiometer SST satellite data, Casey et al., 2010), surface geostrophic circulation (m/s, black vectors, from CMEMS altimetry data, http://marine.copernicus.eu/), and mean wind stress contours (N/m^2, blue solid lines, from CFSR reanalysis from National Center for Atmospheric Research, Saha et al., 2010).

The South Vietnam upwelling (SVU) occurs off the Vietnamese coast, in the SCS, during the active southwest summer monsoon (Fig. 0.2). It strongly affects marine ecosystems, and this region is a key area for biodiversity and fishery resources. According to the General Statistics Office of Vietnam (Statistical Yearbook of Vietnam, https://www.gso.gov.vn/en/data-and-statistics/), fishery production in south-central Vietnam reached 734,000 tons/year (accounting for 11% of the national production) during 2010-2019.

The large-scale summer circulation over the SCS is usually characterized by an overall anticyclonic circulation resulting from southwest summer monsoon winds (Wang et al., 2004). It is composed more precisely of a western boundary current and a dipole structure that develops along the Vietnamese coast, with an anticyclonic gyre (AC) in the south and cyclonic gyre (C) in the north (Fig. 0.2). This dipole structure induces northward/southward alongshore coastal currents which are the western components of the AC/C gyres, and a marked eastward offshore jet that develops in the area of convergence of both coastal currents and between both gyres, around ~12°N (Xu et al., 1982, Fang et al., 2002, Xie et al., 2003,2007, Chen and Wang 2014, Li et al., 2014, 2017).

The first observational studies related to the upwelling off Vietnam coasts were done by Chevey (1934) and Krenpf & Chevey (1934), who observed an increase in the fishery production in summer along the Vietnam coast. The NAGA project focusing on the SVU was later carried out by Wyrtki (1961), Robinson (1961) and LaFond (1961). Vietnam has done further studies about the SVU with the 48B program (1981 - 1990) and KT.03 program (1991-1995) led by the Institute of Oceanography (IO, Nha Trang, Vietnam). *In-situ* SVU studies were then performed during the cooperative project between Vietnam (IO) and Germany (The Leibniz Institute for Baltic Sea Research Warnemünde, and Institute of Biogeochemistry and Marine Chemistry) in 2003-2006. These campaigns allowed to identify the regional extension (from 10.5°N to 11.5°N) and period (from May to September, stronger in July-August) of the SVU (Dippner et al., 2007, Hein 2008). Moreover, these campaigns as well as the observational and modeling studies made during the last two decades greatly contributed to our understanding of the functioning and variability of the SVU.

Summer wind forcing and the resulting large-scale circulation induce the SVU. The SVU is driven at the first order by atmospheric forcing, namely Ekman transport and pumping induced by the southwest monsoon wind (Xie et al., 2003). It is moreover reinforced by the eastward eastward jet that enhances the offshore advection of coastal water (Dippner et al., 2007) and by the combination of wind-induced Ekman pumping and positive surface current vorticity associated with cyclonic eddies in the offshore area (Da et al., 2019, Ngo and Hsin, 2021). Previous field campaigns (Dippner et al., 2007, Bombar et al., 2010, Loick-Wilde et al., 2017), satellite observations (Xie et al., 2003, Kuo et al., 2004, Ngo and Hsin, 2021) and modeling studies (Li et al., 2014, Da et al., 2019), showed that the SVU can strongly vary from one year to another. This interannual variability depends in particular on the intensity of the summer monsoon southwest wind and on ENSO, but also on cross-equatorial winds (Wu et al., 2019) and decadal climate variability (Wang et al., 2020). Two recent studies used long simulations or datasets to establish statistical relationships between the interannual variability of SVU intensity, the atmospheric forcing and the background circulation. They quantified the

link between the interannual variability of the southern coastal and offshore upwellings and the intensity of the summer ocean circulation (eastward jet, AC/C dipole and associated northward/southward boundary currents) induced by the summer monsoon wind. These studies moreover showed that upwelling sometimes develops along the northern part of the coast from 11°N to 15°N. Da et al., (2019) also revealed and quantified the important contribution of ocean intrinsic variability (OIV) in the SVU interannual variability in the offshore area, mainly related to the role of vorticity associated with submesoscale structures of strongly chaotic nature.

Most of those previous studies were based on numerical or observational datasets associated with several methodological choices and hypothesis: short study periods and limited spatial coverage of in-situ datasets, models resolution not finer than ~10 km, cloud cover and proximity of the coast hindering satellite data quality, gridded current datasets built from along-track sea level satellite data that can not capture small scale and non-geostrophic dynamics, synoptic view based on spatially and seasonally integrated indicators, no or simplified representation of tides and river plumes… This limited their ability to capture or represent the full range of scales involved in the SVU variability, which goes from regional circulation to submesoscale and coastal dynamics and from daily to interannual variability. Further investigations are therefore needed to better understand the role of these processes at different scales and their interactions, in order to improve our knowledge of ocean dynamics and its impacts in the SCS and SVU regions. This is the main objective of this thesis.

The objective of the work presented here is therefore both methodological and scientific. With the goal of better modelling and understanding the functioning, variability and influence of ocean dynamics in this area, we developed a very high resolution configuration of a numerical ocean model, able to represent ocean dynamics and water masses over a very wide range of scales from the Vietnamese coast to the offshore region. Our specific goal was to focus on small temporal and spatial scales, which were hardly studied until now, in order to understand their role in the seasonal to interannual variability of the upwelling: high frequency of atmospheric forcing, mesoscale ocean structures, coastal circulation, ocean intrinsic variability.

The thesis structure is the following. Chapter 1 provides an overview of the SCS and SVU area (geographical features, physical forcings and hydrodynamic circulation and processes), details the existing knowledge about the SVU and the related limitations, and finally identifies the main open questions about the SVU. Chapter 2 describes our methodology, i.e. the high resolution configuration developed for the SVU study and the forcing datasets used for boundary conditions and model evaluation. Chapter 3 presents the evaluation of our numerical tool based on comparisons with satellite observations and *in-situ*

measurements, examining its capacity to simulate the oceanic circulation and water masses at different scales over the computational domain. Chapter 4 analyzes the results of a simulation performed over the period 2009-2018 to evaluate and physically explain the interannual variability of the SVU over its main areas of occurrence. Next, thanks to an ensemble of 10 simulations with perturbed initial conditions, we investigate in Chapter 5 the mechanisms involved in the daily to intraseasonal variability of the SVU for the case study of summer 2018. Finally, Chapter 6 summarizes the main results of the thesis, and discusses some of the remaining questions that will be explored in future works.

Chapter 1: Introduction: bibliography about the area of study and the Vietnam Upwelling

This chapter presents an overview of the scientific literature on the study area, the South China Sea (SCS) and the South Vietnam Upwelling (SVU) region. The first part briefly presents the scope of study, the geographical features and the different forcings and hydrodynamic processes in SCS. The second part details the existing knowledge about SVU on space/time scales and some challenges and limitations as well as open questions from existing research. Finally, we present the scientific objectives of the thesis.

1.1. Area of Study: the SCS and Vietnam coastal area

The SCS is located in the western part of the Pacific Ocean and is the largest marginal sea in the world (Sverdrup et al., 1942), located in Southeast Asia, stretching from 2.5°S - 25° N and 99°E - 121°E, and covering an area of approximately ~3.6 million km² (Fig. 1.1). Fig. 1.1 shows the topography of the SCS and their adjoining sea areas. It is connected to the East China Sea through the Taiwan Strait to the north, the Java Sea through the Karimata Strait to the south, the Western Pacific Ocean through the Luzon Strait and the Sulu Sea through the Mindoro and Balabac Straits.

The bottom topography of the SCS basin is characterized in the west by a shallow continental shelf (depth <100m) stretching from north to south and more than 300 km wide, tightened in central Vietnam to about 40-50 km. A deep basin characterizes the central part of the SCS (maximum depth up to 5000m). The western and southern slopes include the Hoang Sa and Truong Sa archipelagoes, respectively. These two archipelagoes form the two main island groups in the SCS.

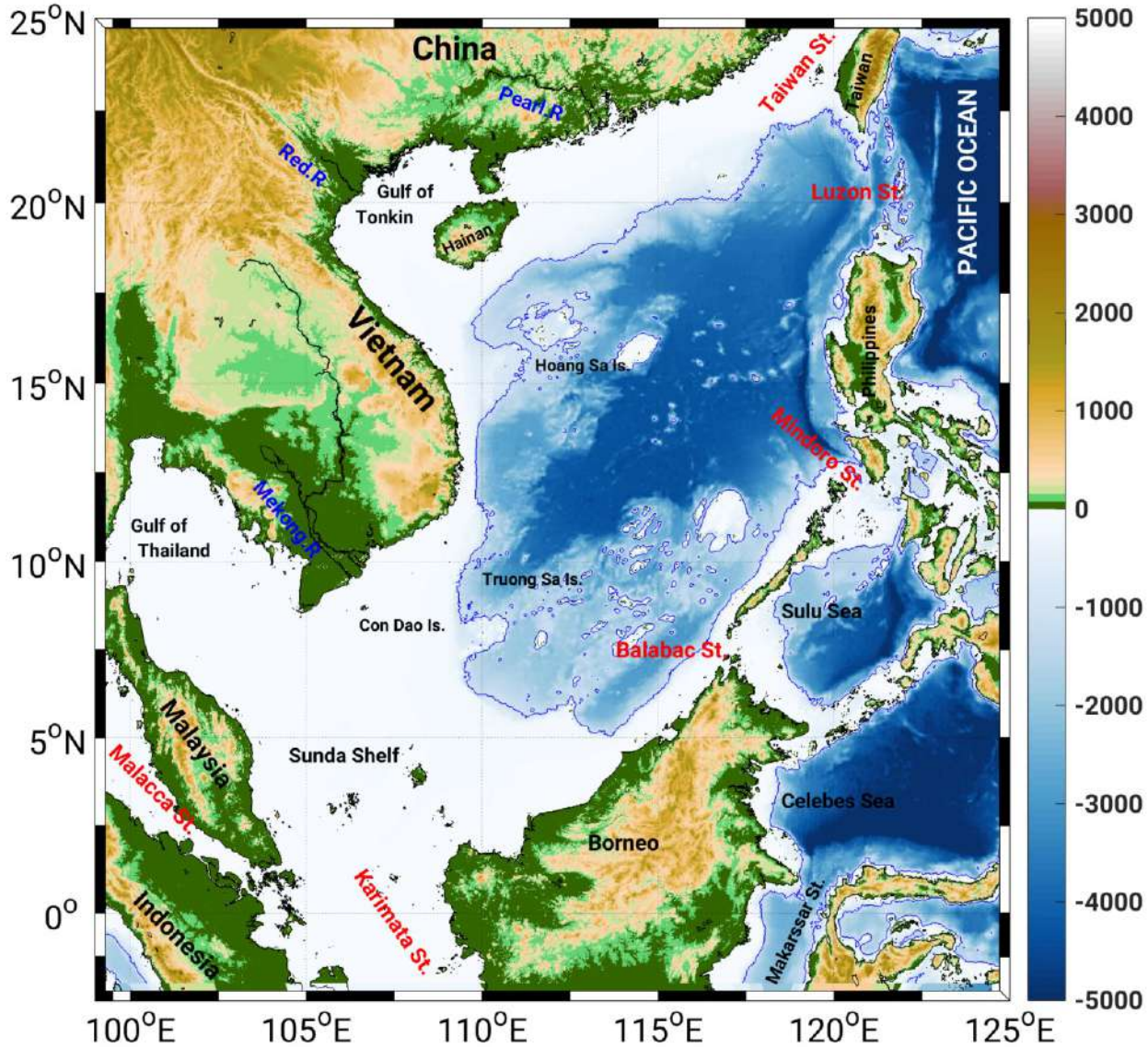

Figure 1. 1 The SCS topography and bathymetry (in meters, resolution 1/4°) released by the General Bathymetric Chart of the Oceans (GEBCO_2021 grid, https://www.gebco.net). The blue contours indicate the 1000 m isobath.

1.1.1. Forcings

a) Atmospheric forcing

- **Wind forcing:**

The SCS is located in the tropical Pacific Northwest system (Wang et al., 2009) and is connected to other monsoon systems including the East Asian monsoon, Indian monsoon and Australian monsoon. SCS has become one of the focal points of monsoon research because of its special geographical situation (Park and Choi, 2016). The seasonal action of the monsoons on the SCS was first fully studied by Wyrki (Wyrki, 1961). For a more detailed presentation, we use Reanalysis ECMWF's 42-year data series from 1979-2020

(https://cds.climate.copernicus.eu/) to calculate the average seasonal wind for 4 seasons (winter, spring, summer, autumn) over the SCS (Fig. 1.2). In winter (Fig. 1.2a), the northeast monsoon blowing over the SCS is the result of the Siberian high pressure cold and dry system located on mainland East Asia. It starts around mid-October, develops fully in January and lasts until April of the next year. The intensity of the northeast monsoon is strongest (about 10-13 m/s) in the Taiwan Strait area (due to the Venturi effect of the terrain) and the southern coast of Vietnam (due to the coastal mountain range) of Vietnam, Fig. 1.1), while winds are the weakest (<5 m/s) in the Gulf of Thailand (where the topography is flat).

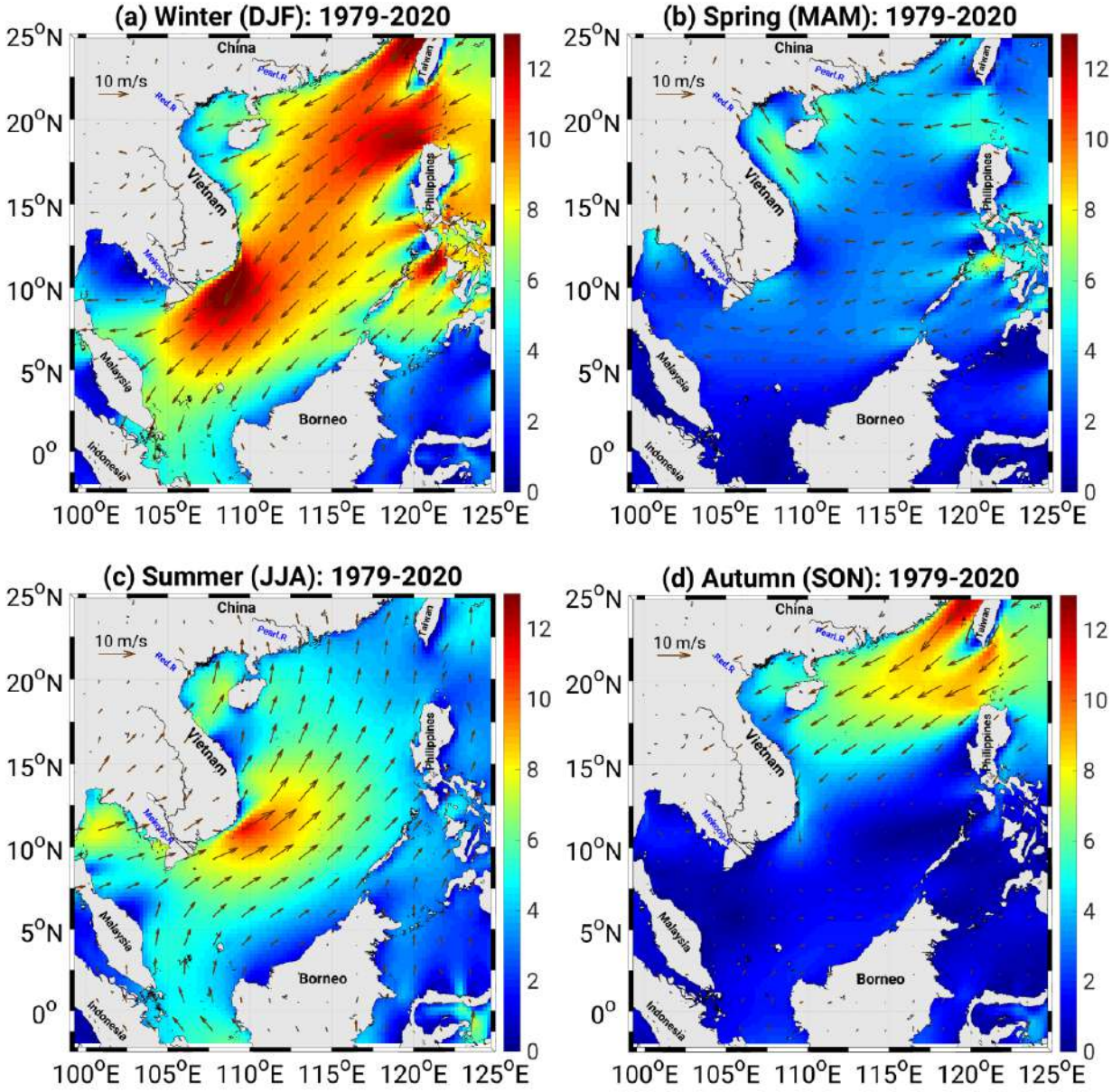

Figure *1. 2 SCS seasonal maps of wind velocity (m/s) 10m above sea level in Winter (a), Spring (b), Summer (c), and Autumn (d) from the ECMWF reanalysis dataset (1979 -2020).*

In summer (Fig. 1.2c), the southwest monsoon starts from the equator through the Thailand peninsula and the Karimata Strait (see Fig. 1.1) in June with a speed of about 5-6

m/s. These two winds meet in the coastal area of South Vietnam, combined with coastal mountainous terrain, forming an area with maximum wind intensity with a speed of about 9-11 m/s, then moving northward at a decreasing speed. Xie et al., (2003, 2007) proposed that the wind jet off southern Vietnam in summer is due to an orographic effect, passing around the mountainous area in Southern Vietnam (see Fig. 1.1).

Between those two main wind seasons there are two transitional monsoon seasons. In spring (March-May, Fig. 1.2b), the easterly wind blows into the SCS through the Luzon Strait and the Philippines and partly through the Taiwan Strait at <5 m/s, then splits into two directions to the northwest and southwest. The transition from Spring to Summer monsoon in the second half of May is marked by an abrupt increase in rainfall over the entire SCS (Lau and Yang, 1997; Wang et al., 2009; Fig. 1.3). In autumn (September-November, Fig. 1.2d), the strongest winds are in the Taiwan Strait and the Luzon Strait with average wind speeds from 9-12 m/s. However, their impacts reduce at 15°N latitude and the rest of the SCS shows very small wind speeds (<2 m/s).

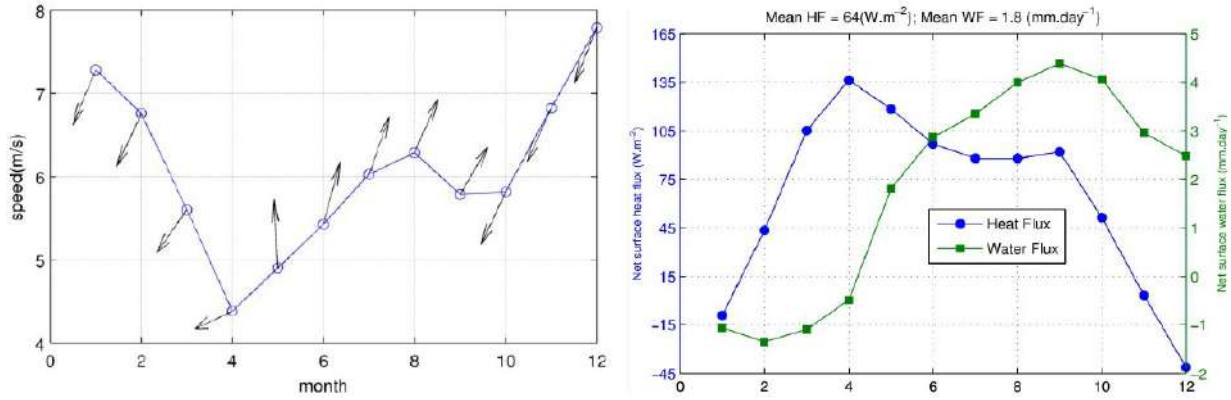

Figure 1. 3 Monthly mean of wind, heat flux and water flux in the SCS. Evolution of the 10m above sea level wind speed (blue line) and direction (black arrows with oceanographic convention) averaged over SCS (from QuickScat data 2000-2008) (left). Climatological mean surface net heat flux and water flux over the SCS computed based on NCEP CFSR reanalysis over the period 1991-2004 (right) (taken from Da, 2018).

- **Atmospheric heat and water fluxes:**

The SCS is located in the area of strong positive heat flux along the equator (Huang, 2015). The yearly averaged air to sea heat flux is positive over almost the whole SCS, except the northern basin, with a strong spatial variability: the northern basin receives less heat than the southern basin. Estimates from observations (23 $W.m^{-2}$, Oberhuber, 1988; 30 $W.m^{-2}$, Haijun et al., 1999; 49 $W.m^{-2}$, Yu and Weller, 2007) and numerical studies (17 $W.m^{-2}$, Qu et al., 2004; 19 $W.m^{-2}$, Fang et al., 2009; 51 $W.m^{-2}$, Wang Yan et al., 2019) of the atmospheric net heat flux into the SCS vary from ~15 to ~50 $W.m^{-2}$. Similarly to wind forcing, heat and water fluxes are not uniformly distributed over the SCS. In winter, the SCS loses heat in the

northern part while it gains heat in the south (Fig. 1.4a). It gains heat over almost the whole domain in summer with stronger flux in the northern part (Fig. 1.4b).

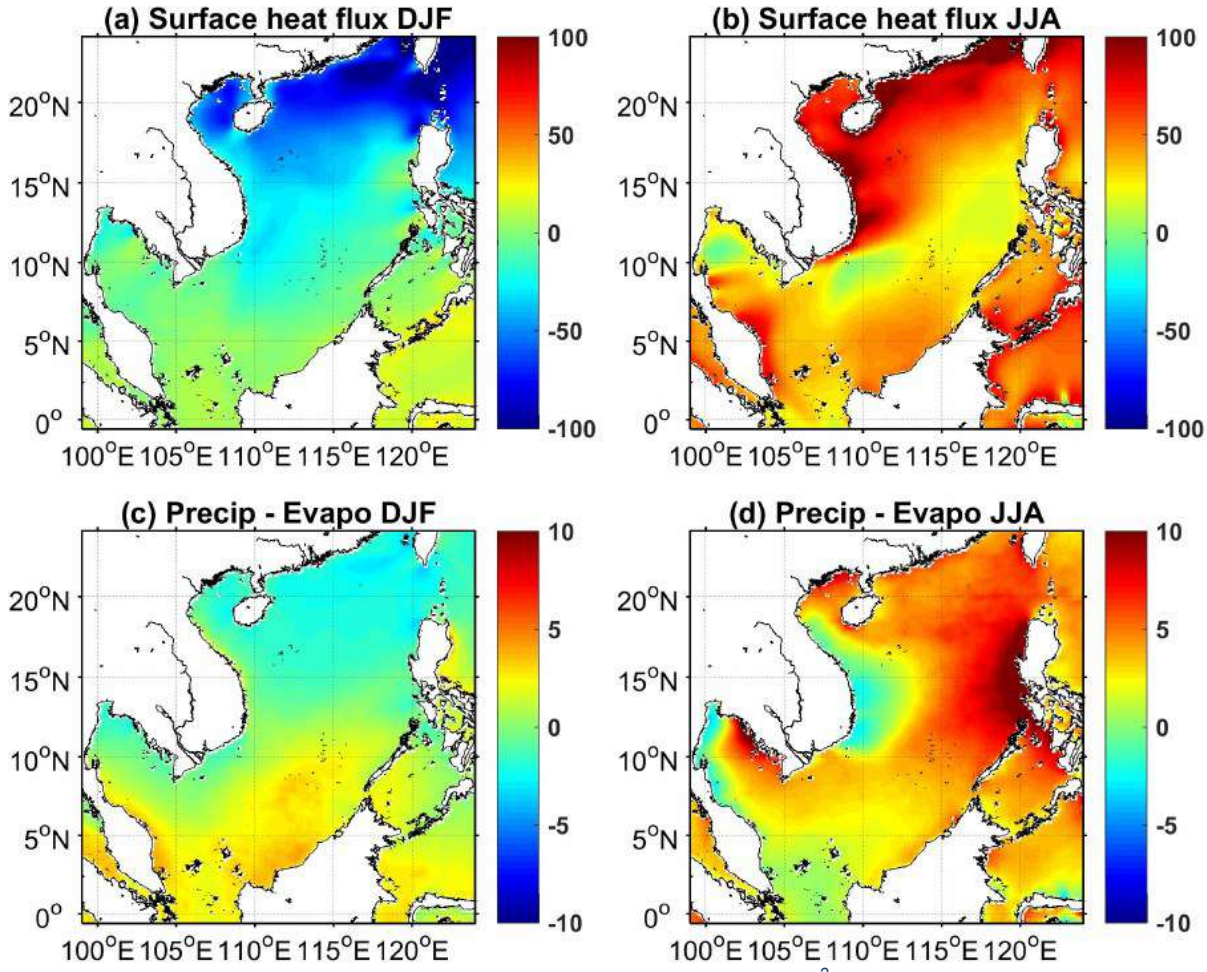

Figure 1. 4 SCS seasonal maps of net atmospheric heat flux (W.m^{-2}) and freshwater flux (mm/day) averaged in winter (a, c) and in summer (b, d) from the ECMWF dataset over the period: 2009 -2018 (Trinh, 2020)

The net flux of fresh water in the atmosphere corresponds to the difference between the part gained from precipitation and the part lost to evaporation. All studies showed that overall SCS fresh water is positive, with precipitation exceeding evaporation. Freshwater flux estimates vary between 1.5 and 2.5 mm/day (Qu et al., 2006, Da, 2018, Fang et al., 2006, Trinh 2020). The amount of freshwater gained by the ocean makes the sea surface salinity (SSS) of the SCS much lower than that of neighboring seas and oceans (averaged SSS ~33.2 psu over SCS and ~34.2 psu over Pacific, Qu et al., 2009).

The seasonal freshwater flux is not uniformly distributed over the SCS. In winter (Fig. 1.4c), evaporation exceeds precipitation in the northern part of the SCS and in the Gulf of Thailand and Gulf of Tonkin areas because of the cold and dry northeast monsoon winds. Rainfall is more abundant in the southwest SCS and the western part of Borneo due to the orographic effect (Wang et al., 2009). In summer (Fig. 1.4b), precipitation predominates over

most of the SCS as the southwest monsoon brings a large amount of moisture. In particular, rainfall is maximum along the western coast of the Philippines.

- **El Niño–Southern Oscillation (ENSO):**

ENSO has a large influence on the interseasonal to interannual variability of dynamical processes in the tropics and causes a series of global extreme climate events. As ENSO's hot/cold phase occurs, the eastern Equatorial Pacific SST becomes warmer/colder (El Niño/La Niña) with lower/higher pressure and weaker/stronger trade winds. ENSO has a significant impact on the SCS region (Xie et al., 2003; Liu et al., 2004; Wang et al., 2006a). During the strong phase of El Niño/La Niña, the winter monsoon in East Asia becomes weaker/stronger (Chen, 2002). ENSO also affects the onset of summer monsoon in the SCS, which occurs later/earlier in the El Niño/La Niña waning year (Wu and Wang, 2000; Lau and Nath, 2009; Zhou et al., 2008). The SCS SST anomaly and SLA (Sea Level Anomaly) during ENSO events are the target of several studies (Wang et al., 2006a, Tan et al., 2016, Peng et al., 2013, Rong et al., 2007). Studies show two warming anomalies during the winter in the developing El Niño period and in the following summer (Wang et al., 2006a; Du et al., 2009). ENSO also has a significant influence on the SCS ocean circulation, including the inter-ocean fluxes. Wang et al., (2006) found that the interannual variations of the SCS upper layer currents are highly correlated with ENSO, and anomalous SCS circulation has been observed during El Niño events: both the winter basin-wide cyclonic gyre and the summer double gyres weaken. According to Qu et al., (2004), Wang et al., (2006) and Liu et al., (2008), the intrusion of Pacific water into the SCS through the Luzon strait (see 1.1.1.b) tends to be higher/lower during El Niño/La Niña years.

Fig. 1.5 shows the phases of ENSO during 2008-2018, which will be our period of study in this PhD (see following chapters): Moderate La Niña (2011-2012; 2017-2018), Strong La Niña (2007-2008; 2010-2011); Strong El Niño (2009-2010); and a Very strong El Niño (2015-2016).

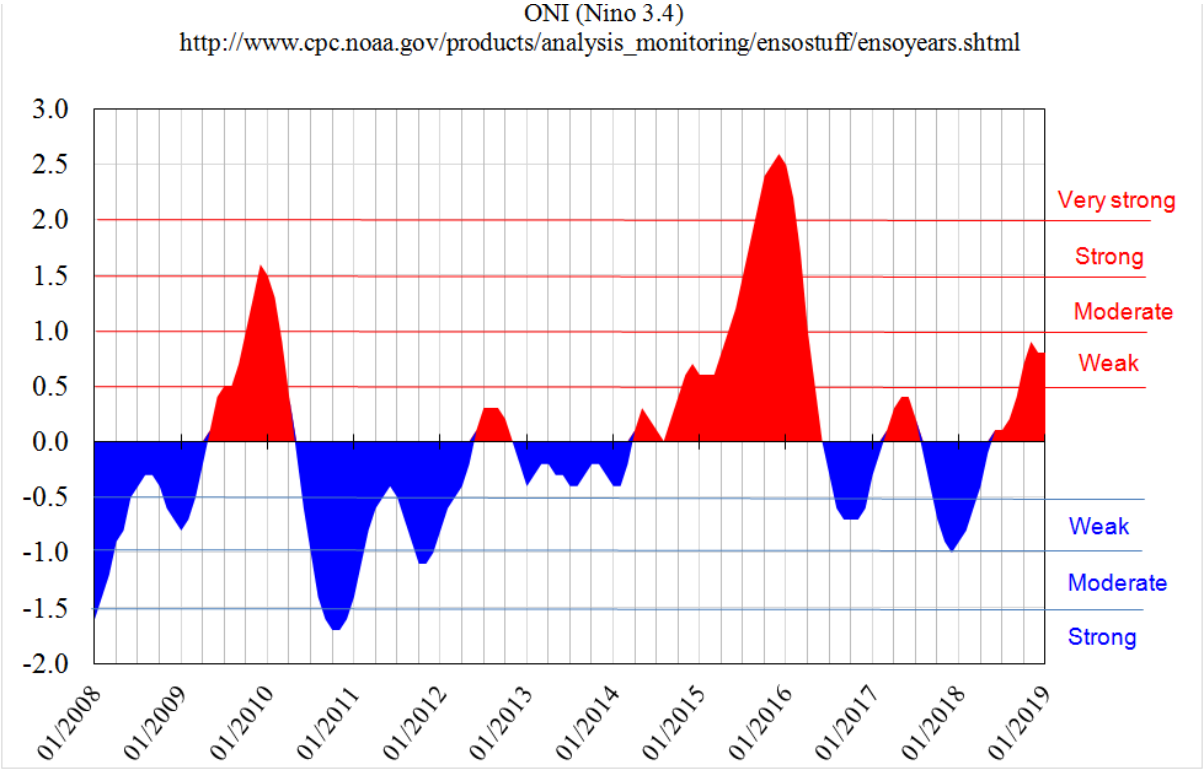

Figure 1. 5 Oceanic Niño Index (ONI) [3-month mean of ERSST.v5 with anomalous SST in the Niño region 3.4 (5N-5S, 120-170W)] during 2008-2018

b) The South China Sea throughflow (SCSTF)

The SCS plays an important role in global ocean circulation and climate, connecting the Pacific and Indian Oceans through the South China Sea Throughflow (SCSTF, Qu et al., 2005, Tozuka et al., 2007). The SCSTF is defined by a current from the Western Pacific Ocean, originating from the Kuroshio Stream that flows northward along the Philippines and entering the SCS through the Luzon Strait, outflowing to the Java Sea through the Karimata Strait, and then out to the Indian Ocean, Flores Sea, Celebes Sea through Straits of Lombok and Makassar, respectively (Qu et al., 2005, Tozuka et al., 2007). A small tributary outflows to the Sulu Sea through the Mindoro Strait and the East China Sea through the Taiwan Strait (Fig. 1.6). Many authors have studied the SCSTF through numerical models such as Qu et al., (2005), while Yu et al., (2007) found the existence of SCSTF through satellite images and numerical experiments, and Yaremchuk et al., (2009) analyzed data from the climatological temperature and salinity data of World Ocean Atlas 2001. The contributions of atmosphere, rivers and ocean fluxes and of ENSO to the seasonal to intraseasonal variability of the SCSTF was examined in detail by Trinh (2020) using a high resolution numerical model over the region for the period 2009-2018. They showed in particular the leading role of atmospheric water flux in the variability of SCS water and salt budgets.

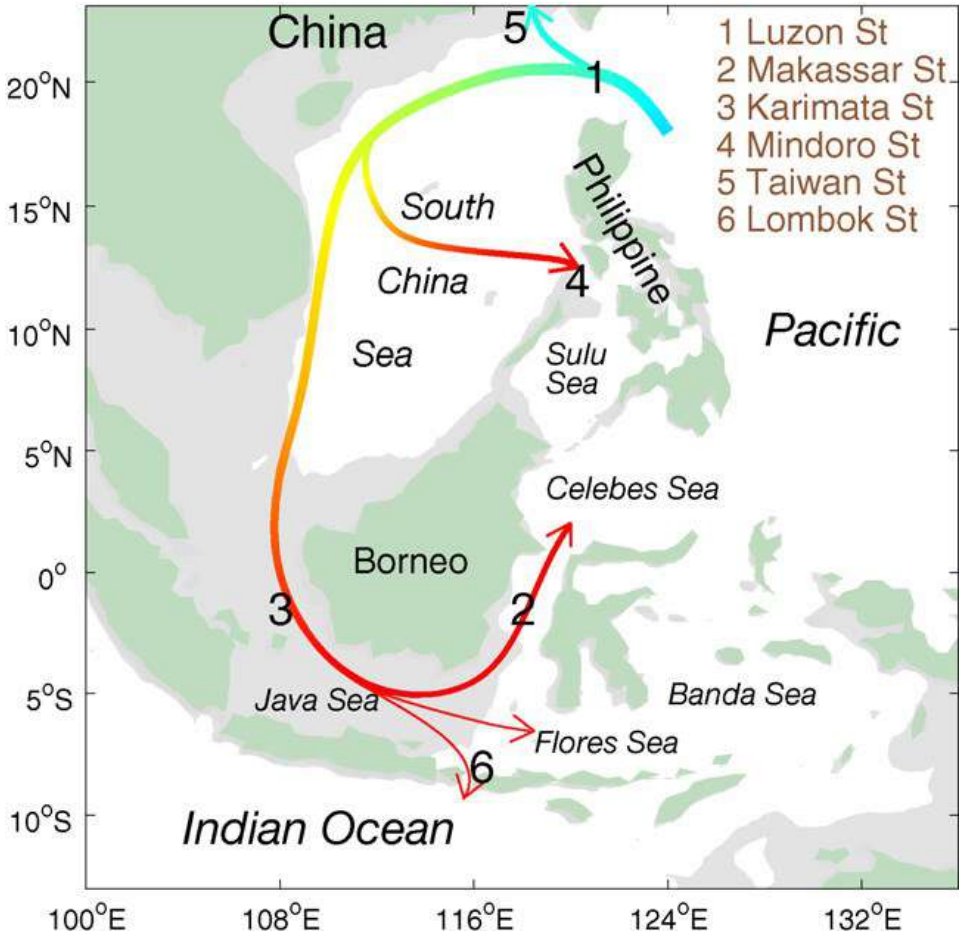

Figure 1. 6 A schematic diagram of the South China Sea throughflow (Qu et al., 2005)

c) Tides

Tidal currents and tidal breaking internal waves play an important role in ocean mixing at all depths and are involved in driving deep circulation (Stewart 2008). Tidal mixing is also particularly strong in shallow areas and can strongly influence coastal sediment transport and mixing in estuaries. The SCS is covered by about 50% of shallow continental shelves and three major river systems: Mekong, Red, and Pearl (Fig. 1.1). In deep regions, however, barotropic tides only have a minor impact on the upper layer thermal structure compared to other forcings (Chang et al., 2010), although there are strong seasonal variations in the internal tide amplitude in the north SCS (Ray and Zaron, 2011). Several studies have shown that tidal waves enter the SCS mainly through the Luzon Strait, and that several amphidromic systems exist on its continental shelves (Yanagi et al., 1997; Ye and Robinson, 1983 and Fang et al., 1999).

Fig. 1.7 describes the propagation of the main tidal components in the SCS. The semi-diurnal M2 propagates mainly southwest from the Pacific Ocean through the Luzon Strait into the SCS as an ascending wave, and a minor part of the M2 tide turns northward into the Taiwan Strait as a Kelvin wave. Most of the M2's influence is in the Mekong region, west of

Borneo and north of Hainan Island. The K1 diurnal component also propagates into the SCS as M2, but it dominates almost the entire SCS. S2 has a similar propagation direction with M2 but the amplitude is much smaller, while O1 contributes much to the formation of diurnal tides in the Gulf of Thailand and Gulf of Tonkin.

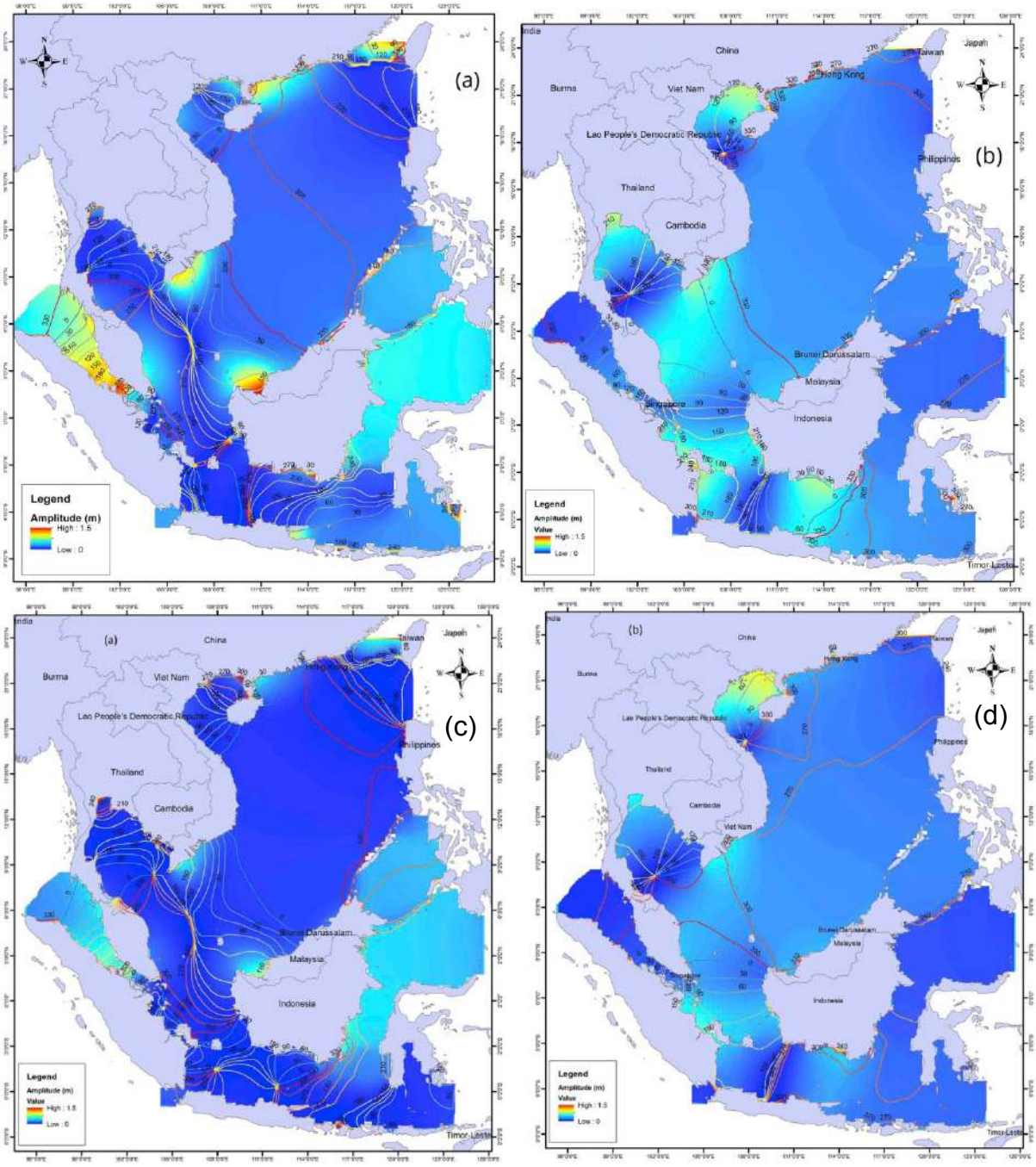

Figure 1. 7 Co-tidal charts of semi-diurnal M2 (a), diurnal K1 (b), semi-diurnal S2 (c), and diurnal O1 (d) (Phan et al., 2019)

The tides are mainly diurnal over the entire SCS, including the Sunda Shelf and Gulf of Thailand, while the semi-diurnal tides are mainly dominant in the zone of freshwater influence of the SCS (Fig. 1. 8). The semidiurnal tides dominate in the regions such as Malacca Strait connected directly to the Indian Ocean, Taiwan Strait linked to the East China Sea and South

West in the Gulf of Thailand. Mixed semidiurnal tides exist in the south of China, the northwest coast of Borneo, the southwest of Thailand and the continental shelf of the Mekong delta. All above regions are shallow continental shelves with concave coastlines, which are significant factors to increase the M2 tidal semi-diurnal amplitude due to the natural oscillation period of these basins close to the semi-diurnal period. Although there are many studies on the tidal characteristics of the SCS, only a few studies have examined tides in the continental shelf along South Vietnam (Phan et al., 2019). At the mouths of the Mekong River, the maximum and mean tidal amplitudes are 3.8 m and 2.5 m (Saito et al., 2015), respectively.

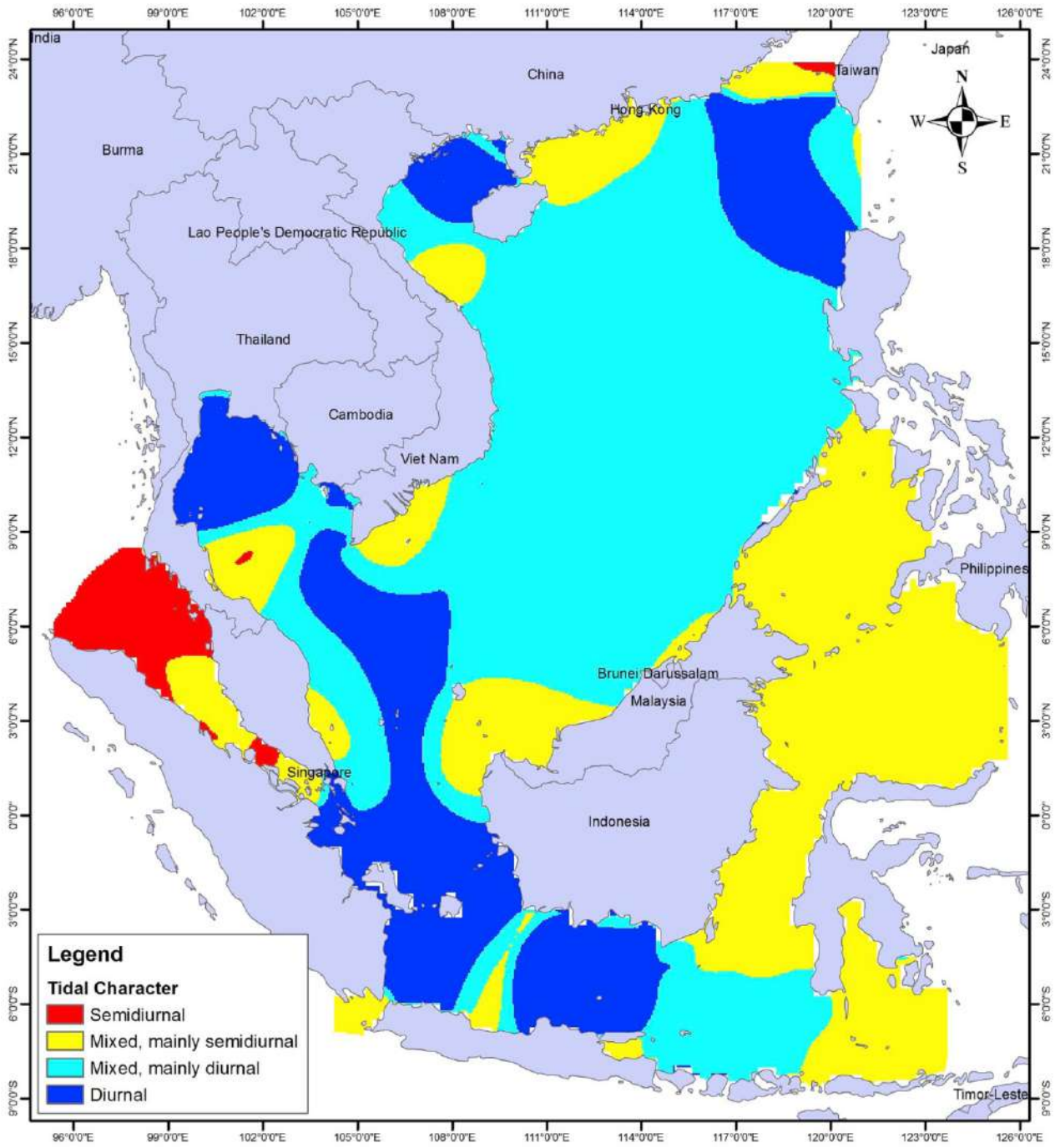

Figure 1. 8 Tidal character in the South China Sea (Phan et al., 2019)

d) Rivers

The SCS is a tropical-subtropical region located in an area with a prevailing monsoon climate, with lengthy rainy seasons during which the watersheds receive very high rainwater input. Although the volume of rivers discharge into the SCS (~50,000 m^3/s according to Fang et al., 2009) is small compared to the entire volume of the SCS, it can cause large-scale impacts due to the surface large-scale circulation that advect freshwater masses hundreds of kilometers from river mouths (Gan et al., 2009). The river discharge provides a large amount of freshwater, sediments and nutrients into the estuary areas. It therefore affects water mass and coastal dynamics processes by changes in salinity as well as impacts on coastal ecosystems. The three major river systems in the SCS are located in the western part where the southeast Asia continent allows the formation of large catchments for the Mekong, Red and Pearl rivers (Fig. 1.1). The Mekong River has the highest water discharge (500 billion m^3/year), nearly twice that of the Pearl River (285 billion m^3/year), and more than four times the Red River (120 billion m^3/year). These differences are primarily related to the size of the catchment areas (Table 1.2).

Table 1. 1 Discharge of 3 major rivers into the SCS

River name	Mean annual discharge, 10^9 m^3/year	Mean rate ($10^3.m^3$/s)	Area ($10^3.m^3$)
Mekong (Dai et al., 2002)	500	15.9	810
Pearl (Huang et al., 2004; Dai et al., 2008)	285	9.0	440
Red (Wang et at., 2011)	120	3.8	150

Fig. 1.9 shows the seasonal and interannual variations of a total of 35 rivers in SCS (see more detail about the computation of those values in section 2.2.2, chapter 2). The average monthly climatological river runoff is highest in August (~15.000 m^3/s) coinciding with the prevailing southwest monsoon in SCS. The low-flow month is March (~2.500 m^3/s) which corresponds to the transition time from the northeast monsoon to the southwest monsoon. Thus, discharge variation is strongly influenced by monsoon rains (Gao et al., 2015). During the period from 2009 to 2018, the total volume of freshwater flows into SCS was highest in 2011, 2013 and lowest in 2010, 2015. These period coincide with the influence of El Niño (2009-2010 and 2015-2016) and La Niña (2011-2012).

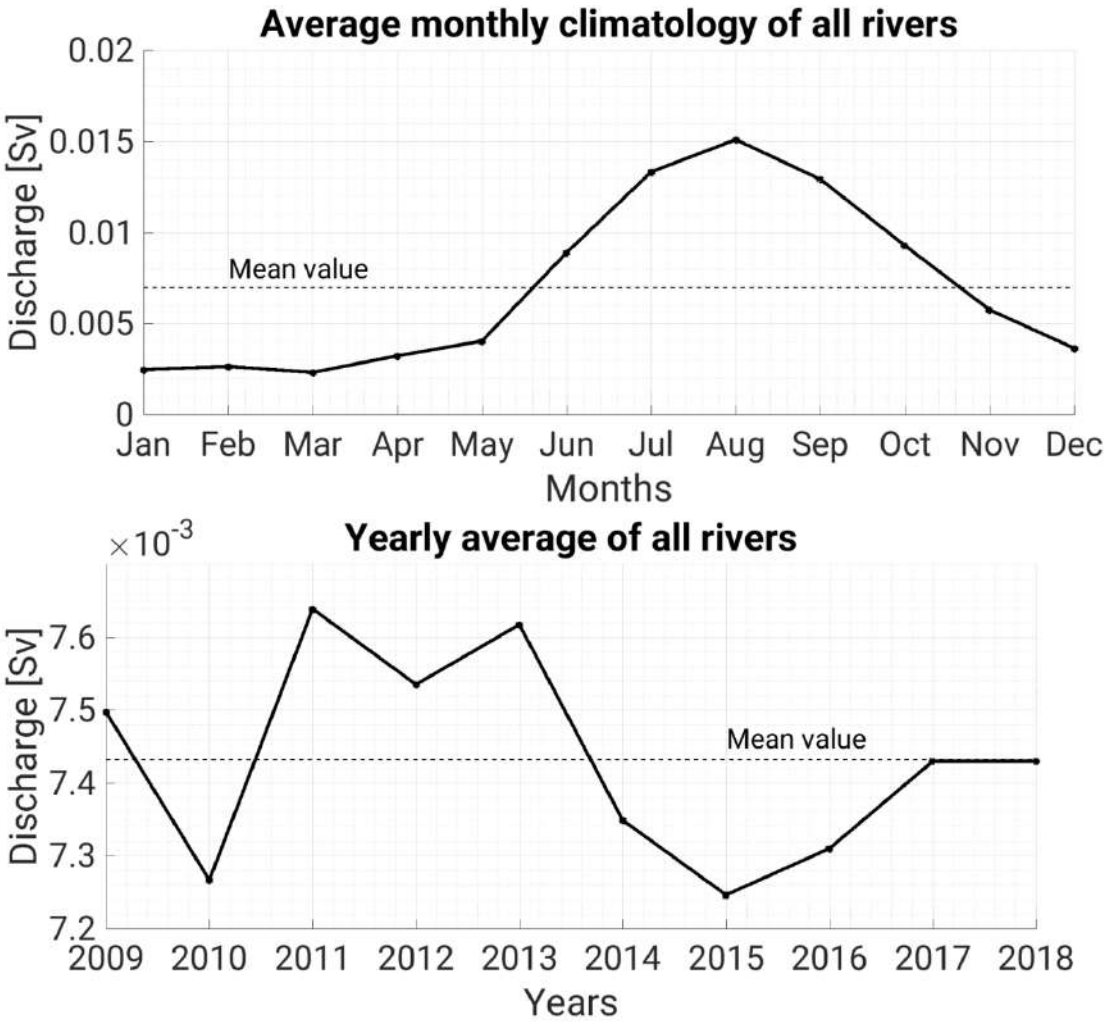

Figure 1. 9 Monthly climatology of monthly (above) and annual river runoff (below) for all the rivers in the SCS. Data issued from CLS (Collecte Localisation Satellites, INDESO project, Tranchant et al., 2016) and from the National Hydro-Meteorological Service (NHMS) of Vietnam. (See section 2.2.2 for more details about this river dataset)

1.1.2. Circulation in the SCS

Ocean circulation in the SCS depends on many different factors and is the result of a combination of influences of topographic conditions and external atmospheric and oceanic forcings. At the surface layer (density σ_θ <24.2 kg/m^3) corresponding to the Ekman layer (Zhu et al., 2019), the circulation is completely dominated by the monsoon system with a clear alternation between the northeast and southwest monsoon (Wyrtki, 1961, Liu et al., 2001). The subsurface layer (density 24.2< σ_θ <26.4 kg/m^3) is influenced by the westward Kuroshio intrusion from the Luzon Strait, and the western boundary current is caused by monsoonal wind stress and its curl (Shu et al., 2016, Quan et al., 2016). The compensatory eastward flow (Chen and Huang, 1996) occurs in the intermediate layer (density 26.4< σ_θ <27.62 kg/m^3), where the circulation is characterized by a relatively steady flow pattern, dominated by local gyres and eddies (Gan et al., 2016a). In the deep layer (σ_θ >27.62 kg/m^3), the current through

the Luzon Strait overflow drives the SCS circulation sluggishly, but still exists (Qu et al., 2006, Wang et al., 2011).

a) Surface and subsurface circulation

A detailed bimonthly description of the surface SCS circulation was given by Wyrtki (1961) using drifter data and sea level records, and concluding that the monsoon winds are the main factor driving the SCS surface circulation. Since then, several studies on the SCS surface circulation have been conducted, broadening our understanding on this subject and further confirming the major role of the Southeast Asian monsoon which induces surface current reversal (Shaw and Chao., 1994, Chu and Li., 2000, Liu et al ., 2001, Fang et al., 2002). In winter, the strong northeast monsoon covers the whole of the SCS and induces 2 cyclonic gyres in the northern and southern parts (Fig. 1.10). Kuroshio intrusion moreover influences the winter upper layer SCS circulation (Wyrtki, 1961, Chen and Huang, 1996, Hu et al., 2000, Qu et al., 2000, Qu and et al., 2004, Xue et al., 2004, Su, 2004, Wang et al., 2006b), especially in north SCS and the western boundary area. The current from the northern Pacific Ocean divides into 2 branches into the SCS: one branch flows northward through the Taiwan Strait, the other branch flows southward, with a maximum current speed along the Vietnam coast. Then it flows out of the SCS through the Karimata Strait, meets the currents from the Celebes Sea and flows towards the Indian Ocean to form the inter-oceanic current (Fig. 1.10). Qu (2000) and Li and Qu (2006) also confirmed that a cyclonic circulation characterizes the subsurface layer in winter.

In summer, under the influence of the southwest monsoon, the current entering the SCS through the Karimata Strait closely follows the west coast along the coasts of Malaysia and Vietnam. At 12^{o}N, the current separates into two branches: one flows eastward to form an anticyclonic gyre in the Southern part of the SCS, the other flows northward, forms a cyclonic gyre in the North then exits the SCS via the Taiwan Strait (Fig. 1.10b). Offshore central Vietnam, the large scale circulation is characterized by an eddy dipole (cyclonic in the north, anticyclonic in the south) and an associated eastward jet develops between both gyres, in the area of convergence of the northern southward and southern northward boundary currents associated respectively with the cyclonic and anticyclonic gyres. This circulation is induced by nonlinear interactions between different factors (Wyrtki 1961; Xu et al., 1982; Fang et al., 2002; Kuo et al., 2000; Xie et al., 2003, 2007; Dippner et al., 2007; Hein 2008): the large-scale circulation just described above, driven by large-scale and steady monsoon winds, but also strong local winds induced by the presence of mountainous coastal regions, and abrupt bathymetry gradients. The location of the eddy dipole and eastward jet and associated coastal upwelling can vary around 10 - 14^{o}N with a mean position around 12^{o}N (Li et al., 2014). The

subsurface circulation is also cyclonic in the Northern SCS and anticyclonic in the Southern SCS (Zhu et al., 2017). Year-round intrusion of Pacific water into the SCS through the Luzon Strait at 500m depth (Tian et al., 2006, Zhang et al., 2015) plays an important role in the upper SCS circulation: this westward current maintains cyclonic circulation over the North SCS basin in summer although the southwest monsoon still predominates over the whole basin.

A subsurface current out of the SCS through the Mindanao Strait persists year-round despite variations in wind stress curl (long-dashed lines, Fig. 1.10).

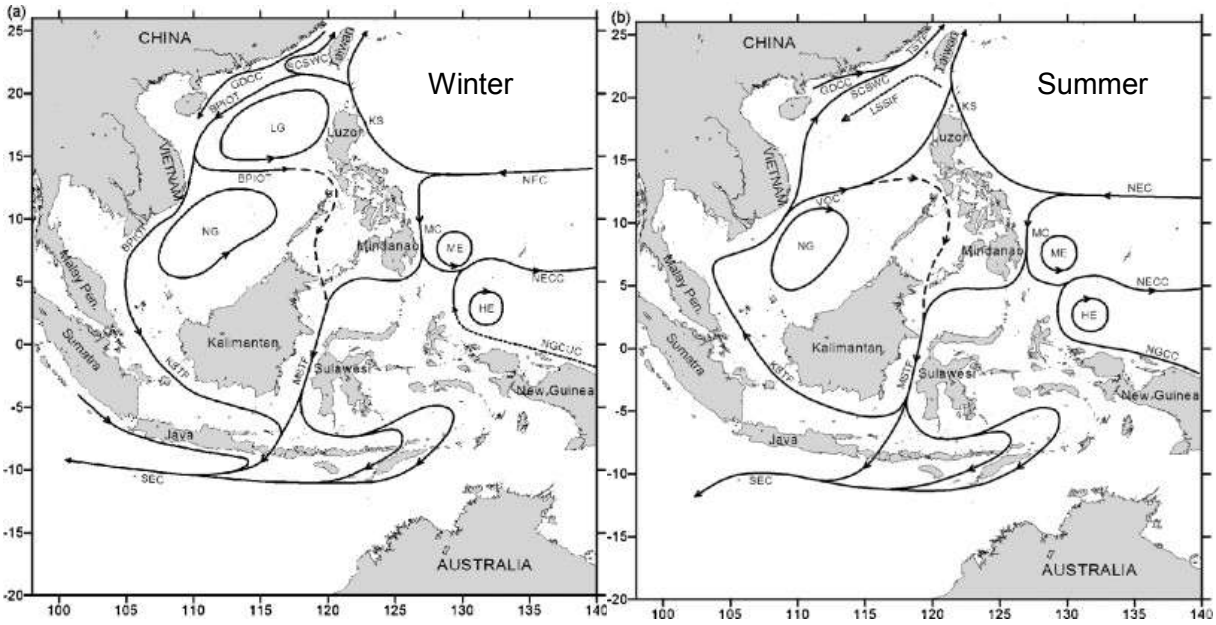

Figure 1. 10 Interocean circulation of the SCS and Indonesian Seas in Winter (a) and Summer (b). The short-dashed lines indicate the Luzon Strait Subsurface Inflow. The long-dashed lines represent the Mindanao Strait Subsurface Outflow. (after Fang et al., 2009)

b) Intermediate and deep layer circulation

In the intermediate layer (potential density range of 26.40–27.62 kg /m^3, with an average depth range of 500 - 1700m, Zhu et al., 2017, Li and Qu, 2006), previous studies suggested that all year round 2 dipole gyres occur in the east near the coast of Vietnam and north of the SCS (Fig. 1.11d, e), meaning that the intermediate layer circulation is characterized by a relatively steady flow pattern, dominated by local gyres and eddies. Most numerical studies show an anticyclonic circulation in yearly mean and in winter (Yuan, 2002, Xu and Oey, 2014), but results differ in summer: Gan et al., (2016) found a basin-wide anticyclonic circulation in both winter and summer, while Wei et al., (2016) found a sub-basin anticyclonic gyre in winter and a sub-basin cyclonic gyre in summer in both the southwestern SCS and west side of Luzon Strait. Zhu et al., (2017) also obtained an average anticyclonic pattern in the intermediate layer (Fig. 1.11f).

In the deep layer (potential density range σ_θ >27.62 kg/m^3, Li and Qu, 2006, Xu and Oey, 2014, Gan et al., 2016a, Gan et al., 2016b, Wei et al., 2016), the abyssal circulation is reinforced by up to 2 orders of magnitude compared with its counterpart in the Western Pacific. This maintains a baroclinic pressure gradient across the Luzon Strait, pushing deep water flows from the Pacific Ocean into the SCS and affecting deep circulation in the SCS (Qu et al., 2006, Zhao et al., 2014, Wang et al., 2017, Qu et al., 2006, Wang et al., 2011, Gan et al., 2016, Lan et al., 2015, and Zhu et al., 2017). A strong current from the Western Pacific enters the SCS through the Luzon Strait, turns to the northwest, flows southwest away and strengthens in the southwestern SCS, eventually forming a cyclonic circulation (Fig. 1.11g, h).

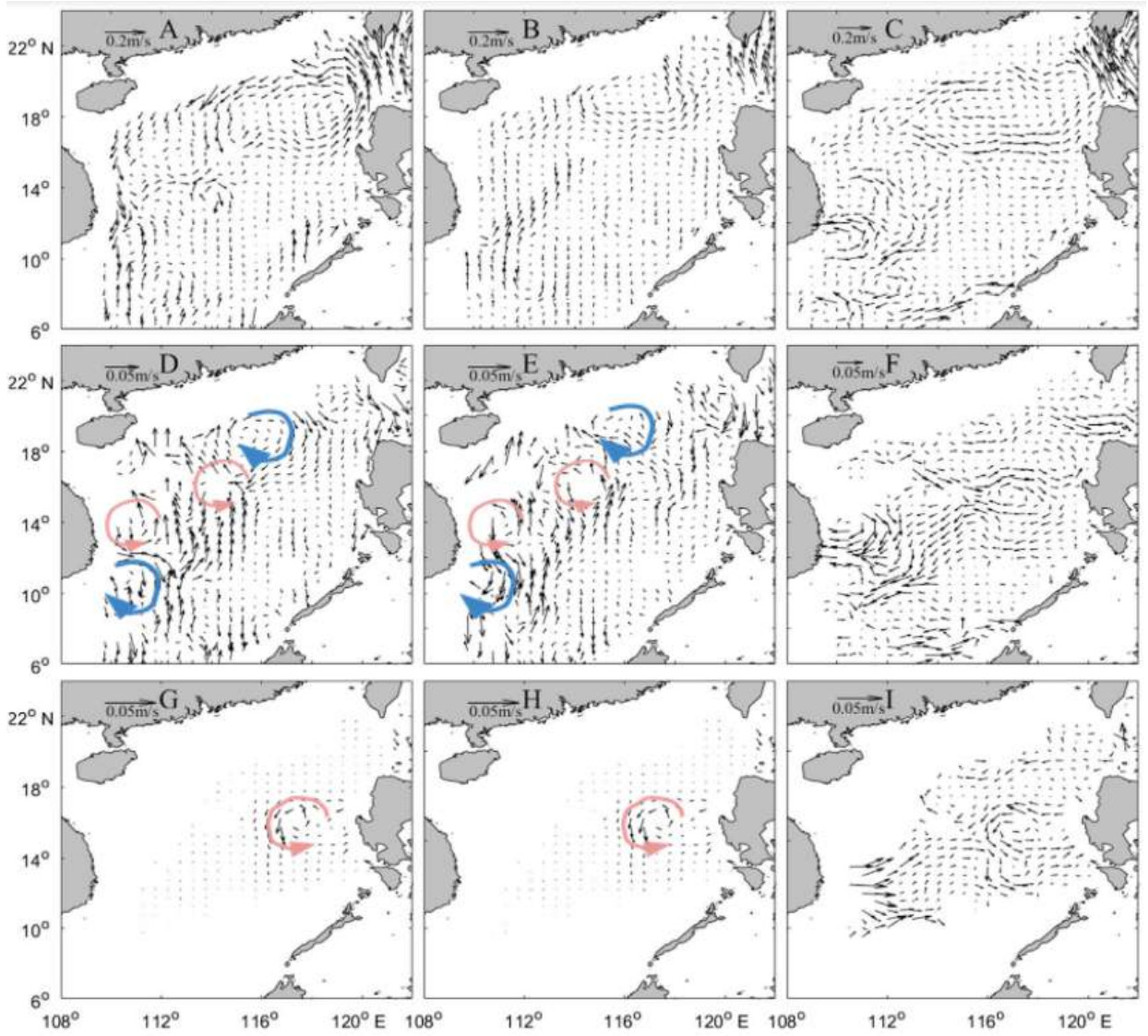

Figure 1. 11 Geostrophic currents (after Zhu et al., 2019). Left and middle panels represent currents in winter (A, D, G) and summer (B, E, H) at σ_θ=25.6, 27.4 and 27.65 isopycnal surfaces, indicative of the subsurface, intermediate and deep layers, respectively, derived from thermal wind relation. Right panels (C, F, I) indicate time and layer-averaged currents in the subsurface, intermediate and deep layers, respectively, derived from the P-vector method.

c) Meso-scale eddies and upwelling distribution

Mesoscale eddies are ubiquitous in the SCS and play an important role in local thermodynamics and biochemistry (Guo et al., 2015). Mesoscale eddies with a spatial scale of tens to hundreds of kilometers and temporal scale of weeks to months are more energetic than the mean circulation (Richardson, 1983; Chelton et al., 2007). They are often formed by barotropic/baroclinic instabilities in the mean circulation (Holland, 1978; Qiu and Chen, 2004) Eddies are produced almost everywhere in the deep SCS basin, especially southwest of Taiwan, west of Luzon and southeast of Vietnam (Fig. 1.12a). The mean radius and lifetime of eddies are ~130 km and ~9 weeks, respectively, both depending on where the eddies are formed (Chen et al., 2011). The mesoscale related to the Kuroshio intrusion through the Luzon strait also contributes to the upper-layer thermal variation as well as to the heat-salt exchange with the Western Pacific across the Luzon Strait (Wu and Chiang, 2007; Chen et al., 2011). In the eastern part of Vietnam, the summer wind stress dipole structure combined with the complex topography produces medium-high mesoscale eddy activities (Hwang and Chen, 2000; Chen et al., 2010). Xu et al., (1982), based on synthesis of available observations, were among the first who discovered the existence of permanent cyclonic eddies west of Luzon and southeast of Vietnam in winter, and of an anticyclonic eddy southeast of Vietnam paired with a cyclonic eddy off central Vietnam in summer. These seasonal permanent eddies are formed in response to the reversal of monsoon in the SCS.

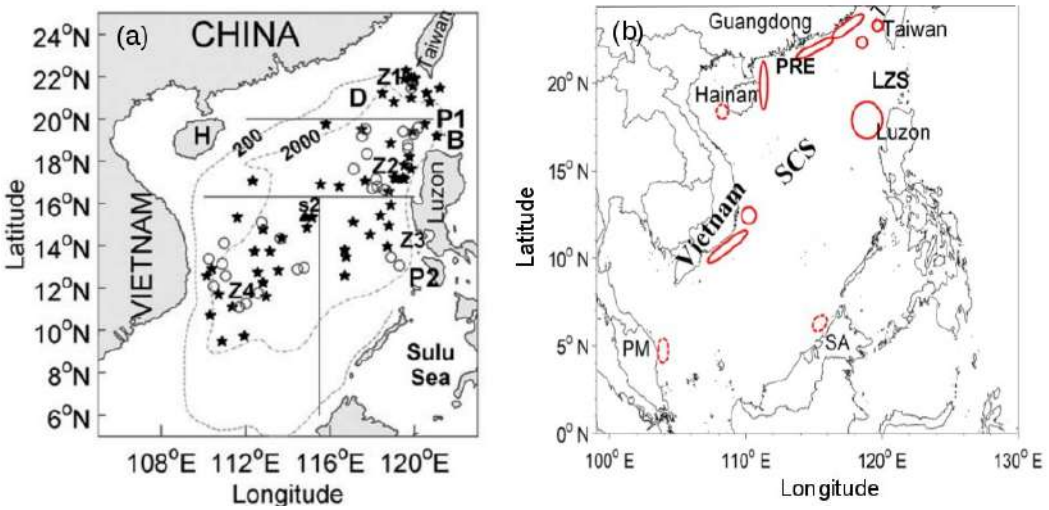

*Figure 1. 12 (a) Location of eddies (o: cyclonic, *: anticyclonic) in the SCS from 1993-2000 (after Wang et al., 2003). (b) Distribution of upwelling zones in the SCS (after Hu & Wang., 2016)*

Related to those two eddies, coastal upwelling develops off the southern coast of Vietnam in the summer (SVU region) and off the island of Luzon in the winter (Western Luzon Upwelling WZU, Fig. 1.12b).

1.2. The South Vietnam Upwelling

1.2.1. General presentations

Upwelling is defined as the upward vertical velocity of seawater, with speeds ranging from 10^{-6} to 10^{-4} m/s (Hu et al., 2016). Large amounts of cold and nutrient-rich waters are lifted from deep to surface layers, leading to rapid increase of marine phytoplankton in the surface layer where photosynthesis occurs. The SVU occurs during the active southwest monsoon period from June to August, greatly affects the marine ecosystem and is a key area for biodiversity and fishery resources (Fig. 1.13).

a) Dynamic and biogeochemical functioning

There have been many studies about the SVU during the last decade. Two areas of SVU (Fig. 1.12b) have been identified: a strong coastal upwelling along the Vietnamese coast (Barthel et al., 2009; Dippner and Loick-Wilde, 2011), and an upwelling that develops offshore, which is related to the dipole structure (He et al., 2002; Gou et al., 2006). The low SST coastal water, about 1- 2°C colder than the surrounding water, is located near 11.5°N, 109°E. The cold surface water is then advected offshore by the eastward jet that develops offshore central Vietnam (Xie et al., 2007). Using data analysis from CMEMS (Copernicus Marine and Environment Monitoring Service) altimetry satellite data as well as Advanced Very High Resolution Radiometer (AVHRR) SST in the SCS, Xie et al., (2007) indeed indicate that this jet is associated with a large surface cooling over the central SCS. This cold water area extends to 114°E as observed in the JAXA Himawari Monitor satellite observations (Fig. 1.13a).

The upwelling area is a key region for the fisheries and seafood industry of the Binh Thuan province, with a big halieutic production, especially from April to October. It is also one of the largest fishing grounds in Vietnam. The SVU impact on ecosystems is associated with a high bio-productivity (Tang et al., 2004; Loick et al., 2007; Bombar et al., 2010). Fig. 1.13b shows a high concentration of Chlorophyll-a during the period and in the area of the SVU, in July 2018. However, high levels of chlorophyll also lead to eutrophication caused by haptophyte blooms, which in turn are harmful to coastal ecosystems and aquaculture (Hai et al., 2010; Dippner et al., 2011).

SVU also influences the local weather and climate. Xie et al., (2007) indeed showed that rainfall decreased and surface wind speed increased (by 3 m/s) in the SVU area compared to the area outside the SVU due to the surface cooling. They obtained a positive

correlation between SST and precipitation. Their results showed that surface cooling not only reduces precipitation but also contributes to stabilize the upper atmosphere, preventing air convection. Moreover, by cooling the temperature and bringing salt to the surface water layer of the central SCS, the South Vietnam Upwelling may influence the SCSTF heat and salt transport into the surrounding seas and oceans, which could impact the climate of the whole Indo-Pacific region.

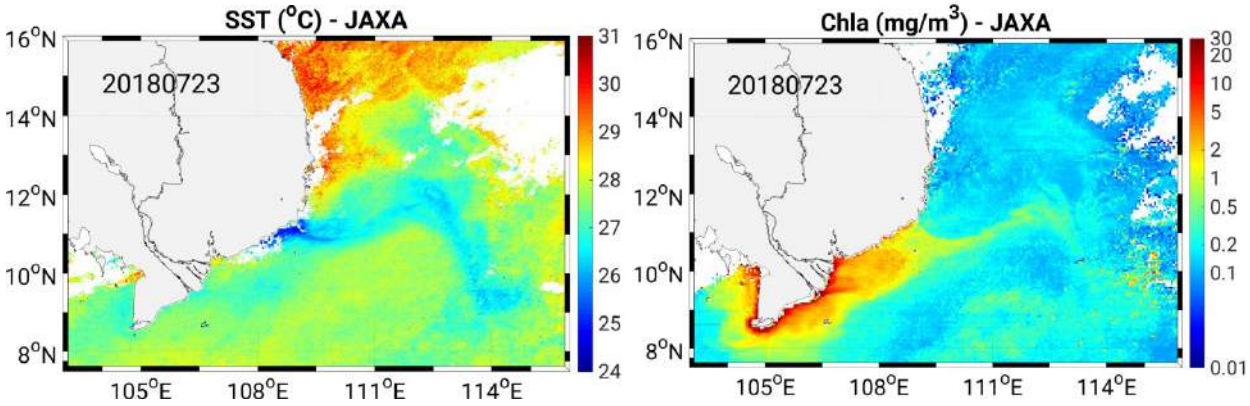

Figure 1. 13 Map of SST (right, °C) and Chlorophyll-a (left, log10 scale, unit: mg/m^3) on 23/07/2018 from JAXA Himawari Monitor

b) SVU Mechanism

Several mechanisms were identified in previous studies to explain the coastal and offshore upwelling that develops in the southwestern SCS.

- **Southwest summer monsoon wind and Ekman transport**

According to the classical theory of Ekman transport, the alongshore wind causes the Ekman transport that brings the surface water offshore in a direction perpendicular to the coast to the right of the wind direction (in the Northern Hemisphere). This mechanism is responsible for the SVU: this area is under the influence of a stable southwest summer monsoon wind, parallel to the Vietnamese coast (Dippner, 2007; Qiao and Lü, 2008; Wang et al., 2012). The topography of the Truong Son mountain range in central Vietnam indeed drives the wind direction, resulting in an alongshore wind, and increases its intensity in the area (Fig. 1.14).

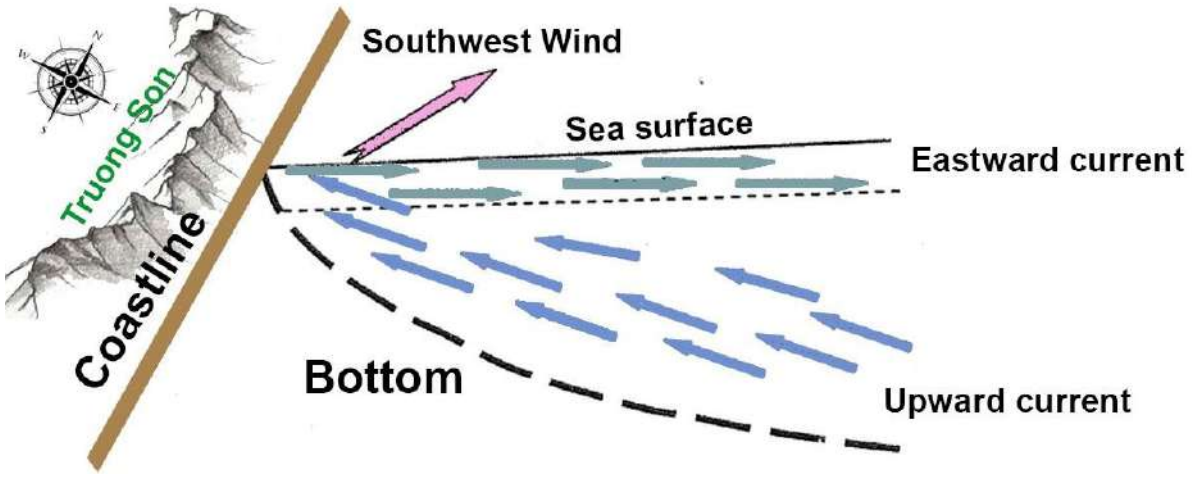

Figure 1. 14 Mechanism of coastal upwelling under the influence of wind

- **Wind stress curl and Ekman pumping**

Upwelling is also induced by Ekman pumping. Xie et al., (2003) studied the interseasonal variation of summer upwelling in coastal and offshore areas of Vietnam, using observational data from satellite images. They showed that the strong southwest monsoon wind in the area was associated with a strong positive wind stress curl that results from the local topography. In the offshore area, this cyclonic wind field forms a cyclonic ocean circulation associated with surface divergence that results in upwelling, the so-called Ekman pumping. Fig. 1.15a shows the area off the southern coast of Vietnam (9-15°N; 110-115°E) where the maximum wind speed occurs, associated with negative and positive wind stress curl leading to Ekman pumping (Fig. 1.15b).

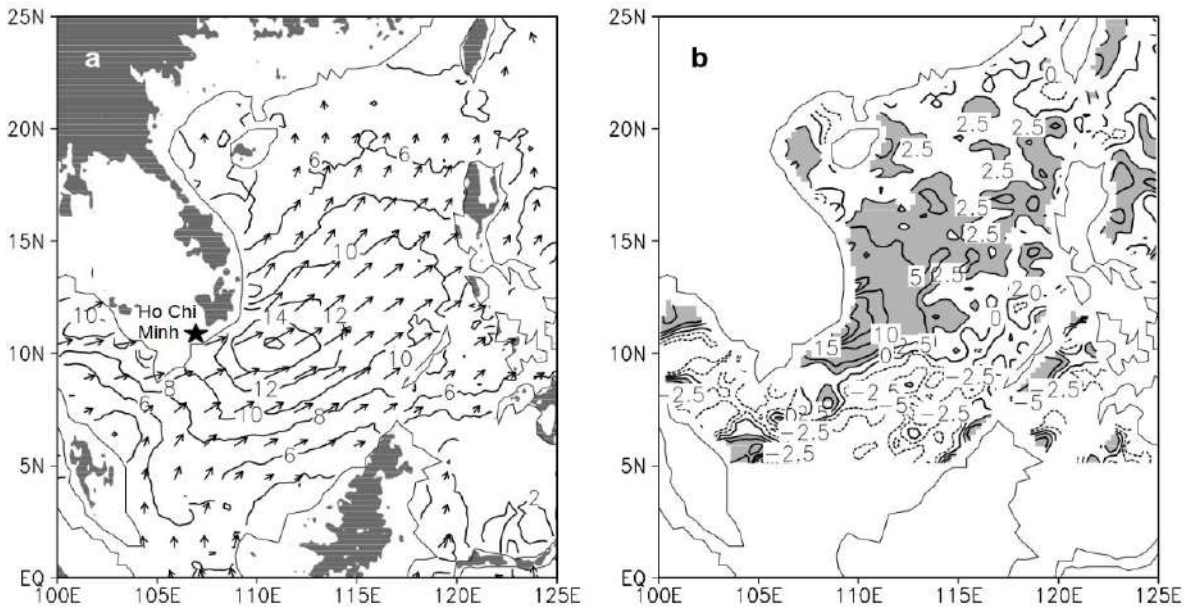

Figure 1. 15 (a) QuikSCAT surface wind stress vectors and their magnitude (contours in 10^{-2} N/m^2) averaged for June–August 2000–2002. (b) Ekman pumping velocity (upward positive in 10^{-6} m/s; contour intervals are 2.5 for values between -5 and 5, and are otherwise 5, with values greater than 2.5 shaded). In (a), land topography with elevations greater than 500 m is shaded (after Xie et al., 2003).

- **Background flow:**

As explained in section 1.1.2.a, the summer ocean surface circulation in the SVU area is characterized by an eastward jet and an eddy dipole (cyclonic in the north, anticyclonic in the south). This jet advects coastal upwelled water offshore and forms a tongue-like SST pattern as shown in Fig. 1.13 (see also Kuo et al., 2000). Moreover, the cyclonic circulation northward of the jet, combined with positive wind stress curl, contributes to the formation of the offshore upwelling through Ekman pumping (Da et al., 2019, Ngo and Hsin, 2021).

1.2.2. SVU scales of variability

a) Interannual Variability

The interannual variability of dynamics in the SCS, involving the SVU, has been examined by previous studies, based on satellite observations of SST, SSH, wind, or chlorophyll (Morimoto et al., 2000; Hwang and Chen, 2000; Xie et al., 2003; Hein, 2008; Hai et al., 2010; Li et al., 2014, Ngo & Hsin., 2021), in situ data (Wang et al., 2006a; Dippner et al., 2007; Rong et al., 2007; Bombar et al., 2010; Hein et al., 2013), and numerical modeling (Qu et al., 2004; Wu and Chang, 2005; Wang et al., 2006b; Wang et al., 2006c; Chang et al., 2008; Li et al., 2014, Da et al., 2019).

Previous studies showed that ENSO strongly affects the SVU interannual variability, through its impact on the summer southwest wind and regional circulation (Xie et al., 2003, Kuo et al., 2004, Wang et al., 2006c, Dippner et al., 2007, Bombar et al., 2010, Hein et al., 2013, Loick-Wilde et al., 2017, Da et al., 2018). They showed that ENSO oscillation strongly affects the general winter and summer surface SCS circulation, including the SVU. Post El Niño years are associated with a weakening of the summer monsoon, hence the wind-induced summer double gyre, eventually causing the weakening and sometimes even disappearance of SVU, and a strong decrease of biological productivity. And inversely for La Niña.

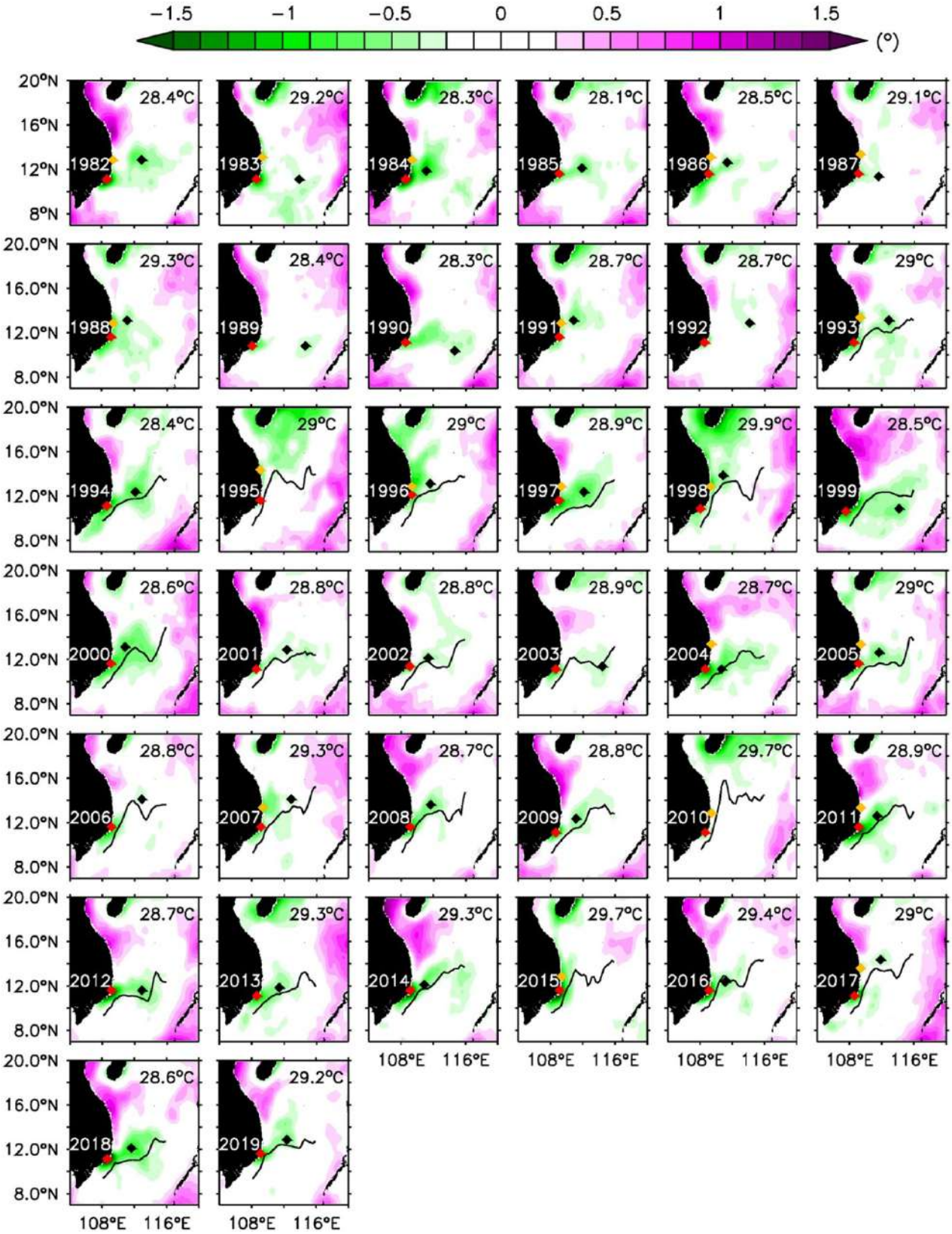

Figure 1. 16 Summertime (June–September) SST anomaly in 1982–2019. Based on the NOAA OISST data, the SST anomaly is derived by subtracting the time-varying T_{ref} (labels described in the upper-right corner) year by year. Red, yellow, and black dots denote the locations of SST minima in the SCU, NCU, and OU, respectively. Black curves denote the central positions of the eastward-flowing jet. NCU, Northern Coastal Upwelling; OU, Offshore Upwelling; SCU, Southern Coastal Upwelling; SST, sea surface temperature (after Ngo & Hsin, 2021).

Two recent studies used long simulations or datasets to better understand the factors involved in the SVU interannual variability, establishing statistical relationships between the interannual variability of SVU intensity, the atmospheric forcing and the background circulation. Da et al., (2019), using a 1/12° (9 km) 14-years simulation, confirmed that summer wind is the main mechanism causing upwelling, and that coastal upwelling variability is related to eastward jet strength while offshore upwelling variability is strongly driven by the spatiotemporal collocation of wind stress curl and cyclonic eddies. Ngo and Hsin (2021), based on 1/4° (28 km) datasets of 38-years SST and reanalysis winds and 28-years satellite-altimeter derived sea surface current (Fig. 1.16), confirmed that the upwelling develops both along and offshore the Vietnamese coast. They highlighted and quantified the link between the interannual variability of the southern coastal and offshore upwellings and the intensity of the summer wind and ocean circulation (eastward jet and associated dipole, itself related to the intensity of the summer monsoon wind). In sum, two major factors have been proposed to govern the interannual variability of the summertime Vietnamese upwelling: the wind forcing (Ekman transport + Ekman pumping) and the eastward jet associated with the dipole east of the central Vietnamese coast.

b) Intraseasonal variability

SVU variability studies largely focused on interannual variability, and more rarely on intraseasonal variability. Kuo et al., (2000) studied the development of upwelling in the summer of 1997 and showed that the cold eddy center started to form at 15°N in May, after which it moved to 11°N, gradually increased with some small peaks in phase with the alongshore wind stress peaks, formed a cold eddy moving outward and reached its maximum in mid-August. SST variations at the intraseasonal scale were also studied by Xie et al., (2003) through an analysis of 15-year satellite images. It indicated that, on average, upwelling begins in June, gradually increases in intensity in July and peaks in August. This was also confirmed by Li et al., (2014) using NOAA optimally interpolated SST for the 1992-2012 period. Xie et al., (2007) examined intraseasonal variation in the SCS using weekly averages of high-resolution satellite images: see Fig. 1.17 which shows that two to four cooling events develop during three of the four summers examined. Their results indicated that the cold filament experiences 2-3 cycles of development and decay during the summer. This intraseasonal variation of the SST was attributed either to a response to the intraseasonal monsoon variability or to the internal variability of the double gyre structure.

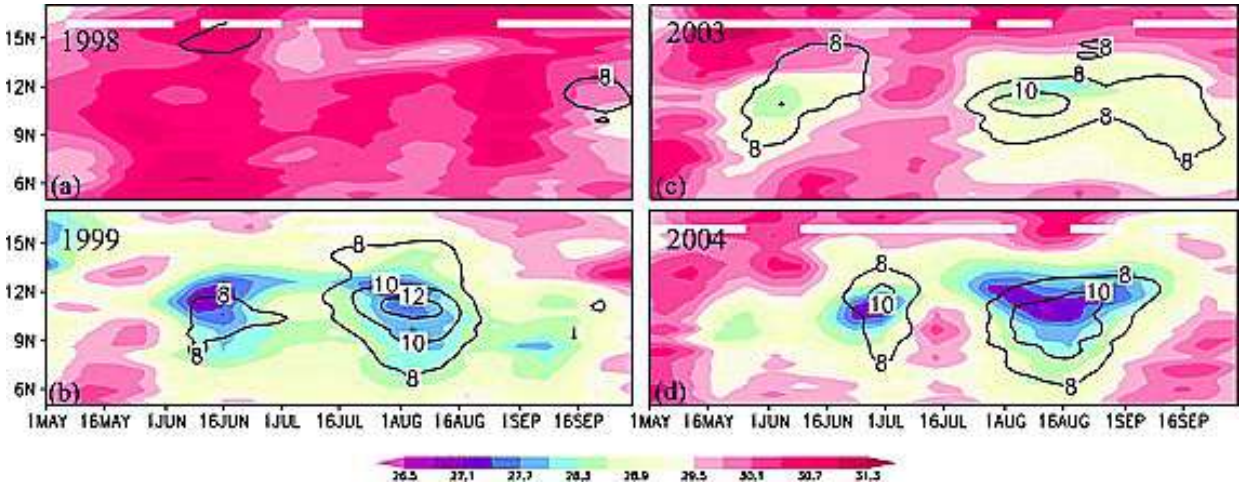

Figure 1. 17 Summer intraseasonal pulses seen in time-latitude sections of SST (°C, color shading) and wind speed (ms−1, contour) at 111°E for the summer (May to September) of (a) 1998, (b) 1999, (c) 2003, and (d) 2004. (after Xie et al., 2007)

c) Long-term Variability

Very few studies focused on the long-term variability of SVU. Su et al., (2013) showed an increasing trend of the longshore wind stress time series which intensified the upwelling during May to October for the period of 20-years (1988–2008). Ngo & Hsin (2021) considered the SVU over 3 detailed regions (northern and southern coasts, offshore region). From a 38-years time series of satellite SST they showed an apparent intensification of upwelling along the southern coast over the entire studied period. The upwelling in the northern coastal region was stronger in the 1980s and 1990s, and weaker in the 2000s and 2010s, leading to a weakening but not statistically significant trend of −0.02°C/decade. In the offshore region, the upwelling index did not show a significant trend, although most of the intense upwelling events took place in the early stage of the studied period.

1.2.3. Limitations and questions from existing studies

a) Role of OIV, eddies, and mesoscale to submesoscale structures

The SCS area has very complex active mesoscale eddies systems, facilitating the formation of submesoscale structures of the order of 1-20 km (Wang et al., 2003, Hu & Wang, 2016, Lin et al., 2020). Due to challenges in both numerical modeling and observations at this scale, studies on the SCS submesoscale dynamics have been very limited. In the SVU area, Lin et al., (2020) however used a high-resolution numerical model (~2.2 km) and showed that energetic submesoscale eddies and filaments develop southeast of Vietnam in summer, associated with the strong summer eastward jet (Shaw & Chao, 1994).

Recent studies performed for the global ocean or other regional seas (Grégorio et al., 2015; Penduff et al., 2011; Sérazin et al., 2016; Waldman et al., 2018; Da et al., 2019) showed that the interannual variability of oceanic circulation can also be significantly influenced by ocean intrinsic variability (OIV, the unpredictable part of variability due to mesoscale-eddying circulation), and that mesoscale to submesoscale structures and eddies are a major source of this OIV. Only a few studies have examined the impact of OIV on the variability of the SCS circulation and SVU. Gan et al., (2008) showed that cyclonic and anticyclonic eddies drive the summer circulation in the south SCS with strong variation generated by the separation of the eastward coastal wind from the coast of central Vietnam, that they attributed to OIV. Li et al., (2014), provided a first assessment of this OIV impact: in their simulations, OIV related to eddy- current interactions could explain 20% of the interannual variability of the eastward jet. However, given the coarse resolution of their model (1/4°), they could not reproduce thoroughly the multiscale dynamics and eddy activity in the SCS. Da et al., (2019) revealed the important role of OIV in the interannual variability of SVU based on 1/12° resolution sensitivity simulations. They showed that this impact of OIV was related to the influence of vorticity related to mesoscale structures that propagate in a chaotic way in the offshore area.

Previous studies were based on satellite data of high spatial resolution but limited temporal coverage or of low resolution over longer periods; on in-situ observations of limited temporal and spatial coverages; on numerical models of resolution not finer than ~10 km. Therefore, these studies could not completely capture those mesoscale to submesoscale structures and examine their contribution to the variability of the SVU.

b) Role of tide and rivers

Tides, through the effect of tidal mixing and internal tide, play a key role in modulating the upwelling (Hu et al., 2016). This role has been studied mainly in the northern SCS region. Strong tidal mixing transporting cold water at a depth of about 25m to the surface is responsible for upwelling in the Taiwan Bank area (Hong et al., 2011; Jiang et al., 2011). Tidal mixing front causing upwelling in southwestern Hainan Island (Hu, 2003, Lü et al., 2008), or surface cooling in the Gulf of Tonkin could be induced by tides (Piton et al., 2021). Meanwhile in the SVU area, studies on the influence of tides on upwelling are still sparse. To our knowledge, only Chen et al., (2012) demonstrated that under an unstratified condition with the absence of the southwesterly monsoon wind, tidal rectification can produce a northeastward along-shore residual current in the coastal region near 11.25^{o}N, which forms as a result of the southward current from upstream and a northeastward current from the downstream Mekong River area. Tides could therefore contribute to enhancing the upwelling that develops along the eastward jet.

The influence of river freshwater plume on the SVU functioning and variability has to be accurately estimated. Chen et al., (2012) showed that river discharge from the Red River and the Mekong River contributes to the current separation along the southeast coast of Vietnam during a southwesterly monsoon. Da et al (2019) obtained a non-significant impact of river discharges on the mean upwelling intensity and its variability, but indicated that river forcing can have a strong impact at the scale of individual years. Those previous studies were mainly based on monthly climatological river discharge data, and the role of river discharge on the SVU needs to be studied in more detail.

1.3. Objectives of the PhD

As described in the previous sections, previous modeling studies have revealed and examined some of the mechanisms involved in the functioning and variability at different scales of the SVU: alongshore wind, wind stress curl, background circulation, tides, river plumes, OIV related to mesoscale structures, ENSO. However, limitations of those studies prevented them from studying in detail the whole range of scales and mechanisms involved in the SVU, in particular the role of small scale and high frequency atmospheric forcing and ocean dynamics. The main objectives of this thesis are the following.

(1) Methodological objective: our goal is to develop a very high resolution configuration of a hydrodynamical model able to represent a wide range of processes at different spatial and temporal scales, evaluated and optimized by comparison with numerous in-situ data and high resolution satellite observations over the area that goes from the Vietnamese coast to the open SCS. This tool will be used to study ocean dynamics and its variability, as done in this thesis, but also its influence on other compartments (ecosystems, contaminants propagation….), if necessary by coupling with other models (biogeochemistry, lagrangian…).

(2) Scientific objective. Our goal is to study the role of different oceanic processes at different scales, from the regional circulation to the submesoscale and coastal dynamics, in the intraseasonal to interannual variability of the SVU, based on our high-resolution modeling tool. In the first part, we focus on the interannual variability of the upwelling. For that, we go beyond existing studies, separating the upwelling area into 3 sub-regions (two coastal areas and an area offshore) for which the mechanisms of upwelling formation differ very clearly. In order to understand this interannual variability, we carry out and analyze a simulation of 10 very contrasted years. We then perform an analysis of these 10 years based on wind, general circulation, mesoscale and fine scales structures and on a detailed analysis of intraseasonal variability. The importance of mesoscale and small-scale circulations led us to study more specifically the role of intrinsic ocean variability (OIV) on the upwelling. For this purpose, we

perform a set of 10 simulations of perturbed initial conditions forced by the same meteorology of a very intense upwelling year. This study allowed us to study how OIV modulates the upwelling intensity variability at the daily to intraseasonal scales, in the different regions of the SVU.

The structure of this manuscript is as follows:

Chapter 2 describes the hydrodynamical model SYMPHONIE used for this study, the VNC high resolution configuration developed for the SVU study, and the forcing datasets used for boundary conditions. We present satellite observations as well as *in-situ* measurements used for the model evaluation. We finally present statistical tools used for model validation.

Chapter 3 shows the evaluation of the 3D model in its representation of the oceanic circulation and water masses in the whole computational domain. We first compare the simulation outputs with satellite observations of surface circulation and water masses at seasonal and interannual scales over the period 2009-2018. Then we compare them with *in-situ* data of vertical temperature and salinity profiles collected over the whole SCS, from coastal to open-sea regions.

Chapter 4 analyzes the results of the SYMPHONIE VNC simulation performed during the period 2009-2018 to determine and understand the interannual variability of upwelling in 3 areas of the SVU area.

Thanks to an ensemble of 10 simulations with perturbed initial conditions, Chapter 5 investigates the daily to intraseasonal variability of SVU and the impact of OIV for the case study of summer 2018.

Chapter 6 summarizes the main results of the thesis. Remaining questions to be explored in future work are also discussed.

Chapter 2: Materials and Methods

Ocean numerical modelling, especially open source models, are increasingly used due to their complementarity with *in-situ* and satellite observations and their much smaller human and financial cost. Models moreover allow researchers to fully explore the 4 dimensions of the virtual ocean that they represent and to study various temporal and spatial scales (from extreme events to climate change) and periods (past or future) not accessible to observations. Nowadays, computation time has also been shortened thanks to the support of High Performance Computing clusters, allowing the development of very high resolution models that can represent a large range of physical processes involved in ocean dynamics. To study the functioning and variability of the South Vietnam Upwelling (SVU), our research-oriented approach was thus to develop over the South China Sea a high resolution configuration of the SYMPHONIE (SYM) model combined with satellite observations and *in-situ* data.

2.1 The regional hydrodynamic ocean model SYMPHONIE

We use the 3-D ocean circulation model SYMPHONIE (Marsaleix et al., 2008, 2009, 2012, 2019) developed by the Sirocco group (LEGOS, CNRS, IRD, Université de Toulouse, France). The SYMPHONIE model has been applied and validated in many different research projects covering many subjects and processes: the formation and variability of shelf and open sea dense waters (Herrmann and Somot, 2008, Herrmann et at. 2008, Ulses et al., 2008a, b, Waldman et al., 2016, Estournel et al., 2016), internal waves and wave-current interaction (Auclair et al., 2011, Michaud et al., 2011, Marsaleix et al., 2019), radioactive elements propagation over Japanese coastal zone (Estournel et al., 2012, Masumoto et al., 2012).

The SYMPHONIE model used in our study was already described in detail in the thesis of Trinh Bich Ngoc (Trinh, 2020), who used SYMPHONIE to examine the climatological average and seasonal cycle of the components of the heat and salt budgets over the SCS. The difference in our configuration is that our computational domain is based on an orthogonal curvilinear stretched grid that covers most of the SCS but focus on the upwelling area, with a very high resolution of approximately 1 km at the coast to 4 km offshore for Viet Nam Coasts (VNC) domain. For the completeness of this document, we provide here the description of the model extracted from Trinh (2020).

2.1.1 The governing equations

SYMPHONIE is a free surface model based on energy conserving finite differences as detailed in Marsaleix et al., (2008). We use a version based on the Navier–Stokes primitive equations under the hydrostatic equilibrium hypothesis, incompressibility hypothesis and Boussinesq approximations. The equations compute six state variables: three velocity components (*u, v, w*), the temperature *T*, the salinity *S* and the sea surface elevation *η*.

Given the Cartesian coordinate system, the origin O corresponds to the level of the sea surface at rest; Ox and Oy are the horizontal axes and Oz is the vertical ascending axis, the velocity components u, v and w (following respectively Ox, Oy and Oz axes) are determined via the continuity and momentum equations:

$$\frac{\delta u}{\delta x}+\frac{\delta v}{\delta v}+\frac{\delta w}{\delta z}=0 \qquad \text{(Eq. 2.1)}$$

$$\frac{\delta u}{\delta t}+\frac{\delta uu}{\delta x}+\frac{\delta uv}{\delta y}+\frac{\delta uw}{\delta z}-fv=\frac{-1}{\rho_0}\frac{\delta \rho}{\delta x}+v\Delta^2 u+\frac{\delta}{\delta z}\left(K_m\frac{\delta u}{\delta z}\right) \qquad \text{(Eq. 2.2)}$$

$$\frac{\delta v}{\delta t}+\frac{\delta uv}{\delta x}+\frac{\delta vv}{\delta y}+\frac{\delta wv}{\delta z}+fu=\frac{-1}{\rho_0}\frac{\delta \rho}{\delta y}+v\Delta^2 v+\frac{\delta}{\delta z}\left(K_m\frac{\delta v}{\delta z}\right) \qquad \text{(Eq. 2.3)}$$

where *f* is the Coriolis parameter, ρ_0 the reference water density, *p* the pressure, v the kinematic viscosity, Δ^2 the horizontal bi-Laplacian operator, and K_m the vertical coefficient of eddy diffusivity, determined by the turbulence closure scheme (detailed below).

The vertical pressure gradient is computed using the hydrostatic hypothesis:

$$p(z)=\int_z^n g\rho dz \qquad \text{(Eq. 2.4)}$$

Where g is the acceleration due to gravity, ρ the density, and η the free surface elevation, derived from the equation for the depth-averaged component of the current: $(\underline{u},\underline{v})=\frac{1}{H}\int_{-h}^{\eta}(u,v)dz$ by:

$$\frac{\delta \eta}{\delta t}+\frac{\delta}{\delta x}(H\underline{u})+\frac{\delta}{\delta y}(H\underline{v})=0 \qquad \text{(Eq. 2.5)}$$

where H = h + η is the sum of the water column thickness at rest (h) and the free surface elevation.

Temperature and salinity variations are computed from an advection diffusion tracer equation:

$$\frac{\delta T}{\delta t}+\frac{\delta uT}{\delta x}+\frac{\delta vT}{\delta y}+\frac{\delta wT}{\delta z}=\frac{\delta}{\delta z}\left(K_h\frac{\delta T}{\delta z}\right)+\frac{1}{\rho_0 C_p}\frac{\delta I_s}{\delta z}+\frac{\delta F_x^T}{\delta x}+\frac{\delta F_y^T}{\delta y} \qquad \text{(Eq. 2.6)}$$

$$\frac{\delta S}{\delta t} + \frac{\delta uS}{\delta x} + \frac{\delta vS}{\delta y} + \frac{\delta wS}{\delta z} = \frac{\delta}{\delta z}\left(K_h \frac{\delta S}{\delta z}\right) + \frac{\delta F_x^S}{\delta x} + \frac{\delta F_y^S}{\delta y} \quad \text{(Eq. 2.7)}$$

where I_s is the solar radiation flux, C_p the water heat capacity and $F_{x,y}^{T,S}$ the horizontal diffusion fluxes for temperature and salinity. The density is deduced from the non-linear state equation (Jackett et al., 2006). The vertical eddy diffusivity coefficient K_h for temperature and salinity tracers is computed by the turbulence closure scheme detailed hereafter.

2.1.2 Turbulence closure scheme

The K-epsilon turbulence closure scheme (Burchard and Bolding, 2001) used in this study has been used in SYMPHONIE by Michaud et al., (2012). The vertical eddy diffusivity and viscosity coefficients K_h and K_m are given by:

$$K_h = \sqrt{2E_k} l_k S_h \quad \text{(Eq. 2.8)}$$

$$K_m = \sqrt{2E_k} l_k S_m \quad \text{(Eq. 2.9)}$$

where E_k is the turbulent kinetic energy, l_k the mixing length depending on the eddy's dimension, S_h and S_m are the stability factors given by Canuto (2001).

The kinetic energy equation is deduced from the momentum equation:

$$\frac{\delta E_k}{\delta t} + \frac{\delta uE_k}{\delta x} + \frac{\delta vE_k}{\delta y} + \frac{\delta wE_k}{\delta z} = K_m\left[\left(\frac{\delta u}{\delta z}\right)^2 + \left(\frac{\delta v}{\delta z}\right)^2\right] + \frac{\delta}{\delta z}\left(K_h \frac{\delta E_k}{\delta z}\right) + \frac{g}{\rho_0} K_h \frac{\delta \rho}{\delta z} - \epsilon \quad \text{(Eq. 2.10)}$$

where

$K_M\left\{\left(\frac{\partial u}{\partial z}\right)^2 + \left(\frac{\partial v}{\partial z}\right)^2\right\}$ is the production term and $\frac{g}{\rho_0} K_h \frac{\delta \rho}{\delta z}$ is the buoyancy term

The mixing length l_k is related to the turbulent kinetic energy E_k and the dissipation rate ϵ by $l = {c_0}^3 {E_k}^{3/2} \varepsilon^{-1}$

The equation for the dissipation rate is

$$\frac{d\varepsilon}{dt} = \frac{\partial}{\partial z}\left(\frac{K_M}{\sigma}\frac{\partial E_k}{\partial z}\right) + \frac{\varepsilon}{k}(c_1 P + c_3 B - c_2 \varepsilon) \quad \text{(Eq. 2.11)}$$

Where P is the production term, B is the buoyancy term and constants are:

$\sigma = 1.3$	$c_0 = 0.5544$	$c_1 = 1.44$	$c_2 = 1.92$	$c_3 = 1\ if\ B \geq 0$ $c_3 = -0.52\ if\ B < 0$

2.1.3 Boundary conditions

a) Free surface boundary

At the free surface (the atmosphere – ocean interface), the boundary conditions of the kinetic energy and the horizontal component of current are determined in function of the wind stress τ_s (τ_{sx}, τ_{sy}). The vertical flux of turbulent kinetic energy $F_z = K_m \frac{\delta E_k}{\delta z}$ at the sea surface can be expressed, following Craig and Banner (1994), as:

$$F_z = 100 \left(\frac{\tau_s}{\rho}\right)^{\frac{3}{2}} \quad \text{(Eq. 2.12)}$$

with τ_s the wind stress computed by the bulk formula.

The surface current condition affected by the wind stress τ_s is determined as follows:

$$\rho_0 K_m \left(\frac{\delta u}{\delta z}, \frac{\delta v}{\delta z}\right) = (\tau_{sx}, \tau_{sy}) \quad \text{(Eq. 2.13)}$$

The heat flux at the sea surface is the sum of the sensible heat flux Q_{SEN}, the latent heat flux Q_{LATENT}, and the longwave radiative flux Q_{LR}:

$$K_h \frac{\delta T}{\delta z} = Q_{SEN} + Q_{LATENT} + Q_{LR} \quad \text{(Eq. 2.14)}$$

The surface salinity depends on the net freshwater budget at the sea surface, estimated from the surface boundary conditions applied to the vertical velocity W_{surf}:

$$W_{surf} = -\left(\frac{Q_{LATENT}}{\rho L_v} + Pr\right) \quad \text{(Eq. 2.15)}$$

where L_v is the latent heat of condensation of water (L_v=2.5*10^6 J/kg) and P_r the precipitation rate. Q_{SEN}, Q_{LATENT}, and the wind stress τ_s are calculated from the atmospheric dataset (surface pressure, wind at 10 meters, temperature and humidity at 2 meters) using bulk formulas described in Large and Yeager (2004), the longwave upward flux is calculated with the sea surface temperature while the shortwave (I_s) and downward longwave radiation flux (Q_{LR}) and the precipitation rate are deduced from the atmospheric model dataset (see 2.2 below).

b) Bottom

The heat and salt turbulent fluxes at the sea bottom are equal to 0.

$$K_m \left(\frac{\delta T}{\delta z}, \frac{\delta S}{\delta z}\right)_{z=-h} = 0 \quad \text{(Eq. 2.16)}$$

The boundary condition approximation for turbulent energy kinetics at the sea bottom corresponds to the equilibrium between energy production and dissipation. The later is generated by the friction of currents on the sea bed, related to the bottom stress τb:

$$E_{k_{z=-h}} = \frac{\|\tau_b\|}{\rho_0 \sqrt{2^{0.5} c_0^3 S_m}} \quad \text{(Eq. 2.17)}$$

where τb is determined by a quadratic relation of the bottom velocity $\overrightarrow{V_b}$, calculated at the first layer of the model grid of height z1

$$\overrightarrow{\tau_b} = \rho_0 C_D \|\overrightarrow{V_b}\| \quad \text{(Eq. 2.18)}$$

where $\overrightarrow{V_b}$ the bottom velocity, and C_D the non-dimensional bottom drag coefficient. C_D is related to the bottom roughness z_0 through a relation based on a logarithmic form of the bottom current:

$$C_D = \left(\frac{\kappa}{log\left(\frac{z_1}{z_0}\right)}\right)^2 \quad \text{(Eq. 2.19)}$$

where κ = 0.41 is the Von Karman's constant and z_1 is the distance of the first level of the model to the seafloor.

c) Lateral boundaries

At closed lateral boundaries such as continents or islands, the normal current velocity component is equal to 0. At the open sea borders, the boundary conditions play two roles: the radiation of outgoing waves and the forcing at every time step issued from a larger scale model and a tidal model. Following Marsaleix et al., (2006), the open boundary conditions scheme applied in the SYMPHONIE model applies to the difference between the modeled variables and the forcing variables.

Given the open ocean boundaries at x=0 and x=m, we distinguish the barotropic and baroclinic currents.

For the barotropic current $(\bar{u}, \bar{v})$, the Flather type condition is applied to the surface elevation η:

$$\eta - \eta_f = -\sqrt{\frac{H}{g}}\left(u^- - u_f^-\right) \text{ at x =0} \quad \text{(Eq. 2.20a)}$$

$$\eta - \eta_f = \sqrt{\frac{H}{g}}\left(u^- - u_f^-\right) \text{ at x = m} \quad \text{(Eq. 2.20b)}$$

where the f index indicates the forcing (large scale circulation and tidal circulation).

The tangential transport at the boundaries is computed using the Neumann condition:

$$\frac{\delta H\left(v^- - v_f^-\right)}{\delta x} = 0 \text{ at x = 0 and x = m} \quad \text{(Eq. 2.21)}$$

For the baroclinic currents (u, v), the radiative condition of Sommerfeld type is applied on the difference between the SYMPHONIE variables (Φ for u and v) and the forcing variables (Φ_f):

$$\frac{\delta\left(\phi - \phi_f\right)}{\delta t} + C_c \frac{\delta(\phi - \phi_t)}{\delta x} = 0 \text{ at x = 0} \quad \text{(Eq. 2.22a)}$$

$$\frac{\delta\left(\phi - \phi_f\right)}{\delta t} - C_c \frac{\delta(\phi - \phi_t)}{\delta x} = 0 \text{ at x = m} \quad \text{(Eq. 2.22b)}$$

where C_c is the phase velocity of baroclinic waves.

Regarding the scalar variables (T, S), the open boundary conditions of the advection scheme are applied using a hybrid scheme composed of an upstream scheme and a centered scheme. In case of incoming flow, the temperature and salinity (T_f, S_f) are deduced from the forcing of a larger scale model. In case of outgoing flow, these variables are issued from the simulated domain.

In combination with equations 25, 26, 27, forcing terms (relaxation terms) are applied. At the open boundary x=0, this term is written as:

$$e^{\frac{-x}{d}} \frac{\phi - \phi_f}{\tau_r} \quad \text{(Eq. 2.23)}$$

where Φ stands for velocity, T or S depending on the equation considered; d corresponds to a distance depending on the domain size; T_r corresponds to the relaxation time addressed by the user.

d) Tide

Variables u, v and η also include the tidal circulation. Tidal forcing consists mainly of tidal surface elevations and currents, written as follows:

$$\eta(\lambda,\varphi,t) = \sum_k f_k \eta_{0,k}(\lambda,\varphi) cos\left(\omega_k(t-t_0) + V_{0,k} + u_k - G_{\eta,k}(\lambda,\varphi)\right) \quad \text{(Eq. 2.24a)}$$

$$u(\lambda,\varphi,t) = \sum_k f_k u_{0,k}(\lambda,\varphi) cos\left(\omega_k(t-t_0) + V_{0,k} + u_k - G_{u,k}(\lambda,\varphi)\right) \quad \text{(Eq. 2.24b)}$$

$$v(\lambda,\varphi,t) = \sum_k f_k v_{0,k}(\lambda,\varphi) cos\left(\omega_k(t-t_0) + V_{0,k} + u_k - G_{v,k}(\lambda,\varphi)\right) \quad \text{(Eq. 2.24c)}$$

where η_0, u_0, v_0 and G_η, G_u, G_v are the amplitudes and phase for sea surface elevations and currents depending on the longitude λ and the latitude φ; the subscript k represents the tidal components considered in the configuration. The nodal factors f_k and u_k are considered as constants (Doodson, 1927), ω is the tidal frequency and V_0 is a constant related to the reference time t_0.

The tidal forcing also consists of astronomical and loading potential (respectively Π_A and Π_L), providing a barotropic force added to the momentum equation, through the horizontal components of their gradients. The tidal potential due to astronomical effects Π_A (Hendershott, 1972) is taken into account as follows:

$$\Pi_A = (1 + k_2 + h_2) fa * \left(v_0 \frac{1-3sin^2(\varphi)}{2} + v_1 sin(2\varphi) + v_2 cos^2(\varphi)\right) * cos\big(\omega(t-t_0)\big) + \nu\lambda + V_0 + u$$

(Eq. 2.25)

where k_2, h_2 are the Love numbers, the equilibrium amplitude of the tidal constituents considered, the term (v_0, v_1, v_2) and ν vary with the type of tide. In case of long period tide v_0 = 1 and ν = 0, of diurnal tide v_1 = 1 and ν = 1, of semi diurnal tide v_2 = 1 and ν = 2.

The loading potential Π_L (LSA potential) is expressed as:

$$\Pi_L = f\Pi_0(\lambda,\varphi) cos(\omega(t-t_0) + G_\Pi(\lambda,\varphi) + V_0 + u) \quad \text{(Eq. 2.26)}$$

The horizontal momentum equation for the hydrostatic pressure force is determined as:

$$-\frac{\nabla p}{\rho_0} = -\frac{g}{\rho_0}\nabla \int_z^\eta (\rho - \rho_0) dz' - g\nabla(\eta - \Pi_A - \Pi_L) \quad \text{(Eq. 2.27)}$$

e) Rivers

At the river mouths, the salinity value is considered equal to 0 and the temperature varies as a cosinusoidal function with a one-year period between a minimum and a maximum value. The barotropic velocity U is calculated based on the river runoff flux F following the relationship:

$$U = \frac{F}{l} \qquad \text{(Eq. 2.28)}$$

where *l* is the horizontal grid spacing. More details on the river mouth's open boundaries in SYMPHONIE are described in Reffray et al., (2004).

2.1.4 Discretization of equations

a) Spatial discretization

The SYMPHONIE model equations are solved using the finite difference method on the Arakawa staggered C-grid (Arakawa and Suarez 1983) scheme, as illustrated in Fig. 2.1 Horizontal velocity components u, v are defined in the middle of the edges of the grid volume at each half level, whereas the tracers (temperature, salinity, surface elevation) are defined at the center of the grid cell. The vertical velocity and kinetic energy are calculated at the center of the grid edges at each vertical level.

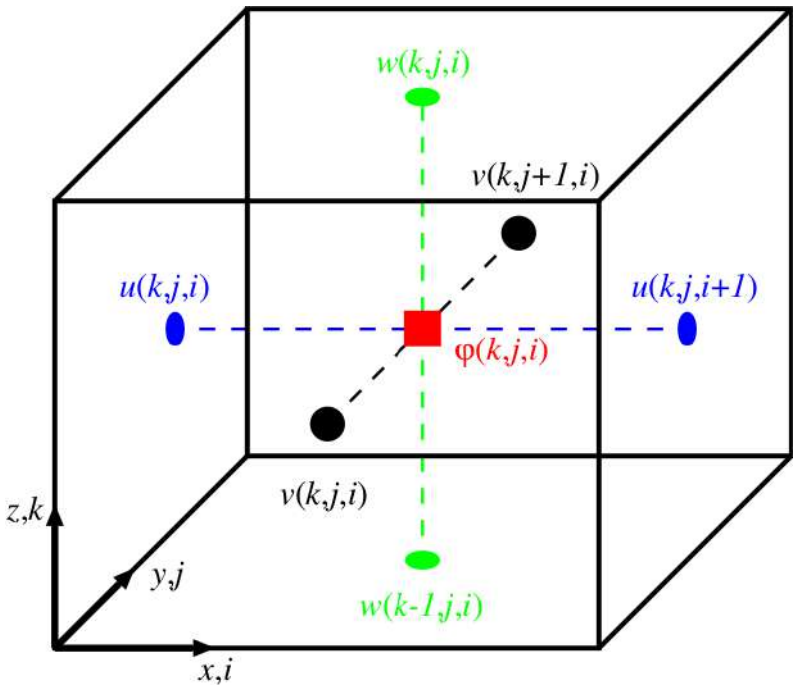

Figure 2. 1: The Arakawa staggered C-grid (Piton, 2019). The i, j, k indices respectively correspond to x, y, z direction; φ the scalar quantities (T, S, SSH). Turbulent fields are defined at green points (the same position as vertical components of velocity).

Regarding the vertical grid, SYMPHONIE employs a system of vanishing quasi-sigma (VQS) vertical coordinate concept described in Dukhovskoy et al., (2009). An example of the vertical grid of SYMPHONIE is presented in Fig. 2.2 This original choice of this "hybrid" grid allows to take advantage of the generalized sigma coordinate grid: providing a good representation of the bathymetry and avoiding hydrostatic inconsistencies in calculation of pressure gradient for strong slopes (Siddorn et al., 2013). The VQS coordinate also helps to limit the number of vertical levels at very shallow zones while maintaining an accurate description in deep regions.

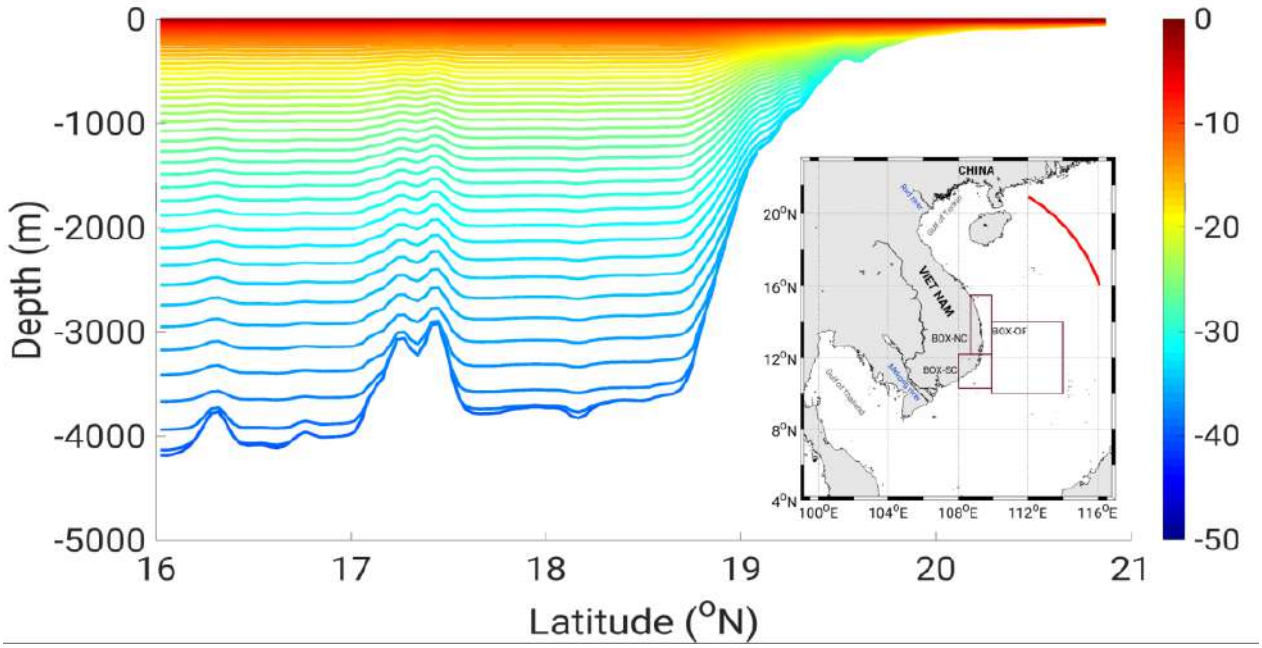

Figure 2. 2 Vertical section in the VNC computation domain (red line) showing the distribution of vertical levels (color bar) with the VQS vertical coordinate system.

The vertical advection is computed using a centered scheme. The QUICKEST scheme (Leonard, 1979) is used for horizontal advection and diffusion of temperature and salinity. Horizontal advection and diffusion of momentum are each computed with a fourth order centered biharmonic scheme. The biharmonic viscosity of momentum is calculated according to a Smagorinsky-like formulation derived from Griffies and Hallberg (2000).

b) Temporal discretization

The forward-backward (FB) time stepping scheme is used for the temporal discretization of the equations. In this explicit time stepping method, the variable value at time t+1 is deduced by the variable value at time t:

$$F' = F^t + \Delta t\, f(F^t) \qquad \text{(Eq. 2.29a)}$$

$$F^{t+1} = F^t + \Delta t\, f(F') \qquad \text{(Eq. 2.29b)}$$

More details of the FB time stepping application and chronology of variables in SYMPHONIE are further described in Marsaleix et al., (2012).

A summary of the features of the schemes for the SYMPHONIE model is given in Table 2.1.

Table 2. 1 Summary of the numerical schemes

Contents	Numerical schemes	References
Numerical method	Curvilinear C-grid, vanishing quasi-sigma vertical coordinate, energy conserving finite difference method	Marsaleix et al., 2008 Dukhovskoy et al., 2009 Yinglong et al., 2015
Time stepping	Forward-backward Leapfrog + Laplacian Filter	Marsaleix et al., 2012
Pressure Gradient	Jacobian pressure gradient	Marsaleix et al., 2009
Equation of state	Jackett et al., 2006	Marsaleix et al., 2011
Turbulence scheme	K-epsilon	Michaud et al., 2012
T,S advection	QUICKEST (horizontal and diffusion) Centered biharmonic (vertical)	Leonard, 1979 Griffies and Hallberg, 2000
Open boundary condition	Radiation conditions combined with nudging conditions	Marsaleix et al., 2006
Sea surface condition	Bulk formulae (Large and Yeager, 2004), Turbulence Kinetic Energy boundary conditions (Craig & Banner., 1994)	Estournel et al., 2009
River input	Lateral condition	Estournel et al., 2001 Reffray et al., 2004

2.2 The South Vietnam Upwelling configuration and modeling strategy

2.2.1 Computation domain VNC

The standard horizontal bipolar grid (where the poles are separated by 180 degrees of latitude) is adapted to our coastal problem by tilting the axis of the poles in order to place one of the 2 poles in the continental part near the coastal zone of interest where the resolution is increased as in Estournel et al (2012). Here the nearest pole is located in the centre of the

Vietnamese center (Fig. 2.3). The resolution is maximum (1km x 1km) over most of the coastline (including the upwelling region studied) and decreases almost linearly seaward, the resolution at the open boundary being about 4.5 km x 4.5 km.

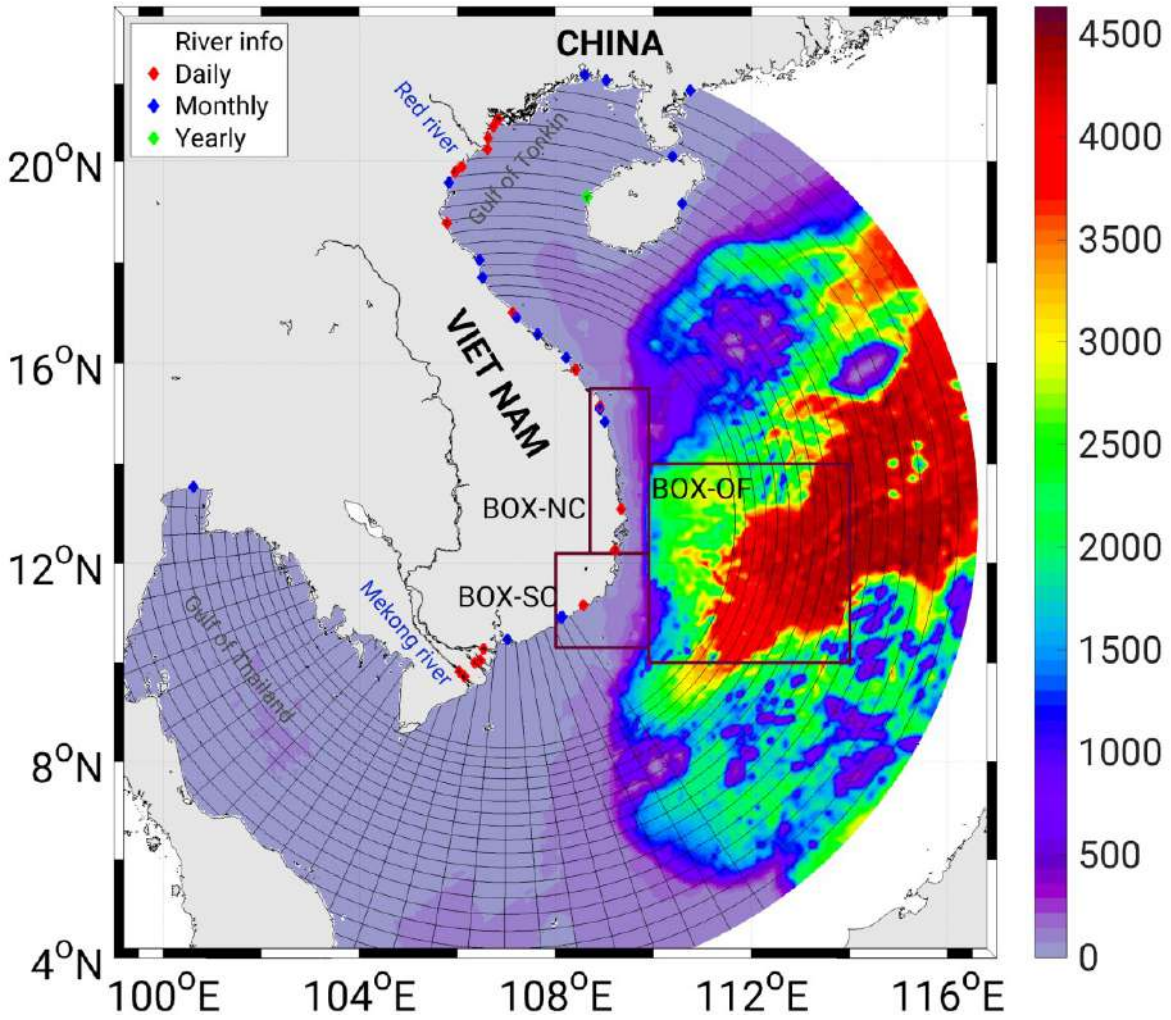

Figure 2. 3 Characteristics of the orthogonal curvilinear grid (black grid) and bathymetry (colors, m, GEBCO_2014, ~1km resolution) used over our VNC SYMPHONIE computation domain, and location of river discharge with daily (red), monthly climatology (blue), yearly (green) values. Dark brown rectangles represent the location of key study regions (see chapter 4).

2.2.2 Forcings

We used the following products to prescribe external forcings to our SYMPHONIE VNC configuration.

The surface forcing is prescribed using the 3-hourly output of the European Center for Medium-Range Weather Forecasts (ECMWF) 1/8° atmospheric analysis. The product used is a forecast CF-1.0, including: atmospheric pressure, wind velocity at 10 m above sea level, air temperature and humidity at 2m above sea level, respectively, total precipitation, solar and longwave downward radiation.

The initial and lateral ocean boundary conditions (current, sea surface height, temperature, salinity) are prescribed using the daily outputs of the global ocean 1/12° analysis distributed by the COPERNICUS European service on http://marine.copernicus.eu.

The implementation of the tides, described in Pairaud et al (2008, 2010), consists on one hand of the amplitude and phase of the tide introduced at the open lateral boundaries, and on the other hand of the astronomical plus loading and self-attraction potentials. As in Pairaud et al (2008, 2010), the 9 main tidal harmonics are considered (M2, N2, S2, K2, K1, O1, P1, Q1, M4), and provided by the 2014 release of the FES global tidal model (Lyard et al., 2006).

For the river forcing, we have 3 kinds of river runoff data, with a total of 36 rivers over the modeled domain (locations shown in Fig. 2.3): monthly climatology (17 rivers), yearly value (1 river) and interannual daily data (18 rivers). Fig. 2.4 shows the interannual variability of total river discharge over our domain during the period 2009-2018. The annual mean for the total 36 rivers (black curve) is about 21400 m^3/s over 2009-2018. The discharges of the rivers for which a monthly climatology is available (~6500 m^3/s) represents half of the discharge of the rivers for which interannual values are specified (~15000 m^3/s). So, to account for the interannual variability of river discharges for which we only had monthly climatological data, we applied an interannually varying multiplying factor, obtained from an interannually varying dataset (red curve in Fig. 2.4, called “interpolated monthly”). This factor was computed from the time series of the average of the interannual discharge data (green curve on Fig. 2.4).

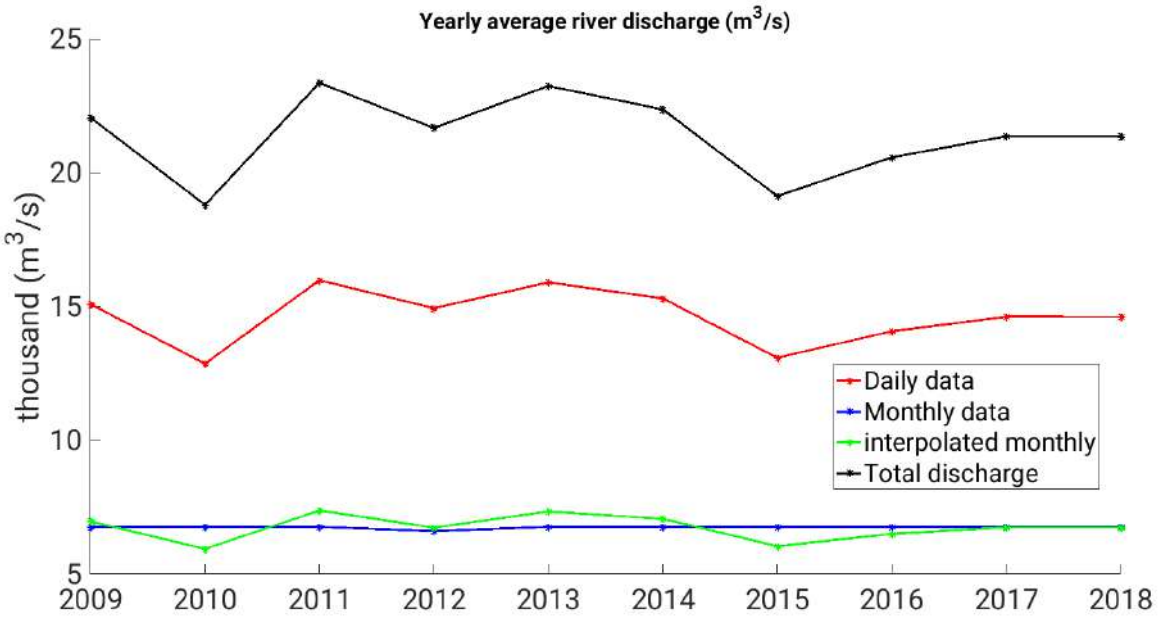

Figure 2. 4 Time series of annual average of the total river discharge input to the VNC domain: sum of daily interannual data (red), of climatological monthly data (blue), interpolated monthly data (green) and total discharge (black)

2.3 Satellite and in-situ observations

2.3.1 Satellite observations

To evaluate and calibrate the model, we use satellite observation of Sea Surface Temperature (SST), Sea Surface Salinity (SSS), and Sea Level Anomaly (SLA). For model-data comparisons, we interpolate model outputs on satellite data spatial and temporal grids.

a) OSTIA/GHRSST

We use OSTIA (Operational Sea Surface Temperature and Sea Ice Analysis) level 4 analysis produced by the Group for High Resolution SST (GHRSST) (UK MetOffice, 2005, see https://podaac.jpl.nasa.gov/dataset/UKMO-L4HRfnd-GLOB-OSTIA). This retrospective dataset is produced on a global 0.05° grid over the period 2009-present using wavelets as basic functions in an optimal interpolation approach. OSTIA data are used for model evaluation and for identification of SVU periods and areas. They are available at ftp://data.nodc.noaa.gov/pub/data.nodc/ghrsst/L4/GLOB/UKMO/OSTIA/.

b) SMOS

The first soil moisture and ocean salinity (SMOS) satellite was launched by the European Space Agency (ESA) in 2009, which represented the first use of spaceborne remote sensing tools to probe global sea surface salinity (SSS). SMOS satellite carries a microwave imaging radiometer with aperture synthesis (MIRAS), which provides a global SSS distribution. We use the SMOS version 3 developed by Boutin et al., (2018): a 9 day averaged level 3 SSS with a resolution of 0.25° over 2010-2017, available on ftp://ext-catds-cecos-locean:catds2010@ftp.ifremer.fr.

c) AVISO

Daily altimetry sea level anomaly (SLA) data are produced by AVISO (Archiving, Validation and Interpretation of Satellite Oceanographic data) at a resolution of 0.25°. These altimeter products cover the period from 1993 up to now (Ablain et al., 2015, Ray and Zaron 2015) and are distributed by the Copernicus Marine and Environment Monitoring Service (CMEMS, http://marine.copernicu.eu).

d) JAXA Himawari Monitor

JAXA's P-Tree system, that provides multi-satellite products, releases the geostationary satellite Himawari Standard Data provided by the Japan Meteorological Agency (JMA) as well as the geophysical parameter data produced by JAXA using the Himawari Standard Data. We use the daily Sea Surface Temperature (Level 3) provided by this data set over the period 2015 - present with a 2 km spatial SST resolution.

2.3.2 *In-situ* data

To evaluate the ability of the model to reproduce the characteristics of water masses over the South China Sea and particularly over the SVU region, we collected and processed temperature and salinity *in-situ* data available over the study area. Observations were available from ARGO floats (2009-2018), from a sea-glider collaborative project between Vietnam and USA (January to May 2017), and from the IO-18 boat cruise performed by the Institute of Oceanography (IO, spring 2018). In addition, continuous SST and SSS *in-situ* thermosalinometer data as well as XBT profiles were measured during the ALIS campaign performed by IRD in summer 2014 along the Vietnamese coast. The location of those measurements is shown in Fig. 2.5 and their main characteristics are presented in Table 2.2.

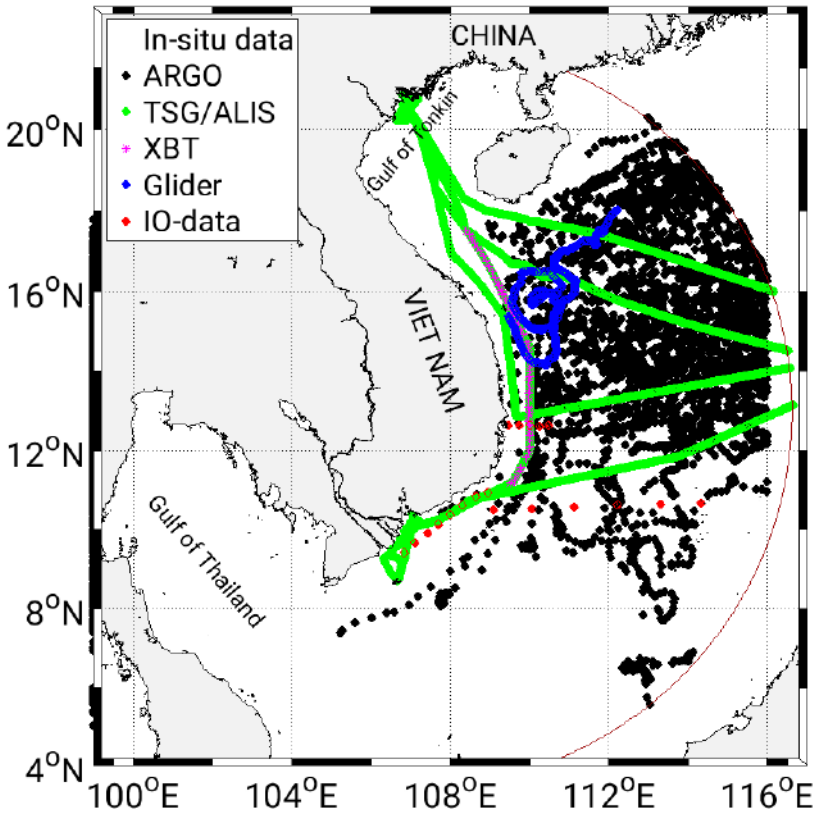

Figure 2. 5 Locations of in-situ data available over the VNC domain: ARGO buoys (black), ALIS R/V campaign (thermosalinometer: green; XBT: pink), IO-data (red), and Sea-Glider (blue)

Table 2. 2 Information about in-situ measurements used in our study: period, number of stations and type of instrument

Name of dataset	Period	Number of stations/points	Type of profiles
ARGO	01.01.2009-31.12.2018	3675	CTD, T,S profiles
TSG/ ALIS	22.05-21.07.2014	573,803 (every ~40s/point)	TSG, SSS, SST
XBT/ALIS	29.06-01.07.2014	52	XBT, T profiles
Glider	22.01-16.05.2017	552	CTD, T,S profiles
IO-18	12.09-25.09.2018	43	CTD, T,S profiles

a) ARGO floats

ARGO is a global system consisting of about 3,800 free-floating devices that automatically collect temperature and salinity data from the surface layer down to a depth of 2000 m in the ocean with a very good spatial and temporal coverage. Data are continuously forwarded and updated to the ARGO database source, and publicly available within a few hours of collection. We collected more than 3 600 profiles over the period 2009-2018 in our study area (black points in Fig. 2.5) via ftp://ftp.ifremer.fr/ifremer/argo/geo/pacific_ocean/

b) Sea-glider Vietnam-US campaign

Under the framework of a cooperative international research program, including Vietnamese and U.S. scientific institutions (Rogowski et al. 2019), a glider-based observational program was initiated. Seaglider sg206 was deployed on 22 Jan 2017 and crossed the strong southward currents near the shelf break approximately 4 times before the steering mechanism malfunctioned on 21 Apr 2017. Ultimately, the mission ended on 16 May 2017 without recovery. The glider collected 555 vertical profiles over the 114 days of deployment (blue points in Fig. 2.5).

c) ALIS TSG and XBT data

In the framework of the VITEL (VIetnam TELédétection remote sensing) program (TOSCA CNES project, PI OUILLON Sylvain), the VITEL cruise was organized in May – July 2014 on the French scientific vessel ALIS. Two main campaigns were held in the Northern and Southern Vietnamese coastal zones respectively. During the trajectory of the ALIS vessel

in the South China Sea, surface temperature and salinity were measured every 6 seconds, from 10 May 2014 to 28 July 2014 (green points in Fig. 2.5) by the automatic thermosalinometer Seabird SBE21 (hereafter called TSG data). Moreover, when the vessel crossed the SVU area (beginning of July), 52 XBT sensors were deployed providing temperature profiles over the area (pink points in Fig. 2.5). More detailed information on ALIS equipment (in french) is found at:

https://www.flotteoceanographique.fr/La-Flotte/Navires-semi-hauturiers/Alis/Caracteristiques-detaillees.

d) IO-18 CTD data

Meteorological, current, temperature, and salinity parameters were measured in the framework of the Vietnamese State project (code DTDL.CN-28/17, PI. Vo Si Tuan) in September 2018. Location of stations are shown in Fig. 2.5 (red points): measurements were performed at 19 stations. This included 16 instantaneous measurement stations, and 3 continuous measurement stations where measurements were collected every 3 hours during 24 hours. As a result, a total of 43 T,S profiles were measured by a Sea-Bird 19plus CTD.

2.4 Statistical methods

In the following, when comparing model and data, the relationship between the simulated dataset S and observational dataset O (of size N) is investigated using three statistical parameters: the bias, Normalized Root Mean Square Error (NRMSE) and the Pearson correlation coefficient R. We keep the same convention for the three statistic formulas:

Si, Oi: the simulation and observation series

$\underline{S}$, $\underline{O}$: mean value of respectively the simulation and observation series.

2.4.1 Bias

The bias between two time series S and O is equal to the difference between the two mean value of the two time series

$$bias = \underline{S} - \underline{O} \qquad \text{(Eq. 2.30)}$$

2.4.2 Normalized root mean square error (NRMSE)

The NRMSE between the two dataset is computed as follows:

$$NRMSE = \frac{\sqrt{\frac{1}{N}\sum_{i=1}^{n}(Si-Oi)^2}}{(O_{max}-O_{min})} \quad \text{(Eq. 2.31)}$$

2.4.3 Pearson correlation coefficient R

The Pearson correlation coefficient R is a statistical parameter which measures the strength of a linear relation between two variables S and O.

$$R = \frac{\sum_{i=1}^{N}(O_i-\underline{O})(S_i-\underline{S})}{\sum_{i=1}^{N}(O_i-\underline{O})^2 \sum_{i=1}^{N}(S_i-\underline{S})^2} \quad \text{(Eq. 2.32)}$$

To quantify the statistical significance of a correlation, we moreover compute for each correlation coefficient the associated p-value, defined as the probability that the null hypothesis (= there is no relationship between the two variables being studied) is true. The p-value is calculated using a t-distribution with (n - 2) degrees of freedom (n = number of pairs of scores). In practice, a table of critical values for Pearson correlation is used for the determination of p-values. The smaller the p-value, the stronger the evidence that the null hypothesis is rejected. If the p-value <0.05, resp 0.01, the correlation coefficient is called statistically significant at 95% (significant), resp. 99% (highly significant).

Chapter 3: Evaluation of The LONG-SYM Simulation over 2009-18

The section provides the evaluation of the 3D model in its representation of the oceanic circulation and water masses in the whole computational domain. We first compare the simulation performed over the period 2009-2018, called “LONG-SYM” hereafter, with satellite observations (SST, SSS, SLA) at seasonal and interannual scales. Then we compare it with i*n-situ* data for vertical temperature and salinity profiles as well as water mass characteristics in the SCS. This numerical tool and its evaluation were presented in a paper submitted to Ocean Science (Thai To Duy, Marine Herrmann, Claude Estournel, Patrick Marsaleix, Thomas Duhaut, Long Bui Hong, and Ngoc Trinh Bich. *Role of wind, mesoscale dynamics and coastal circulation in the interannual variability of South Vietnam Upwelling, South China Sea*. *Answers from a high resolution ocean model*. Ocean Science, *accepted*).

3.1. Evaluation of the surface characteristics

3.1.1 Annual cycle

The simulated climatological annual cycle of SST (Fig. 3.1a) averaged over the whole computational domain matches well with the one computed from the OSTIA observations over 2009-2018 with a highly significant correlation (coefficient R=1, p-value p<0.01, corresponding to ~100% significant level), an averaged bias of 0.08 ^{o}C and a small NRMSE value (0.02). The SST difference between summer and winter is around 3-3.5 ^{o}C. The monthly climatological SST in both datasets reaches its highest value in May and June during summertime, then drops to its lowest value during wintertime in January and February. This is also completely consistent with the monthly climatological SST in Northern Southeast Asia in the study of Siew et al., (2013), who analyzed HadISST observation data and 10 coupled models over a period from 1961-2000.

The climatological annual cycle of SSS (Fig. 3.1c) from the SMOS satellite over 2010-2017 is saltier than our model (averaged bias of -0.3 psu, NRMSE number is of 0.76), but the seasonal variability is well reproduced with maximum and minimum values in April and September, respectively. The correlation coefficient between both datasets is high, R=0.89 (p<0.01). This salinity difference could be at least partially due to the difference of spatial

resolution between the satellite (28 km) and the model (approximately 1 km in the nearshore area). The simulated climatological seasonal cycle is also similar to the results obtained by Zeng et al., (2014). The factors controlling patterns of seasonal SSS distribution are closely related to both the external freshwater forcing and ocean processes over the entire SCS monsoon system (Yi et al., 2020).

The climatological annual cycle of SLA over the period 2009-2016 (Fig. 3.1e) deduced from the AVISO altimetric data, has a very high similarity with our model. We obtained the highest significant correlation coefficient of R=1 (p-value P<0.01) between SYMPHONIE (LONG-SYM) and AVISO data, with a small NRMSE of 0.06. Both datasets show a maximum SLA (7 cm for AVISO and 6 cm for LONG-SYM) in the winter (December) and a minimum in the summer (June) of -5.9 cm (AVISO) and of -5 cm (LONG-SYM). Moreover the monthly climatological SLA from our model is in agreement with the studies of Shaw et al., (1999) and Ho et al., (2000), who used TOPEX/Poseidon altimeter data from 1992-1997 over the SCS.

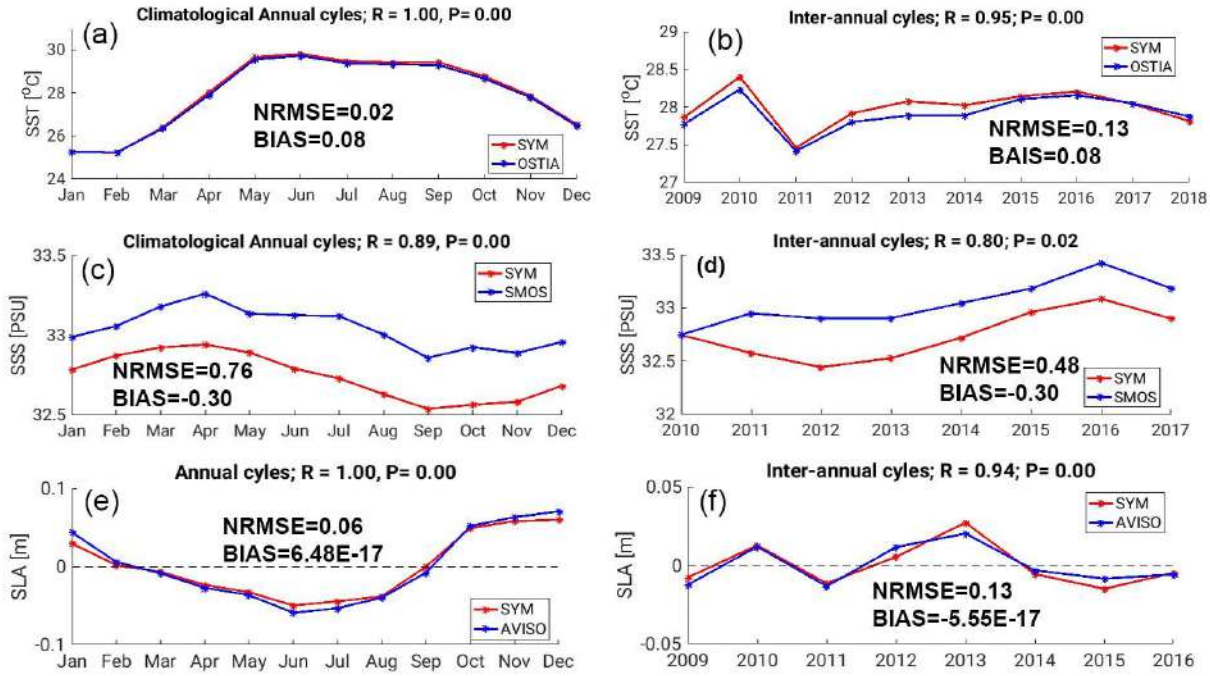

Figure 3. 1 Climatological annual cycle (left) and interannual cycle (right) of SST (°C, a, b), SSS (PSU, c, d) and SLA (m, e, f) from SYMPHONIE (red) and satellite observations (blue). R is correlation coefficient and P is p-value. Values are averaged over the numerical domain.

3.1.2. Interannual variability

The inter-annual cycle of SST of OSTIA and our simulation LONG-SYM (Fig. 3.1b) present a high correlation coefficient of 0.95 (p<0.01), with an averaged temperature bias of 0.08 °C and a NRMSE of 0.13. SST shows strong variations between 2009-2011 with the highest amplitude of about 1 °C between the years of maximum (2010, 28.5 °C) and minimum

(2011, 27.5 ^{o}C), respectively. Then temperature increases regularly during 2012-2016 by about 0.16 ^{o}C per year on average. To explain these variations, Yu et al., (2019) showed through the analysis of satellite observations for 15 years from 2003 to 2017 that the cause of the 2 maximum SST anomaly peaks in SCS is due to the influence of the 2009-2010 and 2015-2016 El Nino events and the minimum is due to the impact of 2011-2012 La Nina period.

We obtained a significant correlation coefficient of R=0.80 ($p<0.02$) and a NRMSE is 0.48 for the interannual cycle of SSS (Fig. 3.1d). A SSS increase is shown by both our model and SMOS observation in the period 2012-2016. A persistent salinification occurred during 2015-2016 over the SCS due to oceanic and atmospheric dynamics, in particular precipitation loss, associated with a strong El Nino event was indeed shown by several authors (Zeng et al., 2016), Yi et al., 2020, Trinh, 2020).

For the inter-annual cycle of SLA (Fig. 3.1f), we obtain a high similarity between AVISO and LONG-SYM over 2009-2016 with a correlation coefficient of R=0.94 ($p<0.01$) and a NRMSE value of 0.13. The overall averaged SLA computed from both OSTIA and LONG-SYM during the study period was minimum in 2009, 2011 and 2015 (about 1.3 cm), and maximum in 2015 (about 2 cm in the model and 2.7 cm in AVISO).

Overall, our model reproduces very well the variations of the surface hydrology and dynamics of the SCS shown by satellite observations and is in agreement with the conclusions of previous studies. Our model reproduces very well the annual cycle and the inter-annual variability.

3.1.3. Seasonal variability of surface patterns

In this section, we evaluated the simulated climatological spatial patterns(8-10 year averaged) of SST, SSS, SLA and geostrophic current in winter (December, January, February) and summer (June, July, August) by comparison with satellite observations.

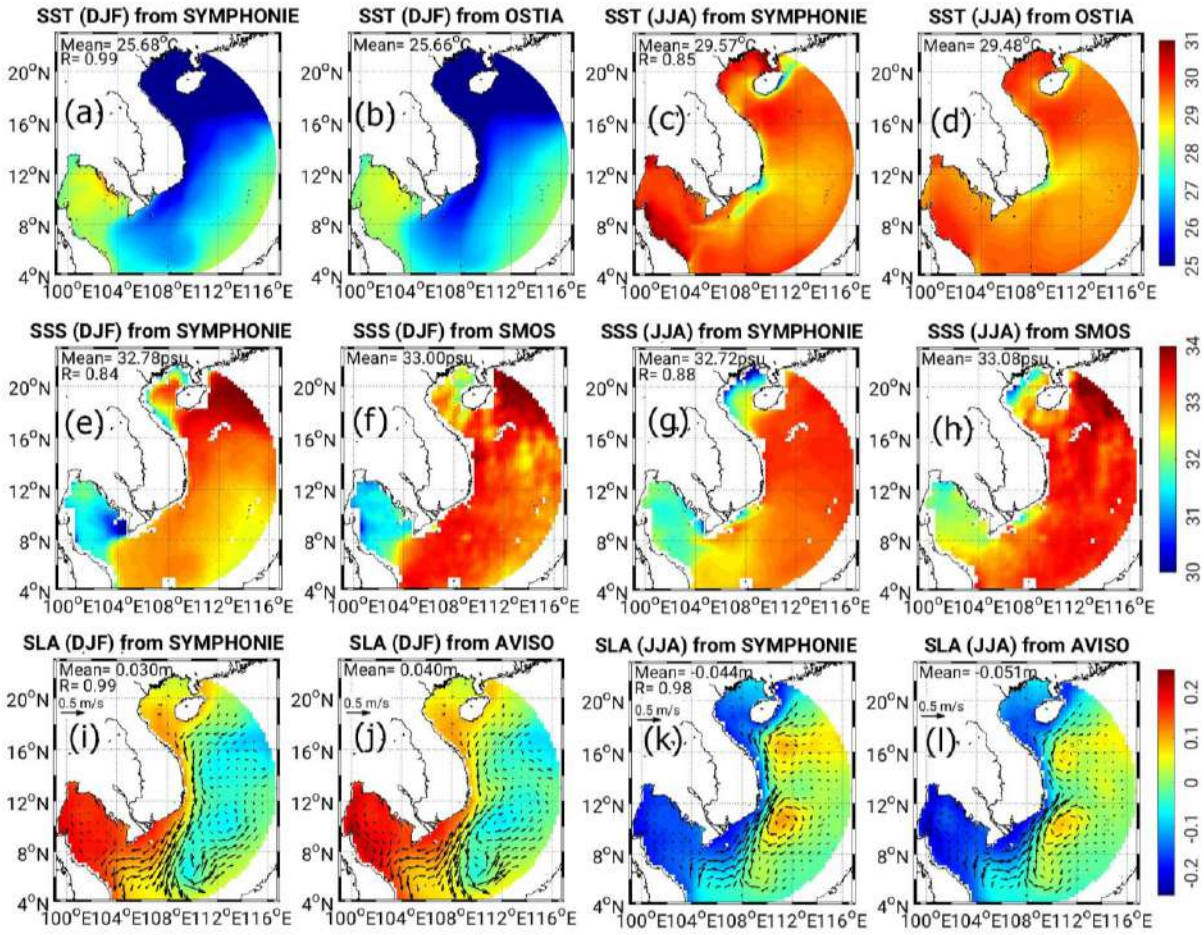

Figure 3. 2 Spatial distribution for winter (DJF) and summer (JJA) of climatological SST (°C, a, b, c, d), SSS (psu, e, f, g, h), SLA (m) and total surface geostrophic current (m/s, i, j, k, l) in SYMPHONIE and satellite observations. R indicates the spatial correlation coefficient (here p-value is always smaller than 0.01)

The simulation LONG-SYM reproduces realistically the spatial patterns of SST shown by OSTIA observations, with highly significant correlation in winter (Fig. 3.2a, b) and summer (Fig. 3.2c, d, coefficient R=0.99 and 0.85 respectively, p<0.01). There is almost no significant difference in SST between LONG-SYM and OSTIA in winter (averaged bias equal 0.02 ^{o}C) as well as in summer (averaged bias equal 0.09 ^{o}C). The whole basin SST in summer is higher than in winter by about 3.89 ^{o}C and 3.82^{o}C by LONG-SYM and OSTIA respectively. In winter, cold water is concentrated in the north of the SCS with a tongue (water temperature less than 26 ^{o}C) extending southward along the Vietnamese coast to latitude 5^{o}N (Fig. 3.2c,d). This climatological SST mean distribution in the SCS is influenced by the East Asia Monsoon (Wyrtky, 1961; Chao et al., 1996; Fang et al., 2006), with its northeasterly wind which induces a basin wide cyclonic circulation pattern advecting cold surface waters from the northern basin to the south. On the contrary, with the southwesterly wind in summer, the circulation consists in an anticyclonic gyre associated with an eastward jet at around 12 ^{o}N (Wu et al., 1998) and an Ekman transport generating the upwelling along Vietnamese coast from June to

September (Xie et al., 2003, Dippner et al., 2007, Da et al, 2019). This upwelling is traceable with the presence of cold water near the coast of Vietnam from 10-12 ^{o}N and 108-111 ^{o}E in the OSTIA dataset as well as in our LONG-SYM outputs (Fig. 3.2c, d).

The spatial seasonal SSS in LONG-SYM also has a high significant correlation with SMOS in winter (Fig. 3.2e, f) and summer Fig. 3.2g, h), with coefficients of R=0.84 and 0.88 (both p-value <0.01) respectively. As presented in the annual cycle, the SSS of SMOS is larger than in LONG-SYM (negative bias of -0.22 psu in winter and -0.36 psu), both with lower salinity in the south of the SCS and the Gulf of Thailand as well as in coastal zones. The affected areas are around major rivers such as the Mekong, Red, and Pearl rivers. In the northeastern SCS area, both LONG-SYM and SMOS show high SSS due to the influence of water from the Western Pacific Ocean entering the SCS through the Luzon Strait round the year (Qu et al., 2000; Zeng et al., 2016).

For the seasonal distribution of SLA and surface geostrophic current, we analyze and compare model outputs with AVISO altimetric data. There is a very high spatial correlation both in winter (R=0.99, p<0.01) and summer (R=0.98, p<0.01). We obtained a great similarity with AVISO with the a cyclonic circulation in winter under northeast monsoon, also described by previous observations (such as Wyrtki 1961, Qu 2000) as well as by numerical studies (Shaw and Chao 1994; Metzger and Hurlburt 1996; Wu et al., 1998; Chu et al., 1999; Xue et al., 2004; Gan et al., 2006; Chern et al., 2010; Wei et al., 2014; Zhang and Von Storch 2017). In winter (Fig. 3.2i, j), the southern cyclonic circulation covering the whole south of the SCS is associated with cold and salty surface water as shown on the seasonal SSS above, and a low sea level pressure zone during December to February (Fang et al., 2009). Both LONG-SYM and AVISO show a higher SLA in western shallow fresher water part (Gulf of Thailand, Gulf of Tonkin and along Vietnamese coast) due to atmospheric pressure and local wind (Amiruddin et al., 2015). They show a lower SLA in the eastern region of the deeper and denser water area (the Philippines Sea) due to the major contributor of the steric component (expansion and contraction of water masses, Amiruddin et al., 2015). During summer in both datasets (Fig. 3.2k, l), the surface geostrophic current turns to the north forming an anticyclonic circulation in the south of the SCS causing water to accumulate in the interior of the gyre, which increases the SLA. These circulation patterns are related to the southwest monsoon (Ho et al., 2000; Fang et al., 2002) and their forcing mechanisms are opposite to those prevailing in the winter period.

3.2 Vertical profiles - Water masses characteristics

For this section, we evaluate the model's capability to reproduce the vertical structures of different water masses in coastal Vietnam by comparing the modeled temperature and salinity with ARGO, GLIDER, IO cruise, and TSG/XBT from the ALIS R/V *in-situ* data. Fig. 3.3 shows for each dataset the vertical profiles of temperature and salinity for *in-situ* data and for the colocalized model outputs, and their difference (Table. 2.3).

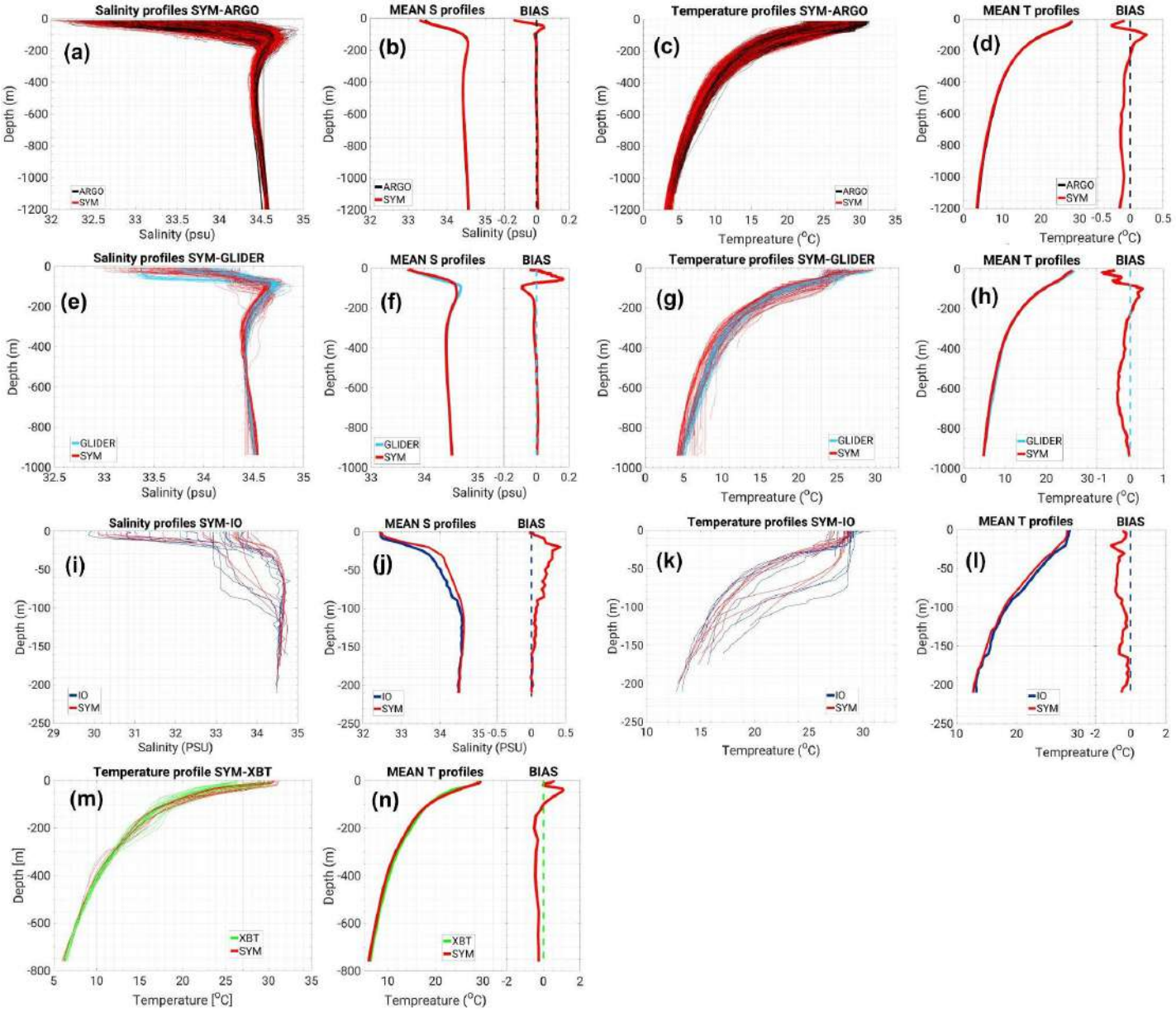

Figure 3. 3 Vertical observed and simulated profiles of temperature (oC), salinity (psu) for measurements from ARGO floats (black, a-d), GLIDER (cyan, e-h), IO (dark blue, i-l) and XBT (green, m-l): all profiles, mean profiles and mean bias between model outputs (red) and in-situ data (other colors)

3.2.1. Comparison with ARGO, GLIDER, IO and ALIS R/V Dataset

a) ARGO

We obtain a good agreement between the model outputs and ARGO floats in terms of temperature and salinity vertical profiles (Fig. 3.3a-d) during the period 2009-2018. At depths from 100m to 1200m, the model outputs reproduce almost perfectly the averaged salinity profile. The maximum salinity at depth around 100m which was initially an issue for our simulation (presented at Chapter 2, section 2.2.3) is also well represented (Fig. 3.3b). The averaged vertical salinity profile of the model outputs is slightly lower than the ARGO one from the surface down to 50m deep (averaged bias is about -0.15 psu) and higher at depths 50-100m (averaged bias is about 0.05 psu). Meanwhile, the averaged vertical distribution of temperature (Fig. 3.3c-d) from the model output is colder than ARGO below 200m (average bias -0.1 ^{o}C). From the surface down to 150m deep, the average bias of temperature compared to ARGO varies between -0.3 and +0.25 ^{o}C.

b) GLIDER

The comparison between our model outputs with the GLIDER measurement (at very high resolution, sampling interval is 6 seconds) in winter-spring 2017 is presented in Fig. 3.3e-h (see Fig. 3.4 for the trajectory and surface values). The comparison shows a good agreement for both vertical salinity and temperature profiles. Mean salinity profiles from model and *in-situ* data are very close from 150m to 950m depth (the maximum depth this glider can measure, Fig. 3.3f). Both datasets indicate a salinity maximum at ~100m, as for ARGO data. The model also correctly reproduces the vertical distribution of temperature with a bias of -0.5 ^{o}C. The GLIDER was sampled during the period of strong activity of the northeast monsoon and the transition period to the southwest monsoon in the area affected by a periodic anticyclonic eddy in the western SCS (Chu et al., 2019). Fig. 3.4 shows the distribution of SSS and SST superimposed with the simulated surface current (m.s^{-1}) averaged over March. The SST agreement between LONG-SYM and GLIDER ($R=0.97$, $p<0.01$) is better than for SSS ($R=0.31$, $p<0.01$) showing lower salinities for the simulation in the outer part of the circular trajectory and higher in its center (see black circle, Fig. 3.4). This disagreement may come from a complex field of mesoscale structures that is differently simulated in the model.

The distribution of temperature and salinity of both LONG-SYM and GLIDER is shown in a TS-diagram (Fig. 3.8b). The model reproduces realistically not only the deep water masses down to 1000 m depth, but also the 2 branches of surface water masses that were

sampled by the glider: the fresher branch (SSS<34.5) observed at the beginning of the glider cruise south of 16°N, and the warmer branch (reaching 20°C) observed at the end of the cruise north of 17°N.

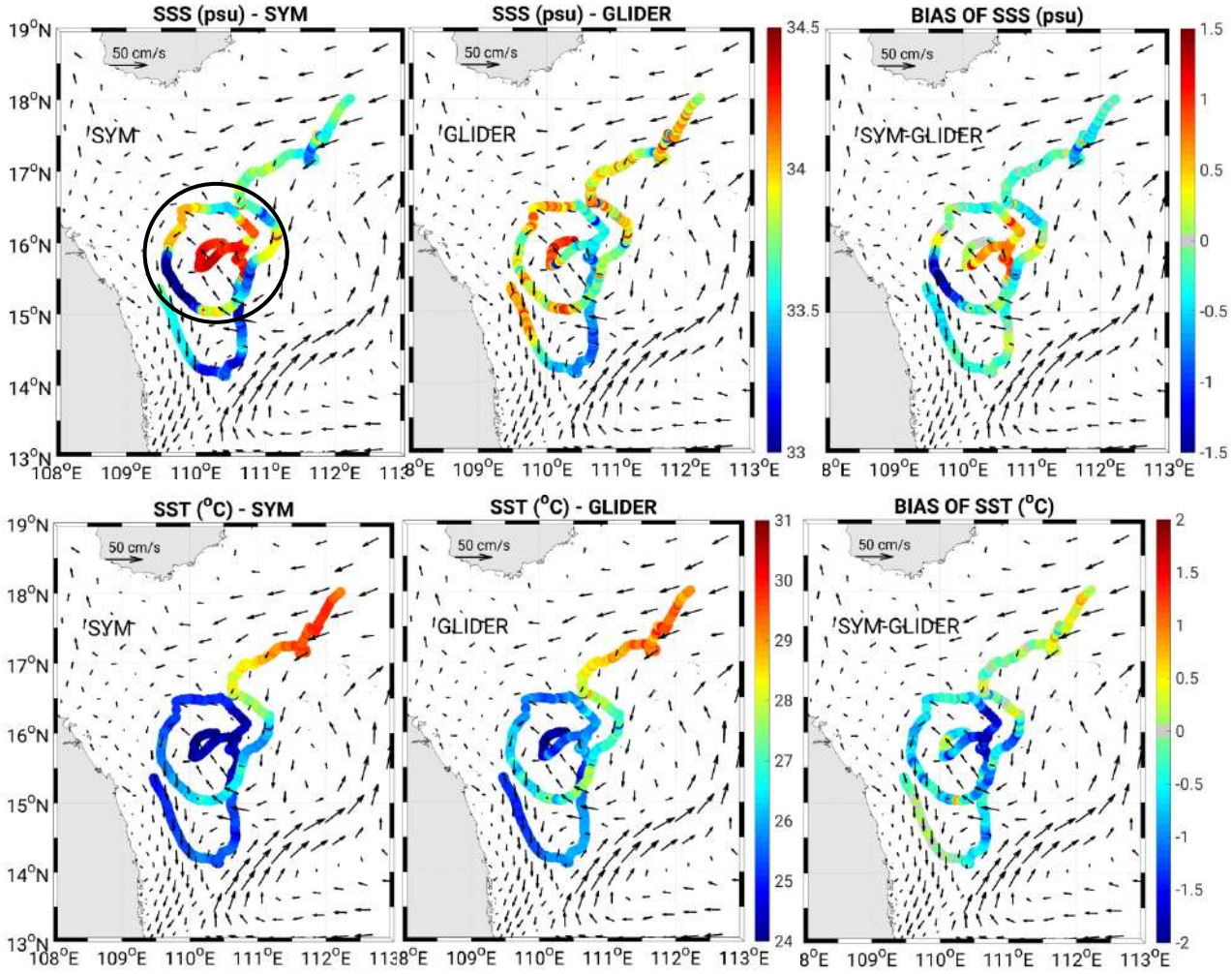

Figure 3. 4 Averaged daily SSS (psu, above) and SST (°C, below) from SYM (left), GLIDER (middle), and their difference (right). Black arrow indicates the average surface current (m.s-1) from the model in March 2017

c) IO cruise

The comparison with salinity and temperature data from the IO cruise (Fig. 3.3i-l) shows a good similarity between IO and model output in the surface and deep layers and a positive/negative bias on salinity/temperature between 20 and 150 m. The coastal shallow region, submitted to the influence of the Mekong freshwater, shows warm (> 27°C) and fresh (<34) water, corresponding to the nearly horizontal branch of the T-S diagram (Fig. 3.8c). In the deeper offshore region the water is much colder and saltier (<20°C and > 34.5, the nearly vertical branch). Again, the model reproduces well the temperature and salinity characteristics

of both types of water masses and areas. The difference is no higher than 0.5, especially in the coastal and Mekong region (Fig. 3.5).

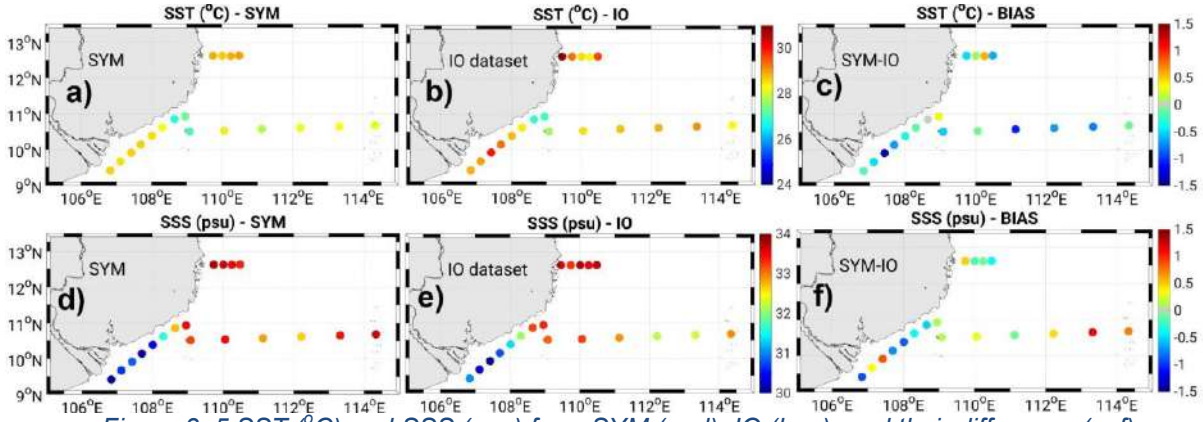

Figure 3. 5 SST (°C) and SSS (psu) from SYM (a, d), IO (b, e), and their difference (c, f)

d) ALIS cruise

The comparison of our model with *in-situ* data from ALIS R/V is done through the vertical sampling of the temperature with XBT Fig. 3.3m,n, Fig. 3.6) and through continuous SST and SSS measurements with the thermosalinometer (Fig. 3.7). The north south gradient of temperature observed along the coast of Vietnam is well represented. The mean vertical temperature profile from the XBT and the model output (Fig. 3.3m,n) are close. The simulated temperature is lower than the XBT at depths below 100m (averaged bias about -0.5 °C). The model also simulates the decrease in SST (<27°C) around 12°N when the vessel crossed the upwelling area on 30/6-01/07/2014 (Fig. 3.6a,b,c). The temperature stratification from the HovMoller diagram is similar in LONG-SYM and XBT from the surface to a depth of 250 m, with of a cooler water mass (about 50-70 m thickness) corresponding to upwelled isotherms in the area of 11-12.5°N (Fig. 3.6d,e).

The SST and SSS from both TSG and LONG-SYM show similar variations in different regions in the SCS. They clearly illustrate first the imprint of the Red river and Mekong river on the salinity as well as the imprint of upwelling on SST along the Vietnam coast between 12 and 14°N and offshore around 12°N (Fig. 3.7). The model represents this transition quite well, demonstrating that the simulation is reliable to represent the extent of the upwelling and its magnitude at least for this period. The model reproduces well the observed SSS and SST spatial and temporal variations along the vessel trajectory in the SCS, with correlation coefficients of 0.89 and 0.93 (both $p<0.01$), respectively.

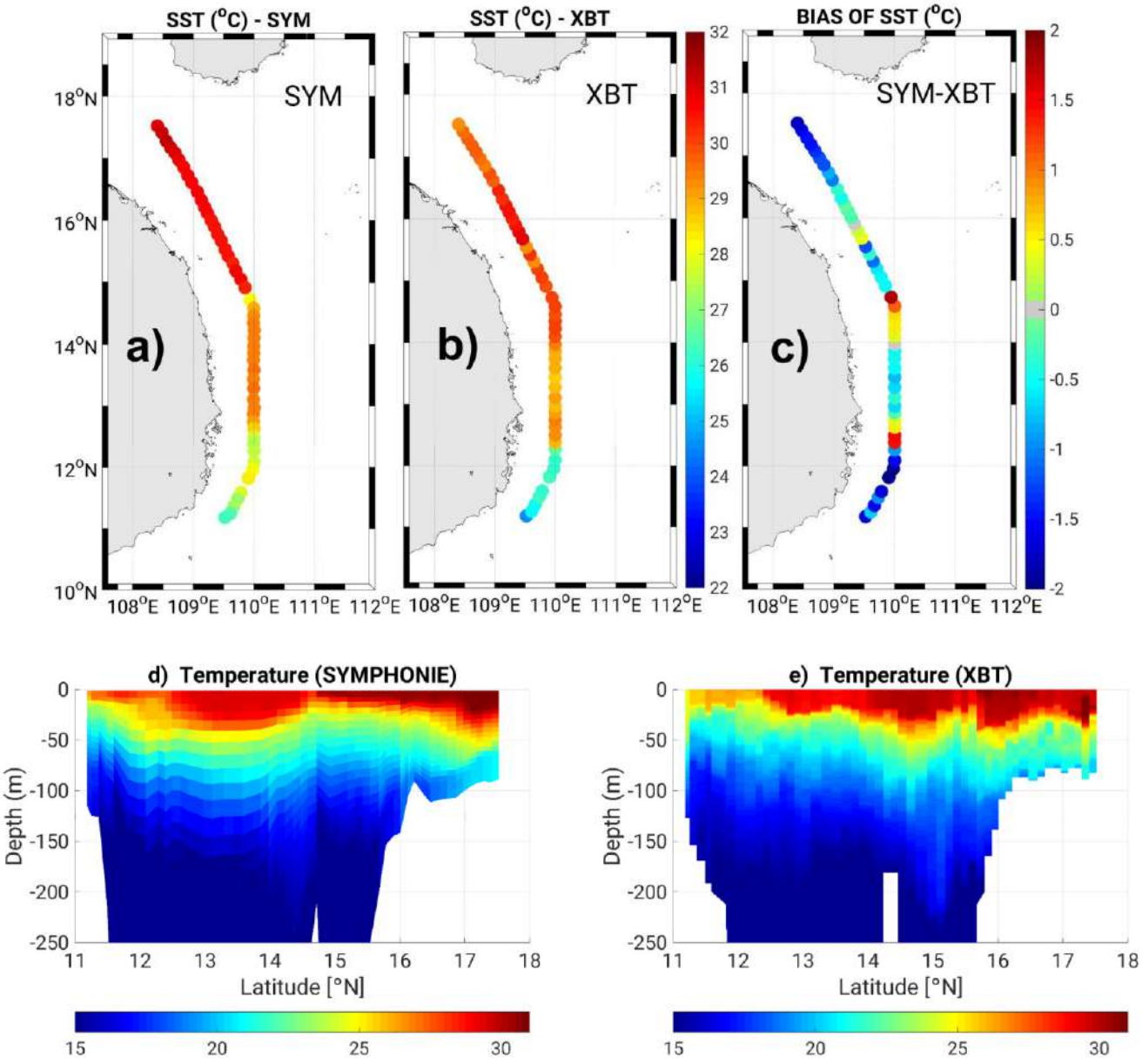

Figure 3. 6 SST (°C) from SYM (a), ALIS-XBT (b), and their difference (c). HovMoller diagram of temperature (oC) over 29/06-01/07/2014 between SYM (d) and ALIS-XBT (e)

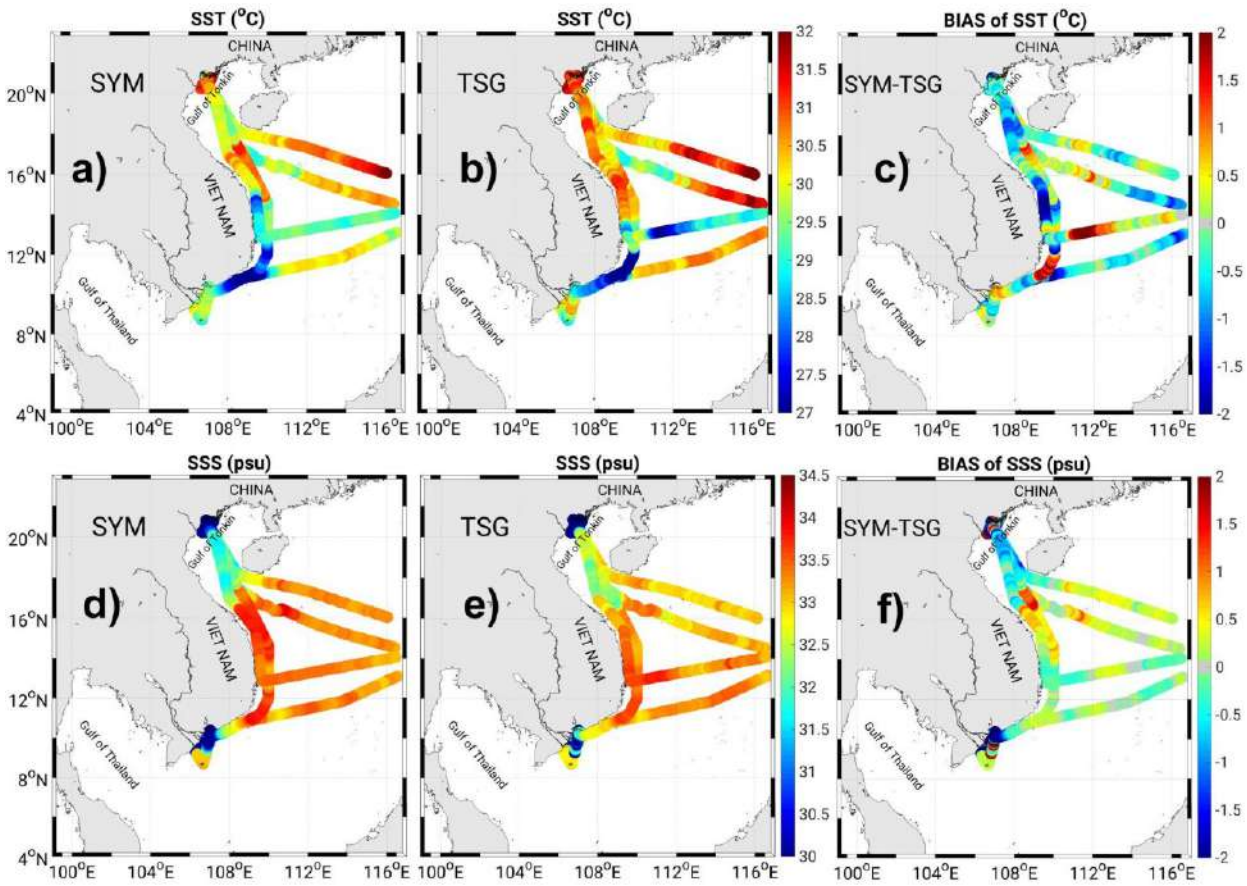

Figure 3. 7 SST (°C) and SSS (psu) from SYM (a, d), ALIS-TSG (b, e), and their difference (c, f)

3.2.2. Representation of SCS water masses

In this section, we show that the model reproduces the characteristics of the main SCS water masses by analyzing TS- diagrams from model outputs and *in-situ* data (Fig. 3.8).

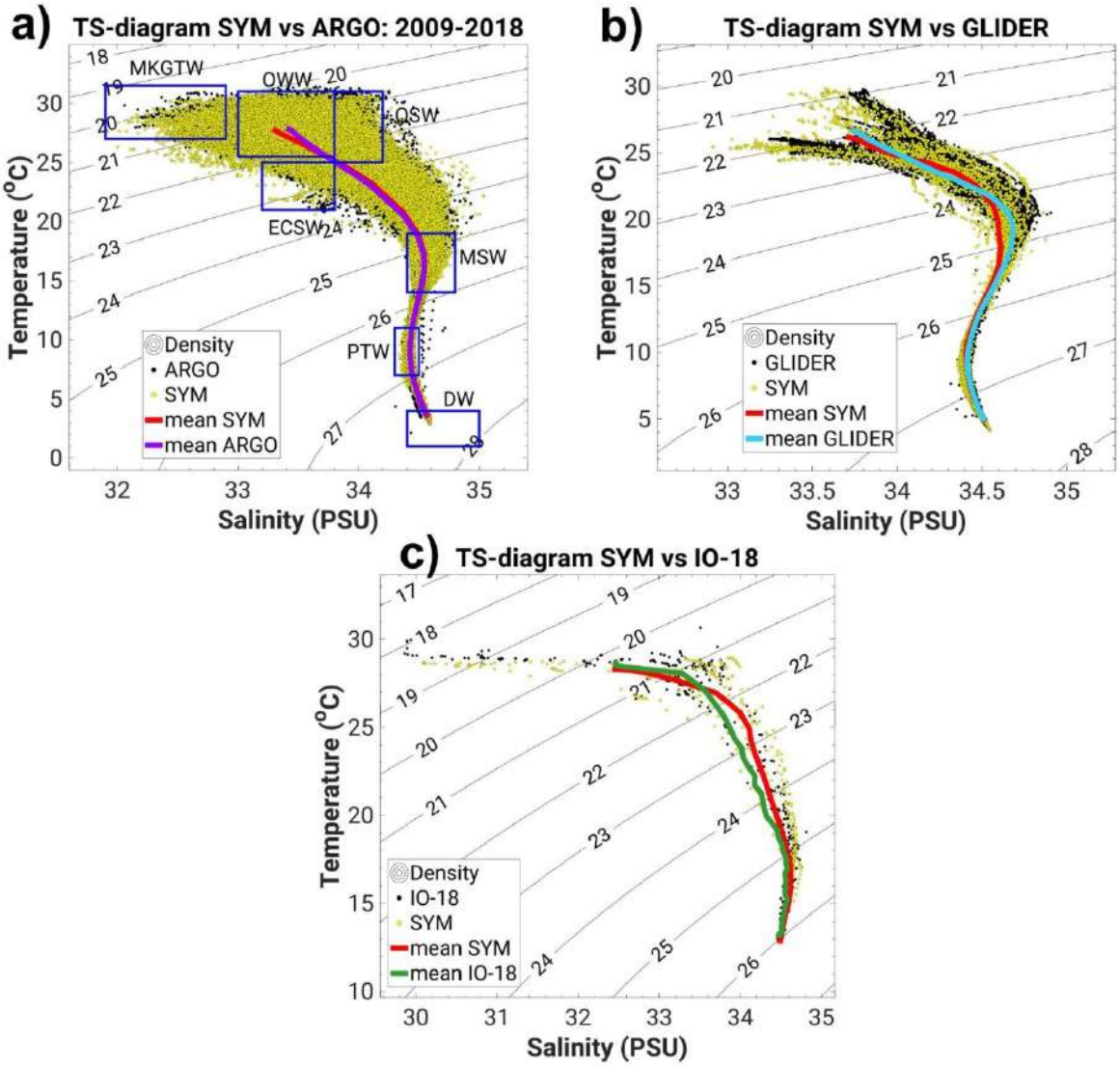

Figure 3. 8 Comparison of TS-diagram between SYM and data: ARGO (left), GLIDER (right), and IO (below). Blue rectangles represent water masses in the SCS

Dippner (2011) re-analyzed the water mass characteristics in the South Vietnam sea and gave a new definition of SCS water masses (Table 3.1). The TS-diagram shows 7 main SCS water masses SCS in agreement with those authors: Deep Water (DW) below 1000 m; Permanent Thermocline Water (PTW) at about 350-550 m; Maximum salinity Water (MSW) around 100-200 m; Offshore Salty Water (OSW) originating from the Western Pacific Ocean flowing through Luzon Strait in the subsurface layer 0-150 m; Offshore Warm Water (OWW) into the SCS coming from the equator and the Java Sea through the Karimata Strait at depth of 50-100 m; East China Sea Water (ECSW) characterized by cold water and low salinity originating from the East China Sea at a depth of 100-150 m; and Mekong & Gulf of Thailand Water (MKGTW) with high temperature and low salinity present in the surface layer to a depth of 60m.

Table 3. 1 Characteristic of water mass in the SCS

Water mass	Temperature range (°C)	Salinity range (psu)	Depth (m)
DW	<4	>34.4	>1,000
PTW	07-11	34.3-34.5	350-550
MSW	14-19	34.4-34.8	100-200
OSW	25-31	33.8-34.2	0-150
OWW	25.5-31	33.0-33.8	50-100
ECSW	21-25	33.2-33.8	100-150
MKGTW	27-31.5	<32.9	0-60

3.3 Conclusion of the chapter

In conclusion, we have shown that our simulation reproduces realistically the surface characteristics (SST, SSS, SLA) in the SCS and SVU region by analyzing and validating it with satellite observations at annual and interannual scales, and spatially at seasonal scales. Moreover, we also showed from several *in-situ* datasets that the vertical distribution of temperature and salinity as well as the water mass characteristics are realistically simulated. These results prove the ability of our model with its very high spatial resolution (1km in the nearshore zone linearly increasing to 4.5km offshore, and 50 layers on the vertical) to represent the ocean water masses and dynamics over the Vietnam coastal region to open SCS. The model can be used reliably for studying the mechanisms involved in the intra-seasonal to inter-annual variability of the South Vietnam Upwelling.

Chapter 4: Interannual variability of the South Vietnam Upwelling over the period 2009-2018

In this chapter, we examine the interannual variability of the South Vietnam Upwelling over the recent period over the coastal and offshore areas, and its relationship with climate conditions (wind, ENSO...). For that we analyse the results of a simulation performed over the period 2009-2018 with SYMPHONIE, called LONG-SYM hereafter. These results were presented in a paper submitted to Ocean Science (Thai To Duy, Marine Herrmann, Claude Estournel, Patrick Marsaleix, Thomas Duhaut, Long Bui Hong, and Ngoc Trinh Bich. *Role of wind, mesoscale dynamics and coastal circulation in the interannual variability of South Vietnam Upwelling, South China Sea. Answers from a high resolution ocean model*. Ocean Science, *submitted*).

4.1 Upwelling Index definition

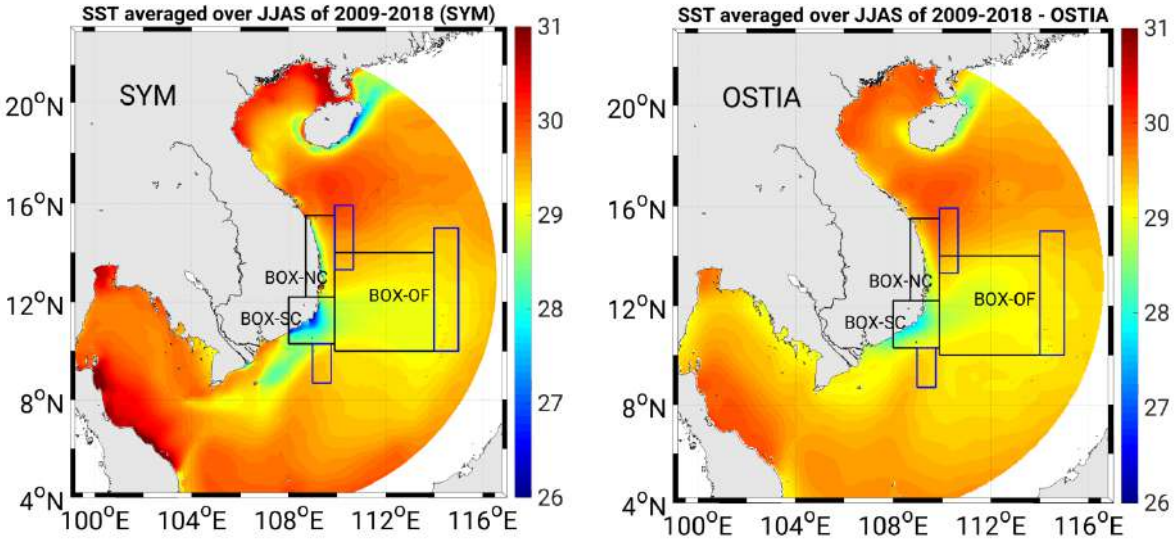

Figure 4. 1 SST average in JJAS of 2009:2018 from SYMPHONIE (left) and OSTIA (right), main areas of upwelling (BoxNC, BoxSC and BoxOF, black rectangles) and the corresponding reference boxes RefNC, RefSC and RefOF (blue rectangles)

We define the upwelling index based on the SST, following Da et al., (2019). Fig. 4.1 presents the SST averaged over the upwelling period June-September (JJAS) over 2009-2018, SST_{JJAS}, computed from the LONG-SYM simulation and from the satellite (OSTIA/GHRSST) observations. LONG-SYM is in very good agreement with OSTIA in terms

of spatial variability and temperature ranges. However, in very coastal areas near Hainan and southern Vietnam coasts where OSTIA shows colder surface water, SYMPHONIE produces even colder SST. This difference could be partly explained by the SST smoothing in OSTIA, as shown for Korean coastal areas by Woo et al., (2020). Piton et al., (2021) also simulated this cold area near Hainan in a high-resolution SYMPHONIE configuration implemented over the Gulf of Tonkin, and suggested, by comparison with a simulation without tide, that this surface cooling could be induced by tides. We will investigate in more detail the effect of tides on SST and SVU in Chapter 6. Low SST (less than 28°C) is also present both in SYM and OSTIA in the central Vietnam area, and is a signature of the SVU. The coldest water corresponding to the upwelling center is around 109°E - 11.5°N. Cold water extends along the coastline until 15.5°N. The presence of cold water is also detected offshore from 109°E to 114°E and from 10°N to 14°N. We therefore define three areas of upwelling. BoxSC corresponds to the most studied area (see literature review in chapter 1), i.e. the strong coastal upwelling that forms near 11°N. BoxOF corresponds to the offshore upwelling, studied in particular by Da et al., (2019). BoxNC shows the northern coastal area where the upwelling develops less frequently between 12°N and 15°N.

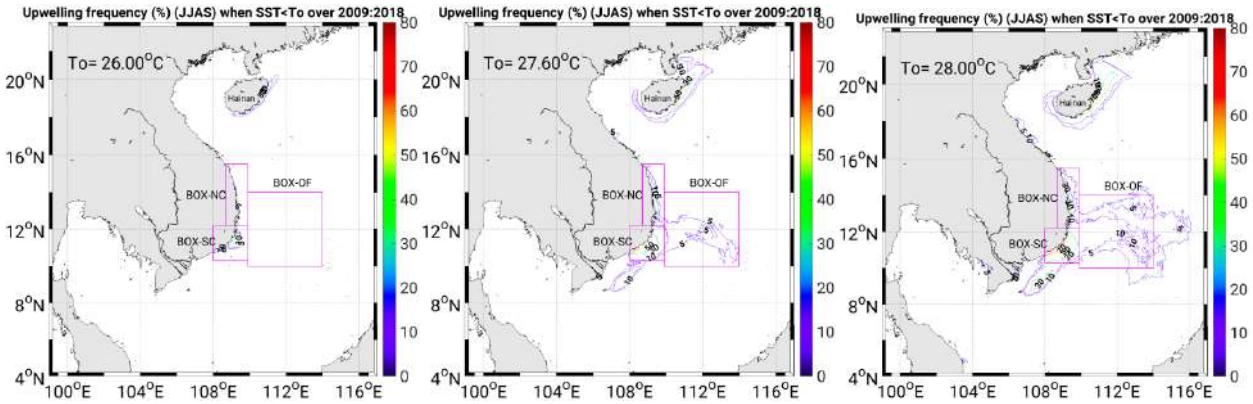

Figure 4. 2 Upwelling index frequency (% of JJAS period) defined as the frequency of events for which SST < T_0 for different choices of T_0 (color contours). Rectangles show the 3 upwelling boxes.

To quantify the intensity of the upwelling at the daily time scale over each box, the daily index of upwelling strength $UI_{d,boxN}(t)$, in °C, is defined, following Da et al., (2019), as:

$$UI_{d,boxN}(t) = \frac{\iint_{(x,y)\ in\ boxN\ so\ that\ SST(x,y,t,i)<T_0} (T_{ref} - SST(x,y,t)).dx.dy}{A_{boxN}} \qquad \text{(Eq. 4.1)}$$

Where $A_{boxN} = \iint_{(x,y)\ in\ boxN} dx.dy$ is the size (in km^2) of boxN (equal to approximately 28500 km^2 for BoxSC, 28,600 km^2 for BoxNC and 198,300 km^2 for BoxOF), T_0 is the threshold temperature below which upwelling happens and T_{ref} is the average temperature over the surrounding area. T_{ref} is defined as the average over the reference box RefN (blue rectangles, Fig. 4.1) and over JJAS of SST computed from the simulation 2009-2018:

$$T_{ref} = \frac{1}{ND_{JJAS}.A_{RefN}} \int_{June}^{Sept} \iint_{(x,y)\ in\ RefN} SST(x,y,t)\ \ dx\ dy\ dt \quad \text{(Eq. 4.2)}$$

Where $A_{RefN} = \iint_{(x,y)\ in\ RefN} dx.dy$ is the size of the reference box RefN and ND_{JJAS} is the duration of the JJAS period.

T_0 is defined from the frequency of occurrence of cold surface water, following Da et al., (2019). For that, we vary T_0 from 26.0°C to 28.0°C to select the threshold temperature. 27.6°C appears as the best choice, allowing to cover the largest number of upwelling occurrences but to avoid taking into account cold water advected between areas (Fig. 4.2).

To estimate the mean strength of the upwelling over the year, we define the yearly index of upwelling in °C, $UI_{y,boxN}$, as:

$$UI_{y,boxN} = \frac{\int_{June}^{September} UI_{d,boxN}(t)\ dt}{ND_{JJAS}} \quad \text{(Eq. 4.3)}$$

And the associated index of upwelling strength $SUI_{y,boxN}$, in °C.km^2.day, as

$$SUI_{y,boxN}(t) = AboxN\ .ND_{JJAS}.\mathrm{UI}_{y,boxN} \quad \text{(Eq. 4.4)}$$

To investigate the spatial distribution of upwelling we also define $UI_{y,map}$ as:

$$UI_{y,map}(x,y) = \frac{\int_{t\ in\ JJAS\ so\ that\ SST(x,y,t)<To}\left(T_{ref}-SST(x,y,t)\right)dt}{ND_{JJAS}} \quad \text{(Eq. 4.5)}$$

4.2 Interannual variability of the South Vietnam upwelling and effect of wind

To study the interannual variability of SVU over the 3 main areas, we examine the indices of upwelling strength $SUI_{y,boxN}$ computed from the simulated SST over 2009-2018. Fig. 4.3 displays for each box the time series over 2009-2018 of upwelling intensity indexes $UI_{y,boxN}$ and $SUI_{y,boxN}$, and of the wind stress averaged over each box and over two periods: June - September (JJAS, $WS_{JJAS,boxN}$) and July - August (JA, $WS_{JA,boxN}$)

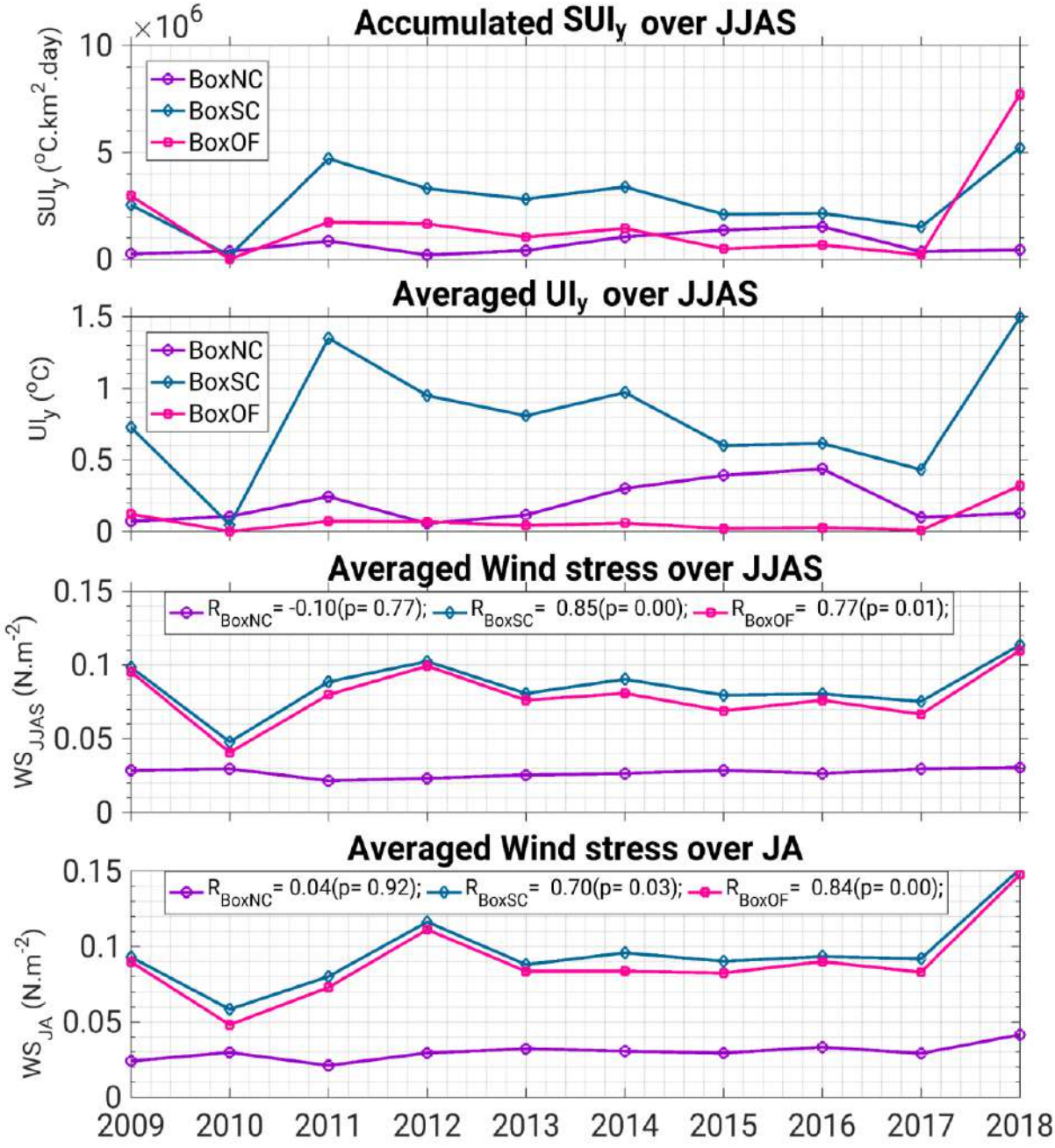

Figure 4. 3 Interannual time series of upwelling indices $UI_{y,boxN}$ and $SUI_{y,boxN}$,and average JJAS and JA wind stress $WS_{JJAS,boxN}$ and $WS_{JA,boxN,}$ over each upwelling boxN (BoxSC: dash-dotted blue line; BoxOF: dash pink line; BoxNC: magenta line). R_{boxN} corresponds to the correlation coefficient (and associated p-value p) between times series of the upwelling index and averaged wind stress for boxN.

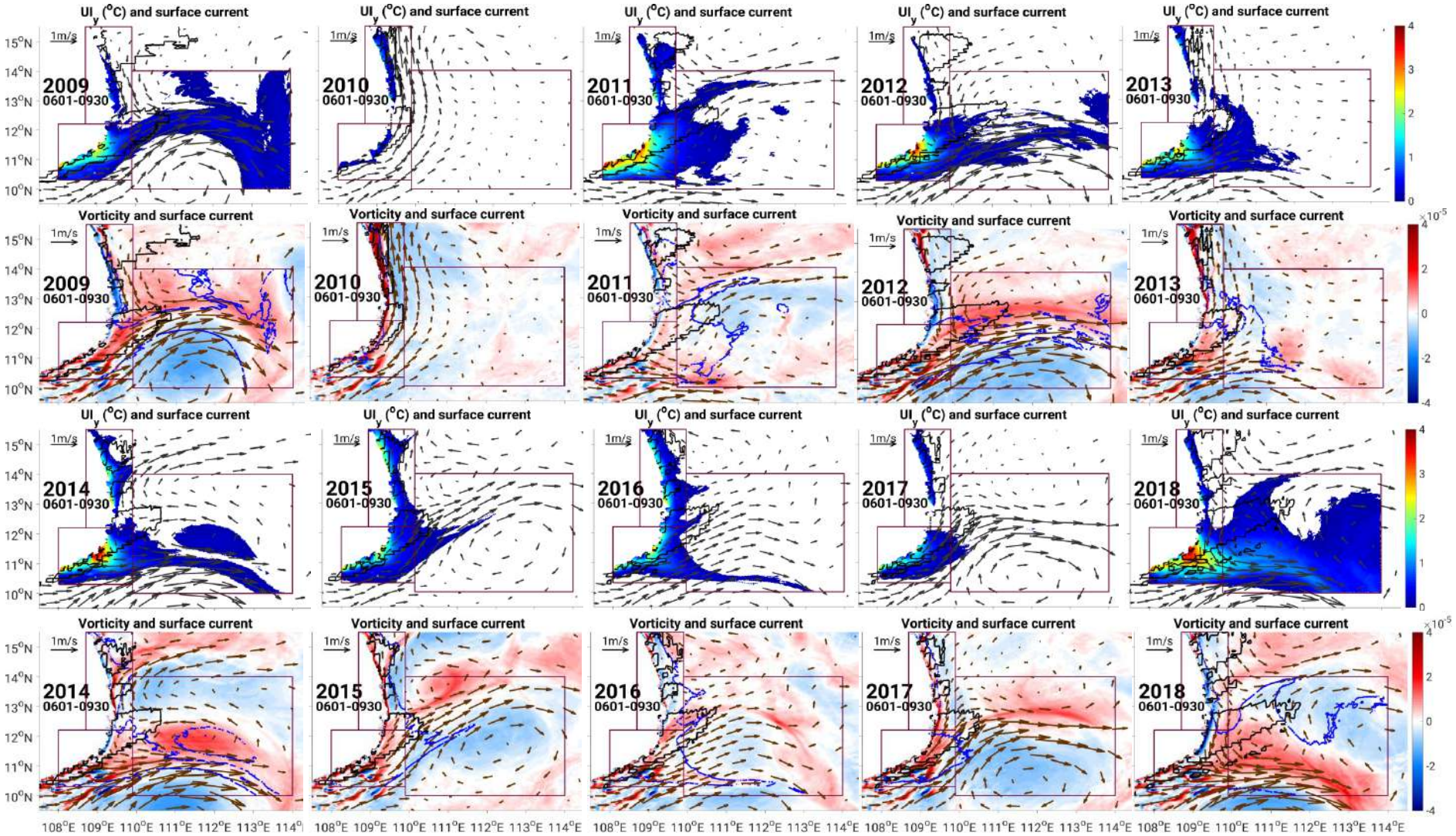

Figure 4. 4 Maps of spatial yearly upwelling index (°C) and of speed and direction (arrows, m.s^{-1}) and vorticity (colors, s^{-1}) of JJAS surface current speed for each year of the simulation. Black contours are averaged by JJAS positive wind stress curl at +3.10^{-7}. Blue contour bold is the 0.1°C isoline of $UI_{map,y}$

Fig. 4.4 shows for each year of the simulation the maps of spatial upwelling index $UI_{map,y}$ and of the JJAS averaged surface current and of its vorticity (ζ, s^{-1}).

$$\zeta(x,y) = \frac{\int_{t\ in\ JJAS}(\frac{\partial v}{\partial x}-\frac{\partial u}{\partial y})dt}{ND_{JJAS}} \quad \text{(Eq. 4.6)}$$

Table 4.1 shows the mean and standard deviation of $SUI_{y,boxN}$ and $UI_{y,boxN}$ for each boxN, the ratio between Standard deviation and Mean (coefficient of variation, CV), and the correlation between the yearly time series of yearly upwelling index and of wind stress averaged over JJAS and JA.

Table 4. 1 For each boxN: Temporal mean and standard deviation of $SUI_{y,boxN}$ and $UI_{y,boxN}$ over 2009-2018 and coefficient of variation, and correlations (coefficient and p-values) between time series of yearly upwelling index and times series of other factors: average wind stress, upwelling index in other boxes, integrated positive and negative vorticity, ENSO with lag (for example, Apr means that the highest correlation is obtained with the time series of ONI in April).

	BoxNC	BoxSC	BoxOF
$SUI_{y,boxN}$ Mean ($^oC.Km^2.day$) x 10^6	0.68	2.78	1.79
$SUI_{y,boxN}$ STD ($^oC.Km^2.day$) x 10^6	0.48	1.48	2.26
$UI_{y,boxN}$ mean (^oC)	0.20	0.80	0.07
$UI_{y,boxN}$ STD (^oC)	0.14	0.42	0.09
CV (%)	71	53	126
Correlation with:	$UI_{y,BoxNC}$	$UI_{y,BoxSC}$	$UI_{y,BoxOF}$
$WS_{JJAS,BoxNC}$	-0.10(0.77)	-0.41(0.24)	0.23(0.53)
$WS_{JJAS,BoxSC}$	-0.13(0.73)	+0.85(0.00)	+0.76(0.01)
$WS_{JJAS,BoxOF}$	-0.19(0.61)	+0.81(0.00)	+0.77(0.01)
$WS_{JA,BoxNC}$	+0.07(0.92)	+0.12(0.62)	+0.54(0.11)
$WS_{JA,BoxSC}$	-0.15(0.69)	+0.70(0.03)	+0.84(0.00)
$W_{JA,BoxOF}$	-0.15(0.67)	+0.69(0.03)	+0.84(0.00)
$UI_{y,BoxNC}$	1	0	-0.26(0.47)
$UI_{y,BoxSC}$	0	1	+0.73(0.02)
$UI_{y,BoxOF}$	-0.26(0.47)	+0.73(0.02)	1
$\zeta_{+,OF}$	-0.28(0.43)	+0.60(0.07)	+0.69(0.03)
ENSO, time lag	0.66 (p=0.04), Apr	-0.69 (p=0.03), Mar	-0.53 (p=0.12), Apr

Table 4. 2 correlation between summer wind stress over each box and: and Nino3.4 (and time lag) and summer wind stress over the other boxes.

	$WS_{JJAS,BoxNC}$	$WS_{JJAS,BoxSC}$	$WS_{JJAS,BoxOF}$
Nino3.4	0.36 (p=0.31), Dec	-0.64 (p=0.05), Mar	-0.60 (p=0.06), Mar
$WS_{JJAS,BoxNC}$	1	-0.20(0.58)	-0.19(0.60)
$WS_{JJAS,BoxSC}$	-0.20(0.58)	1	0.99(0.00)
$WS_{JJAS,BoxOF}$	-0.19(0.60)	0.99(0.00)	1
$\zeta_{+,OF}$	+0.02(0.95)	+0.89(0.00)	+0.89(0.00)

4.2.1 BoxSC

This area has a characteristic morphology of classical coastal upwelling. It shows a significant interannual variability (the ratio between the standard deviation and mean of UI_y, CV=53%, Table 4.1), with years with almost no upwelling (2010) and years of strong upwelling (2011, 2018, Fig. 4.3). BoxSC is, however, the zone with the smallest CV.

Previous studies suggested that the interannual variability of upwelling in the coastal area of Vietnam is mainly triggered by the interannual variability of the summer averaged wind stress (Chao et al., 1996; Dippner et al., 2006; Da et al., 2019). This is also confirmed by our results for BoxSC (Fig. 4.3). In 2010, WS_{JJAS} is minimum ($\simeq$0.05 $N.m^{-2}$) and significantly weaker than for the other years, and almost no upwelling develops over BoxSC ($SUI_y \simeq 0.02x10^6$ °C.km^2.day, $UI_y \simeq 0.05$ °C, one order of magnitude smaller than the average). Conversely, when wind stress peaks in 2018 (WS_{JJAS} $\simeq$0.11 $N.m^{-2}$) the upwelling also reaches its maximum value ($SUI_y \simeq 5.21x10^6$ °C.km^2.day, $UI_y \simeq 1.49$ °C), about twice stronger than the average. We moreover obtain a highly significant correlation between yearly upwelling strength and averaged JJAS wind stress (R=0.85, p<0.01, Table 4.1). JJAS wind stress over BoxSC and BoxOF are very similar (Fig. 4.3) and completely correlated (0.99, p<0.01, Table 4.1): the wind over the coastal area is the same as the wind over the region, i.e. the central SCS. This confirms that the interannual variability of the upwelling in the coastal area is driven at the first order by the intensity of the seasonally averaged summer monsoon wind over the central SCS.

2011 shows the second highest value of upwelling strength ($SUI_y \simeq 4.70x10^6$ °C.Km^2.day, $UI_y \simeq 1.35$ °C), ~90% stronger than for 2009 ($SUI_y \simeq 2.53x10^6$ °C.Km^2.day, $UI_y \simeq 0.73$ °C) and ~40% than for 2012 ($SUI_y \simeq 3.30x10^6$ °C.Km^2.day, $UI_y \simeq 0.95$ °C, Fig. 4.3).

However, the averaged wind stress WS_{JJAS} in 2011 (≃0.09 $N.m^{-2}$) is ~10% lower than in 2009 (≃0.10 $N.m^{-2}$) and 2012 (≃0.10 $N.m^{-2}$). This suggests that other factors than wind can modulate at the second order the interannual variability of upwelling over BoxSC. This could be ocean intrinsic variability (OIV), as suggested for the eastward jet by Li et al., 2014 and for the average SVU over the whole area (covering the 3 boxes) by Da et al., (2019), as well as the chronology of wind forcing during the summer. This will be investigated in Chapter 5.

4.2.2 BoxOF

The interannual chronology of the summer upwelling at BoxOF, but also wind stress, is very similar to BoxSC (Row 3 at Fig. 4.3; R=0.99, p<0.01 at Table 4.2), with a minimum in 2010 and a maximum in 2018. The correlation coefficient between JJAS wind stress and the upwelling strength is also highly statistically significant, though slightly less than for BoxSC (R=0.77, p=0.01, Table 4.1). BoxOF shows the strongest interannual variability (CV≃126%, Table 4.1). The very strong upwelling in 2018 (SUI_y≃7.7x10^6 $^oC.Km^2$.day) compared to other years, 4.3 times higher than the average value (SUI_y≃1.8x10^6 $^oC.Km^2$.day), partly explains this high variability. The high value of SUI_y in 2018 is partly related to the strong wind this summer (Fig. 4.3). However, although averaged wind stress in 2018 (WS_{JJAS}≃0.11 $N.m^{-2}$) is only ~10% higher than in 2009 and 2012 (WS_{JJAS}≃0.10 $N.m^{-2}$), SUI_y in 2018 is 2.6 to 4.6 times larger than SUI_y obtained for 2009 and 2012 (3.0 and 1.7 x10^6 $^oC.km^2$.day, respectively). Comparatively, for BoxSC UI_y in 2018 it is only ~2 times the average value. This, and the fact that the correlation between UI_y and summer wind stress is less significant than for BoxSC, shows that in the offshore area, even more than for BoxCS, factors other than summer wind intensity over the area modulate the interannual variability in upwelling.

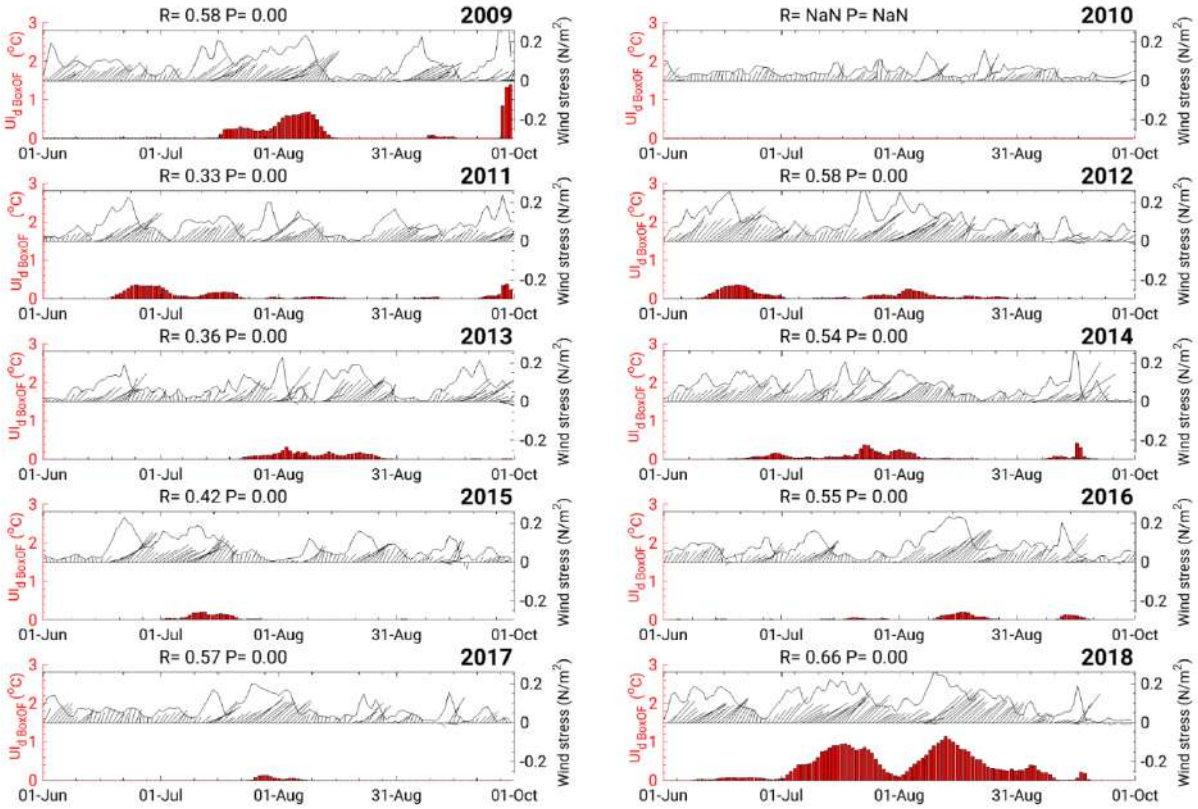

Figure 4. 5 Daily time series of wind stress averaged over BoxOF (black lines, value in N.m^{-2} and direction) and of daily upwelling index $UI_{d,boxN}$ (red bars) for each year of the SYM simulation

The southwest monsoon usually blows over the SCS from June to September. To better understand which factors, besides the strong average summer wind, induced this exceptional upwelling in 2018, we plot for each year the daily timeseries of wind stress averaged over BoxOF and of UI_d (Fig. 4.5) during the JJAS period. We also calculate for each box the monthly average of wind stress and monthly accumulated upwelling intensity SUI_m (°C.km^2.day, with $SUI_{m,boxN} = AboxN.\int_{month\ m} \mathrm{UI}_{\mathrm{d},boxN}(t)\,dt$) in the period 2009-2018 (column 2, Fig. 4.6). As written above, the summer averaged wind stress is similar in 2009, 2011, 2012 and 2018 (row 3, Fig. 4.3). However, in respectively 2009, 2011, and 2012, wind stress peaks (that induce the upwelling) mostly occur in respectively June and September, June and September, and in June and August (for those 3 years, see at row 3, column 1, Fig. 4.6). In contrast, in 2018, wind stress peaks occur in July-August, inducing a very strong upwelling during those months. This suggests that upwelling over BoxOF is stronger when wind peaks occur during the core of the summer season (July-August) than during June or September. To confirm this hypothesis, we compute the correlation between UI_y and July-August averaged wind stress over BoxOF, $WS_{JA,boxN}$, obtaining a higher correlation (0.84, $p<0.01$) than with JJAS wind stress $WS_{JJAS,boxN}$ (0.77, $p<0.01$). Conversely, for BoxSC, this correlation is weaker (0.70, $p=0.03$ for JA vs. 0.85, $p<0.01$, for JJAS) (Table 4.1).

This suggests the development of the coastal upwelling over boxSC occurs during the whole JJAS period, and is mainly induced by wind forcing. Over boxOF, summer wind forcing also appears to be one of the major factors inducing the upwelling, but other factors than wind apparently also contribute to the development of upwelling, favoring in particular its development during July-August more than during June and September. The detailed mechanisms behind this hypothesis will be investigated in more detail in Chapter 5, by examining and analysing the daily to seasonal variability of upwelling during the 2018 case study.

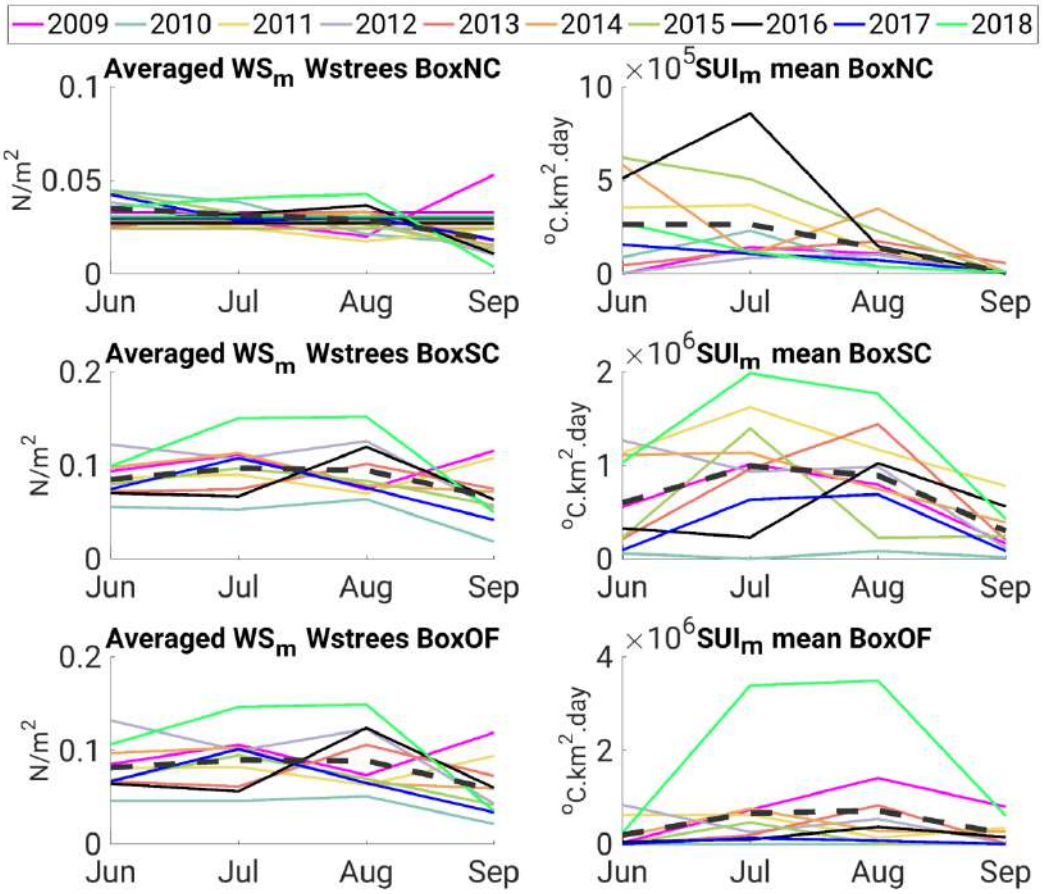

Figure 4. 6 Monthly averaged wind stress (WSm, left, N.m^{-2}) and monthly upwelling strength index (SUIm, right, °C.Km^{-2}.day) for each box and each year from 2009 to 2018. The dashed black line shows the monthly climatological average over the period of simulation.

2010 appears as a particular case since upwelling does practically not develop over BoxOF and BoxSC during summer 2010 (the upwelling strength is one order of magnitude smaller than the average, Fig. 4.3). Fig. 4.7 shows the maps of upwelling strength and average surface circulation averaged over the summer of 2010. The eastward jet and dipole structure usually observed over the area in summer and inducing the development of upwelling do not exist during summer 2010: for this year, extreme weak wind conditions as well as circulation background both prevent the development of upwelling.

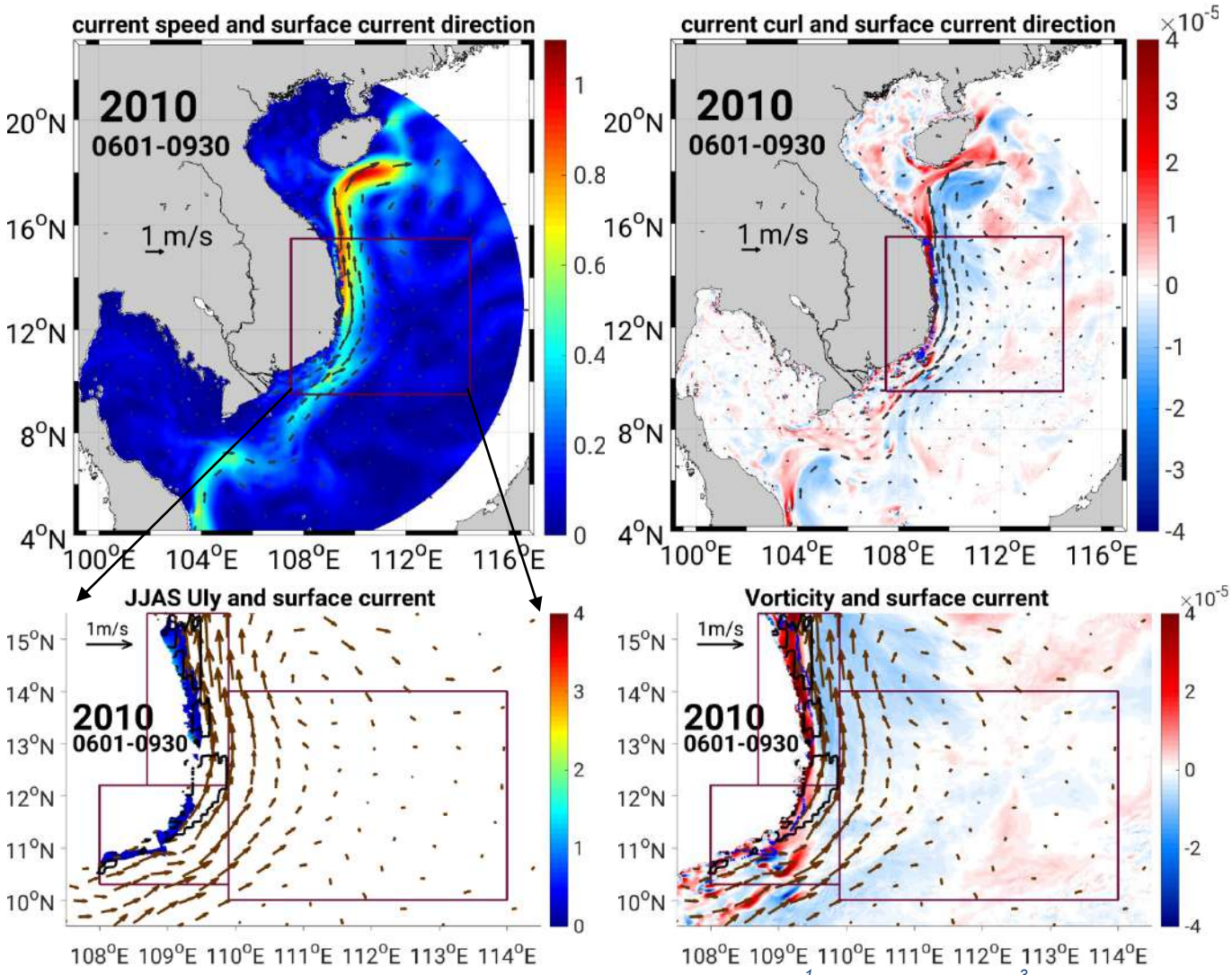

Figure 4. 7 Top: Maps of averaged JJAS surface current speed (left, m.s^{-1}) and vorticity (N.m^{-3}, right) over the VNC domain in 2010. Bottom: maps of averaged $UI_{y,map}$ over 3 boxes (^{o}C, left) and JJAS averaged current speed (m.s^{-1}, vector) and vorticity (N.m^{-3}, right) over the SVU region in 2010.

Moreover, previous studies suggested that the interannual variability of the SVU is related to the intensity of the eastward jet in the coastal area and to the vorticity associated with cyclonic activity present over BoxOF in the offshore area (Kuo et al., 2000; Li et al., 2014; Xie et al., 2003; Xie et al., 2007, Li et al., 2014; Da et al., 2019, Ngo and Hsin, 2021)…

We plot in Fig. 4.3 the time series of $\zeta_{+,OF}$, the spatial integral over BoxOF of the positive part of summer averaged relative vorticity.

$$\zeta_{+,OF} = \frac{\iint_{(x,y)\ in\ BoxOF\ so\ that\ \zeta JJAS(x,y)>0} \zeta(x,y).dx.dy}{A_{boxN}} \qquad \text{(Eq. 4.7)}$$

Where ζ(x,y) is the summer average of the surface current vorticity (Eq. 4.6). It integrates both the cyclonic activity north of the jet and the positive vorticity on the northern flank of the eastward jet (a more intense and narrow eastward current being characterized

by a higher vorticity). $\zeta_{+,OF}$ is an indicator of the intensity of the large-scale circulation (dipole+eastward jet) in the region. The interannual variability of this intensity is actually strongly induced by the variability of wind forcing, which can be quantified by the highly significant correlation between time series of $\zeta_{+,OF}$ and $WS_{JJAS,OF}$ (0.89, p<0.01, Table 4.2). SUI_y at BoxOF is positively correlated with $\zeta_{+,OF}$ (R=0.69, p=0.03, Table 4.1). $UI_{y,SC}$ is also significantly correlated with $\zeta_{+,OF}$ (0.60, p=0.07), which confirms that upwelling in BoxSC is stronger/weaker for years of intense/weak large-scale circulation off Vietnam coast.

Our results therefore confirm the conclusions of previous studies performed over other periods and with simulations at lower resolution.

4.2.3 Box NC

As already observed by Da (2018) for the strong El Niño summer 1998, upwelling also develops, though to a weaker extent along the northern part of the central Vietnam coasts: the mean value of SUI_y for BoxNC is respectively 2.6 and 4 times smaller than for BoxSC and BoxOF (Table 4.1). UI_y for BoxNC shows a relatively strong interannual variability (71%). We obtain no significant correlation between UI_y and the average wind stress, whatever the period considered, for BoxNC. This suggests that wind over the area is a driving factor of the interannual variability of upwelling intensity in BoxSC and BoxOF, whereas it does not seem to drive it over BoxNC. To understand in more detail what mechanisms favor or prevent the development of upwelling in BoxNC we examine maps of summer circulation (surface current and its vorticity) and of upwelling index (Fig. 4.4), and identify four specific situations:

(1) Weak UI_y in BoxNC, but also weak $UI_{y,boxN}$ in BoxOF: year 2010, 2013, 2017 (see SUI_{JJAS}, Fig. 4.3). For those 3 years, both upwelling and summer wind over the region ($WS_{JJAS,OF}$, Fig. 4.3) is weaker than the average or average. The weak wind explains the weak upwelling over BoxSC and BoxOF, as explained above. At BoxNC, the common point of these three years is a strong northward current direction along the coast. For the 2010 El Niño year, the very weak wind explains the fact that there is even no dipole and related eastward jet and that a strong northward current can develop along the coast. This northward longshore current over BoxNC is responsible for preventing Ekman transport, thus upwelling development in the BoxNC.

(2) Weak UI_y in BoxNC, strong UI_y in BoxOF. This case corresponds to the conditions occurring in years 2009, 2012 and 2018 (Fig. 4.3, and Fig. 4.4). Those conditions are the opposite of case (1): the wind over the region is larger than average, and thus the large-

scale circulation and upwelling over BoxSC and BoxOF. Over Box NC, there is a strong alongshore southward current, which actually is the western part of the cyclonic part of the dipole that prevents north of the jet. Again, this alongshore southward current over BoxNC prevents shoreward Ekman transport, thus upwelling, to develop over the area.

Strong UI_y in BoxNC and medium or weak UI_y in BoxOF can appear for 2 situations:

(3) In 2011, 2014, 2015, the usual dipole structure exists, but the alongshore currents also meet in the middle of BoxNC (around 14-14.5°N latitude, Fig. 4.4), so that a secondary dipole (anticyclonic in the south and cyclonic in the north) develops north of the usual dipole structure, forming a secondary small eastward jet. This small eastward jet favors offshore Ekman transport, thus upwelling. This situation happens both for medium (2011, 2014) or weak (2015) upwellings over BoxOF.

(4) 2016 is the last case: wind over the region is weaker than average as well as the dipole structure and eastward jet (see $WS_{JJAS,OF}$ and $\zeta_{+,OF}$ Fig. 4.1), and, consequently, the upwelling over BoxSC and BoxOF. The eastward current is weaker but also wider than average, and an overall offshore circulation is simulated over a large part of the area (Fig. 4.4), which favors Ekman transport and the development of a stronger than average upwelling over BoxNC.

4.2.4 Effect of ENSO

As explained in Chapter 1, ENSO strongly influences the atmospheric circulation (monsoon regimes, rainfall, etc...) as well as ocean circulation and surface characteristics in the South China Sea. Several studies showed that ENSO impacts the South China Sea, mainly through its effect on summer monsoon, which occurs later/earlier and is weaker/stronger after El Niño/La Niña events (Wu and Wang, 2000; Lau and Nath, 2009; Zhou et al., 2008). ENSO also impacts to the SVU through the effect of summer winds on to the strength of eastward jet, which helps to extend the wind-forced coastal upwelling further offshore as shown by Xie et al., (2003), Xie et al., (2007) and Dippner et al., (2007).

We therefore compute the correlation between ENSO Oceanic Niño Index (ONI) monthly index (https://origin.cpc.ncep.noaa.gov/products/analysis_monitoring/ensostuff/ONI_v5.php) and upwelling index as well as wind stress in our 3 study areas (Table 4.2). Fig. 4.8 shows the time series of UI_y for each box and of ONI at the month that produces the best correlation with upwelling index. First, our results are in agreement with previous studies about the effect of ENSO on summer wind stress over the area: for BoxSC and BoxOF, we obtain statistically significant ($p<0.10$) negative correlations between the summer wind stress

and ONI in March: An El Niño (e.g. 2010, 2015, 2016)/La Niña (e.g. 2018) event induces a weakening/strengthening of the wind during the following summer monsoon.

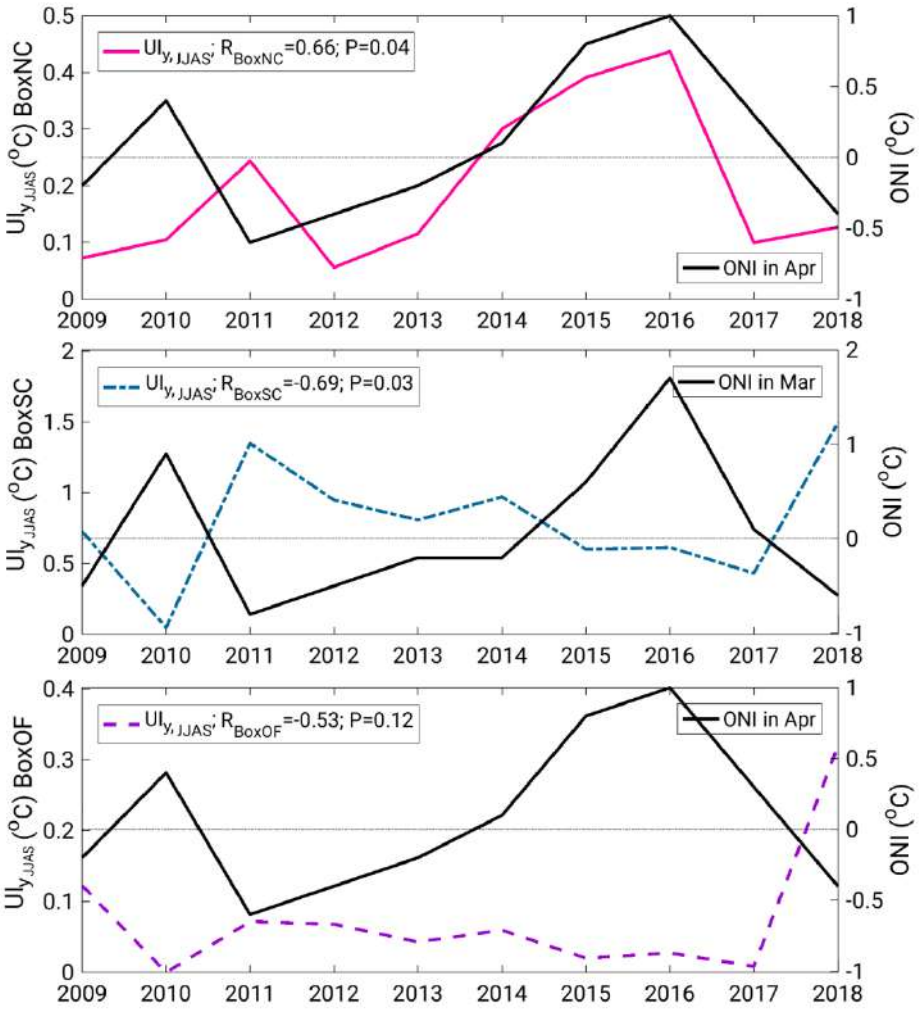

Figure 4. 8 Time series of annual upwelling intensity UI_y at BoxNC (pink), BoxSC (blue) and BoxOF (purple), and of annual ONI (black) at the month that shows the best correlation with UI_y

Second, over BoxSC and BoxOF, El Niño years 2010 and 2015-2016 are associated with weak upwelling, whereas La Niña years 2011 and 2018 are associated with strong upwelling. For BoxSC, we obtain a significant negative correlation (-0.69, p=0.03, Table 4.2) between ONI in March and UI_y. For BoxOF, we also obtain a negative, though less significant correlation (-0.53, p=0.12) with ONI in April. Those results are in agreement with previous studies: El Niño (La Niña) events induce a weakening (strengthening) of wind, hence of upwelling over those areas. The weaker correlation between ONI and UI_y in BoxOF could be explained by a stronger influence of OIV over this area, as suggested by Da et al., (2019). This will be investigated in the 2018 case study in chapter 6.

Over BoxNC, 2015 and 2016 (El Niño years) are associated with strong upwelling, while 2018 (La Niña) is associated with weak upwelling. We obtain a significant positive

correlation (0.66, p=0.04) between ENSO and UI_y in BoxNC, suggesting an opposite relationship to the one obtained for the other 2 boxes. We do not obtain any significant correlation (i.e. with p-values lower than 0.1 or even 0.3) between the average summer wind over the area and ONI (Table 4.2). Moreover, we simulate weak UI_y over BoxNC for 2010 vs. strong UI_y for 2015 and 2016, even though those 3 years are all El Niño years and weak winds. ENSO therefore only partly drives the upwelling variability in BoxNC. We showed above that upwelling over BoxNC is mainly driven by the background situation over the area, explaining that similar situations in terms of large-scale wind and circulation could lead to different strength of upwelling over BoxNC. We will investigate in more detail in the 2018 case study in Chapter 5 which factors trigger the interannual variability of upwelling in boxNC.

4.3 Conclusion of chapter

In this chapter, the analysis of the LONG simulation performed over 2009-2018 allowed to characterize the interannual variability of the SVU over its 3 main areas of occurence: southern coast (“classical” wind driven upwelling), offshore (strong impact of wind, but contribution of other factors that need to be better understood), northern coast (apparently not related to wind over the area, but to small-scale circulation that prevents over the northern coast). A particularly strong upwelling developed over BoxOF and BoxSC during summer 2018, partly induced by the strong wind during this period. In the next chapter, we therefore use summer 2018 as a case study to better identify and characterize the impact of different factors involved in the variability of the SVU.

Chapter 5: Intraseasonal variability of Upwelling for the case study of 2018

We saw in Chapter 4 that, partly due to the strong average summer wind this year, a strong upwelling developed over BoxSC and BoxOF during summer 2018. We therefore select summer 2018 as a case study to better understand the impact of wind and OIV on the upwelling, at the daily to intraseasonal scales.

5.1 Ensemble modeling strategy

To study the roles of wind and OIV, we first performed an ensemble of 10 twin simulations (called FULL hereafter) that run between 01/01/2017 and 31/12/2018 with perturbed initial conditions. Most of the OIV develops at mesoscale (Serazin et al., 2015, Waldman et al., 2018), we therefore only perturbed the mesoscale field, as done by Waldman et al., (2017, 2018) to study of the impact of OIV on Mediterranean ocean deep convection. Following the same methodology, we created 10 different initial conditions for temperature, salinity, sea surface elevation and currents fields in January 2017. In those 10 different initial fields, the large scale states (corresponding to a spatial filter of 100 km radius) are identical and equal to the large scale state of 01/01/2017 of the LONG simulation analysed in Chapter 4. However the small scale states differ: they are extracted from the small scale states of the January 1st fields of the 10 years (2009 to 2018) of the LONG simulation. In the following, member XX of the ensemble simulation FULL corresponds to the simulation performed using the small scale state of 01/01/20XX to perturb the initial conditions.

Fig. 5.1 shows the SST averaged over JJAS in 2018 over the VNC domain for the ensemble average of FULL and for OSTIA. These maps of simulated and observed JJAS SST in 2018 show that strong upwelling developed during this year, not only in the coastal area (BoxSC) but also in the offshore area (BoxOF). As observed in the LONG simulation (Chapters 3, 4), FULL SST is slightly lower in all 3 boxes than OSTIA, especially in the area south of BoxSC and east of Hainan Island.

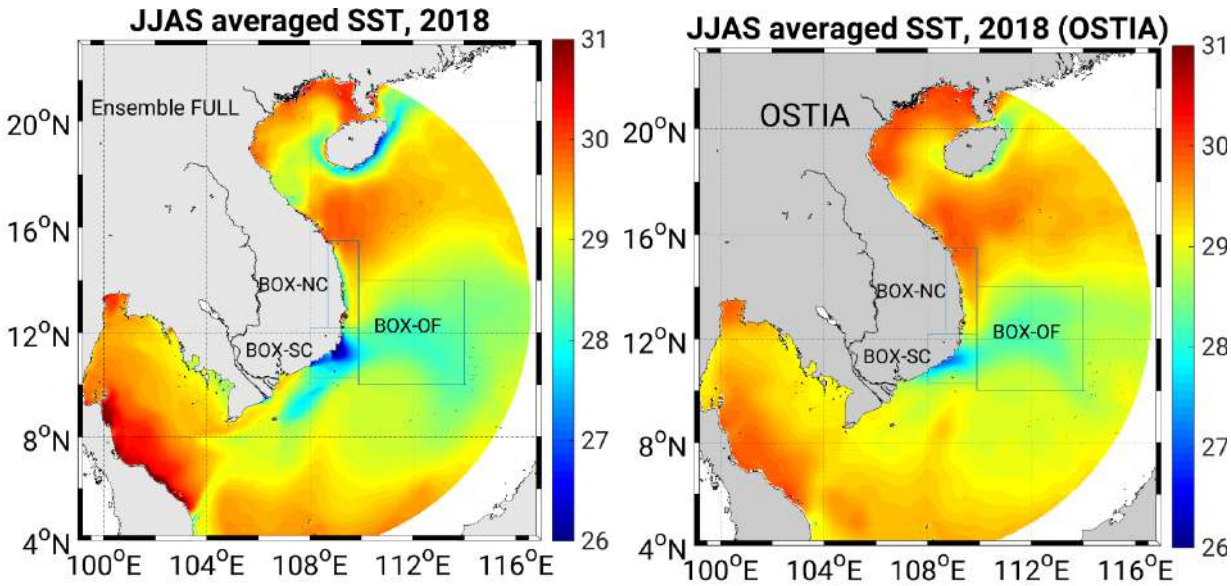

Figure 5. 1 Mean SST during June-September 2018 for the ensemble average of the FULL ensemble (left), for OSTIA reanalysis (right).

To examine the impact of intrinsic variability on the SVU we define two indicators, as done by Waldman et al. (2018): a seasonal indicator and a daily indicator. First, the impact of intrinsic variability on the mean over a given period, typically JJAS 2018, of the variable X, MI(X), is defined as:

$$MI(X) = \frac{\sigma_i(m_t(X(t,i)))}{m_i(m_t(X(t,i)))} \quad \text{(Eq. 5.1)}$$

Where $m_t, m_i,$ and σ_i are respectively the temporal (over the given period) and ensemble means and the ensemble standard deviation. *MI(X)* is thus the intrinsic variability averaged at the seasonal scale.

Second, we quantify the time series of the intrinsic contribution to the total temporal variability over a given period (typically JJAS) as:

$$VI(X(t)) = \frac{\sigma_i(X(t,i))}{\sqrt{m_i(\sigma_t(X(t,i))^2)}} \quad \text{(Eq. 5.2)}$$

which is the daily-varying ratio between the time-dependent intrinsic variability and the temporal variability over this period.

Fig. 5.2 shows for each box the daily time series of UI_d for the 10 members of the FULL ensemble and of their ensemble average, the daily time series of VI (UI_d), and the daily time series of wind speed and direction.

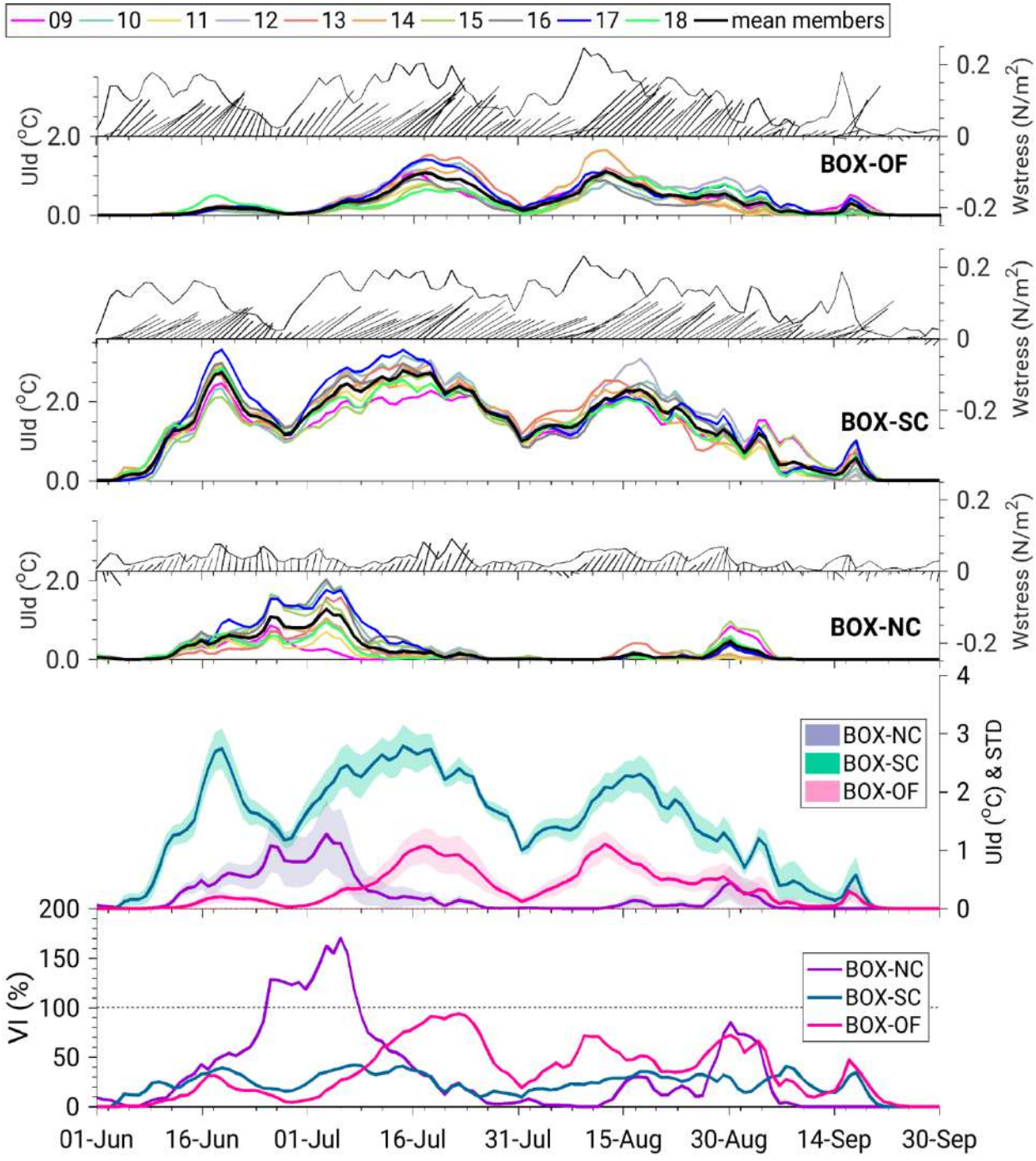

Figure 5. 2 (rows 1 to 6) Daily time series of box averaged wind-stress (speed and direction) and of $UI_d(t,i)$ for each member of the ensemble FULL for each box and for the ensemble average (black); (row 7) daily time series of the ensemble average of $UI_d(t,i)$ with the standard deviation envelope (defined as mean +/- std) (row 7).(row 8) daily time series of VI(UId) for each box expressed in %.

5.2 Circulation during summer 2018

The development of summer circulation in the SVU is closely related to the development of summer wind velocity and wind stress curl, which reaches its maximum intensity in August and disappears in October (Kuo et al., 2000; Xie et al., 2003, 2007;

Dippner et al., 2007). Southwest summer monsoon wind blows from June to September in BoxSC and BoxOF, with several peaks inducing the upwelling (June, July and August in BoxSC, and in July and August in BoxOF, rows 1 and 3, Fig. 5.2).

To find out what drives the daily to intraseasonal variability of upwelling it is necessary to understand the role of background circulation. We examine the surface current velocity and vorticity during the periods of wind and upwelling peaks: June (09-18/06), July (28/06-18/07) and August (01-13/08) (Fig. 5.2). Fig. 5.3 shows the maps of ensemble average of wind stress curl, surface current speed and vorticity and superimposed wind stress curl contours averaged during the 3 peak periods. To quantify the strength of the eastward jet that departs from the Vietnamese coast, we calculate the mean speed and eastward velocity component through the cross meridional section at 109.9°E, between 9.5 and 12.2°N (see red line in Fig. 5.3) in the ensemble FULL during the 3 peaks periods (Table 5.1).

Table 5. 1 Averaged velocity and eastward component ($m.s^{-1}$) through the cross section 109.9°E; 9.5-12.2°N during peaks period

Averaged velocity and eastward component ($m.s^{-1}$)	June peak	July peak	August peak
Cross section at 109.9°E; 9.5-12.2°N;	0.51 (0.49)	0.78 (0.62)	0.88 (0.70)

During the June period (10 days), the positive wind stress curl area extends from the coast to ~ 113°E, but the meridional coverage is narrow (row 1, Fig. 5.3). The eastward jet is mostly concentrated around 10-11°N, forming a weak eastward jet in the south with a maximum speed of about 0.5-0.7 $m.s^{-1}$ (color shading, row 2, Fig. 5.3), and the eddy dipole not yet formed clearly (row 3, Fig. 5.3). The eastward jet strength is 0.51 $m.s^{-1}$ (Table 5.1), with a mainly eastward current (the eastward component is 0.49 $m.s^{-1}$, accounting for ~96% of the speed, Table 5.2). Row 4 of Fig. 5.3 shows the ratio between ensemble standard deviation and ensemble average (i.e. MI) of the current curl during each period. The position of current is stable (MI<50%) in the coastal area, but the circulation is much more unstable in most of the offshore area (MI >200%)).

5.2.1 June period

During the June period (10 days), the positive wind stress curl area extends from the coast to ~ 113°E, but the meridional coverage is narrow (row 1, Fig. 5.3). The eastward jet is mostly concentrated around 10-11°N, forming a weak eastward jet in the south with a

maximum speed of about 0.5-0.7 m.s^{-1} (color shading, row 2, Fig. 5.3), and the eddy dipole is not yet formed clearly (row 3, Fig. 5.3). The eastward jet strength is 0.51 m.s^{-1} (Table 5.1), with a negligible meridional component, Table 5.2). Row 4 of Fig. 5.3 shows the ratio between the ensemble standard deviation and ensemble average (i.e. MI) of the current curl during each period. A high value of MI indicates a chaotic circulation pattern, while a low value indicates a robust circulation pattern. The position of current is stable (MI<50%) in the coastal area, but the circulation is much more chaotic in most of the offshore area (MI >200%).

5.2.2 July period

During the July period, the wind stress peak lasts for 3 weeks. The area of strong positive wind stress curl only extends to 112°E, but its meridional extension is wider (from 10.5°N to 13°N) than in June (row 1, Fig. 5.3). The eastward jet gets more energy from the wind and is enhanced with a speed of about 0.8-1.1m.s^{-1} concentrated in the 11-12°N region (row 1, Fig. 5.3). Its intensity (0.78 m.s^{-1}, Table 5.1) is higher than in June and more northward). The double gyre system with anticyclonic circulation (negative vorticity) in the south and cyclonic (positive) in the north is more marked than in June (row 2, Fig. 5.3). Most of the strong cyclonic eddies are located within the positive wind stress curl area in BoxSC and BoxOF. The current curl is more stable than in June in the coastal zone and the cyclonic gyre area (MI ~around 100%, row 4, Fig. 5.3), but it is more chaotic in regions with weak vorticity (where MI > 200% and can reach 500%).

5.2.3 August period

During the August peak (13 days), the positive wind stress curl has the largest coverage (up to 114°E). The eastward jet is stronger than in June and July, with the highest speed of about 1.2-1.5 m.s^{-1}, concentrated around 10.5-11.5°N (row 1, Fig. 5.3), and a mean strength of 0.88 m.s^{-1} (the eastward component is 0.70 m.s^{-1}, ~80% of the velocity, Table 5.1). The dipole system formed during this period is the strongest, with a well established and large cyclonic gyre (row 2, Fig. 5.3). Vorticity in the August period also shows the highest stability compared to other periods in summer: the surface of relatively low MI of current curl is larger than in July row 4, right, Fig. 5.3).

5.2.4 Summary

To summarize, the development of summer circulation varies at the intra-seasonal scale as follows: in June, the eastward current is weak and mainly concentrated in the south,

no clear dipole system has been formed and the circulation is only stable in the coastal area. In July, under the influence of the continuous southwest wind, the current is enhanced and it moves slightly north. The dipole structure is clearly formed, with a more stable circulation in the area of positive vorticity than in June. Wind in August has the strongest intensity and the most distant influence from the shore. The intensity of both eastward jet and dipole structure is the strongest, and the circulation is stable over an even larger area than in July. In the following, we examine how the intra-seasonal variability of the summer circulation affects the upwelling. In particular we examine the respective contributions of wind and ocean dynamics, including OIV, on the development of upwelling for each area of the upwelling development.

5.3 Upwelling over BoxSC: the strong influence of wind

Table 5. 2 Correlation between the daily time series of meridional and zonal components and speed of the average wind stress averaged over a given box and of the daily time series of the ensemble mean of UI_d over the same box in FULL. Correlations coefficients are only indicated when they are significant at more than 99% (p-value <0.01).

boxN	**BoxOF**			**BoxSC**			**BoxNC**		
Wind stress components	U (N/m2)	V (N/m2)	speed (N/m2)	U (N/m2)	V (N/m2)	speed (N/m2)	U (N/m2)	V (N/m2)	speed (N/m2)
Correlation (p<0.01) between time series of ensemble average of $UI_{d,boxN}$ (^oC) and of with daily wind stress - FULL ensemble	0.62	0.62	0.65	0.6	0.71	0.64	--	0.37	--

For BoxSC, values slightly differ from one member to another, however all the members as well as the ensemble mean show the same daily chronology. The southern coastal upwelling begins to develop during the first half of June, lasts during the whole summer with a strong intraseasonal variability, and disappears during the first half of September. We obtain 3 peaks, near June 19, July 15 and August 16. Those time series are in phase with the wind forcing over the area, also shown over the BoxSC the 3 upwelling peaks correspond to 3 peaks of southwest wind (row 4, Fig. 5.2), and the correlation between time series of UI_d and of the daily averaged wind stress intensity over BoxSC is equal to 0.64 (p<0.01) (0.71 with the meridional component of wind stress, Table 5.2). Last, the intensity of UI_d in BoxSC is similar for the 3 peaks.

VI, which quantifies the contribution of the OIV to the total daily variability (row 8, Fig. 5.2), varies during the period of upwelling occurrence between 10% (when the upwelling is weak during weak wind periods, Fig. 5.2) and 40% (during periods of strong upwelling), showing similar values for the 3 upwelling peaks. On average over the year, UI_y varies between 1.25 °C and 1.49 °C, with an ensemble mean value of 1.36 °C and a weak ensemble standard deviation of 0.09°, i.e. 7% of the mean value (Table 5.3). Fig. 5.3 shows the maps of ensemble average of spatial UI_d (row 4) and of MI of UI_d (row 5) over each period of upwelling development (June, July, August). For BoxSC, upwelling develops for the 10 members of the FULL ensemble in the same area during the whole season (June, July and August peaks): this is shown by the very low value of MI (<50%) over the area of strong upwelling in BoxSC, in particular along the coast and in the convergence zone (Fig. 5.3). Higher values of MI are obtained at the periphery of this area, along the northern and southern flanks of the eastward jet. They are related to the variability of the meridional position of the jet: a jet that flows more northward will induce more northward upwelling.

The upwelling in the southern coastal region therefore develops during the whole JJAS 2018 season over the same area, as long as wind conditions are favorable, with a daily to intraseasonal variability mostly related to the variability of wind, but not to the period of the season. It shows a weak intrinsic variability, both at the daily scale and on average over the summer, both spatially and on spatial average. The level of OIV seems to be mostly related to the level of upwelling intensity, but not to the period of the season. Those results suggest that for the coastal SVU, the daily to intraseasonal variability of the coastal upwelling is mostly driven by the wind, and that the OIV, that mainly results from the meridional position of the jet, affects the upwelling at a second order.

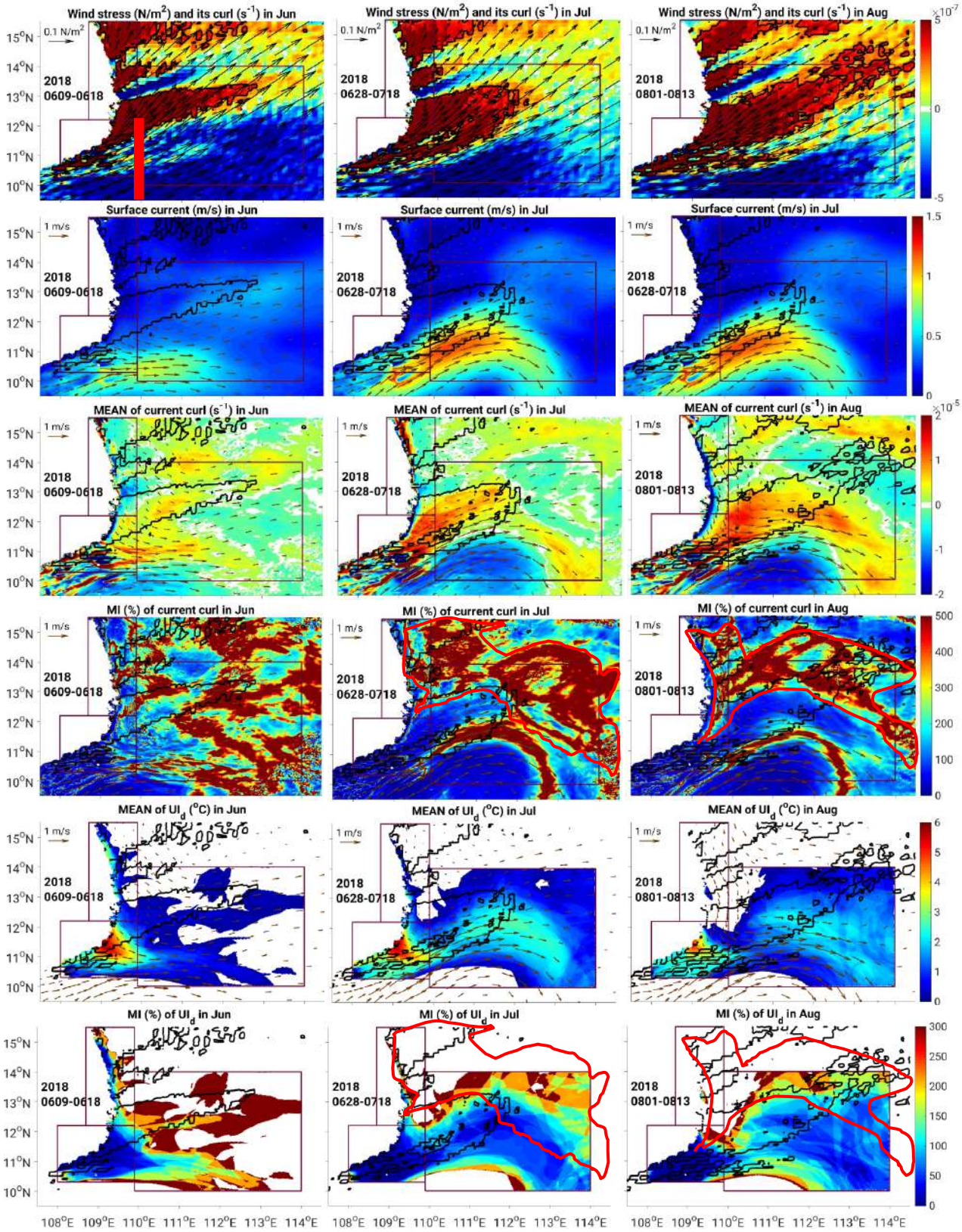

Figure 5. 3 Maps of ensemble average of surface current speed (row 1, m.s^{-1}) and surface vorticity (row 2, s^{-1}) and of MI of surface current vorticity (row 3, %) averaged during the period of upwelling development for June (09-18/06, left), July (28/06-18/07, middle), and August (01-13/08, right); maps of ensemble average (row 4, °C) and MI (row 5, %) of spatial UI$_d$ at the day of maximum UI$_d$, for each period of upwelling development. Black arrows show the average current direction (arrow, m.s^{-1}), black contours show the +3.10^{-7} N.m^{-3} isoline of average wind stress curl and bold red contour show the 200 (%) isoline of average MI of surface current curl during the upwelling development period.

5.4 Upwelling over BoxOF

The daily chronology of UI_d at BoxOF is very similar for the 10 members of the FULL ensemble (row 2, Fig. 5.2), even if there are differences in UI_d values. We obtain 2 strong peaks in the middle of the summer (near 19-July and 13-August), 1 moderate peak near the end of August, and 2 small peaks at the beginning (near 18-June) and end (16-September) of summer. Ensemble averaged UI_d values are quite similar for the 2 strong peaks (~1.2 ^oC in middle July and August, row 7, Fig. 5.2), and for the 2 weak peaks (~0.4 ^oC in middle June and September, row 7, Fig. 5.2). Again, this chronology is in phase with the daily wind stress over BoxOF (row 3, Fig. 5.2), and the correlation coefficient between UId and wind time series is equal to 0.65 ($p < 0.01$, Table 5.2). The regional wind is thus the dominant factor that triggers the daily chronology of UI_d for BoxOF. However, contrary to BoxSC, the strength of peaks varies throughout the season: we observe smaller UId peaks at the beginning and end of summer than in the middle of summer, though wind stress intensity is similar.

On average over the year, UI_y at BoxOF varies among members between 0.26 ^oC and 0.42 ^oC, with an ensemble mean value of 0.33 ^oC and an ensemble standard deviation of 0.06 ^oC (Table 5.3). The relative intrinsic variability MI is thus 18%, higher than for BoxSC (7%). During the summer, the daily values of VI also reach much higher values for BoxOF (exceeding 90%, Fig. 5.2) than for BoxSC (not exceeding 40%). Moreover, compared to BoxSC where VI shows a relatively weak intraseasonal variability, VI at BoxOF varies much more during the season. The OIV is stronger for BoxOF during the periods of strong upwelling development, with 5 VI peaks corresponding to the UI_d peaks (rows 7-8, Fig. 5.2). VI exceeds 90% for the July peak, while it reaches 70% during the two August peaks, and respectively 30% and 50% during the small June and September peaks.

For BoxOF, the regional daily wind stress therefore drives the daily to intraseasonal variability at the first order. However OIV significantly modulates this impact of wind, especially at the daily scale, and that this impact of OIV varies throughout the season. To better understand which mechanisms explain first the impact of OIV on upwelling over BoxOF, and second the intraseasonal variability of both the upwelling intensity and its response to OIV, we examine in details the functioning of upwelling during the 3 main upwelling peak periods: June, July and August.

Table 5. 3 For each box, value for each member (columns 1-10), ensemble mean (11), ensemble standard deviation (12) and MI (13) of UI_y (°C).

Members	09	10	11	12	13	14	15	16	17	18	Ensemble mean UI_y (°C)	STD (°C)	MI of UI_y (STD)/(mean)
UI_y - BoxOF	0.32	0.35	0.26	0.39	0.37	0.39	0.26	0.26	0.42	0.31	0.33	0.06	18 %
UI_y - BoxSC	1.25	1.35	1.25	1.49	1.39	1.42	1.27	1.38	1.48	1.29	1.36	0.09	7 %
UI_y - BoxNC	0.13	0.28	0.09	0.18	0.20	0.17	0.29	0.30	0.31	0.16	0.21	0.08	37 %

5.4.1 July upwelling peak over BoxOF

Da et al., (2019) showed that OIV modulates the impact of annual averaged wind on the interannual variability of offshore upwelling. They showed that this OIV impact is related to the spatial distribution of summer averaged surface current vorticity associated with eddies: cyclonic (anticyclonic) eddies located in the area of positive wind stress curl enhance (weaken) upwelling development induced by Ekman pumping. We therefore expect that eddies and associated surface vorticity could also be involved in the OIV impact on offshore upwelling at the intraseasonal scale. In the following, we therefore examine together the temporal and spatial distribution of upwelling, of wind stress curl and of surface current and associated vorticity.

In July, upwelling develops over BoxOF from 29/06 to 19/07. Fig. 5.4 shows for 2 members with strong July upwelling (13, max UI_d = 1.53 °C; 17, max UI_d = 1.42 °C; Fig. 5.2) and 2 members with weak July upwelling (15, max UI_d = 0.77 °C; 18, max UI_d = 0.65 °C; Fig. 5.2), the maps of UI_d at the day of its maximum value and the maps of average surface current curl and direction and of wind stress curl averaged during the upwelling development period (29/06-19/07, Fig. 5.4). Offshore upwelling develops for each member in the area of positive current curl, mainly along the northern flank of the strong eastward jet and in the cyclonic gyre, submitted to positive wind stress curl: upwelling develops when the position of this positive current vorticity north of the jet coincides with the position of positive wind stress curl. When the position of the eastward jet and the southern anticyclonic eddy is more southern (maximum latitude of negative vorticity ~11.5-12.0 °N), as observed for members 13 and 17, the area where positive wind stress curl and positive surface current curl coincide is large, and a stronger than average upwelling develops, in particular in the northeastern part of BoxOF. Conversely, when this position is more northern (maximum latitude of negative vorticity ~12.5-13.0 °N), this area is smaller, and upwelling is weaker than average, with a smaller northeastern extension (members 15, 18).

Those results show that the chronology and intensity of the upwelling peak in July is driven first by the chronology and intensity of wind stress, then modulated by the meridional position of the eastward jet and associated dipole, which varies significantly from one member to another in July: a southern (northern) position of the jet induces a larger (smaller) common area between positive curl of wind stress and current, hence induces a stronger (weaker) upwelling.

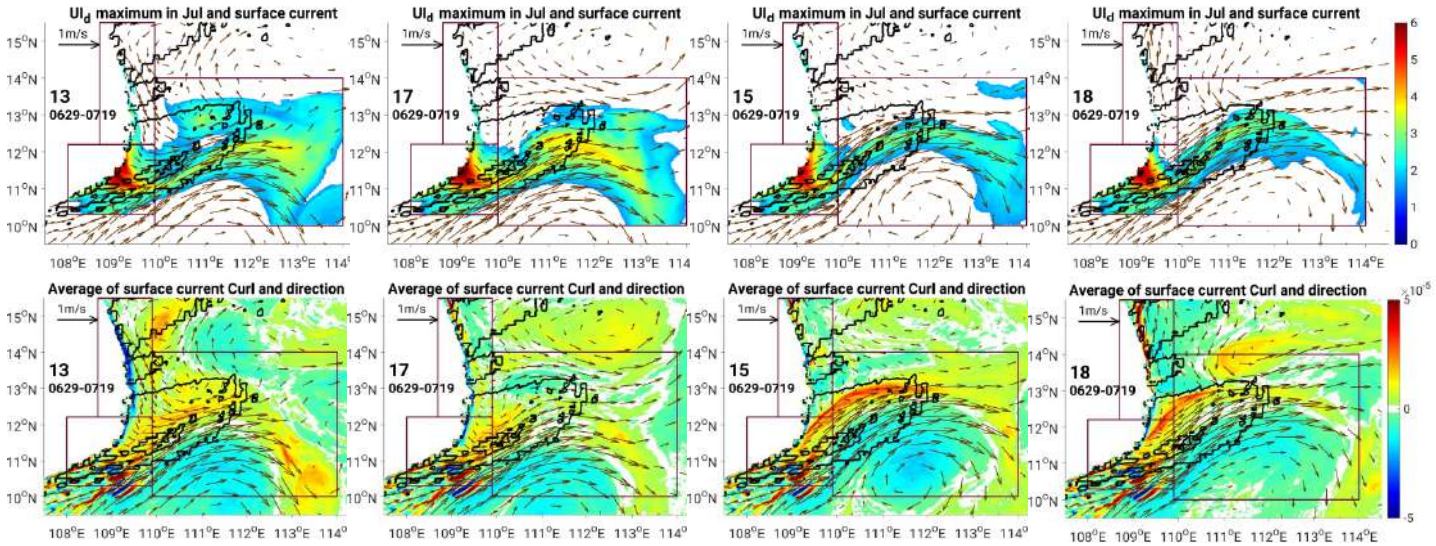

Figure 5. 4 Maps of of spatial UI_d (^oC) at the day of maximum $UI_{d,OF}$ (row 1), and maps of averaged surface current curl (color, s^{-1}) and direction (arrow, $m.s^{-1}$) and of wind stress curl ($N.m^{-3}$) averaged during the upwelling development for 2 members of strong (13, 17) and of weak (15, 18) UI_y. Black contours (rows 1,2) show wind stress curl at $+3.10^{-7}$ $N.m^{-3}$. Black contour bold (row 2) is average UI_d at 1.8 ^oC.

5.4.2 August upwelling peak

The August upwelling develops during the strong wind period from 01/08 to 13/08. The chaotic variability of upwelling is smaller during the August peak. The maximum of VI(UId) indeed reaches ~70% in August vs. 90% in July (Fig. 5.2), and the area where MI(UId) <100% (area of "stable" upwelling) covers ~96862 km^2 in August (~49% of BoxOF), vs. ~85426 km^2 in July (~43% of BoxOF). To understand which mechanisms, drive the development and OIV of the upwelling in August, we examine several case studies.

Fig. 5.5 shows the maps of UI_d at the day of its maximum value in August and the maps of average surface current curl and direction and of wind stress curl averaged during the upwelling development period (1-13/08) for 2 members of strong (14, max UI_d = 1.65 ^oC; and, to a lesser extent, 13, max UI_d = 1.20 ^oC) and weak (10, max UI_d = 0.82 ^oC; 16, max UI_d = 0.89 ^oC, Fig. 5.2) upwelling in August. The spatial distribution of the upwelling is different from July. As observed in July, part of the upwelling develops in the area of positive surface vorticity along the northern flank of the eastward jet. However, contrary to what is observed

in July, the meridional position of the jet, and thus the part of the upwelling that develops along the jet, are quite similar from one member to another. Moreover, upwelling also develops north of the jet, in the area of positive vorticity associated with the cyclonic eddy of the bipolar structure. Only this part of the upwelling differs from one member to another and is responsible for the August OIV.

Member 14 is a particular case, for which the August upwelling peak is significantly stronger than for all the other members of the FULL ensemble (Fig. 5.2). For this member, a cyclonic eddy associated with positive current curl develops stably in the area of high positive wind stress curl (≥ 5.10^{-5} $N.m^{-3}$, Fig. 5.5). This cyclonic eddy, which corresponds to the cyclonic component of the double gyre, is surrounded by 2 anticyclonic eddies: the anticyclonic component of the double gyre in the south and a smaller eddy in the north. As a result, this area of positive vorticity is stably trapped between those 2 anticyclonic eddies in the area of influence of very high positive wind stress curl relatively close to the coast, leading to the strong upwelling obtained for member 14. The other members show weaker and relatively similar maximum UI_d values, though differences can be observed (Fig. 5.5). These differences can actually be linked to the position of the cyclonic eddy. Indeed, we obtain the same alternance of anticyclonic-cyclonic-anticyclonic eddies for the other members shown on Fig. 5.5, but the position of this tripole varies. From members 13, 10 to 16, the cyclonic eddy and the northern anticyclonic are located more and more eastward, the area of positive vorticity is consequently located further and further away from the area of strong wind stress curl, resulting in a weaker and weaker upwelling.

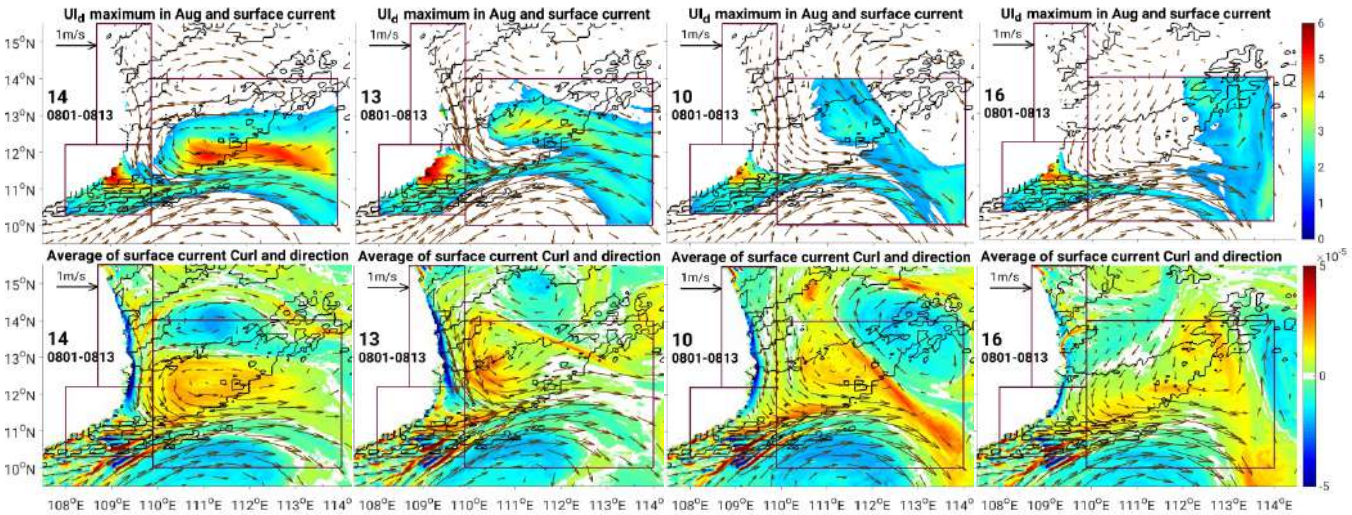

Figure 5. 5 Same as Fig. 5.4 for members of strong (13, 14) and weak (10, 16) upwelling over BoxOF during the period of upwelling development in August.

Those case studies suggest that in August, the meridional position of the eastward jet is quite stable from one member to another in the FULL ensemble. It is thus not the main driver of the OIV, contrary to what we concluded in July. Instead, the variability of the

upwelling is mainly related to the spatial organization of the tripolar structure, in particular to the zonal position of the cyclonic eddy (that develops north of the eastward jet) with respect to the area of maximum positive wind curl.

5.4.3 Intraseasonal variability of upwelling over BoxOF and large-scale circulation strength and stability

To confirm this hypothesis, and explain the intraseasonal variations of the upwelling maximum value and intrinsic variability, we examine the maps of ensemble average and of MI of average current speed and vorticity and of maximum UI_d during the 3 peaks of upwelling over BoxOF and BoxSC: June, July, and August (Fig. 5.3).

We first investigate why the upwelling hardly develops in BoxOF during June wind peak, although the wind stress is similar during this period to July and August peaks (Fig. 5.2). As explained in Section 5.2, in June the eastward jet is still weak and the associated dipole structure that develops in July and August in BoxOF is not established (see maps of ensemble averaged current velocity and curl, Fig. 5.3). Moreover, the area of positive wind stress curl is not located over an area of strong positive current curl, which would favor the development of offshore upwelling induced by Ekman pumping as seen above for the July peak. Conversely, in July and August, the eastward jet as well as the dipole structure are well established, and upwelling can develop in BoxOF due to the spatial combination of strong positive wind stress curl and positive surface current vorticity.

Second, we examine why the OIV of upwelling in BoxOF is weaker in August than in July, although upwelling and wind peaks are very similar. In August, the eastward jet is stronger than in July (Fig. 5.3, row 1 and Section 5.2). Moreover, its meridional position is also more stable than in July. This was seen above when examining case studies for July and August, and is confirmed by Fig. 5.3 (rows 1-3): MI of the surface vorticity in the area of the eastward jet is much smaller in August than in July, with a much larger area where MI < 100%. The chaotic variability of the eastward jet is thus smaller in August than in July. Moreover, MI of the current vorticity in the rest of BoxOF, in particular in the northeast part, is also weaker in August (the area where MI<100% covers ~57601 km^2, i.e ~29% of BoxOF) than in July (MI<100% covers ~ 42757 km^2, i.e ~22% of BoxOF), as well as VI of the maximum UI_d (70% in August vs. 90% in July, Fig. 5.2, row 8, pink color). This northeast area corresponds to the area where case studies suggested that upwelling is enhanced or inhibited in July depending on the meridional position of the eastward jet. These results therefore first confirm our conclusion from those case studies for July: the OIV of the meridional position of the eastward jet in July drives the OIV of current vorticity in the

northeast part of BoxOF, which favors or prevents the upwelling in this area, and hence drives the OIV of upwelling in BoxOF. Second, it also confirms our conclusion from case studies above for August and explains why the OIV of upwelling over BoxOF is smaller in August. The more stable jet in August results in a smaller OIV of current vorticity in the northeastern part of BoxOF, hence in a smaller OIV of upwelling in this area. OIV of August upwelling is thus driven by the (weaker) OIV of vorticity north of the eastward jet, rather than by the meridional position of the jet.

5.5 Upwelling over BoxNC: the role of background circulation

Da et al., (2019) showed that under given conditions, e.g. strong El Niño events like 1998, upwelling can develop along the northern part of central Vietnam. This was confirmed recently by Ngo and Hsin (2021). Our simulation indeed simulates coastal upwelling in BoxNC. UI_y of the 10 members varies from 0.09 to 0.31 ^oC, with an ensemble average value of 0.21 ^oC, weaker than for BoxOF and BoxSC (Table 5.3). UI_y ensemble standard deviation is equal to 0.08 ^oC, i.e. 37% of the mean value. BoxNC is thus the area where the upwelling is the weakest, but shows the highest intrinsic variability. The chronology of upwelling in BoxNC is also significantly different from BoxSC and BoxOF. UI_d shows mainly has 2 peaks in BoxNC: a first strong peak in June-July, and a second, weaker, at the end of August (rows 5-6, Fig. 5.2). Those peaks are however much weaker than for BoxSC, never exceeding 2°C. Moreover, upwelling does not develop between early July and end of August, even if wind peaks also occur during this period (near July 20th and August 15th for example). The daily variability of BoxNC upwelling during those 2 peaks seems to be driven partly by the wind: UI_d from the 10 members have the same chronology, with UI_d peaks corresponding to wind peaks. However, although the wind stress is of almost equal magnitude during these events (row 5, Fig. 5.2), the upwelling weakens and disappears despite the wind peak in July. Moreover, there is no significant correlation between the time series of UI_d and of daily wind stress over BoxNC (Table 5.1), whatever the period considered. This suggests that another factor than the wind, or atmospheric forcing in general, predominantly drives the development of upwelling over BoxNC.

To understand what is the driving factor of upwelling development for BoxNC we examine 3 periods: (1) period of strong upwelling and strong wind, from June 10th to July 4th; (2) period of strong wind but no upwelling, from July 17th to July 22th; (3) period of strong wind but small upwelling, from August 26th to August 31st. Fig. 5.6 shows for those 3

periods the maps of average surface current, of average surface current curl, of average upwelling daily intensity, and of MI of upwelling intensity and surface current curl.

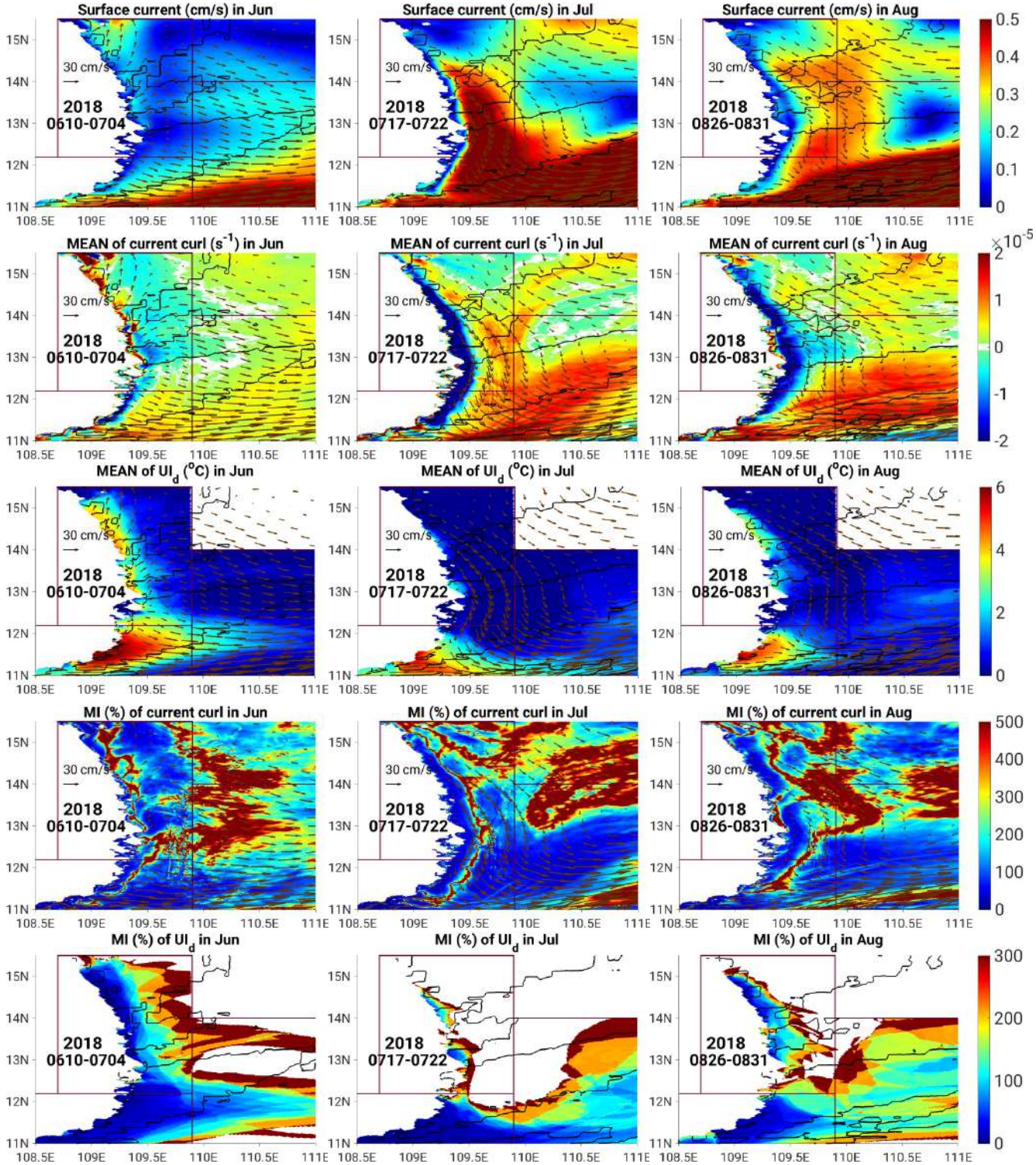

Figure 5. 6 Ensemble average of surface current (m.s^{-1}), maps of averaged surface current curl (color, s^{-1}), and maximum UI$_d$ (^{o}C) during upwelling development in June-July (left), middle of July (middle), and end of August (right) at BoxNC. Black arrows represent surface current direction. Black and pink contours are wind stress curl at +3.10^{-7}(N.m^{-3}) and MI of current at 300 (%), respectively.

5.5.1 June upwelling peak over BoxNC

During the first event, the circulation is offshore oriented, which allows Ekman transport hence the upwelling to develop. Moreover, the intrinsic variability of upwelling is very high, with VI greater than 150% (row 8, Fig. 5.2). This strong OIV during his June-July peak explains the high (37%) MI obtained for UI_y at BoxNC (Table 5.3): for the rest of the summer, the OIV is indeed much smaller, reaching at most ~80% during the short late August peak (row 8, Fig. 5.2). To understand this strong OIV during his June-July peak, we examine several members, for which respectively strong (members 10 and 16) and weak (members 09 and 11) upwelling develops over BoxNC during this period (Fig. 5.7). For members 10 and 16, a cyclonic gyre (C) in the north and anticyclonic (A) in the south meet in BoxNC. This induces an offshore convergence current at 13.5 - 15 ^{o}N, favoring the development of upwelling. For members 09 and 11, cyclonic and anticyclonic gyres do not meet in BoxNC, but either north or south of BoxNC, thus not inducing current toward the open sea.

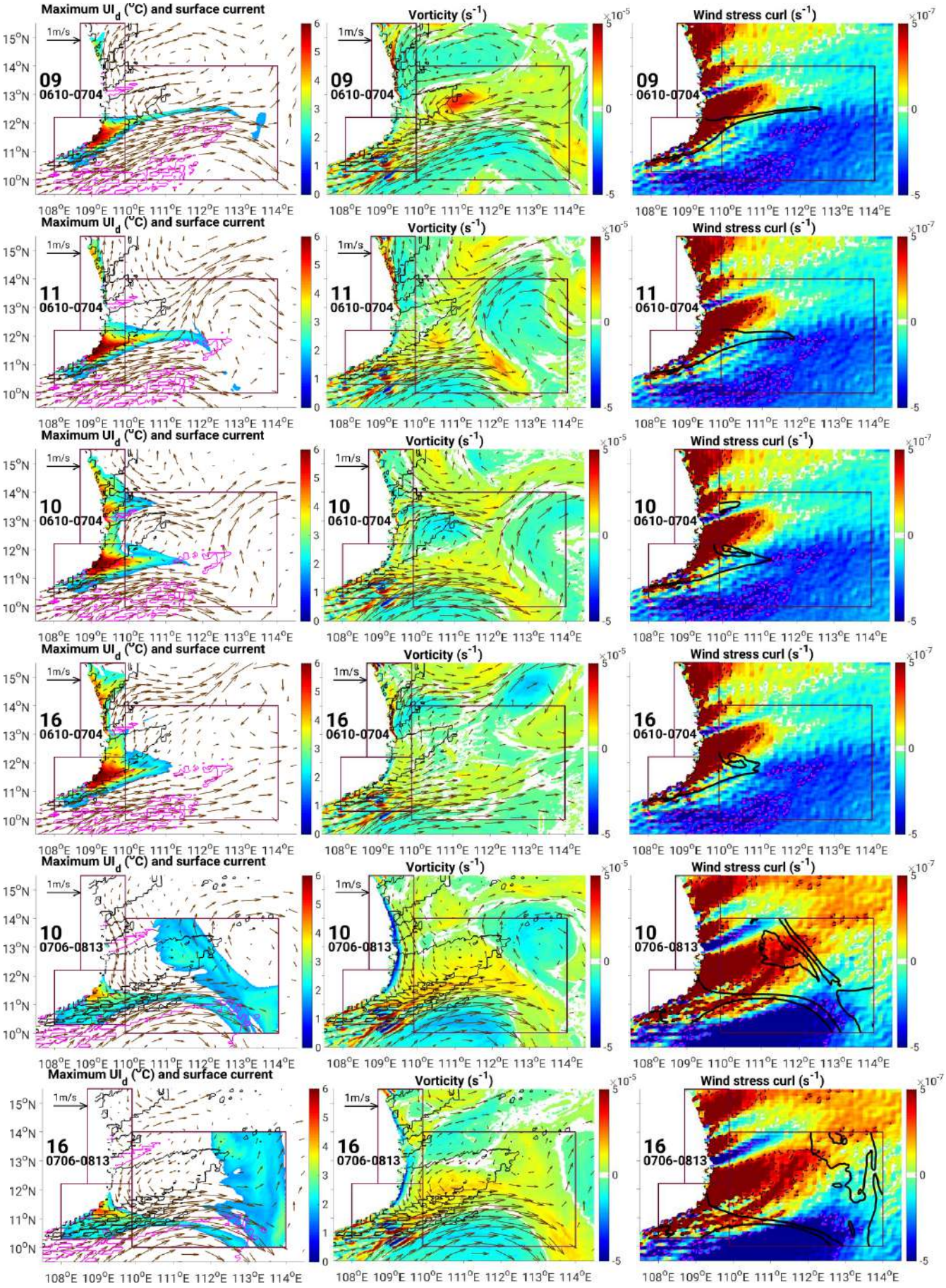
Maximum UI$_d$ (°C) and surface current
Vorticity (s^{-1})
Wind stress curl (s^{-1})
1m/s
09 0610-0704
11 0610-0704
10 0610-0704
16 0610-0704
10 0706-0813
16 0706-0813
15°N
14°N
13°N
12°N
11°N
10°N
108°E 109°E 110°E 111°E 112°E 113°E 114°E

Figure 5. 7 From left to right: maps of UI_d at the day of maximum UId over BoxNC (^oC), maps of averaged surface current curl (color, s^{-1}) and direction of surface current ($m.s^{-1}$, arrows) and maps of wind stress curl (s^{-1}) during the 1st period of upwelling (June 10th - July 4th) for 2 members of weak maximum UI_d (09, 11) and 2 members of strong maximum UI_d (10, 16), and during the period of annihilated upwelling for members 10 and 16. Black arrows represent surface current direction. Black and pink contours on the left frames and black contours on the middle frames are wind stress curls at $+3.10^{-7}$ and -3.10^{-7} $N.m^{-3}$, respectively. Black contour on the right frame is the 2°C isoline of maximum UI_d.

5.5.2 July no-upwelling period

During the second event, the large-scale circulation is more established than in June, with a strong cyclonic eddy over BoxNC, that corresponds to the cyclonic part of the large-scale dipole structure. The average circulation is thus strongly southward and alongshore over BoxNC, with a very high negative vorticity near the coast (row 6, Fig. 5.7). This prevents the Ekman transport and upwelling to develop. VI is very weak during this whole period of annihilated upwelling. The large-scale ocean circulation associated with the dipole structure is common for the 10 members and systematically prevents the upwelling to develop (see members 10 and 16 in Fig. 5.7 and ensemble average and MI of current and vorticity in Fig. 5.6).

5.5.3 End of august upwelling peak

During the third event, the average circulation is similar to the circulation simulated for the 2nd event (Fig. 5.6). However the dipole structure is progressively weakening, the negative vorticity is less strong and the current is a bit more offshore oriented: upwelling is not as strong as in June, but it can develop easier than in July.

Our results therefore first show that coastal upwelling can develop along the northern part of the central Vietnam coast in summer, even when upwelling is strong over BoxOF and BoxSC. This upwelling is partly driven by the wind, but its development (growth or decline) is related to the background circulation, both at the large regional scale and at the small local scale. At the beginning and, to a smaller extent, end of the JJAS period, the large-scale dipole structure and associated eastward current are not strongly established, allowing offshore current to develop. Upwelling can develop at those locations of offshore current, and shows a strong intrinsic variability related to the chaotic variability of those offshore structures. During the core of the summer on the contrary, from mid-July to end August, the dipole-jet structure is strongly established, inducing a strong southward alongshore current over this area which annihilates the upwelling over BoxNC, with a very low intrinsic variability.

5.6 Conclusion of the chapter

In this chapter, results of an ensemble of 10 simulations with perturbed initial conditions were used to investigate the impact of intrinsic variability (OIV) on the daily to intraseasonal variability of upwelling and on its yearly strength. For the 3 areas examined here, those 10 simulations showed the same daily chronology of UId, suggesting that this chronology is mainly induced by an external driver. In BoxSC and BoxOF, the upwelling development varies in the intra-seasonal scale, mainly driven by the wind, the OIV affects the upwelling at a second order, but it is more significant for BoxOF than for BoxSC. For BoxOF we first showed that the position of mesoscale eddies of chaotic nature contributes to the OIV, as already shown by Da et al., (2019) at the interannual scale. We moreover revealed that the impact of OIV varies seasonally: it is stronger in July than in August, due to the fact that the large-scale circulation and associated vorticity is more stable in August. In BoxNC, OIV related to the chaotic variability of the mesoscale coastal circulation impacts strongly the upwelling. Moreover, the background circulation contributes to growth/decline of upwelling development and explains the strong intraseasonal variability of upwelling over BoxNC.

Chapter 6: Conclusion and Perspectives

6.1 Summary of work done during the PhD

6.1.1 Development and evaluation of a high-resolution numerical configuration

Ocean numerical modelling is widely used due to its complementarity with *in-situ* and satellite observations and its much smaller human and financial cost. Models moreover allow to fully explore the 4 dimensions of the virtual ocean that they represent and to study various temporal and spatial scales (from extreme events to climate change). Nowadays, computation time has also been shortened thanks to High Performance Computing clusters, allowing the development of very high resolution models that can represent a large range of physical processes involved in ocean dynamics.

To study the SVU, our methodological approach was to develop a model configuration that has a high spatial resolution at the coast in order to better represent the small scale processes occurring in the upwelling region, and cover a domain large enough to take into account the exchanges with open sea. At the same time, it was important to maintain a reasonable computational cost to perform long simulation (to study the interannual variability) and as well as sensitivity simulations, including ensemble simulations allowing to consider and study the role of OIV.

During my PhD, we therefore developed a VNC configuration of the SYMPHONIE model, based on a very high resolution for coastal regions (~1km) increasing linearly in the offshore region to ~4.5km, and 50 vertical layers. We used the VQS (vanishing quasi-sigma) vertical coordinate described in Estournel et al. (2021) to avoid an excess of vertical levels in very shallow areas while maintaining an accurate description of the bathymetry and reducing the truncation errors associated with the sigma coordinate (Siddorn et al. 2013). With the above advantages, the model can be applied to study specific questions about ocean dynamics, impact on ecosystems, propagation of pollution, etc from the Vietnam coast to open-sea SCS region.

We first performed a 10-year simulation over the period 2009-2018, called LONG. It has been evaluated and optimised using satellite and in-situ observations. We have detailed how our simulation reproduces realistically the temporal (from seasonal to interannual) and spatial patterns of surface characteristics (SST, SSS, SLA) by comparison with satellite observations. Moreover, using *in-situ* datasets collected from ARGO and field campaigns (2 R/V campaigns and a glider campaign), we showed that the vertical distribution of the water mass characteristics are realistically simulated over the basin, from the coastal areas to the open sea, during the whole simulation.

6.1.2 Conclusions about interannual variability of SVU

The analysis of the simulation LONG over 2009-2018 allowed to characterize the interannual variability of the SVU over its 3 main areas of occurrence: southern coast (BoxSC), offshore (BoxOF), northern coast (BoxNC). The results from our high resolution model confirm but also deepens the conclusions about the mechanisms of the interannual variability of SVU of previous studies performed over other periods and with simulations and satellite images at lower resolution.

a) Upwelling along the southern coast (BoxSC) and in the offshore area (BoxOF)

The interannual variability of summer upwelling intensity in BoxSC and BoxOF is strongly driven by the intensity of summer monsoon wind over the SVU region. Summer wind induces Ekman transport, and also triggers the larger scale circulation over the area, with the eastward current around 10.5-12^{o}N and the dipole gyre (cyclonic in the north and anticyclonic in the south). Our results showed that the intensity of upwelling over BoxSC and BoxOF is first driven by the average regional summer wind and larger scale circulation (itself driven by the summer wind). The upwelling in BoxSC and BoxOF is indeed stronger/weaker for years of intense/weak summer wind and large-scale circulation off the Vietnam coast.

We also showed that the upwelling yearly intensity is modulated by the wind variability at higher frequency, daily to intraseasonal. For a given summer average wind intensity, upwelling over boxSC is stronger when wind peaks occur regularly throughout the 4 months of the whole summer period, compared to situations where peaks occur only during some of the 4 months. Moreover, wind peaks of same intensity induce upwelling peaks of similar intensity, whatever their months of occurrence. In the offshore area (BoxOF), the correlation between upwelling and summer wind stress is less significant than for BoxSC. This could be due to a strong influence of mesoscale structures, hence of OIV, which is confirmed later by results from Chapter 5. Moreover, wind peaks occurring in June

or September cause weaker upwelling than peaks of the same magnitude occurring in July-August, the core of the summer season.

Finally, we confirm that the ENSO situation in March affects the regional summer wind and the upwelling over BoxSC and BoxOF. An El Niño event induces a weakening of the monsoon wind over the upwelling region during the following summer, affecting similarly the upwelling intensity, and vice-versa for La Niña.

b) Upwelling along the northern coast (BoxNC)

For upwelling that develops along the northern part of the coast, we obtain no significant correlations between the interannual variations of upwelling intensity and of summer wind and/or circulation. Different formation mechanisms than in BoxSC and BoxOF have been identified.

First, two opposite situations were identified, with opposite effects on upwelling over BoxNC compared to BoxSC and BoxOF. The first situation corresponds to cases where strong regional summer wind and intense offshore circulation favorable to upwelling in BoxOF and BoxSC strengthen alongshore currents and weaken offshore currents along the northern part of the coast. Offshore advection of cold water that could result from Ekman transport therefore weakens, resulting in weak upwelling over BoxNC. The second and opposite situation corresponds to cases of weak summer wind and offshore circulation, which result in stronger upwelling over BoxNC.

Second, we identified situations where wind conditions favorable to upwelling over BoxSC and BoxOF are also favorable to upwelling over BoxNC, due to the development of multiple dipoles and eastward jets; and the opposite (unfavorable for the three areas), due to weak wind and to an alongshore northward current all along the coast. Similar summer wind conditions can therefore result in very different upwelling intensity over BoxNC, and conversely opposite wind conditions can result in similar intensity over BoxNC.

Finally, El Niño/La Niña events induce a strengthening/weakening of the upwelling in BoxNC with a positive though not highly significant correlation.

6.1.3 Conclusions about intraseasonal variability of SVU

Previous numerical modeling studies have shown that the OIV contributes to the interannual variability of SVU (Li et al., 2014, Da et al., 2019). We show for the first time with higher resolution models that OIV also modulates the upwelling intensity at the daily to intraseasonal scales in the different regions of the SVU. The LONG simulation showed that

the upwelling intensity in 2018 was very strong. We therefore took this year as a case study to examine the impact of OIV on the daily to intraseasonal variability of the SVU. For that, we performed an ensemble of 10 twin simulations with perturbed initial conditions on January 1st, 2017.

a) Southern coast and offshore regions

In BoxSC and BoxOF, the daily to intraseasonal chronology of wind is the first order driver of the upwelling evolution at those scales. The OIV affects the upwelling at the second order, more strongly for BoxOF than BoxSC.The impact of intrinsic variability on the average summer intensity of upwelling is higher for BoxOF (18%) than for BoxSC (7%). At the daily scale, the intrinsic contribution to the total daily variability reaches 90% during periods of strong upwelling BoxOF, whereas it does never exceed 40% for BoxSC.

For summer 2018, the intraseasonal variability of upwelling follows the following stages:

- In June, upwelling is active in BoxSC due to the influence of alongshore winds. There is no or very weak upwelling at BoxOF. This is due to the fact that the circulation in the offshore area, namely the eastward jet and dipole structure including the cyclonic gyre, which is a key factor for the development of offshore upwelling, is still weak.
- In July, upwelling in BoxSC is of similar intensity as in June. The eastward jet gets more energy from the wind and the dipole structure forms offshore. Upwelling in BoxOF is thus enhanced both by the positive surface vorticity along the eastward jet and by the presence of cyclonic eddies north of the jet, within the positive wind stress curl area. The meridional variability of the eastward jet position, whose chaotic part is important, drives the variability of the current vorticity in the northeast part of BoxOF. This position hence favors or prevents the upwelling in this area, and explains the strong influence of OIV in July for BoxOF. An eastward current positioned more in the south indeed results in a larger northern area of positive vorticity located in the area of positive wind stress curl, hence in a stronger BoxOF upwelling. And vice-versa for a position more in the north.
- In August, the regional wind is still the dominant factor that triggers the daily chronology of upwelling over BoxSC and BoxOF. The chaotic variability of offshore upwelling is smaller during August than July although upwelling and wind peaks are very similar. This comes from the fact that the eastward jet is stronger and its meridional position is more stable in August than in July. The influence of OIV on the offshore upwelling in August is thus not driven by the chaotic variability of the meridional position of the jet, but by the (weaker) chaotic variability of the vorticity field north of the eastward jet.

b) Northern coast

In BoxNC, the area where the upwelling is the weakest, OIV impacts strongly the upwelling, though the chronology of wind and the large-scale circulation also drive the upwelling in this region. The upwelling occurs with a first strong peak in late June and early July, and a weaker second peak at the end of August. During the core of the summer, the strong cyclonic circulation offshore the northern coast induces a divergent, hence coastward circulation in BoxNC, completely prohibiting the upwelling to develop over BoxNC. In June and late August-September, the large scale circulation is weaker, allowing the upwelling to develop in BoxNC, with a strong impact of OIV. The influence of the intrinsic variability on the summer average intensity is 37%, and the intrinsic contribution to the total daily variability exceeds 150%. This impact of OIV is related to the chaotic variability of the coastal and small mesoscale circulation over BoxNC. Although the variation of upwelling is partly driven by the wind, its daily to intraseasonal development is thus strongly related to the background regional to local circulation.

Note that we examined the intraseasonal to daily variability of the SVU from the case study of 2018, which was exceptional in terms of summer wind and upwelling intensity. It would be interesting to study other years to confirm that our conclusions are still valid or depend on the period of study

6.2 Perspectives

This thesis aimed at quantifying the factors driving the variability of SVU over its different areas of occurrence using a very high resolution model combined with a large volume of satellite observations and *in-situ* data. Our goal was to provide a more detailed understanding of the SVU variability at the daily to intraseasonal scales and physically explain the obtained statistical results. Three major perspectives are given here.

6.2.1 Influence of tides and river plumes

The role of tides and river plumes was not presented in this manuscript, but preliminary studies on their effect were done during this PhD, presented in Appendix. To quantify the effect of tides and rivers on the upwelling strength and on its chaotic variability, we performed 2 sensitivity ensemble simulations. In the ensemble NoTide, the effect of tides is not taken into account. In the ensemble NoRivers, we don't prescribe any river discharge. We have calculated the relative difference between ensembles, and its significance, for the ensemble mean and for the ensemble standard deviation (Table A.1).

Results first show that the impact of tides and rivers is very small, both at the seasonal and daily scale, over the 3 boxes. We obtained no significant difference between the ensembles mean and standard deviation concerning the summer average of upwelling intensity (Table A.1). The 3 ensembles moreover show the same daily to intraseasonal chronology of ensemble mean and standard deviation of upwelling intensity during June-September over 3 boxes (Fig. A.1). The most significant, though weak, impacts were obtained for the southern coastal area (BoxSC): 1) a small effect of tides during the decaying phase of upwelling in July and 2) a small effect of rivers during the decaying phase of upwelling in August (Figure A.1). Those effects still need to be understood, and this influence of tides and rivers will be examined into more detail in the coming months.

6.2.2 Influence on biogeochemistry: development of a coupled physical-biogeochemical model

Dr. Trinh Bich Ngoc, a lecturer at USTH (VAST, Vietnam) who defended her doctoral thesis in 2020 (Trinh, 2020), is working in collaboration with LEGOS in the framework of the International Joint Laboratory LOTUS (lotus.usth.edu.vn) on the coupling between the biogeochemical model Eco3M-S and the SYMPHONIE hydrodynamic model. Her objective is to study the evolution of planktonic systems under the influence of ocean dynamics and of their variability over the South China Sea.

I will collaborate with her to develop a coupled physical-biogeochemical VNC configuration to study the influence of SVU on biogeochemistry and ecosystems. We will focus on the following scientific questions? (1) How does the upwelling influence the marine pelagic planktonic ecosystem that constitutes the first trophic level of the food chain? (2) How does it influence the associated carbon and nitrogen cycle? (3) How is the hydrodynamics variability transmitted to the planktonic pelagic ecosystem? What will be the long-term evolution of this ecosystem?

6.2.3 Influence on atmosphere: development of a coupled ocean atmosphere model

The ocean model used during this PhD was forced by ECMWF atmospheric outputs. We thus ignored the retroactions between the ocean and the atmosphere. How SVU affects atmospheric dynamics needs to be further investigated. In particular, SVU develops in summer, which is also the period of strong typhoon activity in the area. The influence of cold upwelled water on those typhoons has not been investigated yet. An on-going work performed in the framework of LOTUS and CORDEX-SEA project, with a strong

collaboration between LEGOS and USTH (Dr. Ngo Duc Thanh) and an on-going PhD, aims at coupling the ocean model SYMPHONIE and the atmospheric model RegCM. This tool could be used to examine the role of air-sea interactions in the area and during the period of SVU.

6.2.4 Need for in-situ data: organize campaigns and international collaborations

This PhD both benefited from and contributed to the collaboration between LEGOS and Institute of Oceanography (IO, Nha Trang, Vietnam), which are both members of LOTUS. As a permanent researcher in the IO, I will continue to investigate the functioning, variability and influence of SVU, in collaboration with LEGOS. In particular, IO has purchased a Sea-Explorer glider from ALSEAMAR (France). I will bring my modelling skills back to IO, and fully participate in glider campaigns to perform measurements of physics as well as biogeochemistry in the Vietnam upwelling region, which will be greatly supporting my future research.

Conclusion Générale

1 Résumé des travaux réalisés au cours de la thèse

1.1 Développement et évaluation d'une configuration numérique haute résolution

La modélisation numérique de l'océan est de plus en plus utilisée en raison de sa complémentarité avec les observations in-situ et satellitaires et de son coût humain et financier beaucoup plus faible. Les modèles permettent en outre aux chercheurs d'explorer pleinement les 4 dimensions de l'océan virtuel qu'ils représentent, et d'étudier différentes échelles temporelles et spatiales, des événements extrêmes au changement climatique. De nos jours, le temps de calcul a également été réduit grâce aux clusters de calcul haute performance, permettant le développement de modèles à très haute résolution qui peuvent représenter une large gamme de processus physiques impliqués dans la dynamique océanique.

Pour étudier le SVU, notre approche méthodologique était de développer une configuration de modèle océanique qui soit à haute résolution spatiale à la côte, afin de mieux représenter les processus à petite échelle se produisant dans la région d'upwelling, et qui couvre un domaine suffisamment large pour prendre en compte les échanges avec les bassins voisins. En même temps, il était important de maintenir un coût de calcul raisonnable pour effectuer des simulations longues (afin d'étudier la variabilité interannuelle en particulier) et d'effectuer des simulations de sensibilité, y compris des simulations d'ensemble permettant de considérer et d'étudier le rôle de la variabilité intrinsèque océanique (OIV).

Pendant mon doctorat, nous avons donc développé une configuration VNC du modèle SYMPHONIE, basée sur une très haute résolution pour les régions côtières (~1km) augmentant linéairement dans la région offshore jusqu'à ~4.5km, et 50 couches verticales. Nous avons utilisé la coordonnée verticale VQS (vanishing quasi-sigma) décrite dans Estournel et al. (2021) pour éviter un excès de niveaux verticaux dans les zones très peu profondes tout en maintenant une description précise de la bathymétrie et en réduisant les erreurs de troncature associées à la coordonnée sigma (Siddorn et al. 2013). Avec les avantages ci-dessus, ce modèle pourra être utilisé des côtes vietnamiennes à l'océan ouvert

en SCS pour étudier des questions spécifiques sur la dynamique océanique, son influence sur les écosystèmes, sur la propagation de la pollution, etc.

Nous avons d'abord réalisé une simulation sur la période 2009-2018, LONG. Elle a été évaluée par comparaison à des données satellitaires et in-situ. Nous avons montré que cette simulation reproduit de façon réaliste la variabilité temporelle (de l'échelle saisonnière à interannuelle) et spatiale des caractéristiques de surface (SST, SSS, SLA) par comparaison aux observations satellitaires. Nous avons également montré, à partir de plusieurs ensembles de données in-situ provenant de flotteurs ARGO et de campagnes de terrain (2 campagnes bateau et une campagne avec un gliders), que la distribution verticale des caractéristiques des masses d'eau sont simulées de manière réaliste sur le bassin, des zones côtières aux région profondes de la SCS, pendant toute la simulation.

1.2 Conclusions concernant la variabilité interannuelle de l'upwelling

L'analyse de la simulation LONG réalisée sur la période 2009-2018 a permis de caractériser la variabilité interannuelle du SVU sur ses 3 principales zones d'occurrence: côte sud (BoxSC), offshore (BoxOF), côte nord (BoxNC). Les résultats de notre modèle à haute résolution confirment mais aussi approfondissent les conclusions d'études précédentes concernant les mécanismes impliqués dans la variabilité interannuelle du SVU, réalisées sur d'autres périodes et avec des simulations et des images satellites à plus basse résolution.

a) Upwelling le long de la côte sud (BoxSC) et dans la zone offshore (BoxOF)

La variabilité interannuelle de l'intensité de l'upwelling le long de la côte sud et au large est fortement déterminée par l'intensité du vent de mousson d'été dans la région. Le vent d'été induit le transport d'Ekman, et déclenche également la circulation à plus grande échelle sur la zone, avec le dipôle (un gyre cyclonique au nord et un gyre anticyclonique au sud) et le courant associé autour de 10,5-12°N. Nos résultats ont montré que l'intensité de l'upwelling dans BoxSC et BoxOF est d'abord déterminée par le vent d'été moyen et par cette circulation à plus grande échelle (elle-même déterminée par le vent d'été). L'upwelling y est en effet plus fort/faible pour les étés de vent et circulation intenses/faibles.

Nous avons également montré que l'intensité annuelle de l'upwelling est modulée par la variabilité du vent à plus haute fréquence, quotidienne à intrasaisonnière. Pour une

intensité moyenne estivale de vent donnée, l'upwelling dans BoxSC est plus fort lorsque les pics de vent se produisent régulièrement tout au long des 4 mois de la période estivale, par rapport aux situations où les pics ne se produisent que pendant certains des 4 mois. De plus, des pics de vent de même intensité induisent des pics d'upwelling d'intensité similaire, quels que soient les mois où ils se produisent. Dans la zone offshore (BoxOF), la corrélation entre l'intensité de l'upwelling et la tension du vent en été est moins significative que pour BoxSC. Cela pourrait être dû à une forte influence des structures de méso-échelle, donc de l'OIV, ce que confirment ensuite les résultats du chapitre 5. De plus, les pics de vent survenant en juin ou en septembre provoquent un upwelling plus faible que les pics de même amplitude survenant en juillet-août, le cœur de la saison estivale.

Enfin, nous confirmons que la situation ENSO en mars affecte le vent d'été régional et l'upwelling dans les BoxCS et BoxOF. Un événement El Niño induit un affaiblissement du vent de mousson l'été suivant sur la région d'upwelling, affectant de la même manière l'intensité de l'upwelling, et inversement pour La Niña.

b) Upwelling le long de la côte nord (BoxNC)

Pour l'upwelling qui se développe le long de la partie nord de la côte, nous n'avons pas obtenu de corrélation significative entre les variations interannuelles de l'intensité de l'upwelling et celles de l'intensité du vent ou de la circulation régionale en été. Des mécanismes de formation différents de ceux de BoxSC et BoxOF ont été identifiés.

Premièrement, deux situations opposées ont été identifiées, avec des effets contraires sur la zone côtière nord par rapport aux zones côtière sud et offshore. La première situation correspond à des cas où un vent d'été fort et une circulation offshore intense, favorables à l'upwelling dans les zones BoxOF et BoxSC, renforcent les courants le long de la côte et affaiblissent les courants offshore le long de la partie nord de la côte. L'advection vers le large d'eau froide qui pourrait résulter du transport d'Ekman est donc affaiblie, résultant en un faible upwelling dans la zone BoxNC. Et inversement pour la deuxième situation qui correspond à un vent et une circulation d'été faibles.

Deuxièmement, nous avons identifié des situations où les conditions de vent favorables à l'upwelling dans les zones côtière sud et offshore sont également favorables à l'upwelling dans la zone côtière nord, en raison du développement de multiples dipôles et de jets vers l'est; et l'inverse (défavorable pour les trois zones), en raison d'un vent faible et d'un courant vers le nord le long de la côte. Des conditions de vent estivales similaires peuvent donc se traduire par une intensité d'upwelling sur BoxNC très différente, et

inversement des conditions de vent opposées peuvent se traduire par une intensité sur BoxNC similaire.

Enfin, les événements El Niño/La Niña induisent un renforcement/affaiblissement de l'upwelling dans la zone côtière nord, mais avec une corrélation faiblement significative.

1.3 Conclusions concernant la variabilité intrasaisonnière de l'upwelling

Les études précédentes de modélisation numérique menées ont montré que l'OIV contribue à la variabilité interannuelle du SVU (Li et al., 2014; Da et al., 2019). Nous montrons pour la première fois avec un modèle à haute résolution que l'OIV module également l'intensité de l'upwelling aux échelles quotidienne à intrasaisonnière, et dans différentes régions du SVU. La simulation LONG a montré que l'intensité de l'upwelling en 2018 était très forte. Nous avons donc pris cette année comme cas d'étude pour examiner et comprendre l'impact de l'OIV sur la variabilité journalière à intrasaisonnière du SVU. Pour cela, nous avons réalisé un ensemble de 10 simulations jumelles avec des conditions initiales perturbées le 1er janvier 2017.

a) Côte sud et régions offshore

Dans les BoxSC et BoxOF, l'évolution de l'upwelling à l'échelle intrasaisonnière est pilotée au premier ordre par la chronologie du vent. L'OIV affecte l'upwelling au second ordre, plus fortement pour BoxOF que pour BoxSC. L'influence de la variabilité intrinsèque sur l'intensité estivale moyenne de l'upwelling est plus élevée pour BoxOF (18%) que pour BoxSC (7%). La contribution intrinsèque à la variabilité journalière totale dépasse 90% pour BoxOF lors des pics d'upwelling, alors qu'elle ne dépasse pas 40% pour BoxSC.

La variabilité intrasaisonnière de l'upwelling suit les étapes suivantes:

- En juin, l'upwelling est actif dans la zone BoxSC en raison de l'influence des vents parallèles à la côte. Il n'y a pas ou très peu d'upwelling dans la zone BoxOF. Ceci est dû au fait que la circulation dans la zone offshore, qui est un facteur clé pour le développement de l'upwelling offshore, à savoir le courant Est et la structure dipolaire y compris le tourbillon cyclonique, est encore faible.

- En juillet, l'upwelling dans la zone BoxSC est d'une intensité similaire à celle de juin. Le courant Est reçoit plus d'énergie du vent et la structure dipolaire se forme au large avec une circulation anticyclonique au sud et cyclonique au nord. L'upwelling dans la

zone BoxOF est renforcé par la vorticité positive le long du courant Est ainsi que la présence de tourbillons cycloniques situés dans la zone de vorticité positive du vent. La variabilité méridionale de la position du courant Est, dont la partie chaotique est importante, pilote la variabilité de la vorticité océanique dans la partie nord-est de BoxOF. Cette position favorise ou empêche l'upwelling dans cette zone, et explique la forte influence de l'OIV en juillet. Une courant Est positionné plus au sud conduit en effet à ce que la zone d'activité cyclonique au nord du courant soit davantage positionnée dans la région de rotationnel de vent positif, ce qui renforce l'upwelling offshore. Et inversement pour un positionnement plus au nord.

- En août, le vent régional reste le facteur dominant qui pilote la chronologie journalière de l'upwelling pour BoxOF et BoxSC. La variabilité chaotique de l'upwelling offshore est plus faible qu'en juillet bien que l'intensité des pics d'upwelling et de vent soit très similaire à celle en juillet. Cela vient du fait que le courant Est est plus fort et sa position méridionale plus stable en août qu'en juillet. L'influence de l'OIV sur l'upwelling offshore est alors liée en août à la variabilité chaotique (plus faible) de la vorticité de la zone au nord du courant Est, plutôt qu'à la variabilité chaotique de la position méridienne du jet.

b) Côte nord

Dans la région côtière nord, l'upwelling est le plus faible, et l'OIV a un impact important, bien que la chronologie du vent et la circulation à grande échelle soient également des facteurs clés dans cette région dans cette région. L'upwelling se produit avec un premier pic fin juin - début juillet et un second pic plus faible fin août. Au cœur de l'été, la forte circulation cyclonique au large de la côte nord, liée au dipôle dans la région offshore, induit une circulation divergente, donc vers la côte, dans la BoxNC. Ceci empêche complètement l'upwelling de s'y développer. En juin et fin août-septembre, la circulation à grande échelle est plus faible, permettant à l'upwelling de se développer dans cette zone, avec un fort impact de l'OIV. L'influence de la variabilité intrinsèque sur la moyenne annuelle de l'upwelling dans la BoxNC est de 37%, et la contribution intrinsèque à la variabilité quotidienne totale dépasse 150%. Cet impact de l'OIV est principalement lié à la variabilité chaotique de la circulation côtière et de mésoéchelle dans cette région. Bien que la variabilité de l'upwelling dans la zone côtière nord soit en partie déterminée par le vent, son développement est donc fortement influencé par la circulation régionale à locale, que ce soit à l'échelle journalière ou intrasaisonnière.

2 Perspectives

Cette thèse avait pour but de quantifier les facteurs de variabilité du SVU dans ses différentes zones d'occurrence en utilisant un modèle à très haute résolution combiné à un grand volume d'observations satellitaires et de données in-situ. Notre objectif était de permettre une compréhension plus détaillée de la variabilité de l'upwelling à l'échelle journalière et intrasaisonnière et une meilleure explication physique des résultats statistiques obtenus. Trois perspectives majeures à ce travail sont données ici.

2.1 Effet des marées et des panaches de rivières

Le rôle des marées et des rivières n'a pas été examiné dans ce manuscrit, mais des études préliminaires sur leur effet ont été réalisées au cours de cette thèse, présentées en annexe. Pour quantifier l'effet des marées et des rivières sur l'intensité de l'upwelling et sur sa variabilité chaotique, nous avons effectué deux simulations d'ensemble de sensibilité. Dans l'ensemble NoTide, l'effet des marées n'est pas pris en compte. Dans l'ensemble NoRivers, nous ne prescrivons aucun débit de rivière. Nous avons calculé la différence relative entre les ensembles, et leur significativité, pour la moyenne de l'ensemble et pour l'écart-type de l'ensemble (Table A.1).

Les résultats montrent d'abord que l'impact des marées et des rivières est très faible, tant à l'échelle saisonnière que quotidienne, sur les 3 ensembles. Nous n'avons obtenu aucune différence significative entre la moyenne et l'écart-type des ensembles concernant la moyenne saisonnière de l'intensité de l'upwelling (Table A.1). Les 3 ensembles montrent d'ailleurs la même chronologie journalière à intrasaisonnière de la moyenne et de l'écart-type d'ensemble de l'intensité de l'upwelling pendant l'été sur les 3 boîtes (Fig. A.2). Les effets les plus significatifs, bien que faibles, ont été obtenus pour la zone BoxSC: 1) un petit effet des marées pendant la phase de décroissance de l'upwelling en juillet et 2) un petit effet des rivières pendant la phase de décroissance de l'upwelling en août (Figure A.2). Ces effets restent à mieux comprendre, et cette influence des marées et des rivières sera examinée plus en détail dans les mois à venir.

2.2 Influence sur la biogéochimie: développement d'un modèle couplé physique-biogéochimique

Trinh Bich Ngoc, maître de conférences à l'USTH (VAST, Vietnam) qui a soutenu sa thèse de doctorat en 2020 (Trinh, 2020), travaille en collaboration avec le LEGOS dans le cadre du LMI LOTUS (lotus.usth.edu.vn) sur le couplage entre le modèle biogéochimique Eco3M-S et le modèle hydrodynamique SYMPHONIE. Son objectif est d'étudier l'évolution des systèmes planctoniques sous l'influence de la dynamique océanique et de sa variabilité en Mer de Chine du Sud.

Je collaborerai avec elle pour développer une configuration VNC couplée physique-biogéochimique pour comprendre l'influence du SVU sur la biogéochimie et les écosystèmes. Nous nous concentrerons sur les questions scientifiques suivantes. (1) Comment l'upwelling influence-t-il l'écosystème planctonique pélagique marin qui constitue le premier niveau trophique de la chaîne alimentaire ? (2) Comment influence-t-il le cycle du carbone et de l'azote associé ? (3) Comment la variabilité hydrodynamique se transmet-elle à l'écosystème planctonique pélagique ? Quelle sera l'évolution à long terme de cet écosystème ?

2.3 Impact sur l'atmosphère: développement d'un modèle couplé océan atmosphère

Le modèle océanique utilisé pour cette thèse est forcé par les sorties atmosphériques ECMWF. Nous ne prenons donc pas en compte les rétroactions entre l'océan et l'atmosphère. La façon dont le SVU affecte la dynamique atmosphérique mérite d'être étudiée plus en détail. En particulier, le SVU se développe en été, qui est aussi la période de forte activité des typhons dans la région. L'influence de l'eau froide remontée par l'upwelling sur ces typhons n'a pas encore été étudiée. Un travail en cours réalisé dans le cadre du LMI LOTUS et du projet CORDEX-SEA, avec une forte collaboration entre LEGOS et USTH (Dr. Ngo Duc Thanh) et un doctorat en cours, vise à coupler le modèle océanique SYMPHONIE et le modèle atmosphérique RegCM. Cet outil pourra être utilisé pour examiner le rôle des interactions air-mer dans la région et pendant la période du SVU.

2.4 Besoin de données in-situ: organiser des campagnes et des collaborations internationales

Cette thèse a bénéficié et contribué à la collaboration entre le LEGOS et l'Institut d'océanographie (IO, Nha Trang, Vietnam), qui sont tous deux membres du LMI LOTUS. En tant que chercheur permanent à l'IO, je continuerai à étudier le fonctionnement, la variabilité et l'influence du SVU, en collaboration avec le LEGOS. En particulier, l'IO a acheté un glider Sea-Explorer à ALSEAMAR (France). J'apporterai mes compétences en matière de modélisation à l'IO et participerai pleinement aux campagnes de gliders pour effectuer des mesures de physique et de biogéochimie dans la région d'upwelling du Vietnam, ce qui contribuera significativement à mes futures recherches.

APPENDIX

To investigate the impact of tides and rivers on the functioning and intraseasonal variability of the upwelling that develop along the Vietnam coast, and on its intrinsic variability at the daily to seasonal scales, we perform 2 additional sensitivity ensemble simulations. Those sensitivity ensembles are identical to the reference ensemble, except for one thing: in the ensemble NoTide, the effect of tides is not taken into account; in the ensemble NoRivers, we don't prescribe any river discharge. Due to time constraints, we did not present the detailed results of those simulations in the manuscrit, and present preliminary results in this appendix.

To quantify the effect of tides and rivers on the upwelling strength and on its chaotic variability, we compute the relative difference of the ensemble mean, RevMean, and of the ensemble standard deviation, RevSTD, between the sensitivity ensembles and the reference ensemble:

$$RevMean(\%) = \frac{Mean_{ens}(UIy \text{ or } UId) - Mean_{Ref}(UIy \text{ or } UId)}{Mean_{Ref}(UIy \text{ or } UId)} \times 100 \quad \text{(A.1)}$$

$$RevSTD(\%) = \frac{STD_{ens}(UIy \text{ or } UId) - STD_{Ref}(UIy \text{ or } UId)}{STD_{Ref}(UIy \text{ or } UId)} \times 100 \quad \text{(A.2)}$$

Where the subscript *"ens"* corresponds to the sensitivity ensemble (NoTide or NoRivers), and the subscript "*Ref*" corresponds to the reference ensemble (for us, FULL). To evaluate the significance of those differences, we compute the p values associated with respectively a t-test for the ensemble mean (p_{mean} indicates the significance of the difference between the mean values), and a f-test for the ensemble standard deviation (p_{std} indicates the significance of the difference between the standard deviation values): a p value lower than 0.01, resp. 0.05, means that the difference between the sensitivity ensemble and the reference ensemble is significant at 99%, resp. 95%. Table A.1 shows, for each box, the value of yearly UI_y (°C) in each member simulation, the ensemble mean, the ensemble standard deviation and MI (standard deviation over mean). It also shows RevMean and p_{mean} and RevSTD and p_{std} for NoTide and NoRivers ensembles compared to FULL, and the correlation coefficient between the daily time series of ensemble mean UI_d in each sensitivity ensemble and in FULL.

Table A. 1 For each box, value of yearly UI_y (°C) in each member simulation (columns 1-10), ensemble mean (11), ensemble standard deviation (13) and MI (14), RevMean and p_{mean} (12) and RevSTD and p_{std} (15) for NoTide and NoRivers compared to FULL. Correlation coefficient between yearly UI_y (16) and daily UI_d (17) in ensemble mean of FULL with NoTide and NoRivers

BOX OF	*(1)*	*(2)*	*(3)*	*(4)*	*(5)*	*(6)*	*(7)*	*(8)*	*(9)*	*(10)*	*(11)*	*(12)*	*(13)*	*(14)*	*(15)*	*(16)*	*(17)*
Memb simu	09	10	11	12	13	14	15	16	17	18	Mean	RevMean; pmean	STD	MI $\frac{(13)}{(11)}$	RevSTD; Pstd	Corr (UI_y mean) (1-10) p>0.1	Corr (UI_d mean) p<0.01
FULL	0.32	0.35	0.26	0.39	0.37	0.39	0.26	0.26	0.42	0.31	0.33	---	0.06	18 %	---	---	----
NoTide	0.40	0.38	0.35	0.36	0.33	0.39	0.47	0.29	0.55	0.20	0.37	12.5 %; 0.26	0.10	26 %	59.9 %; 0.18	0.34	0.98
NoRivers	0.40	0.32	0.45	0.35	0.41	0.46	0.34	0.22	0.31	0.24	0.35	6.2 %; 0.52	0.08	23 %	35.2 %; 0.38	0.19	0.99

BOX SC	*(1)*	*(2)*	*(3)*	*(4)*	*(5)*	*(6)*	*(7)*	*(8)*	*(9)*	*(10)*	*(11)*	*(12)*	*(13)*	*(14)*	*(15)*	*(16)*	*(17)*
Memb simu	09	10	11	12	13	14	15	16	17	18	Mean	RevMean; pmean	STD	MI $\frac{(13)}{(11)}$	RevSTD; Pstd	Corr (UI_y mean) (1-10) p>0.1	Corr (UI_d mean) p<0.01
FULL	1.25	1.35	1.25	1.49	1.39	1.42	1.27	1.38	1.48	1.29	1.36	---	0.09	7 %	---	---	---
NoTide	1.35	1.28	1.29	1.26	1.24	1.30	1.35	1.29	1.40	1.29	1.31	-3.8 %; 0.13	0.05	4 %	-47.6 %; 0.51	-0.08	0.98
NoRivers	1.40	1.33	1.37	1.42	1.46	1.40	1.35	1.24	1.38	1.25	1.36	0.3 %; 0.92	0.07	5 %	-23.1 %; 0.65	0.28	0.99

BOX NC	*(1)*	*(2)*	*(3)*	*(4)*	*(5)*	*(6)*	*(7)*	*(8)*	*(9)*	*(10)*	*(11)*	*(12)*	*(13)*	*(14)*	*(15)*	*(16)*	*(17)*
Memb simu	09	10	11	12	13	14	15	16	17	18	Mean	RevMean; pmean	STD	MI $\frac{(13)}{(11)}$	RevSTD; Pstd	Corr (UI_y mean) (1-10) p>0.1	Corr (UI_d mean) p<0.01
FULL	0.13	0.28	0.09	0.18	0.20	0.17	0.29	0.30	0.31	0.16	0.21	---	0.08	37 %	---	---	---
NoTide	0.24	0.21	0.30	0.18	0.18	0.31	0.20	0.28	0.32	0.17	0.24	12.8 %; 0.39	0.06	25 %	-24.5 %; 0.97	0.05	0.99
NoRivers	0.13	0.26	0.21	0.16	0.34	0.28	0.14	0.09	0.12	0.11	0.18	-13.2%; 0.45	0.09	46 %	9.4 %; 0.3	-0.22	0.96

A.1. Influence of tides and rivers on the summer average of upwelling intensity

The difference of the ensemble average of UI_y between the ensemble FULL and the sensitivity ensemble is never significant at more than 90% for neither NoTide nor NoRivers, for the 3 boxes. The relative difference of the ensemble mean, RevMean, in all 3 boxes is indeed smaller than ± 13% with $p_{mean} \geq 0.13$ (see column *(12)*, Table A.1).

Concerning the relative difference of the ensemble standard deviation, RevSTD, it is associated with p_{std} values always largely larger than 0.10 ($p_{std} > 0.18$ for NoTide and $p_{std} > 0.30$ for NoRivers, see column 15 of Table A.1).

Those results show that the influence of tides and rivers plumes on the summer 2018 average intensity of the upwelling and on its answer to OIV is negligible for all the 3 boxes.

A.2. Influence of tides and rivers on the daily chronology and intraseasonal variability of UI_d

There is a highly significant correlation between the time series of ensemble mean of UI_d for in FULL and in both sensitivity ensemble, for the 3 boxes ($R>0.96$, $p<0.01$) (column 16, 17, Table A.1). This suggests that tides and river plumes hardly affect the daily chronology of the upwelling for those 3 areas.

Fig. A.1 shows for each ensemble and each box the ensemble average and relative standard deviation VI of UId over each box. Periods when the difference between time series in the ensemble FULL and in the sensitivity ensemble are significant at more than 99% are indicated by shaded area. The first result is that for each box, time series of the ensemble mean and standard deviation are very similar for the 3 ensembles, FULL, NoTide and NoRivers, with only small periods of significant differences. Tides and rivers therefore hardly affect the daily chronology of upwelling intensity, and of its sensitivity to OIV, for the 3 boxes. The most significant, though weak, impacts were obtained for the southern coastal area (BoxSC): 1) a small effect of tides during the decaying phase of upwelling in July and 2) a small effect of rivers during the decaying phase of upwelling in August. Those effects still need to be understood, and this influence of tides and rivers will be examined into more detail in the coming months.

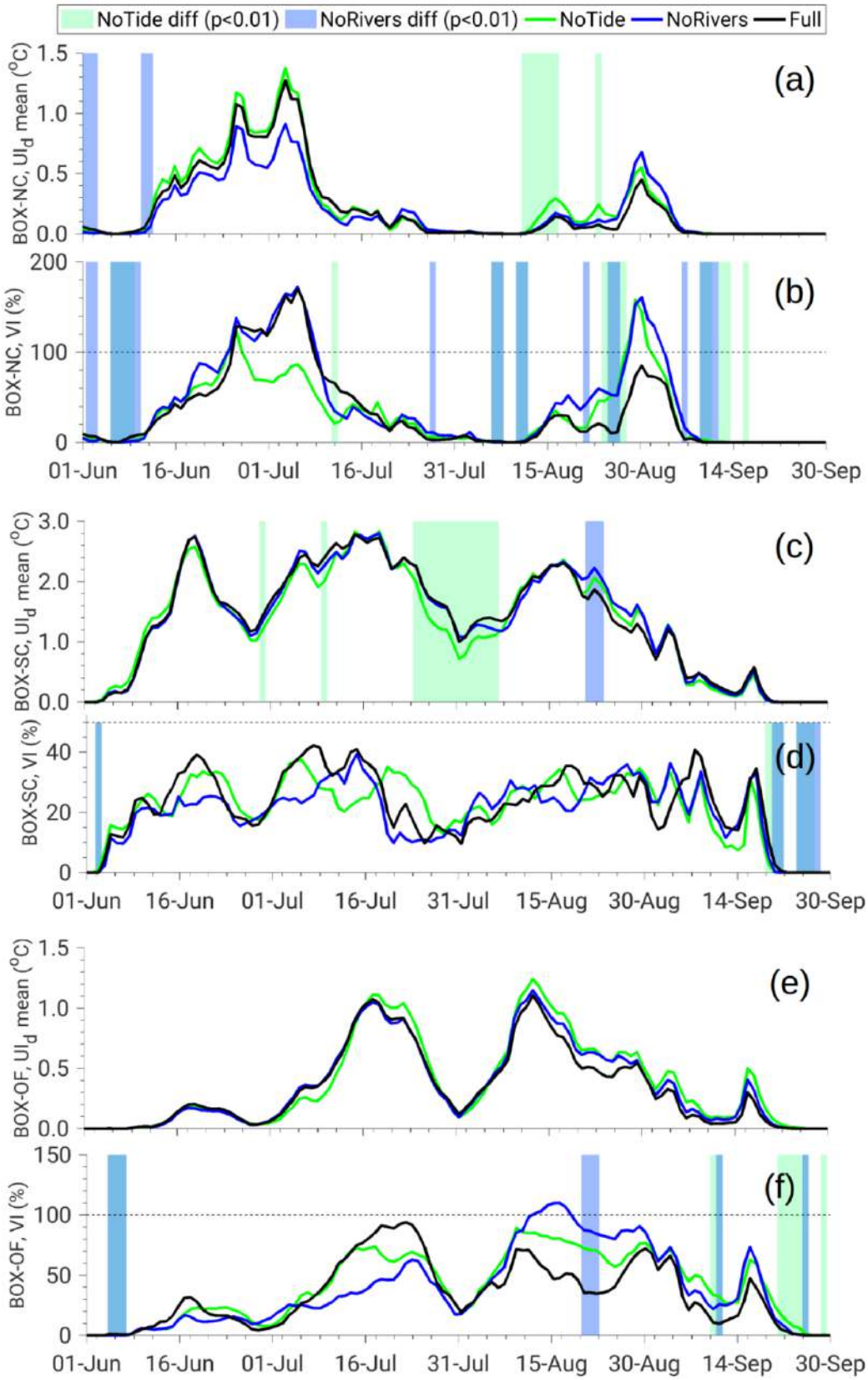

Figure A. 1 Daily time series during June - September of the ensemble mean (UId) and ensemble standard deviation (VI) for each box (a-b: BoxNC, c-d: BoxSC and e-f: BoxOF) in the ensembles FULL (black line), No Tide (green line) and No River (blue line). Periods when the difference between the sensitivity simulations and FULL is significant at more than 99% are indicated by bars: FULL and No Tide (green bar), FULL and No River (blue bar).

REFERENCES

Ablain, M., Cazenave, A., Larnicol, G., Balmaseda, M., Cipollini, P., Faugère, Y., Fernandes, M. J., Henry, O., Johannessen, J. A., Knudsen, P., Andersen, O., Legeais, J., Meyssignac, B., Picot, N., Roca, M., Rudenko, S., Scharffenberg, M. G., Stammer, D., Timms, G., & Benveniste, J. (2015). Improved sea level record over the satellite altimetry era (1993–2010) from the Climate Change Initiative project. Ocean Science, 11(1), 67–82. https://doi.org/10.5194/os-11-67-2015

Amiruddin, A. M., Haigh, I. D., Tsimplis, M. N., Calafat, F. M., & Dangendorf, S. (2015). The seasonal cycle and variability of sea level in the South China Sea. Journal of Geophysical Research: Oceans, 120(8), 5490–5513. https://doi.org/10.1002/2015jc010923

An, S.-I., & Jin, F.-F. (2004). Nonlinearity and asymmetry of ENSO*. Journal of Climate, 17(12), 2399–2412. https://doi.org/10.1175/1520-0442(2004)017<2399:naaoe>2.0.co;2

Anderson, D. M., & Prell, W. L. (1993). A 300 KYR record of upwelling off Oman during the late quaternary: Evidence of the Asian southwest monsoon. *Paleoceanography*, *8*(2), 193–208. https://doi.org/10.1029/93pa00256

Arakawa, A., & Suarez, M. J. (1983). Vertical differencing of the primitive equations in sigma coordinates. Monthly Weather Review, 111(1), 34–45. https://doi.org/10.1175/1520-0493(1983)111<0034:vdotpe>2.0.co;2

Auclair, F., Estournel, C., Floor, J. W., Herrmann, M., Nguyen, C., & Marsaleix, P. (2011). A non-hydrostatic algorithm for free-surface ocean modelling. Ocean Modelling, 36(1–2), 49–70. https://doi.org/10.1016/j.ocemod.2010.09.006

Barthel, K., Rosland, R., & Thai, N. C. (2009). Modelling the circulation on the continental shelf of the province Khanh Hoa in Vietnam. Journal of Marine Systems, 77(1–2), 89–113. https://doi.org/10.1016/j.jmarsys.2008.11.010

Bombar, D., Dippner, J. W., Doan, H. N., Ngoc, L. N., Liskow, I., Loick-Wilde, N., and Voss, M. (2010). Sources of new nitrogen in the Vietnamese upwelling region of the South China Sea. *Journal of Geophysical Research*, *115*(C6). https://doi.org/10.1029/2008jc005154

Boutin, J., Vergely, J. L., Marchand, S., D'Amico, F., Hasson, A., Kolodziejczyk, N., Reul, N., Reverdin, G., & Vialard, J. (2018). New SMOS Sea Surface Salinity with reduced systematic errors and improved variability. Remote Sensing of Environment, 214, 115–134. https://doi.org/10.1016/j.rse.2018.05.022

Burchard, H., & Bolding, K. (2001). Comparative analysis of four second-moment turbulence closure models for the oceanic mixed layer. Journal of Physical Oceanography, 31(8), 1943–1968. https://doi.org/10.1175/1520-0485(2001)031<1943:caofsm>2.0.co;2

Canuto, V. M., Howard, A., Cheng, Y., & Dubovikov, M. S. (2001). Ocean turbulence. Part I: One-Point closure model—momentum and heat vertical diffusivities. Journal of Physical Oceanography, 31(6), 1413–1426. https://doi.org/10.1175/1520-0485(2001)031<1413:otpiop>2.0.co;2

Casey, K. S., Brandon, T. B., Cornillon, P., & Evans, R. (2010). The past, present, and future of the AVHRR pathfinder SST program. In *Oceanography from Space* (pp. 273–287). Springer Netherlands. http://dx.doi.org/10.1007/978-90-481-8681-5_16

Chang, Y., Yung Tang, T., Chao, S., Chang, M., Ko, D. S., Jang Yang, Y., Liang, W., & McPhaden, M. J. (2010). Mooring observations and numerical modeling of thermal structures in the South China Sea. Journal of Geophysical Research: Oceans, 115(C10). https://doi.org/10.1029/2010jc006293

Chao, S.-Y., Shaw, P.-T., & Wu, S. Y. (1996). El Niño modulation of the South China Sea circulation. Progress in Oceanography, 38(1), 51–93. https://doi.org/10.1016/s0079-6611(96)00010-9

Chelton, D. B., Schlax, M. G., Samelson, R. M., & de Szoeke, R. A. (2007). Global observations of large oceanic eddies. Geophysical Research Letters, 34(15). https://doi.org/10.1029/2007gl030812

Chen, C., Lai, Z., Beardsley, R. C., Xu, Q., Lin, H., & Viet, N. T. (2012). Current separation and upwelling over the southeast shelf of Vietnam in the South China Sea. Journal of Geophysical Research: Oceans, 117(C3), n/a-n/a. https://doi.org/10.1029/2011jc007150

Chen, C.-T. A., & Huang, M.-H. (1996). A mid-depth front separating the South China Sea water and the Philippine sea water. *Journal of Oceanography*, *52*(1), 17–25. https://doi.org/10.1007/bf02236530

Chen, G., Hou, Y., & Chu, X. (2011). Mesoscale eddies in the South China Sea: Mean properties, spatiotemporal variability, and impact on thermohaline structure. Journal of Geophysical Research, 116(C6). https://doi.org/10.1029/2010jc006716

Chen, G., Hou, Y., Zhang, Q., & Chu, X. (2010). The eddy pair off eastern Vietnam: Interannual variability and impact on thermohaline structure. Continental Shelf Research, 30(7), 715–723. https://doi.org/10.1016/j.csr.2009.11.013

Chen, T.-C., Tsay, J.-D., & Matsumoto, J. (2017). Interannual variation of the summer rainfall center in the South China Sea. Journal of Climate, 30(19), 7909–7931. https://doi.org/10.1175/jcli-d-16-0889.1

Chevey, P., & Carton, P. (1934). Les courants de la mer de Chine méridionale et leurs rapports avec le climat de l'Indochine.

Chu, P. C., & Li, R. (2000). South China Sea isopycnal-surface circulation. Journal of Physical Oceanography, 30(9), 2419–2438. https://doi.org/10.1175/1520-0485(2000)030<2419:scsisc>2.0.co;2

Craig, P. D., & Banner, M. L. (1994). Modeling wave-enhanced turbulence in the ocean surface layer. Journal of Physical Oceanography, 24(12), 2546–2559. https://doi.org/10.1175/1520-0485(1994)024<2546:mwetit>2.0.co;2

Da, N. D., Herrmann, M., Morrow, R., Niño, F., Huan, N. M., and Trinh, N. Q. (2019). Contributions of wind, ocean intrinsic variability, and ENSO to the interannual variability of the south vietnam upwelling: A modeling study. *Journal of Geophysical Research: Oceans*, *124*(9), 6545–6574. https://doi.org/10.1029/2018jc014647

Dai, A., & Trenberth, K. E. (2002). Estimates of freshwater discharge from continents: Latitudinal and seasonal variations. Journal of Hydrometeorology, 3(6), 660–687. https://doi.org/10.1175/1525-7541(2002)003<0660:eofdfc>2.0.co;2

REFERENCES

Dai, S. B., Yang, S. L., & Cai, A. M. (2008). Impacts of dams on the sediment flux of the Pearl River, southern China. CATENA, 76(1), 36–43. https://doi.org/10.1016/j.catena.2008.08.004

Da Nguyen Dac (2018), Variabilité interannuelle de l'upwelling du Sud Vietnam, PhD manuscrit, Université de Toulouse.

Dippner, J. W., and Loick-Wilde, N. (2011). A redefinition of water masses in the Vietnamese upwelling area. *Journal of Marine Systems*, *84*(1–2), 42–47. https://doi.org/10.1016/j.jmarsys.2010.08.004

Dippner, J. W., Nguyen, K. V., Hein, H., Ohde, T., & Loick, N. (2007). Monsoon-induced upwelling off the Vietnamese coast. Ocean Dynamics, 57(1), 46–62. https://doi.org/10.1007/s10236-006-0091-0

Dongliang, Y. (2002). A numerical study of the South China Sea deep circulation and its relation to the Luzon Strait transport. *Acta Oceanologica Sinica*, *21*(2), 187-202.

Doodson, A. T., & Marmer, H. A. (1927). The Tides for the general reader. Geographical Review, 17(2), 348. https://doi.org/10.2307/208241

Dukhovskoy, D. S., Morey, S. L., Martin, P. J., O'Brien, J. J., & Cooper, C. (2009). Application of a vanishing, quasi-sigma, vertical coordinate for simulation of high-speed, deep currents over the Sigsbee Escarpment in the Gulf of Mexico. Ocean Modelling, 28(4), 250–265. https://doi.org/10.1016/j.ocemod.2009.02.009

Estournel, C., Bosc, E., Bocquet, M., Ulses, C., Marsaleix, P., Winiarek, V., Osvath, I., Nguyen, C., Duhaut, T., Lyard, F., Michaud, H., & Auclair, F. (2012). Assessment of the amount of cesium-137 released into the Pacific Ocean after the Fukushima accident and analysis of its dispersion in Japanese coastal waters. Journal of Geophysical Research: Oceans, 117(C11), n/a-n/a. https://doi.org/10.1029/2012jc007933

Estournel, C., Testor, P., Damien, P., D'Ortenzio, F., Marsaleix, P., Conan, P., Kessouri, F., Durrieu de Madron, X., Coppola, L., Lellouche, J., Belamari, S., Mortier, L., Ulses, C., Bouin, M., & Prieur, L. (2016). High resolution modeling of dense water formation in the north-western Mediterranean during winter 2012–2013: Processes and budget. Journal of Geophysical Research: Oceans, 121(7), 5367–5392. https://doi.org/10.1002/2016jc011935

Fang, G., Chen, H., Wei, Z., Wang, Y., Wang, X., & Li, C. (2006). Trends and interannual variability of the South China Sea surface winds, surface height, and surface temperature in the recent decade. Journal of Geophysical Research, 111(C11). https://doi.org/10.1029/2005jc003276

Fang, G., Kwok, Y.-K., Yu, K., & Zhu, Y. (1999). Numerical simulation of principal tidal constituents in the South China Sea, Gulf of Tonkin and Gulf of Thailand. Continental Shelf Research, 19(7), 845–869. https://doi.org/10.1016/s0278-4343(99)00002-3

Fang, G., Wang, Y., Wei, Z., Fang, Y., Qiao, F., & Hu, X. (2009). Interocean circulation and heat and freshwater budgets of the South China Sea based on a numerical model. Dynamics of Atmospheres and Oceans, 47(1–3), 55–72. https://doi.org/10.1016/j.dynatmoce.2008.09.003

Fang, W. (2002). Seasonal structures of upper layer circulation in the southern South China Sea from in situ observations. Journal of Geophysical Research, 107(C11). https://doi.org/10.1029/2002jc001343

Feng, B., Liu, H., & Lin, P. (2020). Effects of Kuroshio intrusion optimization on the simulation of mesoscale eddies in the northern South China Sea. Acta Oceanologica Sinica, 39(3), 12–24. https://doi.org/10.1007/s13131-020-1565-5

Gan, J., & Qu, T. (2008). Coastal jet separation and associated flow variability in the southwest South China Sea. *Deep Sea Research Part I: Oceanographic Research Papers*, *55*(1), 1–19. https://doi.org/10.1016/j.dsr.2007.09.008

Gan, J., Liu, Z., & Hui, C. R. (2016a). A three-layer alternating spinning circulation in the South China Sea. Journal of Physical Oceanography, 46(8), 2309–2315. https://doi.org/10.1175/jpo-d-16-0044.1

Gan, J., Liu, Z., & Liang, L. (2016b). Numerical modeling of intrinsically and extrinsically forced seasonal circulation in the China Seas: A kinematic study. Journal of Geophysical Research: Oceans, 121(7), 4697–4715. https://doi.org/10.1002/2016jc011800

Garau, B., Ruiz, S., Zhang, W. G., Pascual, A., Heslop, E., Kerfoot, J., & Tintoré, J. (2011). Thermal lag correction on slocum CTD glider data. Journal of Atmospheric and Oceanic Technology, 28(9), 1065–1071. https://doi.org/10.1175/jtech-d-10-05030.1

Gaspar, P., Grégoris, Y., & Lefevre, J.-M. (1990). A simple eddy kinetic energy model for simulations of the oceanic vertical mixing: Tests at station Papa and long-term upper ocean study site. Journal of Geophysical Research, 95(C9), 16179. https://doi.org/10.1029/jc095ic09p16179

Grégorio, S., Penduff, T., Sérazin, G., Molines, J.-M., Barnier, B., & Hirschi, J. (2015). Intrinsic variability of the Atlantic meridional overturning circulation at interannual-to-multidecadal time scales. *Journal of Physical Oceanography*, *45*(7), 1929–1946. https://doi.org/10.1175/jpo-d-14-0163.1

Griffies, S. M., & Hallberg, R. W. (2000). Biharmonic friction with a smagorinsky-like viscosity for use in large-scale eddy-permitting ocean models. Monthly Weather Review, 128(8), 2935–2946. https://doi.org/10.1175/1520-0493(2000)128<2935:bfwasl>2.0.co;2

Guo, J., Fang, W., Fang, G., & Chen, H. (2006). Variability of surface circulation in the South China Sea from satellite altimeter data. Chinese Science Bulletin, 51(S2), 1–8. https://doi.org/10.1007/s11434-006-9001-6

Guo, M., Chai, F., Xiu, P., Li, S., & Rao, S. (2015). Impacts of mesoscale eddies in the South China Sea on biogeochemical cycles. Ocean Dynamics, 65(9–10), 1335–1352. https://doi.org/10.1007/s10236-015-0867-1

Hai, D.-N., Lam, N.-N., & Dippner, J. W. (2010). Development of Phaeocystis globosa blooms in the upwelling waters of the South Central coast of Viet Nam. Journal of Marine Systems, 83(3–4), 253–261. https://doi.org/10.1016/j.jmarsys.2010.04.015

Haijun, Y., Qinyu, L., & Xujing, J. (1999). On the upper oceanic heat budget in the south china sea:Annual Cycle. Advances in Atmospheric Sciences, 16(4), 619–629. https://doi.org/10.1007/s00376-999-0036-x

He, Z. G., D. X. Wang, and J. Y. Hu (2002), Features of eddy kinetic energy and variations of upper circulation in the South China Sea, Acta Oceanol. Sin., 21(2), 305–314.

Hein, H. (2008). *Vietnam Upwelling-Analysis of the upwelling and related processes in the coastal area off South Vietnam* (Doctoral dissertation, Staats-und Universitätsbibliothek Hamburg Carl von Ossietzky).

Hendershott, M. C. (1972). The effects of solid earth deformation on global ocean tides. Geophysical Journal International, 29(4), 389–402. https://doi.org/10.1111/j.1365-246x.1972.tb06167.x

REFERENCES

Herrmann, M., Somot, S., Sevault, F., Estournel, C., & Déqué, M. (2008). Modeling the deep convection in the northwestern Mediterranean Sea using an eddy-permitting and an eddy-resolving model: Case study of winter 1986–1987. Journal of Geophysical Research, 113(C4). https://doi.org/10.1029/2006jc003991

Herrmann, M. J., & Somot, S. (2008). Relevance of ERA40 dynamical downscaling for modeling deep convection in the Mediterranean Sea. Geophysical Research Letters, 35(4). https://doi.org/10.1029/2007gl032442

Ho, C.-R., Kuo, N.-J., Zheng, Q., & Soong, Y. S. (2000). Dynamically active areas in the South China Sea detected from TOPEX/POSEIDON satellite altimeter data. Remote Sensing of Environment, 71(3), 320–328. https://doi.org/10.1016/s0034-4257(99)00094-2

Ho, C.-R., Zheng, Q., Soong, Y. S., Kuo, N.-J., & Hu, J.-H. (2000). Seasonal variability of sea surface height in the South China Sea observed with TOPEX/Poseidon altimeter data. Journal of Geophysical Research: Oceans, 105(C6), 13981–13990. https://doi.org/10.1029/2000jc900001

Holland, W. R. (1978). The role of mesoscale eddies in the general circulation of the ocean—numerical experiments using a wind-driven quasi-geostrophic model. Journal of Physical Oceanography, 8(3), 363–392. https://doi.org/10.1175/1520-0485(1978)008<0363:tromei>2.0.co;2

Hong, H., Chen, C.-T. A., Jiang, Y., Lou, J.-Y., Chen, Z., & Zhu, J. (2011). Source water of two-pronged northward flow in the southern Taiwan Strait in summer. *Journal of Oceanography*, *67*(4), 385–393. https://doi.org/10.1007/s10872-011-0036-1

Hsin, Y.-C., Wu, C.-R., & Chao, S.-Y. (2012). An updated examination of the Luzon Strait transport. Journal of Geophysical Research: Oceans, 117(C3), n/a-n/a. https://doi.org/10.1029/2011jc007714

Hu, J., & Wang, X. H. (2016). Progress on upwelling studies in the China seas. Reviews of Geophysics, 54(3), 653–673. https://doi.org/10.1002/2015rg000505

Hu, J., Kawamura, H., Hong, H., & Qi, Y. (2000). A Review on the Currents in the South China Sea: Seasonal Circulation, South China Sea Warm Current and Kuroshio Intrusion. Journal of Oceanography, 56(6), 607–624. https://doi.org/10.1023/a:1011117531252

Hu, J. Y. (2003). Tidal front around the Hainan Island, northwest of the South China Sea. *Journal of Geophysical Research*, *108*(C11). https://doi.org/10.1029/2003jc001883

Hu, Z., Tan, Y., Song, X., Zhou, L., Lian, X., Huang, L., & He, Y. (2014). Influence of mesoscale eddies on primary production in the South China Sea during spring inter-monsoon period. Acta Oceanologica Sinica, 33(3), 118–128. https://doi.org/10.1007/s13131-014-0431-8

Huang, R. X. (2015). Heaving modes in the world oceans. Climate Dynamics, 45(11–12), 3563–3591. https://doi.org/10.1007/s00382-015-2557-6

Huang, S.-J. (2016). Impacts of coastal upwelling off east Vietnam on the regional winds system: An air-sea-land interaction. *Dynamics of Atmospheres and Oceans*, *76*, 105–115. https://doi.org/10.1016/j.dynatmoce.2016.10.002

Huang, Z., Du, Y., Wu, Y., & Xu, H. (2013). Asymmetric response of the South China Sea SST to El Niño and La Niña. Journal of Ocean University of China, 12(2), 272–278. https://doi.org/10.1007/s11802-013-2169-x

Huang, Z., Zong, Y., & Zhang, W. (2004). Coastal Inundation due to Sea Level Rise in the Pearl River Delta, China. Natural Hazards, 33(2), 247–264. https://doi.org/10.1023/b:nhaz.0000037038.18814.b0

Hwang, C., & Chen, S.-A. (2000). Circulations and eddies over the South China Sea derived from TOPEX/Poseidon altimetry. Journal of Geophysical Research: Oceans, 105(C10), 23943–23965. https://doi.org/10.1029/2000jc900092

Isoguchi, O., & Kawamura, H. (2006). MJO-related summer cooling and phytoplankton blooms in the South China Sea in recent years. Geophysical Research Letters, 33(16). https://doi.org/10.1029/2006gl027046

Jackett, D. R., McDougall, T. J., Feistel, R., Wright, D. G., & Griffies, S. M. (2006). Algorithms for density, potential temperature, conservative temperature, and the freezing temperature of seawater. Journal of Atmospheric and Oceanic Technology, 23(12), 1709–1728. https://doi.org/10.1175/jtech1946.1

Jennings, S., Kaiser, M., & Reynolds, J. D. (2001). *Marine fisheries ecology*. Wiley-Blackwell.

Jiang, Y., Chai, F., Wan, Z., Zhang, X., & Hong, H. (2011). Characteristics and mechanisms of the upwelling in the southern Taiwan Strait: A three-dimensional numerical model study. *Journal of Oceanography*, *67*(6), 699–708. https://doi.org/10.1007/s10872-011-0080-x

Jilan, S. (2004). Overview of the South China Sea circulation and its influence on the coastal physical oceanography outside the Pearl River Estuary. Continental Shelf Research, 24(16), 1745–1760. https://doi.org/10.1016/j.csr.2004.06.005

Jin, F.-F. (2003). Strong El Niño events and nonlinear dynamical heating. Geophysical Research Letters, 30(3). https://doi.org/10.1029/2002gl016356

Krempf A., Chevey P. 1934. The great currents of the China Sea and hydrologic sections of the shores of French Indo-China. Fifth Pacific Science Congress. Proceeding, Vol. I, 693-696. Canada

Kuo, N. (2000). Satellite observation of upwelling along the western coast of the South China Sea. Remote Sensing of Environment, 74(3), 463–470. https://doi.org/10.1016/s0034-4257(00)00138-3

Kuo, N.-J., Zheng, Q., and Ho, C.-R. (2004). Response of Vietnam coastal upwelling to the 1997–1998 ENSO event observed by multisensor data. *Remote Sensing of Environment*, *89*(1), 106–115. https://doi.org/10.1016/j.rse.2003.10.009

LaFond, E.C., 1963. Physical oceanography and its relation to the marine organic production in the South China Sea. In: Ecology of the Gulf of Thailand and the South China Sea. A report on the results of the NAGA expedition, 1959-1961. Southeast Asia research program, University of California, Scripps Institution of Oceanography, La Jolla, pp. 5-33

Large, W. G., & Yeager, S. (2003). Diurnal to decadal global forcing for ocean and sea-ice models: The data sets and flux climatologies (No. NCAR/TN-460+STR). In University Corporation for Atmospheric Research (pp. 1–105).

Lau, K. M., & Yang, S. (1997). Climatology and interannual variability of the southeast asian summer monsoon. Advances in Atmospheric Sciences, 14(2), 141–162. https://doi.org/10.1007/s00376-997-0016-y

REFERENCES

Lau, N.-C., & Nath, M. J. (2009). A model investigation of the role of air–sea interaction in the climatological evolution and enso-related variability of the summer monsoon over the south china sea and western north pacific. Journal of Climate, 22(18), 4771–4792. https://doi.org/10.1175/2009jcli2758.1

Lawrence, D. M., & Webster, P. J. (2002). The boreal summer intraseasonal oscillation: Relationship between northward and eastward movement of convection. Journal of the Atmospheric Sciences, 59(9), 1593–1606. https://doi.org/10.1175/1520-0469(2002)059<1593:tbsior>2.0.co;2

Leonard, B. P. (1979). A stable and accurate convective modelling procedure based on quadratic upstream interpolation. Computer Methods in Applied Mechanics and Engineering, 19(1), 59–98. https://doi.org/10.1016/0045-7825(79)90034-3

Li, L., & Qu, T. (2006). Thermohaline circulation in the deep South China Sea basin inferred from oxygen distributions. Journal of Geophysical Research, 111(C5). https://doi.org/10.1029/2005jc003164

Li, L., Nowlin, W. D., Jr., & Jilan, S. (1998). Anticyclonic rings from the Kuroshio in the South China Sea. Deep Sea Research Part I: Oceanographic Research Papers, 45(9), 1469–1482. https://doi.org/10.1016/s0967-0637(98)00026-0

Li, Y., Han, W., and Zhang, L. (2017). Enhanced decadal warming of the Southeast Indian Ocean during the recent global surface warming slowdown. *Geophysical Research Letters*, *44*(19), 9876–9884. https://doi.org/10.1002/2017gl075050

Li, Y., Han, W., Wilkin, J. L., Zhang, W. G., Arango, H., Zavala-Garay, J., Levin, J., and Castruccio, F. S. (2014). Interannual variability of the surface summertime eastward jet in the South China Sea. *Journal of Geophysical Research: Oceans*, *119*(10), 7205–7228. https://doi.org/10.1002/2014jc010206

Lin, H., Liu, Z., Hu, J., Menemenlis, D., & Huang, Y. (2020). Characterizing meso- to submesoscale features in the South China Sea. *Progress in Oceanography*, *188*, 102420. https://doi.org/10.1016/j.pocean.2020.102420

Liu, F., Ouyang, Y., Wang, B., Yang, J., Ling, J., & Hsu, P.-C. (2020). Seasonal evolution of the intraseasonal variability of China summer precipitation. Climate Dynamics, 54(11–12), 4641–4655. https://doi.org/10.1007/s00382-020-05251-0

Liu, Y., R. H. Weisberg, and Y. Yuan (2008), Patterns of upper layer circulation variability in the South China Sea from satellite altimetry using the self-organizing map, Acta Oceanol. Sin., 27(suppl.), 129–144.

Liu, Z., Yang, H., & Liu, Q. (2001). Regional dynamics of seasonal variability in the South China Sea. Journal of Physical Oceanography, 31(1), 272–284. https://doi.org/10.1175/1520-0485(2001)031<0272:rdosvi>2.0.co;2

Loick, N., Dippner, J., Doan, H. N., Liskow, I., & Voss, M. (2007). Pelagic nitrogen dynamics in the Vietnamese upwelling area according to stable nitrogen and carbon isotope data. Deep Sea Research Part I: Oceanographic Research Papers, 54(4), 596–607. https://doi.org/10.1016/j.dsr.2006.12.009

Loick-Wilde, N., Bombar, D., Doan, H. N., Nguyen, L. N., Nguyen-Thi, A. M., Voss, M., and Dippner, J. W. (2017). Microplankton biomass and diversity in the Vietnamese upwelling area during SW monsoon under normal conditions and after an ENSO event. *Progress in Oceanography*,

153, 1–15. https://doi.org/10.1016/j.pocean.2017.04.007

Lü, X., Qiao, F., Wang, G., Xia, C., & Yuan, Y. (2008). Upwelling off the west coast of Hainan Island in summer: Its detection and mechanisms. *Geophysical Research Letters*, *35*(2). https://doi.org/10.1029/2007gl032440

Lyard, F., Lefevre, F., Letellier, T., & Francis, O. (2006). Modelling the global ocean tides: Modern insights from FES2004. Ocean Dynamics, 56(5–6), 394–415. https://doi.org/10.1007/s10236-006-0086-x

Marsaleix, P., Auclair, F., & Estournel, C. (2006). Considerations on open boundary conditions for regional and Coastal Ocean models. Journal of Atmospheric and Oceanic Technology, 23(11), 1604–1613. https://doi.org/10.1175/jtech1930.1

Marsaleix, P., Auclair, F., & Estournel, C. (2009). Low-order pressure gradient schemes in sigma coordinate models: The seamount test revisited. Ocean Modelling, 30(2–3), 169–177. https://doi.org/10.1016/j.ocemod.2009.06.011

Marsaleix, P., Auclair, F., Duhaut, T., Estournel, C., Nguyen, C., & Ulses, C. (2012). Alternatives to the Robert–Asselin filter. Ocean Modelling, 41, 53–66. https://doi.org/10.1016/j.ocemod.2011.11.002

Marsaleix, P., Auclair, F., Floor, J. W., Herrmann, M. J., Estournel, C., Pairaud, I., & Ulses, C. (2008). Energy conservation issues in sigma-coordinate free-surface ocean models. Ocean Modelling, 20(1), 61–89. https://doi.org/10.1016/j.ocemod.2007.07.005

Marsaleix, P., Michaud, H., & Estournel, C. (2019). 3D phase-resolved wave modelling with a non-hydrostatic ocean circulation model. Ocean Modelling, 136, 28–50. https://doi.org/10.1016/j.ocemod.2019.02.002

Marsaleix, Patrick, Auclair, F., & Estournel, C. (2009). Low-order pressure gradient schemes in sigma coordinate models: The seamount test revisited. Ocean Modelling, 30(2–3), 169–177. https://doi.org/10.1016/j.ocemod.2009.06.011

Marsaleix, Patrick, Auclair, F., Duhaut, T., Estournel, C., Nguyen, C., & Ulses, C. (2012). Alternatives to the Robert–Asselin filter. Ocean Modelling, 41, 53–66. https://doi.org/10.1016/j.ocemod.2011.11.002

Marsaleix, Patrick, Auclair, F., Floor, J. W., Herrmann, M. J., Estournel, C., Pairaud, I., & Ulses, C. (2008). Energy conservation issues in sigma-coordinate free-surface ocean models. Ocean Modelling, 20(1), 61–89. https://doi.org/10.1016/j.ocemod.2007.07.005

Marsaleix, Patrick, Michaud, H., & Estournel, C. (2019). 3D phase-resolved wave modelling with a non-hydrostatic ocean circulation model. Ocean Modelling, 136, 28–50. https://doi.org/10.1016/j.ocemod.2019.02.002

Masumoto, Y., Miyazawa, Y., Tsumune, D., Tsubono, T., Kobayashi, T., Kawamura, H., Estournel, C., Marsaleix, P., Lanerolle, L., Mehra, A., & Garraffo, Z. D. (2012). Oceanic dispersion simulations of 137cs released from the Fukushima daiichi nuclear power plant. Elements, 8(3), 207–212. https://doi.org/10.2113/gselements.8.3.207

McPhaden, M. J., & Zhang, X. (2009). Asymmetry in zonal phase propagation of ENSO sea surface temperature anomalies. Geophysical Research Letters, 36(13). https://doi.org/10.1029/2009gl038774

REFERENCES

Michaud, H., Marsaleix, P., Leredde, Y., Estournel, C., Bourrin, F., Lyard, F., Mayet, C., & Ardhuin, F. (2011). Three-dimensional modelling of wave-induced current from the surf zone to the inner shelf. http://dx.doi.org/10.5194/osd-8-2417-2011

Morimoto, A., K. Yoshimoto, and T. Yanagi (2000), Characteristics of sea surface circulation and eddy field in the South China Sea revealed by satellite altimetric data, J. Oceanogr.,56 (3), 331–344, doi:10.1023/A:1011159818531.

Nan, F., He, Z., Zhou, H., & Wang, D. (2011). Three long-lived anticyclonic eddies in the northern South China Sea. Journal of Geophysical Research, 116(C5). https://doi.org/10.1029/2010jc006790

Ngo, M., and Hsin, Y. (2021). Impacts of wind and current on the interannual variation of the summertime upwelling off southern Vietnam in the South China Sea. *Journal of Geophysical Research: Oceans*, *126*(6). https://doi.org/10.1029/2020jc016892

Ni, Q., Zhai, X., Wilson, C., Chen, C., & Chen, D. (2021). Submesoscale eddies in the South China Sea. Geophysical Research Letters, 48(6). https://doi.org/10.1029/2020gl091555

Oberhuber, J. M., 1988: An atlas based on COADS dataset: The budget of heat, buoyancy and turbulent kinetic energy at the surface of the Global Ocean. MPI Rep. 15, 1999 pp.

Ouillon, S. (2014). VITEL-SOUTH cruise, RV Alis. https://doi.org/10.17600/14004200

Pairaud, I., Staquet, C., Sommeria, J., & Mahdizadeh, M. M. (2010). Generation of harmonics and sub-harmonics from an internal tide in a uniformly stratified fluid: Numerical and laboratory experiments. IUTAM Symposium on Turbulence in the Atmosphere and Oceans, 51–62. http://dx.doi.org/10.1007/978-94-007-0360-5_5

Pairaud, I. L., Lyard, F., Auclair, F., Letellier, T., & Marsaleix, P. (2008). Dynamics of the semi-diurnal and quarter-diurnal internal tides in the Bay of Biscay. Part 1: Barotropic tides. Continental Shelf Research, 28(10–11), 1294–1315. https://doi.org/10.1016/j.csr.2008.03.004

Park, Y.-G., & Choi, A. (2016). Long-term changes of South China Sea surface temperatures in winter and summer. Continental Shelf Research, 143, 185–193. https://doi.org/10.1016/j.csr.2016.07.019

Penduff, T., Juza, M., Barnier, B., Zika, J., Dewar, W. K., Treguier, A.-M., Molines, J.-M., & Audiffren, N. (2011). Sea level expression of intrinsic and forced ocean variabilities at interannual time scales. *Journal of Climate*, *24*(21), 5652–5670. https://doi.org/10.1175/jcli-d-11-00077.1

Peng, D., Palanisamy, H., Cazenave, A., & Meyssignac, B. (2013). Interannual sea level variations in the South China Sea over 1950–2009. Marine Geodesy, 36(2), 164–182. https://doi.org/10.1080/01490419.2013.771595

Perry, G. D., Duffy, P. B., & Miller, N. L. (1996). An extended data set of river discharges for validation of general circulation models. Journal of Geophysical Research: Atmospheres, 101(D16), 21339–21349. https://doi.org/10.1029/96jd00932

Petrichenko, S. A. (2010). Using the databases of the ocean climate laboratory of the NODC NOAA for constructing climatology maps by the example of the upwelling area at the coast of Southern Vietnam. Russian Meteorology and Hydrology, 35(7), 464–467. https://doi.org/10.3103/s1068373910070058

Phan, H. M., Ye, Q., Reniers, A. J. H. M., & Stive, M. J. F. (2019). Tidal wave propagation along The Mekong deltaic coast. Estuarine, Coastal and Shelf Science, 220, 73–98. https://doi.org/10.1016/j.ecss.2019.01.026

Piton, V., Herrmann, M., Marsaleix, P., Duhaut, T., Ngoc, T. B., Tran, M. C., Shearman, K., & Ouillon, S. (2021). Influence of winds, geostrophy and typhoons on the seasonal variability of the circulation in the Gulf of Tonkin: A high-resolution 3D regional modeling study. Regional Studies in Marine Science, 45, 101849. https://doi.org/10.1016/j.rsma.2021.101849

Piton, V. (2019). Du Fleuve Rouge au Golfe du Tonkin: dynamique et transport sédimentaire le long du continuum estuaire-zone côtière. [Doctoral dissertation]. Université de Toulouse, Toulouse, France.

Qiao, F. L., and X. G. Lü (2008), Coastal upwelling in the South China Sea, in Satellite Remote Sensing of South China Sea, edited by A. K. Liu, C. R. Ho, and C. T. Liu, pp. 135–158, Tingmao Publish Co, Taiwan.

Qin, H., Huang, R. X., Wang, W., & Xue, H. (2016). Regulation of South China Sea throughflow by pressure difference. Journal of Geophysical Research: Oceans, 121(6), 4077–4096. https://doi.org/10.1002/2015jc011177

Qiu, B., & Lukas, R. (1996). Seasonal and interannual variability of the North Equatorial Current, the Mindanao Current, and the Kuroshio along the Pacific western boundary. Journal of Geophysical Research: Oceans, 101(C5), 12315–12330. https://doi.org/10.1029/95jc03204

Qu, T., & Lukas, R. (2003). The bifurcation of the north equatorial current in the Pacific*. Journal of Physical Oceanography, 33(1), 5–18. https://doi.org/10.1175/1520-0485(2003)033<0005:tbotne>2.0.co;2

Qu, T., & Song, Y. T. (2009). Mindoro Strait and Sibutu Passage transports estimated from satellite data. Geophysical Research Letters, 36(9). https://doi.org/10.1029/2009gl037314

Qu, T., Du, Y., & Sasaki, H. (2006). South China Sea throughflow: A heat and freshwater conveyor. Geophysical Research Letters, 33(23). https://doi.org/10.1029/2006gl028350

Qu, T., Du, Y., Meyers, G., Ishida, A., & Wang, D. (2005). Connecting the tropical Pacific with Indian Ocean through South China Sea. Geophysical Research Letters, 32(24). https://doi.org/10.1029/2005gl024698

Qu, T., Girton, J. B., & Whitehead, J. A. (2006). Deepwater overflow through Luzon Strait. Journal of Geophysical Research, 111(C1). https://doi.org/10.1029/2005jc003139

Qu, T., Kim, Y. Y., Yaremchuk, M., Tozuka, T., Ishida, A., & Yamagata, T. (2004). Can Luzon Strait transport play a role in conveying the impact of ENSO to the South China Sea?*. Journal of Climate, 17(18), 3644–3657. https://doi.org/10.1175/1520-0442(2004)017<3644:clstpa>2.0.co;2

Qu, T., Mitsudera, H., & Yamagata, T. (2000). Intrusion of the North Pacific waters into the South China Sea. Journal of Geophysical Research: Oceans, 105(C3), 6415–6424. https://doi.org/10.1029/1999jc900323

Qu, T. (2000). Upper-Layer circulation in the South China Sea*. Journal of Physical Oceanography, 30(6), 1450–1460. https://doi.org/10.1175/1520-0485(2000)030<1450:ulcits>2.0.co;2

REFERENCES

Quan, Q., Xue, H., Qin, H., Zeng, X., & Peng, S. (2016). Features and variability of the South China Sea western boundary current from 1992 to 2011. Ocean Dynamics, 66(6–7), 795–810. https://doi.org/10.1007/s10236-016-0951-1

Ray, R. D., & Zaron, E. D. (2011). Non-stationary internal tides observed with satellite altimetry. Geophysical Research Letters, 38(17), n/a-n/a. https://doi.org/10.1029/2011gl048617

Ray, R. D., & Zaron, E. D. (2016). M2 internal tides and their observed wavenumber spectra from satellite altimetry. Journal of Physical Oceanography, 46(1), 3–22. https://doi.org/10.1175/jpo-d-15-0065.1

Reffray, G., Fraunié, P., & Marsaleix, P. (2004). Secondary flows induced by wind forcing in the Rhône region of freshwater influence. Ocean Dynamics, 54(2), 179–196. https://doi.org/10.1007/s10236-003-0079-y

Richardson, P. L. (1983). Eddy kinetic energy in the North Atlantic from surface drifters. Journal of Geophysical Research, 88(C7), 4355. https://doi.org/10.1029/jc088ic07p04355

Robinson, M. K. (1961). The physical oceanography of the Gulf of Thailand, Naga Expedition. Naga Report Volume 3, Part I, Scripps Institution of Oceanography, La Jolla, California, 5-10.

Rogowski, P., Zavala-Garay, J., Shearman, K., Terrill, E., Wilkin, J., & Lam, T. H. (2019). Air-Sea-Land forcing in the Gulf of Tonkin: Assessing seasonal variability using modern tools. Oceanography, 32(2), 150–161. https://doi.org/10.5670/oceanog.2019.223

Rojana-anawat, P., Pradit, S., Sukramongkol, N., & Siriraksophon, S. (2001). Temperature, salinity, dissolved oxygen and water masses of Vietnamese waters. Proceedings of the SEAFDEC Seminar on Fisheries Resources in the South China Sea, Area 4: Vietnamese Waters, 346–355.

Rong, Z., Liu, Y., Zong, H., & Cheng, Y. (2007). Interannual sea level variability in the South China Sea and its response to ENSO. Global and Planetary Change, 55(4), 257–272. https://doi.org/10.1016/j.gloplacha.2006.08.001

Saha, S., Moorthi, S., Pan, H.-L., Wu, X., Wang, J., Nadiga, S., Tripp, P., Kistler, R., Woollen, J., Behringer, D., Liu, H., Stokes, D., Grumbine, R., Gayno, G., Wang, J., Hou, Y.-T., Chuang, H., Juang, H.-M. H., Sela, J., … Goldberg, M. (2010). The NCEP climate forecast system reanalysis. Bulletin of the American Meteorological Society, 91(8), 1015–1058. https://doi.org/10.1175/2010bams3001.1

Saha, S., Moorthi, S., Pan, H.-L., Wu, X., Wang, J., Nadiga, S., Tripp, P., Kistler, R., Woollen, J., Behringer, D., Liu, H., Stokes, D., Grumbine, R., Gayno, G., Wang, J., Hou, Y.-T., Chuang, H., Juang, H.-M. H., Sela, J., … Goldberg, M. (2010). The NCEP climate forecast system reanalysis. *Bulletin of the American Meteorological Society*, *91*(8), 1015–1058. https://doi.org/10.1175/2010bams3001.1

Saito, Y., Nguyen, V. L., Ta, T. K. O., Tamura, T., Kanai, Y., Nakashima, R. (2015). Tide and river influences on distributary channels of the Mekong River delta. American Geophysical Union, Fall Meeting 2015, abstract #GC41F-1148.

Sarhan, T., Lafuente, J. G., Vargas, M., Vargas, J. M., & Plaza, F. (2000). Upwelling mechanisms in the northwestern Alboran Sea. *Journal of Marine Systems*, *23*(4), 317–331. https://doi.org/10.1016/s0924-7963(99)00068-8

Sérazin, G., Meyssignac, B., Penduff, T., Terray, L., Barnier, B., & Molines, J.-M. (2016). Quantifying uncertainties on regional sea level change induced by multidecadal intrinsic oceanic

variability. *Geophysical Research Letters*, *43*(15), 8151–8159. https://doi.org/10.1002/2016gl069273

Sérazin, G., Penduff, T., Grégorio, S., Barnier, B., Molines, J.-M., & Terray, L. (2015). Intrinsic variability of sea level from global ocean simulations: Spatiotemporal scales. Journal of Climate, 28(10), 4279–4292. https://doi.org/10.1175/jcli-d-14-00554.1

Shaw, P.-T., & Chao, S.-Y. (1994). Surface circulation in the South China Sea. Deep Sea Research Part I: Oceanographic Research Papers, 41(11–12), 1663–1683. https://doi.org/10.1016/0967-0637(94)90067-1

Shaw, P.-T., Chao, S.-Y., & Fu, L.-L. (1999). Sea surface height variations in the South China Sea from satellite altimetry. Oceanologica Acta, 22(1), 1–17. https://doi.org/10.1016/s0399-1784(99)80028-0

Shaw, P.-T. (1991). The seasonal variation of the intrusion of the Philippine sea water into the South China Sea. Journal of Geophysical Research: Oceans, 96(C1), 821–827. https://doi.org/10.1029/90jc02367

Shu, Y., Xue, H., Wang, D., Xie, Q., Chen, J., Li, J., Chen, R., He, Y., & Li, D. (2016). Observed evidence of the anomalous South China Sea western boundary current during the summers of 2010 and 2011. Journal of Geophysical Research: Oceans, 121(2), 1145–1159. https://doi.org/10.1002/2015jc011434

Siddorn, J. R., & Furner, R. (2013). An analytical stretching function that combines the best attributes of geopotential and terrain-following vertical coordinates. Ocean Modelling, 66, 1–13. https://doi.org/10.1016/j.ocemod.2013.02.001

Siew, J. H., Tangang, F. T., & Juneng, L. (2013). Evaluation of CMIP5 coupled atmosphere-ocean general circulation models and projection of the Southeast Asian winter monsoon in the 21st century. International Journal of Climatology, 34(9), 2872–2884. https://doi.org/10.1002/joc.3880

Stewart, R. H. (2008). Introduction to physical oceanography. Orange Grove Text Plus.

Stommel, H., & Arons, A. B. (1960). On the abyssal circulation of the world ocean — II. An idealized model of the circulation pattern and amplitude in oceanic basins. Deep Sea Research (1953), 6, 217–233. https://doi.org/10.1016/0146-6313(59)90075-9

Su, J., Xu, M., Pohlmann, T., Xu, D., & Wang, D. (2013). A western boundary upwelling system response to recent climate variation (1960–2006). *Continental Shelf Research*, *57*, 3–9. https://doi.org/10.1016/j.csr.2012.05.010

Sverdrup, H. U., M. W. Johnson, and R. H. Fleming, 1942: The Oceans, their physics, chemistry, and general biology. Printice-Hall, Inc., 1087p

Tan, W., Wang, X., Wang, W., Wang, C., & Zuo, J. (2016). Different responses of sea surface temperature in the South China Sea to various el niño events during boreal autumn. Journal of Climate, 29(3), 1127–1142. https://doi.org/10.1175/jcli-d-15-0338.1

Tang, D., Kawamura, H., Van Dien, T., & Lee, M. (2004). Offshore phytoplankton biomass increase and its oceanographic causes in the South China Sea. Marine Ecology Progress Series, 268, 31–41. https://doi.org/10.3354/meps268031

Tian, J., Yang, Q., Liang, X., Xie, L., Hu, D., Wang, F., & Qu, T. (2006). Observation of Luzon Strait transport. Geophysical Research Letters, 33(19). https://doi.org/10.1029/2006gl026272

REFERENCES

Tozuka, T., Qu, T., & Yamagata, T. (2007). Dramatic impact of the South China Sea on the Indonesian Throughflow. Geophysical Research Letters, 34(12). https://doi.org/10.1029/2007gl030420

Tranchant, B., Reffray, G., Greiner, E., Nugroho, D., Koch-Larrouy, A., & Gaspar, P. (2016). Evaluation of an operational ocean model configuration at 1/12° spatial resolution for the Indonesian seas (NEMO2.3/INDO12) – Part 1: Ocean physics. Geoscientific Model Development, 9(3), 1037–1064. https://doi.org/10.5194/gmd-9-1037-2016

Trinh, B. N. (2020). Cycles de l'eau, de la chaleur et du sel en Mer de Chine Méridionale, de la variation saisonnière à la variabilité interannuelle : modélisation océanique à haute résolution et à bilan fermé [Doctoral dissertation]. Université de Toulouse, Toulouse, France.

Ulses, C., Estournel, C., Bonnin, J., Durrieu de Madron, X., & Marsaleix, P. (2008a). Impact of storms and dense water cascading on shelf-slope exchanges in the Gulf of Lion (NW Mediterranean). Journal of Geophysical Research, 113(C2). https://doi.org/10.1029/2006jc003795

Ulses, C., Estournel, C., Puig, P., Durrieu de Madron, X., & Marsaleix, P. (2008b). Dense shelf water cascading in the northwestern Mediterranean during the cold winter 2005: Quantification of the export through the Gulf of Lion and the Catalan margin. Geophysical Research Letters, 35(7), n/a-n/a. https://doi.org/10.1029/2008gl033257

Uu, D. V., & Brankart, J.-M. (1997). Seasonal variation of temperature and salinity fields and water masses in the Bien Dong (South China) sea. Mathematical and Computer Modelling, 26(12), 97–113. https://doi.org/10.1016/s0895-7177(97)00243-4

Waldman, R., Somot, S., Herrmann, M., Bosse, A., Caniaux, G., Estournel, C., Houpert, L., Prieur, L., Sevault, F., & Testor, P. (2017). Modeling the intense 2012-2013 dense water formation event in the northwestern Mediterranean Sea: Evaluation with an ensemble simulation approach. Journal of Geophysical Research: Oceans, 122(2), 1297–1324. https://doi.org/10.1002/2016jc012437

Waldman, R., Somot, S., Herrmann, M., Sevault, F., & Isachsen, P. E. (2018). On the chaotic variability of deep convection in the Mediterranean Sea. *Geophysical Research Letters*, *45*(5), 2433–2443. https://doi.org/10.1002/2017gl076319

Waldman, R., Somot, S., Herrmann, M., Testor, P., Estournel, C., Sevault, F., Prieur, L., Mortier, L., Coppola, L., Taillandier, V., Conan, P., & Dausse, D. (2016a). Estimating dense water volume and its evolution for the year 2012-2013 in the Northwestern Mediterranean Sea: An observing system simulation experiment approach. Journal of Geophysical Research: Oceans, 121(9), 6696–6716. https://doi.org/10.1002/2016jc011694

Waldman, R., Somot, S., Herrmann, M., Testor, P., Estournel, C., Sevault, F., Prieur, L., Mortier, L., Coppola, L., Taillandier, V., Conan, P., & Dausse, D. (2016b). Estimating dense water volume and its evolution for the year 2012-2013 in the Northwestern Mediterranean Sea: An observing system simulation experiment approach. Journal of Geophysical Research: Oceans, 121(9), 6696–6716. https://doi.org/10.1002/2016jc011694

Wang, B., & Rui, H. (1990). Dynamics of the coupled moist kelvin–rossby wave on an equatorialβ-plane. Journal of the Atmospheric Sciences, 47(4), 397–413. https://doi.org/10.1175/1520-0469(1990)047<0397:dotcmk>2.0.co;2

Wang, C., Wang, W., Wang, D., & Wang, Q. (2006a). Interannual variability of the South China Sea associated with El Niño. *Journal of Geophysical Research*, *111*(C3). https://doi.org/10.1029/2005jc003333

Wang, D., Liu, Q., Huang, R. X., Du, Y., & Qu, T. (2006b). Interannual variability of the South China Sea throughflow inferred from wind data and an ocean data assimilation product. *Geophysical Research Letters*, *33*(14). https://doi.org/10.1029/2006gl026316

Wang, G., Chen, D., & Su, J. (2006). Generation and life cycle of the dipole in the South China Sea summer circulation. Journal of Geophysical Research, 111(C6). https://doi.org/10.1029/2005jc003314

Wang, G., Su, J., & Chu, P. C. (2003). Mesoscale eddies in the South China Sea observed with altimeter data. Geophysical Research Letters, 30(21). https://doi.org/10.1029/2003gl018532

Wang, G., Xie, S.-P., Qu, T., & Huang, R. X. (2011). Deep South China Sea circulation. *Geophysical Research Letters*, *38*(5), n/a-n/a. https://doi.org/10.1029/2010gl046626

Wang, H., & He, S. (2012). Weakening relationship between East Asian winter monsoon and ENSO after the mid-1970s. Chinese Science Bulletin, 57(27), 3535–3540. https://doi.org/10.1007/s11434-012-5285-x

Wang, H., Saito, Y., Zhang, Y., Bi, N., Sun, X., & Yang, Z. (2011). Recent changes of sediment flux to the western Pacific Ocean from major rivers in East and Southeast Asia. Earth-Science Reviews, 108(1–2), 80–100. https://doi.org/10.1016/j.earscirev.2011.06.003

Wang, J., Hong, H., Jiang, Y., Chai, F., & Yan, X.-H. (2013). Summer nitrogenous nutrient transport and its fate in the Taiwan Strait: A coupled physical-biological modeling approach. Journal of Geophysical Research: Oceans, 118(9), 4184–4200. https://doi.org/10.1002/jgrc.20300

Wang, L., C. J. Koblinsky, and S. Howden (2000b), Mesoscale variability in the South China Sea from the TOPEX/Poseidon altimetry data, Deep Sea Res. Part I Oceanogr. Res. Pap., 47 (4), 681–708, doi:10.1016/S0967-0637(99)00068-0

Wang, Q., Cui, H., Zhang, S., & Hu, D. (2009). Water transports through the four main straits around the South China Sea. Chinese Journal of Oceanology and Limnology, 27(2), 229–236. https://doi.org/10.1007/s00343-009-9142-y

Wang, X., Liu, Z., & Peng, S. (2017). Impact of tidal mixing on water mass transformation and circulation in the South China Sea. *Journal of Physical Oceanography*, *47*(2), 419–432. https://doi.org/10.1175/jpo-d-16-0171.1

Wang, Y., G. Fang, Z. Wei, F. Qiao, and H. Chen (2006c), Interannual variation of the South China Sea circulation and its relation to El Nino, as seen from a variable grid global ocean model, J. Geophys. Res. Ocean. , 111 (11), 1–15, doi:10.1029/2005JC003269.

Wang, Y., Xu, T., Li, S., Susanto, R. D., Agustiadi, T., Trenggono, M., Tan, W., & Wei, Z. (2019). Seasonal variation of water transport through the Karimata Strait. Acta Oceanologica Sinica, 38(4), 47–57. https://doi.org/10.1007/s13131-018-1224-2

Wang, Y.-L., and Wu, C.-R. (2020). Nonstationary El Niño teleconnection on the post-summer upwelling off Vietnam. *Scientific Reports*, *10*(1). https://doi.org/10.1038/s41598-020-70147-2

Wei, Z., Fang, G., Xu, T., Wang, Y., & Lian, Z. (2016). Seasonal variability of the isopycnal surface circulation in the South China Sea derived from a variable-grid global ocean circulation model. *Acta Oceanologica Sinica*, *35*(1), 11-20.

Woo, H.-J., & Park, K.-A. (2020). Inter-Comparisons of daily sea surface temperatures and in-situ temperatures in the coastal regions. Remote Sensing, 12(10), 1592. https://doi.org/10.3390/rs12101592

REFERENCES

Wu, C.-R., & Chiang, T.-L. (2007). Mesoscale eddies in the northern South China Sea. Deep Sea Research Part II: Topical Studies in Oceanography, 54(14–15), 1575–1588. https://doi.org/10.1016/j.dsr2.2007.05.008

Wu, C.-R., Shaw, P.-T., & Chao, S.-Y. (1998). Seasonal and interannual variations in the velocity field of the South China Sea. Journal of Oceanography, 54(4), 361–372. https://doi.org/10.1007/bf02742620

Wu, C.-R., Wang, L.-C., Wang, Y.-L., Lin, Y.-F., Chiang, T.-L., & Hsin, Y.-C. (2019). Coherent response of vietnam and sumatra-java upwellings to cross-equatorial winds. Scientific Reports, 9(1). https://doi.org/10.1038/s41598-019-40246-w

Wu, J., Ren, H. L., Xu, X. F., and Gao, L. (2018). Seasonal modulation of MJO's impact on precipitation in China and its dynamical-statistical downscaling prediction. Meteor. Mon. 44, 737–751. doi: 10.7519/j.issn.1000-0526.2018.06.002

Wu, R., & Wang, B. (2000). Interannual variability of summer monsoon onset over the western north pacific and the underlying processes. Journal of Climate, 13(14), 2483–2501. https://doi.org/10.1175/1520-0442(2000)013<2483:ivosmo>2.0.co;2

Wu, X., Okumura, Y. M., and DiNezio, P. N. (2019). What controls the duration of El Niño and La Niña events? *Journal of Climate*, *32*(18), 5941–5965. https://doi.org/10.1175/jcli-d-18-0681.1

Wyrtki, K. (1961). Physical oceanography of the southeast Asian waters. Scientific Results of Marine Investigations of the South China Sea and the Gulf of Thailand. In Scripps Institution of Oceanography. La Jolla, California: ICAc Press (pp. 1–122). NAGA Rep. 2.

Xie, S.-P., Chang, C.-H., Xie, Q., & Wang, D. (2007). Intraseasonal variability in the summer South China Sea: Wind jet, cold filament, and recirculations. Journal of Geophysical Research, 112(C10). https://doi.org/10.1029/2007jc004238

Xie, S.-P., Xie, Q., Wang, D., and Liu, W. T. (2003). Summer upwelling in the South China Sea and its role in regional climate variations. *Journal of Geophysical Research*, *108*(C8). https://doi.org/10.1029/2003jc001867

Xie, S.-P. (2003). Summer upwelling in the South China Sea and its role in regional climate variations. Journal of Geophysical Research, 108(C8). https://doi.org/10.1029/2003jc001867

Xiu, P., Chai, F., Shi, L., Xue, H., & Chao, Y. (2010). A census of eddy activities in the South China Sea during 1993–2007. Journal of Geophysical Research, 115(C3). https://doi.org/10.1029/2009jc005657

Xu, F.-H., & Oey, L.-Y. (2014). State analysis using the Local Ensemble Transform Kalman Filter (LETKF) and the three-layer circulation structure of the Luzon Strait and the South China Sea. *Ocean Dynamics*, *64*(6), 905–923. https://doi.org/10.1007/s10236-014-0720-y

Xu, X. (1982), The general descriptions of the horizontal circulation in the South China Sea, in Proceedings of the 1980 Symposium on Hydrometeorology, Chinese Society of Oceanology and Limnology, pp. 137–145, Science Press.

Xue, H. (2004). Kuroshio intrusion and the circulation in the South China Sea. Journal of Geophysical Research, 109(C2). https://doi.org/10.1029/2002jc001724

Yanagi, T., Morimoto, A., & Ichikawa, K. (1997). Co-tidal and Co-range Charts for the East China Sea and the Yellow Sea Derived from Satellite Altimetric Data. Journal of Oceanography, 53, 303–309.

Yang, Q., Nikurashin, M., Sasaki, H., Sun, H., & Tian, J. (2019). Dissipation of mesoscale eddies and its contribution to mixing in the northern South China Sea. Scientific Reports, 9(1). https://doi.org/10.1038/s41598-018-36610-x

Yaremchuk, M., & Qu, T. (2004). Seasonal variability of the large-scale currents near the Coast of the Philippines*. Journal of Physical Oceanography, 34(4), 844–855. https://doi.org/10.1175/1520-0485(2004)034<0844:svotlc>2.0.co;2

Yaremchuk, M., McCreary, J., Jr., Yu, Z., & Furue, R. (2009). The South China Sea throughflow retrieved from climatological data*. Journal of Physical Oceanography, 39(3), 753–767. https://doi.org/10.1175/2008jpo3955.1

Yasui, M., Uyeda, S., Murauchi, S., & Den, N. (1970). Current aspects of geophysical studies in the Kuroshio and its adjacent seas. In The Kuroshio (pp. 3–18). University of Hawaii Press. http://dx.doi.org/10.1515/9780824885830-002

Ye, A. L., & Robinson, I. S. (1983). Tidal dynamics in the South China Sea. Geophysical Journal International, 72(3), 691–707. https://doi.org/10.1111/j.1365-246x.1983.tb02827.x

Yi, D. L., Melnichenko, O., Hacker, P., & Potemra, J. (2020). Remote sensing of sea surface salinity variability in the South China Sea. Journal of Geophysical Research: Oceans, 125(12). https://doi.org/10.1029/2020jc016827

Yu, L., & Weller, R. A. (2007). Objectively analyzed air–sea heat fluxes for the global ice-free oceans (1981–2005). Bulletin of the American Meteorological Society, 88(4), 527–540. https://doi.org/10.1175/bams-88-4-527

Yu, Y., Zhang, H.-R., Jin, J., & Wang, Y. (2019). Trends of sea surface temperature and sea surface temperature fronts in the South China Sea during 2003–2017. Acta Oceanologica Sinica, 38(4), 106–115. https://doi.org/10.1007/s13131-019-1416-4

Yu, Z., Shen, S., McCreary, J. P., Yaremchuk, M., & Furue, R. (2007). South China Sea throughflow as evidenced by satellite images and numerical experiments. Geophysical Research Letters, 34(1). https://doi.org/10.1029/2006gl028103

Zeng, L., Chassignet, E. P., Schmitt, R. W., Xu, X., & Wang, D. (2018). Salinification in the South China Sea since late 2012: A reversal of the freshening since the 1990s. Geophysical Research Letters, 45(6), 2744–2751. https://doi.org/10.1002/2017gl076574

Zeng, L., Timothy Liu, W., Xue, H., Xiu, P., & Wang, D. (2014). Freshening in the South China Sea during 2012 revealed by Aquarius and in situ data. Journal of Geophysical Research: Oceans, 119(12), 8296–8314. https://doi.org/10.1002/2014jc010108

Zeng, L., Wang, D., Xiu, P., Shu, Y., Wang, Q., & Chen, J. (2016). Decadal variation and trends in subsurface salinity from 1960 to 2012 in the northern South China Sea. Geophysical Research Letters, 43(23), 12,181-12,189. https://doi.org/10.1002/2016gl071439

Zhai, F., & Hu, D. (2013). Revisit the interannual variability of the North Equatorial Current transport with ECMWF ORA-S3. Journal of Geophysical Research: Oceans, 118(3), 1349–1366. https://doi.org/10.1002/jgrc.20093

Zhang, C. (2005). Madden-Julian oscillation. Reviews of Geophysics, 43(2). https://doi.org/10.1029/2004rg000158

Zhang, C. (2013). Madden–Julian oscillation: Bridging weather and climate. Bulletin of the American Meteorological Society, 94(12), 1849–1870. https://doi.org/10.1175/bams-d-12-00026.1

REFERENCES

Zhang, L., Wang, B., & Zeng, Q. (2009). Impact of the madden–julian oscillation on summer rainfall in southeast China. Journal of Climate, 22(2), 201–216. https://doi.org/10.1175/2008jcli1959.1

Zhang, Y. J., Ateljevich, E., Yu, H.-C., Wu, C. H., & Yu, J. C. S. (2015). A new vertical coordinate system for a 3D unstructured-grid model. Ocean Modelling, 85, 16–31. https://doi.org/10.1016/j.ocemod.2014.10.003

Zhang, Z., Zhao, W., Tian, J., Yang, Q., & Qu, T. (2015). Spatial structure and temporal variability of the zonal flow in the Luzon Strait. Journal of Geophysical Research: Oceans, 120(2), 759–776. https://doi.org/10.1002/2014jc010308

Zhao, W., Zhou, C., Tian, J., Yang, Q., Wang, B., Xie, L., & Qu, T. (2014). Deep water circulation in the Luzon Strait. *Journal of Geophysical Research: Oceans*, *119*(2), 790–804. https://doi.org/10.1002/2013jc009587

Zhou, T., Yu, R., Li, H., & Wang, B. (2008). Ocean forcing to changes in global monsoon precipitation over the recent half-century. Journal of Climate, 21(15), 3833–3852. https://doi.org/10.1175/2008jcli2067.1

Zhou, W., & Chan, J. C. L. (2007). ENSO and the South China Sea summer monsoon onset. International Journal of Climatology, 27(2), 157–167. https://doi.org/10.1002/joc.1380

Zhu, Y., Sun, J., Wang, Y., Li, S., Xu, T., Wei, Z., & Qu, T. (2019). Overview of the multi-layer circulation in the South China Sea. Progress in Oceanography, 175, 171–182. https://doi.org/10.1016/j.pocean.2019.04.001

Zhu, Y., Sun, J., Wang, Y., Wei, Z., Yang, D., & Qu, T. (2017). Effect of potential vorticity flux on the circulation in the South China Sea. Journal of Geophysical Research: Oceans, 122(8), 6454–6469. https://doi.org/10.1002/2016jc012375

Zhuang, W., D. X. Wang, J. Y. Hu, and W. S. Ni (2006), Response of the cold water mass in the western South China Sea to the wind stress curl associated with the summer monsoon, Acta Oceanol. Sin., 25(4), 1–13.